Doctoral thesis

(Dissertation)

Purification of nanoparticle-containing environmental media

To obtain the doctoral degree

Doctor rerum naturalium (Dr. rer. nat)

At the Bayreuth Graduate School for Mathematics and

Natural Sciences (BayNat)

University Bayreuth

Submitted by

M.Sc. Ann-Kathrin Müller

Born in Osnabrück

Bayreuth, December 2021

This thesis was prepared from December 2018 to December 2021 at the Chair of Macromolecular Chemistry II (MCII) of the Faculty of Biology, Chemistry and Geosciences at the University of Bayreuth, under the supervision of Prof. Dr. Andreas Greiner.

All of the above work was carried out in the research group of Prof. Dr. Andreas Greiner at the University of Bayreuth. Biological tests were conducted at the animal ecology I (Prof. Laforsch) and process biotechnology (Prof. Freitag).

This is a full reprint of the thesis submitted to obtain the academic degree of Doctor of Natural Science (Dr.rer.nat.) and approved by the Bayreuth Graduate School of Mathematical and Natural Sciences (BayNAT) of the University of Bayreuth.

Dissertation submitted on: 1.12.2021

Approved by the Leitungsgremium: 21.12.2021

Scientific colloquium: 2.05.2022

Acting director: Prof. Dr. Hans Keppler

Audit committee:

Prof. Dr. Andreas Greiner (Reviewer)

Prof. Dr. Peter Strohriegel (Reviewer)

Prof. Dr. Birgit Weber (Chairman)

Prof. Dr. Markus Retsch

(additional reviewer: Prof. Dr. Annette Andrieu-Brunsen)

This thesis is written as cumulative dissertation.

During my doctoral studies, the following four publications were written.

(1) Preparation and Performance Assessment of Low-Pressure Affinity Membranes based on Functionalized, Electrospun Polyacrylates for Gold Nanoparticle Filtration

A-K. Müller, Z-K. Xu, A. Greiner, *ACS Appl. Mater. Interfaces* **2021**, 13, 13, 15659-15667.

https://doi.org/10.1021/acsami.1c01217

Discussion in chapter 2.3, reprinted in chapter 3.1.

(2) Sustainable Electrospun Affinity Membranes for Water Remediation by Removing Metal and Metal Oxide Nanoparticles

A-K. Müller, Z-K. Xu, A. Greiner, *ACS Appl. Poly. Mater.* **2021,** 3, 11, 5739-5748.

https://doi.org/10.1021/acsapm.1c00990

Discussion in chapter 2.4, reprinted in chapter 3.2.

(3) Disentangling biological effects of primary nanoplastics from dispersion paints' additional compounds

A-K. Müller, J. Brehm, M. Völkl, V. Jèrôme, C. Laforsch, R. Freitag, A. Greiner, *Ecotoxicol. Environ. Saf.*, **2022**, 242, 113877.

https://doi.org/10.1016/j.ecoenv.2022.113877

Discussion in chapter 2.5, reprinted in chapter 3.3.

(4) Filtration of Paint-contaminated Water by Electrospun Membranes

A-K. Müller, Z.-K. Xu, A. Greiner, *Macromol. Mater. Eng.*, **2022**, 2299238.

https://doi.org/10.1002/mame.202200238

Discussion in chapter 2.6, reprinted in chapter 3.4.

---

*Additional publications prepared during doctoral time:

J. Dietler et al, Photobiologically Directed Assembly of Gold Nanoparticles, *Adv. Biology* **2020**, 5, 2000179. https://doi.org/10.1002/adbi.202000179

Contents

Zusammenfassung

Diese Arbeit legt eine Grundlage zum umfassenden Verständnis von Mechanismen und Anwendungen von elektrogesponnenen Affinitätsmembranen für die Reinigung von nanopartikelhaltigen Umweltmedien und zeigt neue Strategien zur Separation auch für zukünftige Umweltschadstoffe auf. Basierend auf der Annahme, dass Nanopartikel durch Wechselwirkungen mit der Membranoberfläche adsorbiert werden können, wurden chemischen funktionelle Gruppen zur Herstellung von Affinitätsmembranen genutzt. Auf Adsorption basierende Filtrationsmechanismen sind allgemein als Affinitätsmembranen bekannt und zeichnen sich durch große Vorteile aus, wie z. B. hohe Filtrationseffizienzen und geringe Druckverluste. Diese Membranen wurden aus Copolymeren auf Acrylatbasis hergestellt. Die Copolymere wurden durch radikalische Copolymerisation von Methylmethacrylat und Acrylatmonomeren mit verschiedenen chemischen Funktionsgruppen synthetisiert, die als Adsorptionsstellen für Nanopartikel dienen sollten: Säure (AA), Pyridin (Pyr), Amid (NIPAM) und quaternäres Ammonium (Nplus). Zusätzlich wurde ein Benzophenon-Acrylat-Monomer als ultraviolett (UV)-adressierbare Einheit eingebaut. Die resultierenden Copolymere wurden elektrogesponnen und anschließend mit UV-Licht vernetzt. Die Vernetzung verringerte die Quellung der Fasern und die Schrumpfung der Porengröße in Wasser, und die mechanischen Eigenschaften wurden erheblich verbessert. Darüber hinaus wurde der Druckabfall an der Membran im Wasserdurchfluss bestimmt, welcher eine Korrelation mit der Porengröße der Membran, der mechanischen Festigkeit und der Hydrophilie des Membranmaterials aufzeigte.

Goldnanopartikel mit einem hydrodynamischen Radius von ~9 nm wurden als Modellsystem für Filtrationsexperimente hergestellt. Die folgenden Experimente wurden für Membranen mit den vier chemischen Funktionsgruppen durchgeführt und zeigten eine erfolgreiche Filtration für die Nplus und Pyr funktionelle Gruppe. Die Filtrationseffizienz für beide Gruppen nahm mit der Zeit ab, da die Adsorptionsstellen durch Nanopartikel besetzt wurden. Die Gesamtzahl der Adsorptionsstellen bzw. die Filtrationseffizienz kann durch eine höhere Anzahl von funktionellen Gruppen verbessert werden.

Es wurden weitere wesentliche Einflussfaktoren auf die Filtrationseffizienz ermittelt, wie die Größe der Nanopartikel, das Material und die Liganden der Nanopartikel. Goldnanopartikel mit Größen im Bereich von 20-150 nm wurden durch eine Partikelwachstums-Methode synthetisiert. Diese Nanopartikel wurden mit der Pyr und Nplus Membran gefiltert. Für beide

Membranen wurde eine Abnahme der Filtrationseffizienz mit abnehmender Partikelgröße festgestellt.

Um den Einfluss des Nanopartikelmaterials auf die Filtrationseffizienz zu untersuchen, wurden nicht nur Edelmetall-Nanopartikel, sondern auch Metalloxid-Nanopartikel wie Kupferoxid, Zinkoxid, Eisenoxid und Titandioxid synthetisiert. Diese Metalloxid-Nanopartikel besitzen ein positives Zetapotenzial und wurden durch Membranen mit Säure- und Amidfunktionalität mit hoher Effizienz gefiltert. Darüber hinaus wurden verschiedene Liganden wie Polyvinylpyrrolidon, Pyrophosphat und Citrat als Liganden für die Nanopartikel hinzugefügt wobei festgestellt wurde, dass sie den hydrodynamischen Radius und das Zetapotenzial der Nanopartikel verändern. Negativ geladene Nanopartikel, die durch Zugabe von Pyrophosphat- und Citrat-Liganden erhalten werden können, wurden erfolgreich durch die Nplus Membran gefiltert. Somit wurden günstige Kombinationen für das Erzielen einer hohen Filtrationseffizient identifiziert: positiv geladenen Nanopartikeln/Nplus-Membran und negativ geladenen Nanopartikeln/AA-Membran. Hier basiert der Filtrationsmechanismus entweder auf elektrostatischen Wechselwirkung oder Koordinationschemie.

Es kann davon ausgegangen werden, dass Umweltmedien aus einer Vielzahl von Materialien bestehen, weshalb eine Membran zur Adsorption verschiedener Nanopartikel von Vorteil sein könnte. Um die gleichzeitige Filtration von Nanopartikeln mit unterschiedlichen Materialien und Eigenschaften zu erreichen, wurden die quaternäre Ammonium- und Säurefunktionalität in einer Janus- oder Mischmembran kombiniert. Beide Kombi-Membranen zeigten hohe Filtrationsleistungen und es konnte nachgewiesen werden, dass keines der Nanopartikel bevorzugt adsorbiert wird.

In einem einzigen Filtrationsschritt sind die Adsorptionsstellen der Membranen mit Nanopartikeln gesättigt und die Membran kann ohne einen Regenerationsschritt für die Filtration nicht wiederverwendet werden. Die Membranen wurden nach der Nanopartikelfiltration mit niedrig konzentrierten Säuren gespült. Die Säuren lösten die Nanopartikel auf, wodurch die regenerierten Membranen wiederverwendet werden konnte. Über drei Zyklen von Filtration und Regeneration wurde kein signifikanter Verlust der Filtrationseffizienz festgestellt.

Das erworbene Wissen über Filtrationsprinzipien konnte auf relevantere Systeme des täglichen Lebens übertragen werden. Farben, als Beispiel für kommerzielle Quellen von Nanopartikeln, wurden aufgetrennt und analysiert. Die Farbkomponenten wurden auf potenzielle, negative

Auswirkungen auf biologische Systeme wie Mikroorganismen und Zellen untersucht, um die Bedeutung der Farbfiltration zu verdeutlichen. Daphnia magna und L929-Zellen wurden als Modellsysteme ausgewählt und beide wurden den erhaltenen Farbfraktionen in unterschiedlichen Konzentrationen ausgesetzt: Polyacrylat-Nanopartikel, Titandioxid-Nanopartikel, Calciumcarbonat-Mikropartikel und dispergiertes Polyacrylat. Für alle Fraktionen wurde eine dosisabhängige negative Auswirkung auf die Vitalität der Wasserflöhe und die Stoffwechselaktivität der Zellen festgestellt. Diese Ergebnisse weisen auf den steigenden Bedarf an hochentwickelten Wasserreinigungsmethoden hin. Daher wurde die Nplus Membran für die Filtration von Farben und Farbfraktionen getestet. Alle Farbfraktionen wurden erfolgreich mit hohen Wirkungsgraden gefiltert, die auf unterschiedlichen Filtrationsmechanismen beruhen. Die Mikropartikel wurden durch einen Größenausschluß-Mechanismus abgetrennt, während die Nanopartikel und das dispergierte Polymer durch elektrostatische Adsorption im Membranvolumen gefiltert wurden.

In dieser Arbeit wurden Mechanismen und Anwendungen der Affinitätsmembranen für die Filtration von Nanopartikeln erforscht und das Potenzial von elektrogesponnenen Membranen für Anwendungen in der Filtration von potenziellen Umweltschadstoffen veranschaulicht.

Summary

This thesis delivered profound work for comprehensive understanding of mechanisms and applications of electrospun affinity membranes for the purification of nanoparticle-containing environmental media, and identifies new strategies for the separation of prospective environmental pollutants. Based on the hypothesis that nanoparticles can be filtered through interactions with the fiber surface, chemical functional groups were used to fabricate affinity membranes. Adsorption-based filtration mechanisms are generally known as affinity membranes and have been identified to feature great advantages, such as high filtration efficiencies and low drops in pressure. These membranes were prepared from acrylate-based copolymers. The latter were synthesized by free-radical copolymerization of methyl methacrylate and acrylate monomers with different chemical functional groups, which should act as nanoparticle adsorption sites: acid (AA), pyridine (Pyr), amide (NIPAM), and quaternary ammonium (Nplus). Additionally, a benzophenone acrylate monomer was incorporated as an ultraviolet (UV) responsive unit. The resulting copolymers were electrospun, followed by cross-linking with UV light. The subsequent cross-linking reduced the fiber swelling and pore size shrinkage in water, and enhanced the mechanical properties substantially. Furthermore, the pressure drop on the membrane under water flow conditions was determined, demonstrating a correlation of the membrane pore size, the mechanical strength, and hydrophilicity of the membrane material.

Gold nanoparticles with ~9 nm hydrodynamic radius were prepared as a model system for filtration experiments. The following experiments were executed for membranes with the four chemical functional groups, demonstrating successful filtration for the Nplus and Pyr functional group. The filtration efficiency for both groups declined with time, because adsorption sites were getting blocked by nanoparticles. The total number of adsorption sites, respectively, the filtration efficiency, can be enhanced by a higher number of functional groups.

Other essential influences on the filtration efficiency were determined, such as nanoparticle size, material, and ligands. Gold nanoparticles with sizes in the range of 20–150 nm were synthesized by the particle growth mechanism. These nanoparticles were filtered with the Pyr and Nplus membranes. A decline in filtration efficiency was detected for both membranes with decreasing particle size.

To investigate the impact of the nanoparticle material on the filtration efficiency, not only noble metal nanoparticles but also metal oxide nanoparticles, such as copper oxide, zinc oxide, iron oxide, and titanium dioxide, were synthesized. These metal oxide nanoparticles possess positive zeta potentials and were filtered with high efficiencies by membranes with the acid and amide functionality. Additionally, different ligands were added as nanoparticle ligands and found to change the nanoparticles' hydrodynamic radius and zeta potential. Negatively charged nanoparticles, which can be obtained by the addition of pyrophosphate and citrate ligands, were successfully filtered by the Nplus membrane. Thus, favorable combinations of positively charged nanoparticles/Nplus membrane and negatively charged nanoparticles/AA membrane were identified to achieve high filtration efficiencies. The filtration mechanism here is based on either the electrostatic interaction or coordination chemistry.

Since environmental media can be assumed to be composed of a variety of materials, a membrane for adsorption of different nanoparticles might be advantageous. To achieve the simultaneous filtration of nanoparticles which are different in material and properties, the quaternary ammonium and acid functionalities were combined in a janus or mixed type membrane. Both combi membranes were proved to have high filtration efficiencies and evidenced that none of the nanoparticles had preferential adsorption.

The membranes' adsorption sites are saturated with nanoparticles in a single filtration step and the membrane cannot be reused without a regeneration step. Membrane regeneration was achieved by rinsing the membranes with low-concentrated acids after nanoparticle filtration. The acids dissolved the nanoparticles and the regenerated membranes could be used again. No significant loss in filtration efficiency was observed over three cycles of filtration and regeneration.

The knowledge gained about filtration principles could be transferred to the more relevant systems in daily life. White wall paint, as an example of commercial sources of nanoparticles, was separated and analyzed. The paint's components were investigated for their potential adverse effects on biological systems, such as microorganisms and cells. *Daphnia magna* and L929 cells were chosen as model systems and both were exposed to the paint fractions received at different concentrations: polyacrylate nanoparticles, titanium dioxide nanoparticles, calcium carbonate microparticles, and dispersed polyacrylate. A dose-dependent negative impact on the daphnids' vitality and cells' metabolic activity was determined for all fractions. These results pointed out the rising demand for sophisticated water purifications methods. Thus, the Nplus

membrane was tested for the filtration of paints and paint fractions. All paint fractions were successfully filtered with high efficiencies based on different filtration mechanisms. The microparticles were separated by a size-exclusion mechanism, whereas the nanoparticles and the dispersed polymer are supposed to be filtered in the membrane volume by electrostatic adsorption.

This thesis explored the mechanisms and applications of affinity membranes for nanoparticle filtration and highlights the potential of electrospun membranes for applications in the filtration of prospective environmental contaminants.

1. Introduction and State of the Art

This thesis explores the filtration of nanoparticles by electrospun membranes. Background information regarding nanoparticle synthesis, properties, and their safety and fate in the environment are given to illustrate the motivation of this work. Furthermore, details about the electrospinning setup and process are explained to visualize the concept of electrospun membranes for the unfamiliar reader. Finally, background information about the filtration concepts and mechanisms is described, and new topics occurring and future directions in this field are represented.

1.1 Nanoparticles

The evolution of nanoscience and nanotechnology can be stated as key factors for the technological development in the recent past.[1] Nanomaterials are generally defined as materials in the size range of 1–100 nm and can be subdivided according to their dimensions.[2] Zero-dimensional nanomaterials possess both dimensions on the nanoscale and a prominent example are nanoparticles. Nanorods or nanotubes can be classified as one-dimensional materials, whereas nanosheets are attributed to two-dimensional materials.[3]

1.1.1 Preparation Methods

Nanomaterials can be produced by the top-down or bottom-up method (**Scheme 1**) from different material types, such as carbon, metal, polymers,[4] and lipids. The top-down approach characterizes the fragmentation of bulk materials under the formation of nanostructures.[5] Complex, expensive, and highly energy-intensive setups are often required for top-down approaches, which lack the formation of uniform shapes and sizes, and induce surface-defects.[6] Thus, bottom-up approaches are preferably utilized, especially wet-chemical synthesis is favored due to its simplicity, modularity, and scalability.[7] A wide range of parameters affect the particle formation process in wet-chemical synthesis: the precursor type, heating method, heating/cooling rate, temperature, concentration, mixing, ligand types, solvent properties, sequence and rate of addition.[7] Besides these influences, the nucleation and growth kinetics mainly determine the particle size. However, differences in size and shape can be detected when batches that had been produced according to the same procedure are compared.[8]

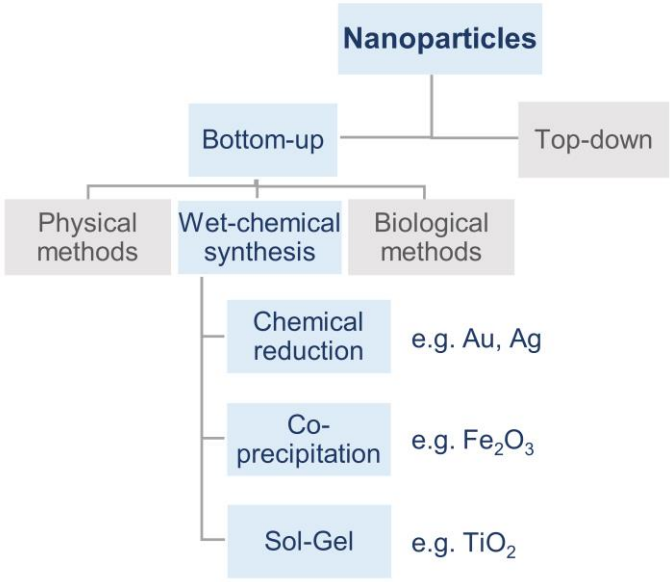

Scheme 1. *Nanoparticle synthesis methods.*

Chemical reduction, co-precipitation, and sol-gel are relevant wet-chemical methods for the production of metal and metal oxide nanoparticles.

The chemical reduction method is applied for the formation of noble metal nanoparticles, such as gold[9] and silver nanoparticles[10]. In the process, metal ions are dissolved in aqueous media and are then reduced in the presence of a reducing agent to zero-valent atoms. A typical reducing agent is sodium borohydride, which is often used in combination with surfactants as nanoparticle stabilizers.[11] The reduced zero-valent atoms shape first clusters, which coalescence under the formation of small nanoparticles. The nanoparticle number remains constant in the following growth process, whereby particle growth is reached by the addition of gold salts on the nanoparticle surface with subsequent surface reduction.[12]

In co-precipitation methods, two or more water-soluble salts of divalent or trivalent metal ions are mixed in an aqueous solution. These metal ions are reduced to form at least one insoluble salt. Reduction is initiated under vigorous stirring at a certain pH value, which is maintained by the addition of alkaline medium.[13] When enough insoluble salts exist to reach supersaturation, the nucleation process is started by precipitation. Nucleation is characterized by the formation of the smallest elementary particles of a new thermodynamic phase. This smallest elementary particle experiences high surface energy, which is a driver for particle growth.[14]

The sol-gel method is another wet-chemical synthesis and is prominent for the preparation of titanium dioxide nanoparticles.[15] The sol-gel method consists of five main steps. In the first

step, metal-alkoxides are hydrolyzed by water or alcohols, which can be catalyzed by acids and bases (**Scheme 2**).[16] The resulting sol is further converted to a gel by increasing viscosity due to the formation of a branched network. The network evolves by the condensation reaction of two hydrolyzed metal centers which can occur by oxolation or olation. The formation of an oxygen bond is termed oxolation, whereas olation means the hydroxyl bond between two metal centers.[17]

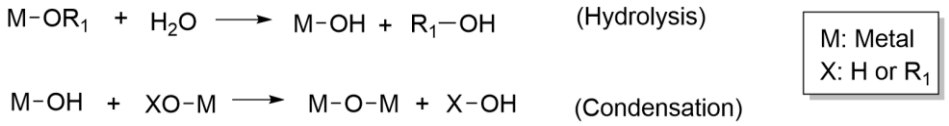

***Scheme 2**. Reaction scheme for sol-gel method.*[17]

The condensation step is followed by the aging step. During aging, the condensation process continues, resulting in a decreasing particle porosity and increased thickness between colloidal particles. These particles can be dried and further calcinated to reduce the particle porosity and remove water or organic compounds.[18]

1.1.2 Stabilization Mechanisms

Surfactants or polymers are often added to stabilize colloidal dispersions. The addition of stabilizers can take place *in-situ*, which might influence particle growth kinetics, or post-synthesis.[19] In general, stabilization of nanoparticles means the avoidance of agglomeration and sedimentation. The rate of nanoparticle agglomeration is dependent on the energetics and frequency of nanoparticle collisions.[20] In addition to the collision frequency, the interaction potentials also determine whether an elastic or inelastic collision occurs. The total interaction potential can be calculated according to the Derjaguin-Landau-Verwey-Overbeek (DLVO) theory as a function of the separation distance and radius of curvature.[21] At short distances, the attractive Van-der-Waals forces dominate, whereas repulsive forces are given by electrostatic interactions. Nowadays, the DLVO theory is extended by a variety of different parameters, since the DLVO theory does not consider the chemical composition, shape, or surface coatings.[22] The probability of flocculation, namely, inelastic collisions, can be estimated by the maximum potential energy barrier and kinetic energy barrier calculated from collision theory. If the potential energy is roughly ten times larger than the product of the absolute temperature and Boltzmann constant particles remain stable in dispersion.[23]

The electrostatic interaction of nanoparticles results from nanoparticle charges. The surface charge attracts oppositely charged dispersants leading to the formation of an electrostatic double

layer (**Figure 1**).[24] When an electrostatic field is applied to a nanoparticle dispersion, negatively charged nanoparticles move toward the positively charged electrode, in contrast to the nanoparticles' positively charged dispersants, which are slipped off at the slipping plane. The potential measured at the slipping plane is defined as the zeta potential. Nanoparticles with the same zeta potential repel each other, resulting in stable nanoparticle dispersions.[25]

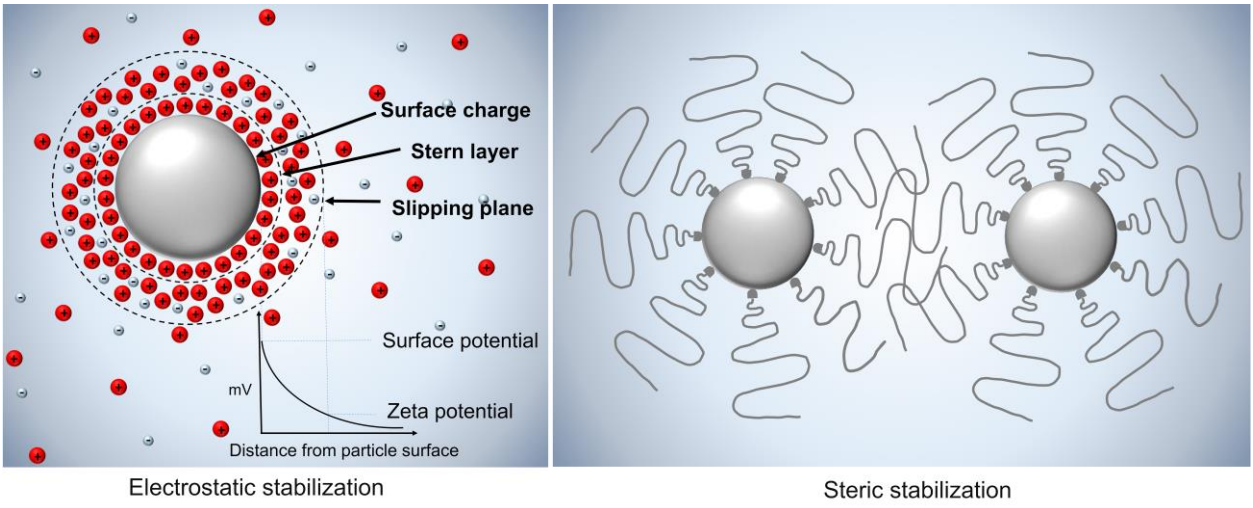

Figure 1. *Electrostatic[26] and steric stabilization[27] of nanoparticles.*

Nanoparticle stabilization cannot only be reached by electrostatic repulsion but also steric stabilization. Steric stabilization is reached by implementing ligands that require significant space due to steric effects and create a steric barrier around the nanoparticle. This barrier restricts the volume and hinders a nanoparticle from approaching another, which is known as the excluded volume effect.[28] If the nanoparticle attraction is still high, the solvent molecules surrounding each nanoparticle are squeezed out upon close approach, generating an osmotic pressure. If attractive forces do not overcome the osmotic pressure, nanoparticle coagulation is inhibited.[29]

Steric stabilization is achieved by polymeric ligands, which are either grafted-to or grafted-from the nanoparticles. In the grafting-from approach, polymerization takes place on the nanoparticle surface, in contrast to the grafted-to approach, where polymers are immobilized on the nanoparticle surface by attractive forces.[30] In the grafting-to method, polymer chains can bind to numerous nanoparticle surface sites at the same time under the formation of different segments: 1) trains are built at the solid-liquid interface, 2) loops bond at both polymer ends, and 3) tails are only fixed at one polymer end on the nanoparticle surface.[31] Non-interacting groups are responsible for the occurrence of loops or tails, which could also be designed by end-capped polymers or block-copolymers.[32],[33] The thickness of the steric barrier can be

controlled by the length of trains, loops, and tails. However, the increase of the steric barrier with increasing polymer chain length is limited since very long polymer chains might fold back onto themselves, leading to flocculation.[31]

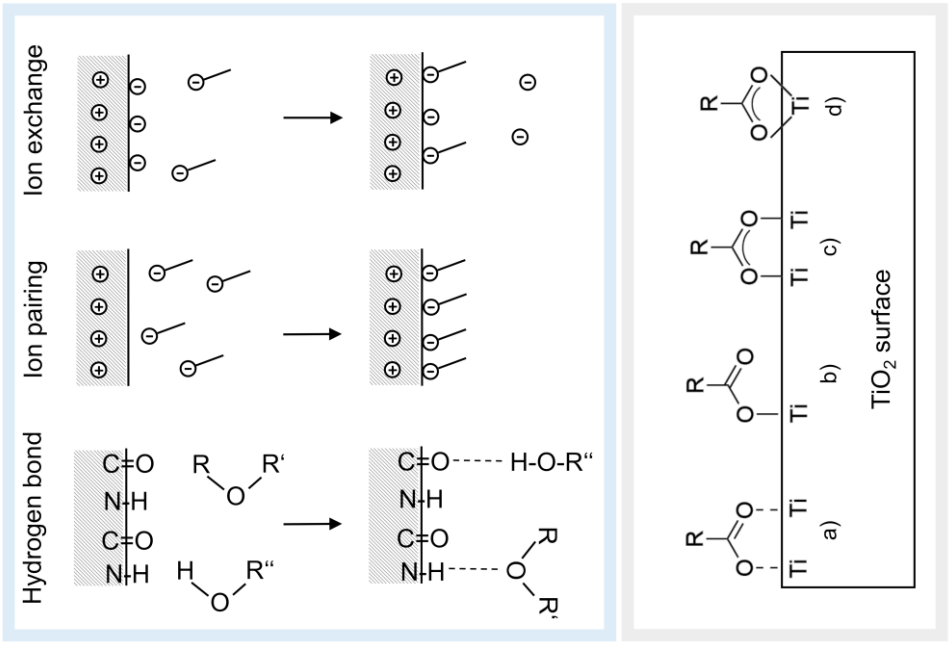

Figure 2. *Common non-covalent adsorption mechanisms onto substrate surfaces (Heinz et al.)[34] and adsorption mechanisms of carboxylate ligands on titanium nanoparticles: a) physical adsorption, b) monodentate coordination, c) bridging chemisorption, d) chelating chemisorption. (Elbasuney et al.)[31]*

Various functional groups have been proven to bind and stabilize successful metal nanoparticles, such as carboxylic acids, thiols, amine, sulfonic, and phosphoric acids.[35] The ligands assemble on the nanoparticle surface via a covalent bond or non-covalent adsorption. A common example of covalent bonds is the thiol group bond onto a gold nanoparticle surface, but metal oxides can also be easily functionalized. The non-covalent adsorption mechanism includes ion exchange, ion pairing, and hydrogen bonding (**Figure 2**).[34] In the case of carboxylic ligands, monodentate coordination, bridging chemisorption or chelating chemisorption are also possible interaction modes.[31]

1.1.3 Physicochemical Properties

The choice of ligands determines the colloidal stability and function of nanoparticles, but the size, shape, and material or the inorganic nanoparticle core is responsible for the properties.[36] Metal and metal oxide nanoparticles feature unique properties, such as high reactivity, surface plasmon resonance, and superparamagnetism, based on their high surface area and quantum confinement (**Figure 3**).

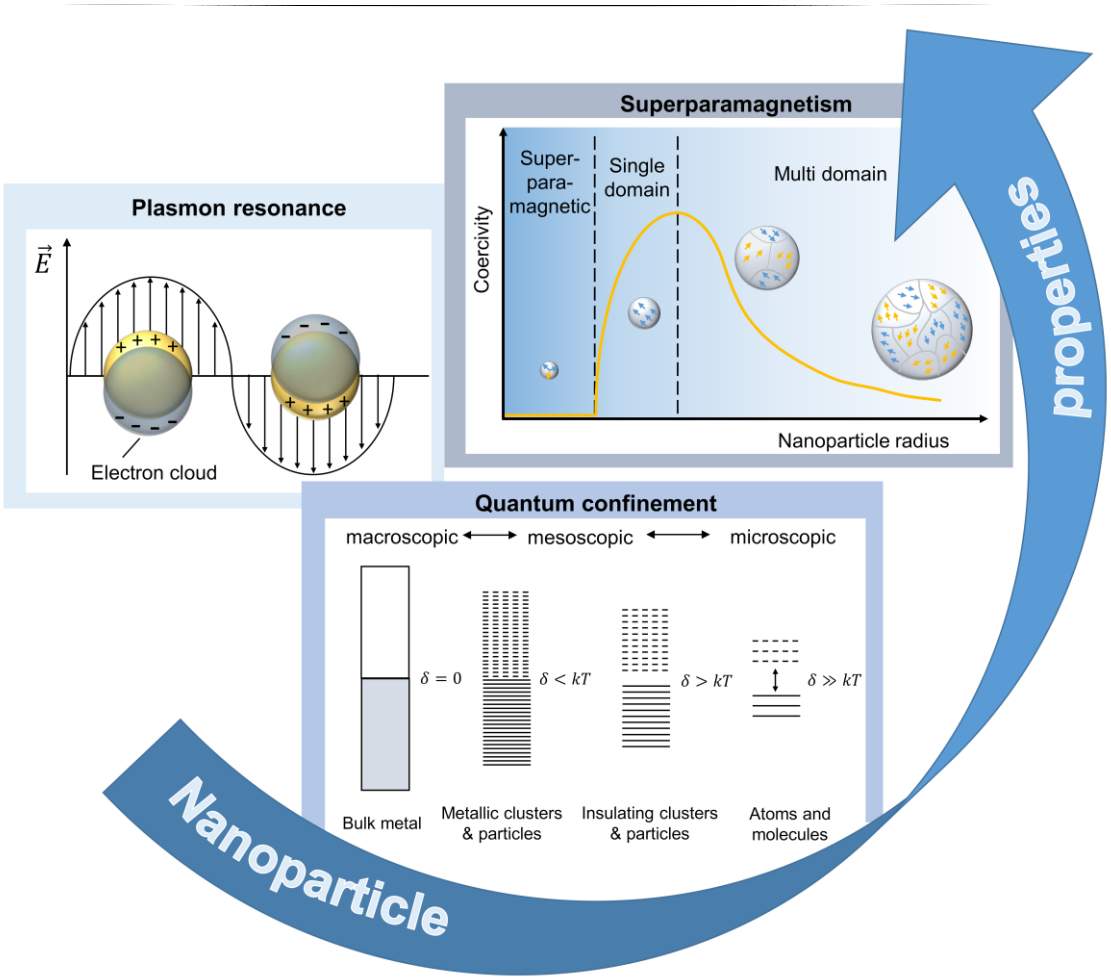

Figure 3. *Basic concept of the nanoparticle properties, such as plasmon resonance,[37] superparamagnetism,[38] and quantum confinement.[39]*

One essential property of nanoparticles is their high reactivity, which is linked to the nanoparticle size. As material size decreases, the number of unsaturated surface atoms increases. Unsaturated surface atoms possess incomplete bonding and, thus, enhance the density of dangling bonds on the nanoparticle surface. The incomplete bonding of the surface atoms increases the surface energy, resulting in a higher nanoparticle reactivity.[40] The reactivity further advances with declining particle size due to the increasing population of unsaturated surface atoms, especially nanoparticles below 5 nm showed distinct reactivity.[41] However, the nanoparticle shape also plays a crucial role. Polygonal-shaped nanoparticles possess active coordination sites at crystal edges, corners, and facets.[42] These coordination sites might affect the binding strength of reactants and intermediates and, thus, determine the reactivity and selectivity.[39],[43] In some cases, even catalytic surface reconstruction or refaceting occurs within the adsorption process.[44] Further influences on nanoparticle reactivity are capping agents,[45] solvents, supports,[42] or the integration of heteroatoms.[46] In addition to coordination surface atoms, quantum size effects are also suspected of manipulating

nanoparticle reactivity. However, the causation between size-dependent electronic properties and catalytic activity has not yet been proven.[39]

Another attractive nanoparticle property is the occurrence of plasmon resonance. Nobel metal nanoparticles, such as gold or silver, possess high electron densities, which is a prerequisite for the preferential interaction with electromagnetic fields.[47],[48] These electrons can be defined as a negatively charged electron cloud displaced around the positively charged atom lattice.[49] Under the radiation of an electromagnetic wave, the electron cloud is displaced from its equilibrium state. For nanoparticles smaller than the excitation wavelength, the electron cloud is driven to the nanoparticle surface opposite to the direction of the electromagnetic field.[50] Since the electromagnetic field is described as a periodic wave with a certain frequency, the electron cloud is shifted from the nanoparticle surface side-to-side along with the frequency of the incoming electromagnetic wave.[51] This collective oscillation of the free electrons is defined as plasmons (**Figure 3**).[52] The plasmons can be considered as a mass-spring harmonic oscillator, where the mass is represented by the electron density and the spring constant is set by the coulomb restoring force between electrons and lattice atoms. The electron oscillation is time-limited due to electron gas confinements or structural imperfections causing energy loss.[47] The interaction between material and light can lead to either light scattering, adsorption, or near-field enhancement.[53] At present, the Mie theory is the main model for interpreting these optical phenomena.[54] Light scattering is provoked by the emission of light from the induced dipole at the same frequency as the incidental light but scattering in all directions. This is in contrast to absorbed light, which is converted to heat or crystal lattice vibration.[55] The plasmon resonance can be affected by the nanoparticle size, shape, and composition, as well as surrounding media.[56]

The third outstanding property of metal nanoparticles is their magnetic behavior. Magnetism usually occurs in metal materials caused by their electrons and is defined as a response of magnetic materials to an applied magnetic field.[57] Five basic types of magnetism exist: diamagnetism, paramagnetism, ferromagnetism, ferrimagnetism, and antiferromagnetism.[58] Ferromagnetic materials, such as iron or iron oxides, are composed of small regions, which are called magnetic domains. These magnetic domains are a result of the balance of different energy terms. The energy for the alignment of all magnetic moments in the same direction counteracts the energy for the orientation of all magnetic moments along a specific direction, and the energy for elimination of the magnetization in the material.[59] Thus, the magnetic moments in each domain are aligned and oriented in the same direction, but the orientation of each domain is

different. Ferromagnetic materials commonly exist in multi domains with domain sizes of roughly 100 nm. Since these domains cannot split further into smaller domains, small nanoparticles may contain only a single domain.[38] The magnetic moment for very small magnetic nanoparticles fluctuates around the center axis of the magnetization until an external magnetic field is applied and leads to the fast alignment of the magnetic moments in the magnetic field. This phenomenon is defined as superparamagnetism and can occur below the blocking temperature.[60] The superparamagnetism can be measured by coercivity, which is the magnetic field required to bring the magnetization back to zero (**Figure 3**).[61]

1.1.4 Fate and Safety

Metal nanoparticles possess unique electronic, optical, and magnetic characteristics and, thus, nanoparticles composed of metals or metal oxides are the most widely used. These qualities facilitate technological development in different economic sectors, such as the automotive, biomedical, cosmetic, energy, and electronic industries.[62] The utilization of nanoparticles in a variety of economic sectors worldwide has led to annual nanoparticle production in high quantities. The highest global production quantities have been estimated for SiO_2 (5500 tons/year), TiO_2 (3000 tons/year), and ZnO (550 tons/year).[63] The rising demand for nanotechnological products and applications has driven the value of the global market in this sector to $39.2 billion in 2016 and it is expected to reach $90 billion in 2021.[64] With the constantly increasing nanoparticle production and use, simultaneously, the possibility for nanoparticle escape into the environment increases as well. Diverse nanoparticle escape scenarios have already been identified, ranging from production to use to disposal.[65] Besides unintentional release, for example, from sunscreen,[66],[67] cosmetics,[68] paints,[69] clothing,[70],[71] and health-related applications,[72] nanoparticles are also intentionally released into the environment. Common examples of intentional release scenarios are the nanoparticle usage for remediation,[73] agriculture,[74] or water purification processing.[75] Nevertheless, both the intentional and unintentional release of nanoparticles has led to their emergence and accumulation in the environment.[76]

Paints are a source of commercially applied nanoparticles, which consume 10–30 % of the total nanoparticle production.[77] Different publications have illustrated the release of titanium dioxide nanoparticles from facades and road markings. These external surfaces are exposed to weathering,[78],[79] leading to the degradation of the paint matrix followed by nanoparticle release with wind, water, or mechanical vibrations.[80] The extent of nanoparticle release is promoted by weathering circumstances, for example, more nanoparticles are released during

heavy rainfall,[81] or in the winter.[69] Azimzada et al. proved the release of 168 ±121 µg/m^2 titanium dioxide nanoparticles from facades during seven weeks in the winter.[69] However, road markings also might contribute to the titanium dioxide nanoparticle release at 150 µg/L and an estimated total discharge of titanium dioxide nanoparticles of at least 190 tons/year in the USA through urban runoff.[82]

Nanoparticles are exposed to a variety of influences in the environment, which might have the ability to induce chemical, physical, or biological transformation.[83] Photochemical processes can occur under the exposure to sunlight, such as photodegradation, oxidation, or reduction. Furthermore, a broad range of different substances can interact with nanoparticles and trigger complexation, agglomeration, aggregation, sedimentation, or dissolution.[84] Biological processes also need to be considered, initiated by microorganisms, cells, and enzymes.[85]

The human body comes into contact with commercial nanoparticles of different size, shape, oxidation state, ligands, and composition,[86] as well as with nanoparticles, which might already have undergone environmentally induced changes. The main uptake routes are via inhalation (respiratory tract), ingestion (gastrointestinal tract), or skin contact (dermal).[87] Once the nanoparticles have entered the human body, they are translocated through human barriers, interacting with the blood and lymphatic immune cells, and reaching secondary organs, such as the heart, liver, spleen, kidney, and brain.[88] All factors mentioned above affect the nanoparticles' toxicity, but for a wide range of metal and metal oxide nanoparticles, *in vitro* and *in vivo* studies have indicated that exposure to nanoparticles could induce the production of reactive oxygen species (ROS), in sequence with inflammation and the subsequent damage of proteins, cell membranes, and DNA.[89]

In addition to metal and metal oxide nanoparticles, another type of particle has attracted enormous attention in recent years: plastic micro- and nanoparticles.[90],[91] Plastics have generally been similar to nanoscience an essential driver for technological development and economic growth. Annual plastic production is continuously increasing, with roughly 335 million tons of plastics in 2016[92] and, consequently, years of incorrect plastic waste management had resulted in massive pollution of the environment.[93] Plastics are often highly durable and persistent and, thus, do not degrade over years.[94] However, micro- and nanoplastics can be formed during mechanical and photo oxidative fragmentation.[95],[96] Particles formed as a consequence of plastic degradation under environmental factors are defined as secondary particles.[97] Primary plastics, by contrast, are commercially produced in

the micro or nano size range for certain applications,[98] such as personal care products,[99] or paints.[100]

The major part of research has so far been conducted in the area of marine ecosystems.[101] Plankton, algae, and fish, as part of the marine ecosystem, have demonstrated possible uptake of micro- and nanoplastics followed by the accumulation of these particles along the food chain up to higher trophic levels. [102] This pathway might only be one eventuality regarding how nanoplastics might end up in the human diet.[103] Since human body is exposed to micro- and nanoplastics, potential material toxicity was investigated. Nanoplastics' toxicity was proven in certain studies, which proposed effects similar to those of metal nanoparticles: production of ROS and translocation to other tissues, while their persistent nature renders their removal by the organism leading to chronic inflammation, increasing the risk of cancer.[104] The toxicity of metal nanoparticles and nanoplastics has recently been compared, demonstrating a higher toxicity effect for certain metal nanoparticles than for nanoplastics.[105] Both metal nanoparticles and micro- or nanoplastics might even interact with each other, creating a broader range of new influences on their toxicity, which need to be considered.[106] Nevertheless, long-term effects of both metal nanoparticles and nanoplastics are still uncertain[107] and, thus, environmental remediation becomes an important issue.[108]

Wastewater treatment plants have so far marked the end-of-life scenario of domestically used nanoparticles.[109] Different studies estimate the removal efficiency for metal nanoparticles range from very low removal efficiencies up to roughly 90 %,[110] similarly to nanoplastics.[111] The removal efficiency depends strongly on the combination of treatments applied.[112] Wastewater treatments can generally be distinguished into up to four treatment steps, which can be differentiated into physical, chemical, and biological methods (**Figure 4**).[113] However, mainly nanoparticles in the upper nanoparticle size range are removed. Therefore, the very small nanoparticles, which might possess even higher toxicity, still remain in the wastewater.[114] Another problem of metal nanoparticles in wastewater treatment plants are the antimicrobial properties of certain metals. Purification in wastewater treatment plants depends largely on the utilization of activated sludge, which is composed of diverse microorganisms. Thus, some metal nanoparticles might negatively affect the composition of the microorganisms and their efficiency for water purification.[115]

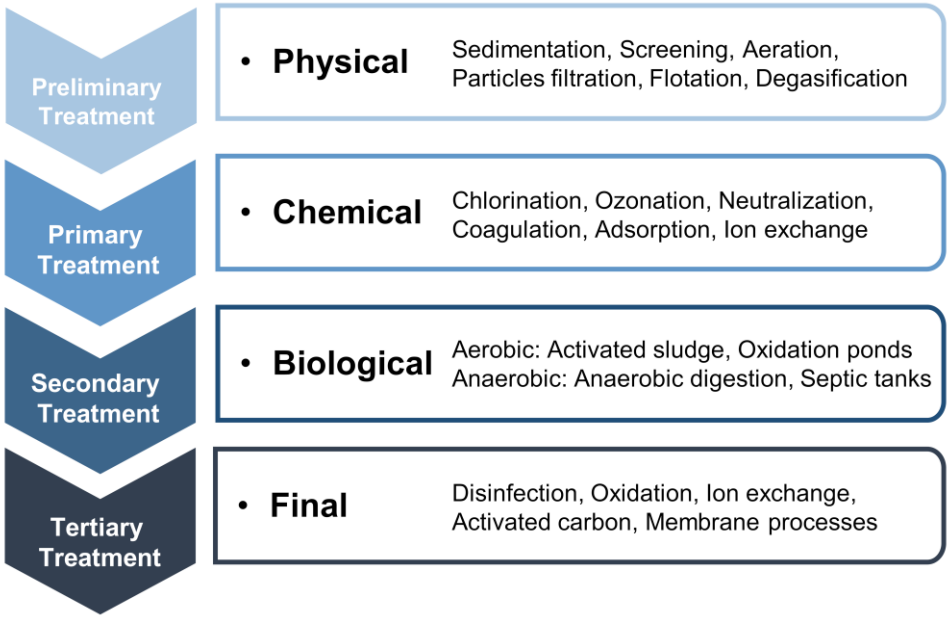

Figure 4. *Classification of wastewater treatment methods.*[113]

Finally, some nanoparticles might reach wastewater treatment plants, whereas others are released directly into the environment or result as production wastewaters, which require additional purification methods. The most promising water purification technique is the utilization of filtration processes, particularly by utilizing electrospun nanofibers.[116]

1.2 Electrospun Nonwovens

The electrospinning technique is the main production method to obtain nanofibers due to its simple, cost-effective, and versatile setup.[117] The definition of the electrospinning process is: the continuous production of fibers from polymer solutions at an applied high electric field voltage.[118] The initial exploration was dated to 1888 by Boys,[119] followed by Cooley[120] and Morton,[121] who yielded the first electrospun fibers and patented the system. Formhals made a large number of highly significant contributions in the 1930s,[122] before Taylor mathematically modeled the conical geometry of the fluid droplet by the electrical field in 1969, which is known today as the taylor cone.[123],[124],[125] Since the late 1990s, the electrospinning technique has experienced a rapid increase in research and has been developed for a broad range of materials for various applications.[126]

1.2.1 Electrospinning Procedure

Today electrospinning is performed in mainly two setups, vertical and horizontal, consisting of a spinneret, a collector, and a high voltage supply (**Figure 5**).[127] In the electrospinning process, a high voltage is applied at the spinneret, elongating the droplet into a conical shape, which is known as the taylor cone. A fine jet is ejected from the taylor cone when the critical voltage is reached and the electrostatic forces overcome the droplet surface tension.[128] Since the fine jet contains high charges, electrostatic repulsion will occur, leading to a series of whipping instabilities. The fine jet is stretched and the solvent evaporates before depositing on the collector.[129]

Traditional electrospinning setups are designed for one component and can be run as a multi-jet device.[130] For two or more components different approaches are possible. Components can be blended prior to the electrospinning if they exhibit suitable miscibility. Immiscible components can be electrospun side by side or in a coaxial setup (**Figure 5**).[131] Coaxial electrospinning can also be utilized for non-electrospinnable materials, such as low-molecular compounds. [132]

Different parameters can affect the success of the electrospinning and determine the fiber morphology and diameter. The parameters can be subdivided into three categories: solution, processing, and ambient factors.[133] Typical solution factors are viscosity, concentration, surface tension, electrical conductivity, molecular weight, and solvents. Process parameters contain the voltage applied, flow rate, collecting electrode, tip-to-collector distance, and the diameter of the needle tip. Temperature and humidity are categorized as ambient factors. In the following, the impact of different parameters on the electrospinning process are discussed.[118]

The polymer solution viscosity related to the solution concentration and polymer molecular weight determines the extent of the polymer chain entanglement. At very low concentrations or low molecular weight, polymer chains exhibit very low entanglement and, thus, micro or nanobeads will form instead of nanofibers. However, at a very high solution viscosity, clogging at the spinneret tip might occur and hinder further solution flow. Additionally, wide and flat ribbon-like fibers can result.[134] The solution conductivity, as one of the **solution factors,** affects the fiber diameter since the electrical conductivity in the droplet is essential for the formation of the taylor cone.[135],[136]

The voltage applied, as one of the **processing factors**, is reasonable for the taylor cone formation. At a higher voltage, the taylor cone decreases and, thus, smaller, beaded fibers occur.

Similarly, beaded fibers can be obtained at a too high solution flow rate because the fine jet cannot properly be dried and elongated. In addition, a very short tip-to-collector distance prevents distinct elongation and, thereby, impacts the fiber diameter.[137]

The **ambient factor**, including humidity and temperature, also influences the fiber diameter, since low humidity and high temperature facilitate fast solvent evaporation, inhibiting the fiber elongation.[116]

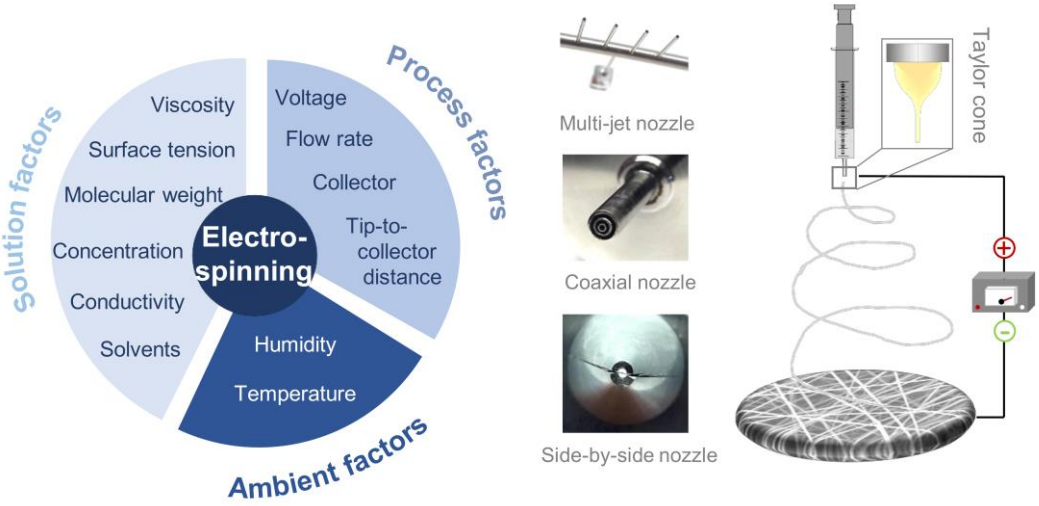

Figure 5. *Electrospinning setup with different nozzles and essential factors on the electrospinning process.*

Electrospun nanofibers possess some unique features and properties due to their fiber diameter and morphology: high porosity with interconnected voids, high surface area,[138] high aspect ratio,[139] surface functionality,[140] and high molecular orientation along the fiber axis.[141]

1.2.2 Cross-linking Electrospun Fibers

In contrast to the unique features and properties mentioned earlier, electrospun fibers often suffer from weak mechanical strength.[142] Polymer chain cross-links can be implemented to improve the fiber strength, which also prevent fiber swelling in good solvents. Cross-links can be obtained by chemical reactions. Poly (vinyl alcohol) fibers, for instance, can be cross-linked by glutaraldehyde, citric acid,[143] malic anhydride,[144] diisocyanate, etc. The chemical reactions can be executed at the electrospun fibers by dispersion in a reactive solvent mixture under acidic catalysis,[145] under thermal treatment,[146] enzymatic reaction,[147] or with reactive vapor.[148] Complex reactions have also been reported, such as converting carboxyl groups under the application of carbodiimide/hydroxysuccinimide systems into amides.[149]

Besides these wet-chemical treatments, plasma-[150] and photo cross-linking can also be utilized. Photo cross-linking possesses many advantages, such as spatio/temporal control under eco-friendly conditions.[151] Photoinitiators are excited by UV-irradiation, causing radical formation. These radicals can abstract hydrogens from the polymer chain leaving polymer radicals behind. These polymer radicals can recombine under the formation of polymer chain cross-links (**Scheme 3**).[152] The photoinitiators can either be a low molecular compound,[153] which needs to be added separately to the reaction medium, or one such as benzophenone, which can be incorporated directly into the polymer backbone.[154]

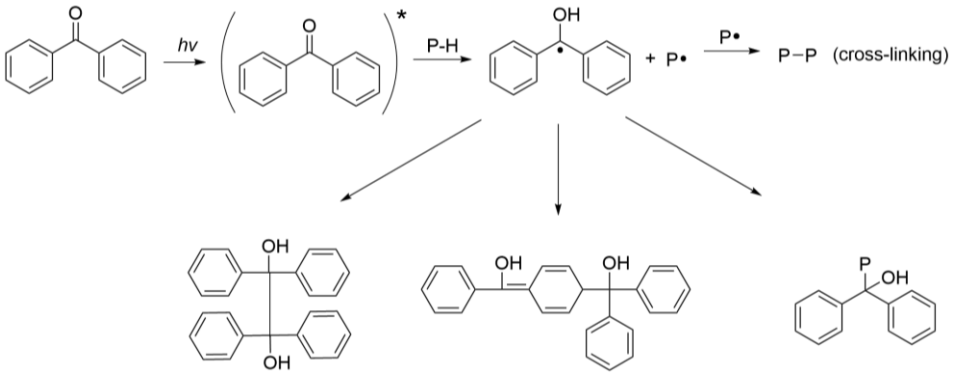

Scheme 3. *Excitation and reaction pathway for UV-cross-linking with benzophenone.*

(Qu et al.)[152]

The advantages of electrospun fibers have enabled potential applications in health/tissue, energy/sensor, catalyst/fuel cell, and environment/filtration issues.[155] Electrospun membranes have recently raised attention in the field of environmental remediation by filtration.

1.3 Filtration

In general, membranes are defined as a semipermeable barrier that separates two phases and moderates the retention or passage of substances across the membrane.[156]

There is a large selection of membrane preparation techniques, such as phase inversion, interfacial polymerization, track-etching, stretching, and electrospinning. Phase inversion refers to a membrane preparation process involving immersing a polymer cast film into a non-solvent. Due to polymer immiscibility, membrane pores are produced with pore sizes in the micro-size range.[157],[158] In order to receive smaller pores, polymerization on the surface of a membrane support can be applied. This procedure is known as interfacial polymerization.[159],[160] Pores in

the lower nano-size range can be fabricated by track-etching, which is executed by exposure of a polymeric film to heavy metal ion irradiation.[161],[162]

Another membrane fabrication technique is the preparation of fibers. Membranes can be prepared, for example, by melt-spinning followed by stretching, producing nano-sized pores in fiber tubes.[163],[164] In addition to melt-spinning electrospinning is also a versatile method for fiber preparation.

1.3.1 Theoretical Background

Membranes can be subdivided into two groups based on their structure: isotropic and anisotropic membranes (**Figure 6**). Examples of an isotropic membrane are microporous membranes and nonporous dense membranes. Microporous membranes can be characterized by a very uniform but physically heterogeneous structure, for example, containing randomly distributed, interconnected pores. The pores size varies between 0.01 and 10 μm and determines the size limit of particles which can pass the membrane. On the contrary, the separation mechanism for nonporous dense membranes is based on the solubility and diffusivity of the permeates in the membrane material. The molecules are transported through a dense film by diffusion, under the driving force of a pressure, concentration, or electrical potential gradient. An anisotropic membrane is not uniform in structure but combines two different layers. Exemplarily, the thin-film composite consists of a very thin dense and a thick porous layer.[165],[166]

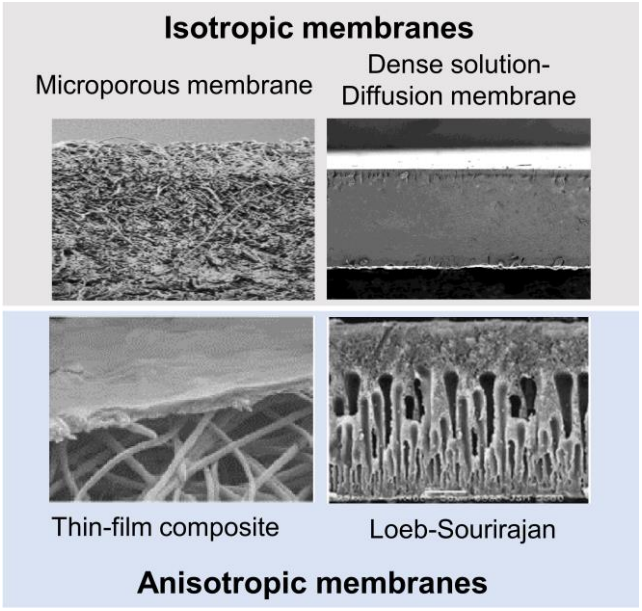

Figure 6. *Microporous membranes and dense solution-diffusion membranes as examples for isotropic membranes, as well as thin-film composite[167] and loeb-soureirajan[168] as examples for anisotropic membranes (Baker et al.).[169]*

The permeation mechanism needs to be distinguished for a microporous and a nonporous dense membrane. The two accepted mechanisms are the pore-flow and the solution-diffusion model. The pore-flow model is valid for microporous membranes and describes the permeate flow as a function of a pressure gradient across the membrane. The solution-diffusion model hypothesized the permeate transport along a concentration gradient across the membrane.[170] These two driving forces are expressed by Fick's (**Equation 1**) and Darcy's law (**Equation 2**):

Fick's law $$J_i = -D_i \frac{dc_i}{dx} \quad (1)$$

Darcy's law $$J_i = K' \cdot c_i \frac{dp_i}{dx} \quad (2)$$

The permeate's transfer rate J_i is, according to Fick's law, dependent on the diffusion constant D_i and on the concentration gradient $\frac{dc_i}{dx}$ for the pore-flow model. According to Darcy's law, the permeate's transfer rate for the solution-diffusion model is dependent on the constant *K'*, reflecting the nature of the medium, the permeate concentration c_i, and the pressure gradient $\frac{dp_i}{dx}$.[169]

The flux across the membrane – not only for porous but also for dense membranes – is dependent on the individual pore size. Poiseuille's law (**Equation 3**) relates the flux J to the pore size d and the pressure gradient Δp. The number of pores N and the pore size can be replaced by the membrane porosity ε. Furthermore, the pore length l and the solvent viscosity μ influence the permeate flux.[169]

Poiseuille's law $$J = N \cdot \frac{\pi \cdot d^4}{128 \cdot \mu \cdot l} \cdot \Delta p = \frac{\varepsilon \cdot \Delta p}{32 \cdot \mu \cdot l} \cdot d^2 \quad (3)$$

The pore size further defines the field of membrane application. Membranes are subdivided by their pore size into four main categories: microfiltration, ultrafiltration, nanofiltration, and reverse osmosis (**Figure 7**).[171]

1) *Microfiltration* is suitable for the removal of particles and finely suspended solids with a minimum size 100 nm. It is applied for liquid clarification and sterile filtration. The operating pressure range is 1–4 bar. [171],[172],[173]
2) *Ultrafiltration* bridges the gap between particle and molecule filtration. Fine particulates, such as viruses, small molecules and enzymes, can be filtered in the size range of 4–100 nm. The operating pressure is in the range of 5–10 bar. [171]

3) *Nanofiltration* is applied for the separation of small organic molecules, such as synthetic dyes and antibiotics, and large ions in the size range of 1.2–12 nm. The pressure under operation is 20–40 bar.[171],[174],[175]
4) *Reverse osmosis* is used for molecule and salt rejection in desalination processes. The size range for rejected permeates is 0.5–1.5 nm. The filtration process is performed at high pressures of 30–60 bar.[171],[176],[177]

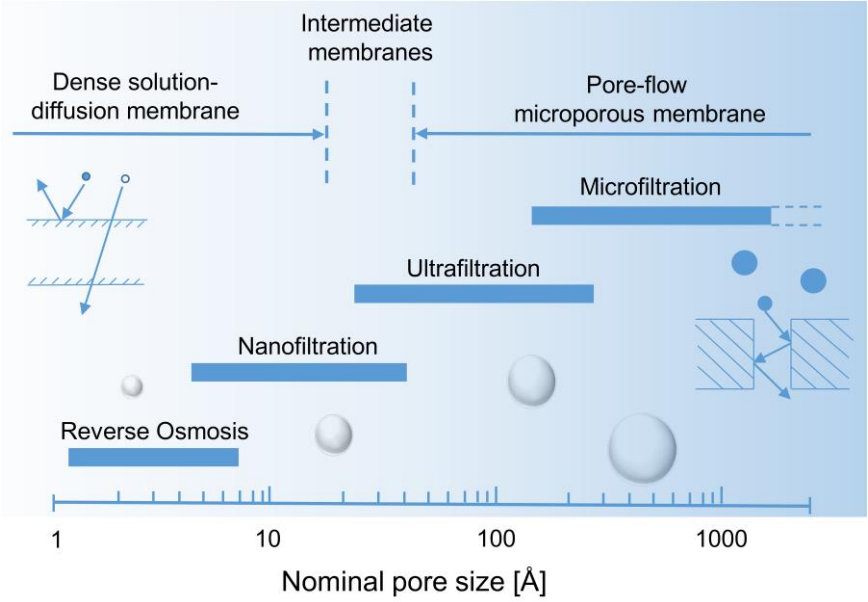

Figure 7. *Schematic representation of the predominant theoretical model dependent on the pore size (Baker et al.).*[169]

Microporous ultrafiltration and microfiltration membranes separate by either surface filtration or depth filtration (**Figure 8**). In the case of surface filtration, particles are captured on the membrane surface because membrane pores are too small for passage. Thus, cake formation takes place.[178] Surface filtration usually occurs at anisotropic membranes with fine porous/dense upper layers or ultrafiltration membranes. Microfiltration membranes possess larger pores, which can be entered by permeates. The process of particle separation in the interior of the membrane is defined as depth filtration. Different particle capture mechanisms can occur here.[169]

1) *Sieving*: Large particles are captured in pores, which are smaller than the average pore diameter.
2) *Inertial*: Relatively large particles cannot follow the fluid flow lines come into contact with the membrane material and are captured.

3) *Brownian Motion*: Small particles mainly follow the fluid flow lines but are also exposed to diffusion and, thus, come into contact with the membrane material where they are captured.
4) *Electrostatic adsorption*: Charged particles can be attracted and adsorbed by oppositely charged membrane surfaces. [169],[179],[180]

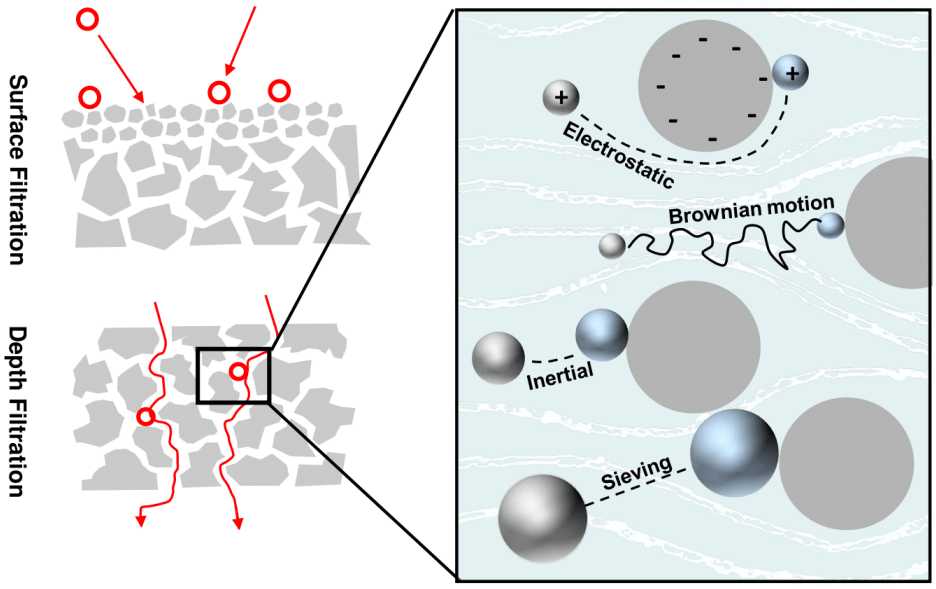

Figure 8. *Scheme for surface and depth filtration membranes with filtration mechanisms: Electrostatic, Brownian motion, inertial, and sieving (Baker et al.).*[169]

Regarding the structure-based and interaction-based filtrations, the filtration efficiency η (**Equation 4**) can be determined from the start concentration c_S and the end concentration c_E of particulate matter.[181]

$$\eta = \frac{c_S - c_E}{c_S} \cdot 100\ \% \tag{4}$$

A high filtration efficiency is greatly desired, but even though many efforts have been made to create advanced filtration materials, the trade-off relationship between the filtration efficiency and the pressure-drop has not yet been overcome.[182] The drop in pressure originates from the flow resistance by the filter media and determines the energy required to purify environmental media. Low drops in pressure are achieved by wide open pore structures, which contradict high filtration efficiencies for common structure-based membranes. This trade-off can be condensed in the quality factor QF (**Equation 5**).[183]

$$QF = -\frac{\ln(1-\eta)}{\Delta P} \tag{5}$$

The quality factor is dependent on the filtration efficiency η and the drop in pressure ΔP. The latter is influenced by several factors, such as the fiber packing density,[184] fiber diameter, filter thickness,[185] and materials' hydrophilicity.[186],[187] The pressure drop was intended to be adjusted by utilizing hybrid materials,[188] stacking layers of electrospun membrane,[189] or membrane morphologies.[190] By contrast, the filtration efficiency can be enhanced by interaction-based membranes, which are preferably designed for advanced filter materials to outperform these drawbacks.[191]

In addition to filtration intended, aqueous samples often contain a variety of additional substances. The accumulation of undesired deposits on the membrane surface or inside the membrane is known as membrane fouling.[192] In the fouling process, particles larger than the membrane pores block the membrane surface sterically. An additional layer on the membrane is formed, also known as the cake layer, prohibiting the unhindered solvent flow. Thus, the membrane resistance is increased, resulting in a decline of flux. In addition, the adsorption of small molecules or particles on the membrane surface or in the membrane pores reinforces membrane resistance. Adsorbed molecules and particles also modify the membrane surface properties impacting filtration performance.[193]

Fouling can be classified into bio-, organic, inorganic, and colloidal fouling.[192] Biofouling is provoked by the adhesion and proliferation of microorganisms on the membrane surface. The biofilm is composed of bacteria and their excreted extracellular polymeric substances.[194] Organic fouling includes the deposition of humic substances, polysaccharides, proteins, lipids, amino acids, and cell components, also defined as natural organic matter.[195],[196] However, inorganic salts can also deposit on the membrane surface if the equilibrium solubility is exceeded or the permeate is supersaturated, which is known as inorganic fouling.[197] In the case of colloidal fouling, both organic or inorganic substances as colloids can be captured on the membrane surface.[198]

The physicochemical interactions between foulants and membrane are characteristic for all types of fouling. The membrane functional groups enable the attraction of foulants by electrostatic forces, hydrogen bonding, and Van-der-Waals forces.[199] The binding strength is determined by the specific interaction and can be enhanced further by morphological properties. Membrane morphology, including the pore size distribution, surface roughness, and porosity, influence the hydrodynamics and, thus, the accumulation of foulants on the membrane surface.[193]

Industrial applications of membrane filtration require low operating costs, which can be realized by prolonging the membrane lifetime. Membrane fouling shortens the membrane lifetime but can be reversibly removed by frequent cleaning procedures.[200] In addition to physical cleaning by back-flushing practices or ultrasound, different chemical cleaning methods can also be applied.[201] Acidic or alkaline rinsing steps can hydrolyze or dissolve contaminants. Persistent contaminants can be removed by oxidizing agents, which also act as disinfectants.[202] Metal ions are eliminated by complexation, particles can be detached with tensides, and proteins or fatty acids can be disintegrated by enzymes.[203]

The membrane material might be partly degraded with every cleaning procedure, and the original membrane properties, such as surface charge, are affected.[204] Thus, scientific research is focused on the development of different membrane materials with low-fouling and high-performance properties.

1.3.2 Materials for Filtration

Membrane fouling has been correlated by researchers to membrane materials' hydrophobicity.[205] Thus, various techniques have been developed to improve the membrane surface chemistry and membrane properties.[206]

Modification techniques can be divided into subsequent treatment after electrospinning or simultaneous incorporation of materials to alter the fiber surface properties.[207] An example of a subsequent treatment method is plasma treatment, which generates hydroxyl, carboxyl, amino, or carbonyl groups on the surface by a reaction with reactive gases.[208] Further reactions, such as aminolysis or hydrolysis, can be can be applied as wet-chemistry modifications,[207] or grafting-from/-to methods.[209],[210] Another well-known technique is surface blending. Here, nanomaterials and other polymers with desirable properties can be simultaneously incorporated into the electrospinning solution in a blending step.[211]

A wide range of different nanoparticles, such as copper oxide,[212] titanium dioxide,[213] zinc oxide,[214] and silver,[215] have already been implemented in electrospun membranes. The implementation can be reached by blending polymer and nanomaterials prior to the electrospinning process, but also by utilizing precursors and coaxial electrospinning or post-treatments on the fiber surface.[216] However, these methods cannot completely secure the even dispersion of nanomaterials in or on the nanofiber.[217] Nevertheless, the resulting composite materials combine the material advantages, for example, the physicochemical stability of ceramics with the easy formation of polymeric materials.[218] Additionally electrospun

membrane properties are enhanced by superb hydrophilicity or hydrophobicity, depending on the nanoparticles' characteristics. Even Janus-type membranes have been prepared by utilizing nanoparticles, changing the fiber surface chemistry.[219] Apart from surface roughness due to nanoparticles,[220],[221] chemical differences on the surface improve the chemical resistance and withstand harsh conditions.[222] Thermal resistance is also enhanced by nanoparticle-polymer interactions and mechanical properties increase significantly.[142],[223]

These remarkable advancements of properties by the incorporation of nanoparticles can also be realized or even outperformed by two-dimensional carbon materials.[224] Carbon-based materials possess excellent mechanical strength, thermal conductivity, and electrical and anti-corrosive properties.[225],[226],[227] Furthermore, graphene can easily be functionalized by introducing functional groups[228] or doping with heteroatoms by converting to graphene oxide.[229] Graphene oxide can be introduced to electrospun membranes by its addition in powder form,[230] whereby adhesion can be improved by thermal treatment.[231] Moreover, the thermal treatment of poly acrylonitrile (PAN) fibers leads to the carbonization of electrospun fibers.[232] Besides the addition of graphene sheets, special frameworks such as carbon nanotubes can also be built by rolling up graphene into hollow cylinders.[233] Carbon nanotubes were introduced to electrospun membranes by cross-linking on hollow fiber surfaces,[234] or via sandwich-like electrospun fibers/carbon nanotube composites.[235] Applications in membrane filtration systems utilizing the electrochemical properties of carbon nanotubes for water remediation show their outstanding performance for future-oriented applications.[236]

The combination of metals and carbon-based three-dimensional materials as secondary building units are also known as metal-organic frameworks.[237] The latter have already been introduced as adsorbents on electrospun membranes in the field of wastewater treatment applications[238] due to their easy preparation, tunable pore size, ability to be modified and large surface area.[239] However, up to now, they are still suffering from disadvantages of weak recyclability, complex operating processes, and potential secondary pollution.[240]

Wettability for low fouling tendencies, excellent mechanical properties, and high filtration performances are major research goals for the application of electrospun membranes in filtration setups.[241],[242] However, these days, more than scientific questions determine research requirements because global issues, such as climate change, impact public priorities and research orientation.[243] Thus, biobased or biodegradable materials have been developed for several applications, for example, filtration membranes.

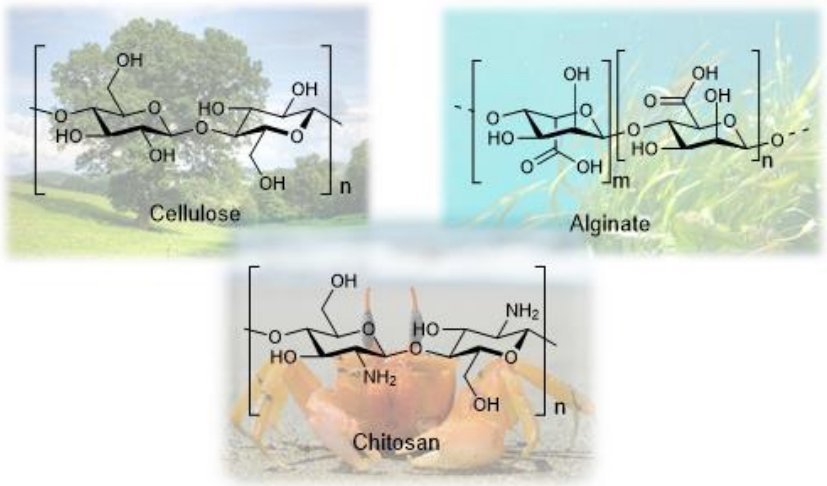

Figure 9. *Cellulose, alginate, and chitosan as examples for biopolymers.*

Images are taken from internet source. [244],[245],[246]

Biopolymers derive from renewable sources, such as wood, plants, crabs, and shrimps (**Figure 9**).[247] The most abundant and intensively researched biopolymers are cellulose, chitosan, alginate, and lignin, besides a variety of other different existing biopolymers: silk, bovine serum albumin, collagen, soy protein, etc.[248] Their main advantages apart from their natural availability, are the ease of chemical modification, mechanical and chemical stability, biocompatibility, non-toxicity, disinfection capacity, and biodegradability.[249],[250] Thus, researchers are interested in utilizing these biopolymers for different applications. Electrospinning is a promising method for processing but faces different limitations. Biopolymers often suffer from limited solubility, which is caused by their polyelectrolytic nature, rigid intra- and intermolecular hydrogen network, and high gelation tendency.[251] Hence, biopolymers cannot be processed alone and need to be blended with other polymers.[252],[253] Nevertheless, their broad multiplicity of functional groups, such as hydroxyl, amino,[254] or carboxylic,[255] and their polyelectrolyte character enable applications in membrane filtration systems for the adsorption of heavy metal ions[256], dyes,[257] or antimicrobial filtration systems.

1.3.3 Filtration of New Pollutants

Membrane filtration is utilized in a vast field of different applications. This chapter is intended to provide a brief overview of the most promising membrane applications for future directions.

A major challenge in underdeveloped countries is water scarcity and the provision of clean and safe drinking water. Water disinfection can be achieved by filtration with antimicrobial

membranes,[258] but membrane biofouling remains a major limiting factor.[259] Besides antibacterial water filtration technologies, membranes can also be applied for air disinfection. Indoor air quality can be severely limited when heating, ventilation, and air conditioning systems are in use. Microbial growth cannot often be inhibited on these components, distributing microbes with the airflow.[260] A major focus shifted recently to the filtration of virus, such as SARS-CoV-2-contaminated air, expressing the urgent need for sufficient air filtration systems.[261]

Antimicrobial systems can generally be differentiated into release- and contact-killing methods.[262] A prominent example of release-killing products are silver nanoparticles. These nanoparticles are often added to a variety of products to increase their antimicrobial properties by gradually releasing toxic silver ions.[263] Silver nanoparticles can be loaded onto electrospun membranes by different techniques, such as immersing-coating, electrospray-coating, or *in-situ* loading.[264] The disadvantage of these systems might be the non-controlled substance release, which might also impact systems other than the target. By contrast, the contact-killing of microbes is restricted to the inevitable contact of microbes with a specific surface.[265] Contact-killing can be introduced by membrane-surface modifications with antibacterial agents, such as quaternary ammonium compounds, carbon nanomaterials, or photoactive agents.[262] Cationic polymers with quaternary amine functionalities act as antibacterial compounds due to their capability of bacteria adsorption.[266] Contact of quaternary amines with bacteria cell walls lead to the destruction of cell integrity and loss of nutrients, leading to cell death.[267],[268] Carbon nanomaterials, such as carbon nanotubes, graphene oxide, or fullerenes, also show antimicrobial effects.[269],[270]

A variety of antimicrobial systems have been developed, but abuse and misuse have led to the emerging phenomena of antibiotic resistance.[271] The permanent low concentration of antibiotics may cause irreversible change to microorganisms, leading to antibiotic resistance.[272] Antibiotics as part of pharmaceuticals and personal care products are produced and consumed in high quantities worldwide.[273] Since the human body does not completely consume the drugs taken, excess and metabolites pass through the digestive system and enter wastewater.[274] Emerging contaminants, such as pharmaceuticals, are frequently detected in the aquatic environment around the world, indicating the lack of current treatment technologies.[275] Electrospun membranes can be applied for the successful separation of emerging contaminants. Ibuprofen, for example, was removed by a chitosan/polyethylene glycol nanofibrous membrane,[276] and fluoxethine can be adsorbed by lignin nanofibers.[277] Separation was often

achieved by the electrostatic attraction of charged pharmaceuticals or steric hindrance.[278],[279] Additionally, metal organic frameworks,[280] or proteins[281] immobilized on electrospun membranes were shown to be highly efficient in water purification. Immobilized proteins demonstrated a new class of filtration techniques based on superior interaction with emerging pollutants by complex-formation at the protein-active site.[282] One of these advanced filtration techniques is the advanced oxidation process.

The most intensively studied class of advanced oxidation processes is photocatalysis. An electrospun membrane combining membrane filtration with photocatalysis in a single unit is utilized for wastewater treatment[283] and air filtration.[284] Photocatalysis is based on electron excitation by irradiation of the membrane with light. An electron crosses over from the valence band to the conduction band by photon adsorption.[285] The electron hole formed further reacts with oxygen and hydroxyl groups in water, generating various ROS.[286] Hydroxyl radicals, as highly reactive oxygen species, can react with organic pollutants, such as pharmaceuticals, through three main mechanisms: 1) hydrogen abstraction, leading to the formation of carbon-centered radicals, 2) electrophilic addition to double bonds, or 3) electron transfer reactions.[287] The high oxidizing capabilities of ROS enable the conversion of organic pollutants to harmless species, probably even CO_2 and H_2O.[288] Thus, the formation of the cake layer on the membrane surface during the filtration procedure and pore blocking is avoided.[288] In addition, low fouling tendencies, even self-cleaning abilities have been reported.[289] Due to these outstanding properties, photocatalytic membrane filtration has become a hot research topic.[290] So far, the focus has been on the utilization of TiO_2 nanoparticles.[291] However, electrons of TiO_2 nanoparticles can only be excited by UV light. The trend recently developed regarding the implementation of materials, which showed photocatalytic activity under visible light.[292] Prominent examples are metal-doped TiO_2 nanoparticles,[293] FeOOH-based systems[294] and g-C_3N_4.[295]

1.3.4 Affinity Separation

In addition to microbes, viruses, or pharmaceuticals, also ions, dyes, and particulate shaped contaminates have attracted enormous attention and diverse purification methods have been developed to remove these contaminates from environmental media. Carbohydrates, such as chitosan, are excellent natural adsorbents for heavy metal ions and dyes,[257] which are associated with pollution, toxicity, and adverse effects on the environment and biota.[296],[297],[298] Heavy metal ions and dyes can be filtered from wastewater by adsorption, which is considered to be the most favorable method because it possesses high energy efficiency, is simple, and a

fast approach.[299] Adsorption is based on the interaction of a contaminant with a chemically active binding site on the membrane, which can be provided by functional groups. The type and number of functional groups control the success of contaminant adsorption.[300],[301] Nitrogen atoms in the amino functional group, for example, are a strong electron donors adsorbing metal ions by chelation or electrostatic interaction. Carboxylic groups and sulfhydroxyl groups, or phosphorus compounds also have the ability to interact with metal ions and dyes.[302] A wide variety of electrospun membranes with different functionalities have been reported for heavy metal ion and dye filtration.[257],[303]

A new field has recently been established focusing on the removal of metal nanoparticles from wastewater. Only a very few publications have demonstrated metal nanoparticle separation by electrospun membranes. Exemplarily, AuNP, AgNP, and TiO_2 NP were filtered from aqueous systems by electrospun carbon nanofiber nonwovens.[304] The AuNP (20 nm) were filtered with efficiencies up to 95%, AgNP (20 nm) up to 98%, and TiO_2 NP (10–15 nm) up to 94%. The batch filtration has been also applied for AuNP and AgNP using electrospun poly(vinyl alcohol) (PVA) membranes with chemically modified surface hydroxyl groups (thiols and amines).[305]

In addition to metal nanoparticles, nanoplastics have also emerged as a potential candidate for affinity separation. Enfrin et al. demonstrated the potential fouling on polysulfone ultrafiltration membranes by polystyrene nano- and microplastics, featuring a rejection of 25%.[306] Up to 30% rejection of polystyrene nanoparticles (300 nm) by PVA/PAN membrane was determined by Liu et al.[307] Both filtration efficiencies were outperformed by a PAN membrane coating with polyethylene imine (PEI) and polyacrylic acid in a layer-by-layer assembly rejecting 89% – 99% of polystyrene (50, 100, and 500 nm).[308] PEI coated electrospun membranes from cellulose also demonstrated high adsorption efficiencies of polyvinyl chloride (PVC), polymethyl methacrylate (PMMA), and polyvinyl acetate (PVAc) (> 98%) nanoparticles.[108]

2. Synopsis

Research on the topic of the doctoral thesis led to the preparation of four publications. Two of these publications have already been published (publication 1, 2; chapter 2.3, 2.4) and two are submitted (publication 3, 4; chapter 2.5, 2.6).

2.1 Aims and Strategy

Nanoparticles possess unique features and properties, which can improve the characteristics of various products.[62] Thus, they are incorporated frequently into diverse products resulting in rising production quantities.[63] Their production, usage, or disposal might lead to nanoparticle release into the environment and worldwide distribution.[65],[76] Organisms, animals, and human beings might be unintentionally exposed to these nanoparticles causing potential adverse effects on health.[86] Thus, a demand might arise for the purification of nanoparticle-contaminated environmental media. So far, no filtration systems have been used commercially, which specifically address nanoparticles. Hence, nanoparticles disturb common wastewater treatment and might not be filtered sufficiently.[110],[111],[115]

In this thesis, the prospective problem was addressed by utilizing electrospun membranes. These membranes should be prepared by electrospinning, a facile method to obtain a highly functional material with beneficial properties. Electrospun membranes exhibit a high surface area, high porosity, and can be functionalized easily.[138],[140] Media can pass through the membrane in flow filtrations, enabled by the membranes' porous structure, and come into contact with the high membrane surface area, where contaminates can be adsorbed. The objective of this thesis is to provide electrospun membranes which successfully remove nanoparticles from aqueous media by affinity filtration. The affinity filtration facilitates desirable high permeate flow and low pressure drops by micro-sized pores and provides high filtration efficiencies due to specific adsorption mechanisms.[309] The in-depth understanding of nanoparticle-membrane interaction is essential to design membranes for the simultaneous filtration of nanoparticles which are different in material, size, and ligands. Membrane regeneration also needs to be investigated, because it is an essential goal in terms of sustainability and costs to prolong the lifetime of electrospun membranes in the field of filtration. Finally, studies on systems in daily life need to be considered to demonstrate the excellent filtration performance for commercial applications.

2.2 Overview of the Thesis

The objective of this thesis was to successfully remove nanoparticles from environmental media by utilizing electrospun membranes. This thesis describes the establishment and development of new filter materials and the detailed investigation of the filtration process in the new research field of nanoparticle filtration. Furthermore, wall and ceiling paints, as an example of systems in daily life containing nanoparticles, were chosen to prove the successful implementation of electrospun filter materials for applications in daily life. The significance of research into the filtration of paints was emphasized by toxicity tests with paint compounds on biological systems.

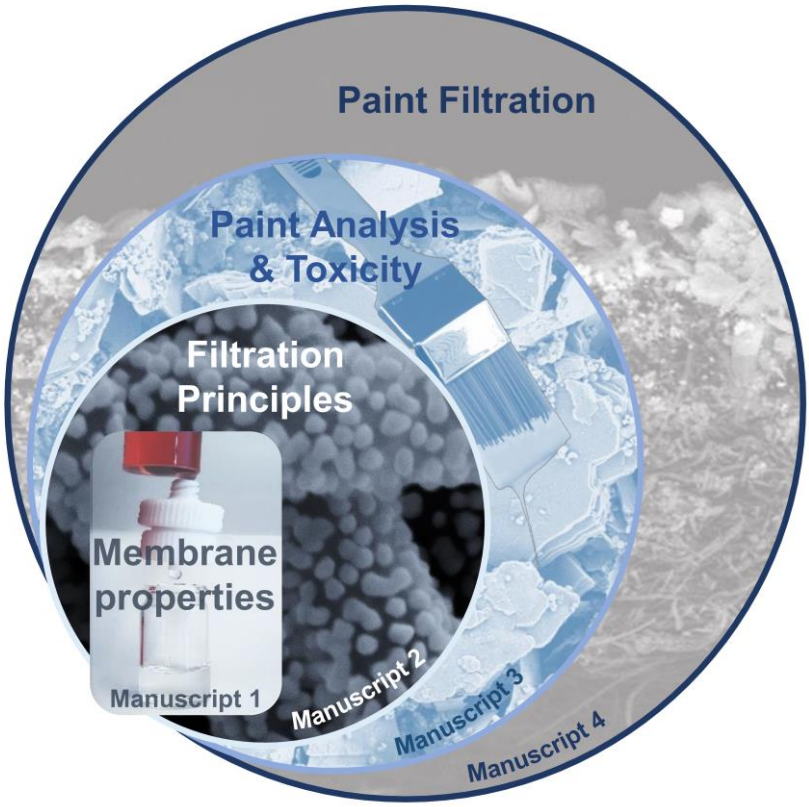

Figure 10. *Table of contents image of the doctoral thesis.*

This development path can be subdivided into four chapters (**Figure 10**), which have formed the basis for four publications, which are described briefly in the following:

The first publication (**chapter 2.3**) describes the polymer synthesis, membrane preparation and characterization which represent the basis for the following work. The membrane characterization focused on the investigation of parameters affecting the drop in pressure and elaborates correlations and the importance of the parameters. The filtration of gold nanoparticles was also reported.

This is followed by the second publication (**chapter 2.4**), which considers the filtration of gold nanoparticles of different sizes, and with different ligands, and expands the filtration model to a variety of metal and metal oxide nanoparticles. General filtration mechanisms were proposed which paved the way for the design of a new membrane for the filtration of nanoparticle mixtures. Finally, membrane regeneration has been successfully conducted to improve the membrane lifetime and, thus, the sustainability of the filter.

After the in-depth investigation of filtration principles, the know-how acquired was implemented in the third publication to systems of daily life (**chapter 2.5**). Here, paints were chosen as an example of a nanoparticle source used commercially. The paint mixtures were separated and their size, shape, and composition were analyzed. To prove the potential adverse effects of these paint fractions on biological systems, *Daphnia magna* and cell cultures were exposed to the paint fractions. These experiments supported the previous evaluation of nanoparticle toxicity in literature, expanded the nanoparticle research to real systems and brought up concerns about dispersed polymers in environmental media.

The evaluation of toxicity on biological systems in surface waters demonstrated the urgent need for sophisticated water purification systems, such as electrospun membranes. Therefore, in the fourth publication (**chapter 2.6**), the filtration of paints with the electrospun membranes prepared was tested and the transfer of the abstracted filtration principles of the former studies to real systems could be demonstrated.

2.3 Preparation and Performance Assessment of Low-Pressure Affinity Membranes Based on Functionalized, Electrospun Polyacrylates for Gold Nanoparticle Filtration

A.-K. Müller, Z.-K. Xu, A. Greiner, *ACS Appl. Mater. Interfaces*, **2021**, 13, 13, 15659-15667.

Full article (**chapter 3.1**) and figures printed with permission of *ACS Appl. Mater. Interfaces*.

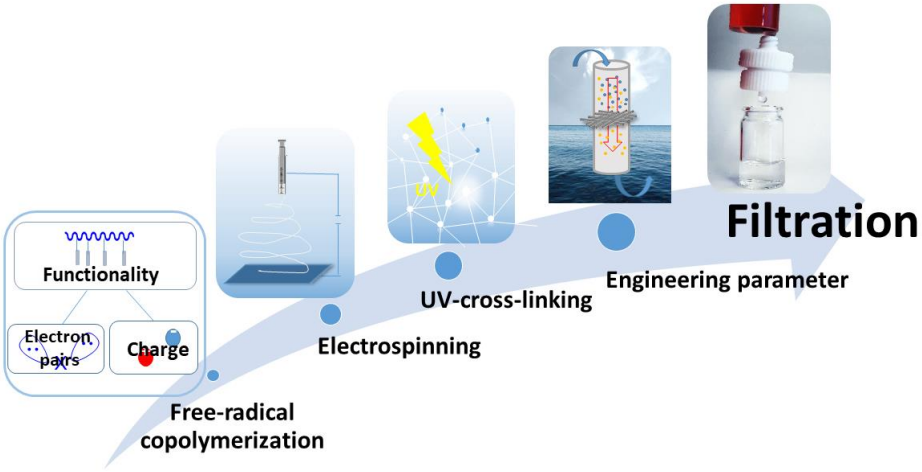

Figure 11. *Table of contents image of publication (1).*

2.3.1 Contribution to Joint Publications

I did the polymer synthesis, characterization (nuclear magnetic resonance (NMR), infrared spectroscopy (IR)), and preparation of electrospun membranes. Size exclusion chromatography (SEC) measurements were performed by Rika Schneider (Technician, Macromolecular Chemistry II, University of Bayreuth). I characterized the electrospun membranes by contact angle, water uptake, fiber diameter, decrease of pore size, and tensile stress. The apparatus for pressure drop measurements was kindly provided by the Macromolecular Chemistry I (University Bayreuth), where I performed the said measurements. I synthesized the gold nanoparticles and conducted the filtration tests, as well as the evaluation of the filtration by UV/Vis, asymmetric flow field flow fractionation (AF-FFF), IR, and scanning electron microscopy (SEM). Inductively coupled plasma optical emission spectroscopy (ICP-OES) measurements of the filtrates and transmission electron microscope (TEM) measurements of the gold nanoparticles were done by Carmen Kunert (Technician, Macromolecular Chemistry II, University of Bayreuth).

I wrote the manuscript and prepared all figures. Prof. Greiner supervised the project and provided support for writing the manuscript. Prof. Greiner and Prof. Xu (Professor, University of Zhejiang) gave valuable feedback and corrective recommendations on the manuscript.

2.3.2 Summary and Discussion

Nanoparticles are prone to escape into the environment, because they are applied and produced in high quantities (**chapter 1.1.4**). Metal and metal oxide nanoparticles are most frequently produced and might end up in surface waters. Since their potential toxicity is not completely known, an urgent need for the purification of nanoparticle-contaminated water has become apparent. Due to the rare number of earlier works in literature, publication (1) should be part of establishing a new research field and help to gain more insights into filtration mechanisms. Membranes with various functional groups, as possible nanoparticle adsorption sites, were prepared in different molar ratios because no relation between membrane properties and nanoparticle adsorption was published. Furthermore, the membranes were intended to be used for flow-mode filtrations to enable water purification to be carried out faster than comparable batch adsorption methods. Since membrane applications often suffer from high pressure drops (**chapter 1.3.1**), main influences on the pressure drop were determined. An overview of the content of publication (1) is given in **Figure 11**.

Polymer Synthesis

Acrylate-based copolymers were synthesized in various compositions by free-radical copolymerization with the functional groups: 4-vinyl pyridine (Pyr), *N*-isopropyl acrylamide (NIPAM), acrylic acid (AA), and dimethyldecyl ammoniumethyl methacrylbromide (Nplus). Those groups were chosen because they might interact with nanoparticles by free electron pairs, hydrogen bonding, coordination or chelation, or electrostatic interaction (**chapter 1.1.2**). The copolymers were synthesized with high molecular weights to facilitate the electrospinning procedure.

Membrane Properties

The copolymers were electrospun and UV cross-linked. The photo cross-linking was enabled by the benzophenone unit, which can be excited by UV light under the formation of radicals. Those radicals recombine and lead to polymer chain cross-links (**chapter 1.2.2**). These cross-links improve the resistance of fiber swelling in aqueous media, and enhanced the mechanical stability in the filtration process. The fiber swelling was evaluated by the water uptake of the

membrane, the fiber diameter, and the decrease in pore size. All parameters demonstrated the low swelling tendency after cross-linking. The cross-linked membranes were then tested for their drop in pressure under water flow conditions. The pressure drop was correlated to membrane properties and illustrated a declining dependence from pore size to mechanical stability to hydrophilicity.

Nanoparticle Filtration

Gold nanoparticles were synthesized by the chemical reduction method (**chapter 1.1.1**) and the filtration was tested with the cross-linked membranes. Only membranes with the Pyr and Nplus functional groups were able to adsorb gold nanoparticles on the membrane surface, which was proven by ICP-OES, AF-FFF, and UV/Vis. Membranes were investigated with SEM after gold nanoparticle filtration. The SEM images showed gold nanoparticles only on the Pyr and Nplus membrane surface (**Figure 12**). The Pyr functional group can interact with the gold nanoparticles by the free electron pair and the Nplus functional group can attract gold nanoparticles by electrostatic interaction. Furthermore, the number of functional groups implemented in the copolymer was reasonable for the filtration efficiency. The number of functional groups correlates with the number of nanoparticle adsorption sites. Hence, a higher number of functional groups leads to higher filtration efficiencies.

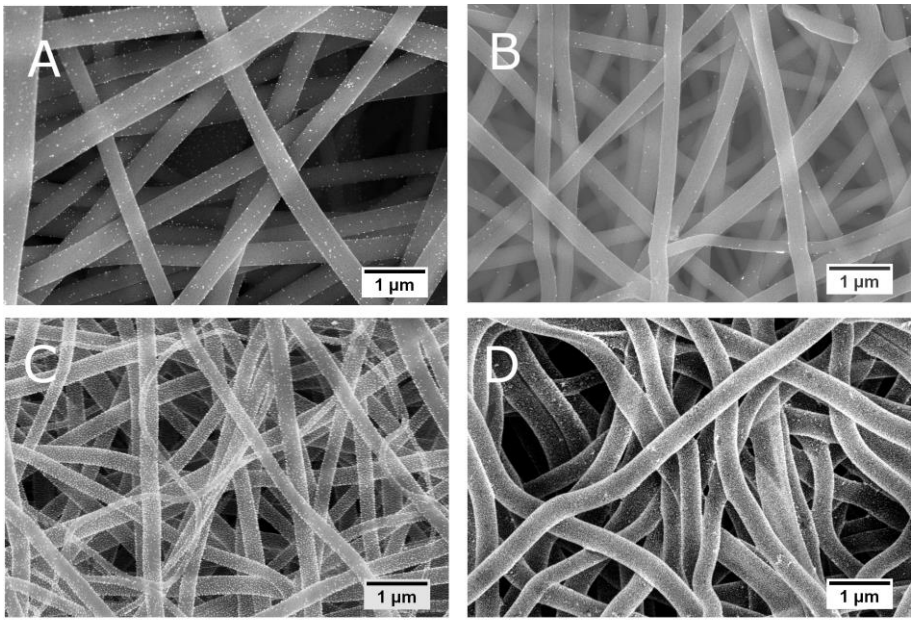

Figure 12. *SEM images after gold nanoparticle filtration with electrospun membranes composed of the functional groups A) NIPAM, B) AA, C) Pyr, D) Nplus.*

2.4 Sustainable Electrospun Affinity Membranes for Water Remediation by Removing Metal and Metal Oxide Nanoparticles

A.-K. Müller, Z.-K. Xu, A. Greiner, *ACS Appl. Polym. Mater.*, **2021,** 3, 11, 5739-5748.

Full article (**chapter 3.2**) and figures printed with permission of *ACS Appl. Polym. Mater*.

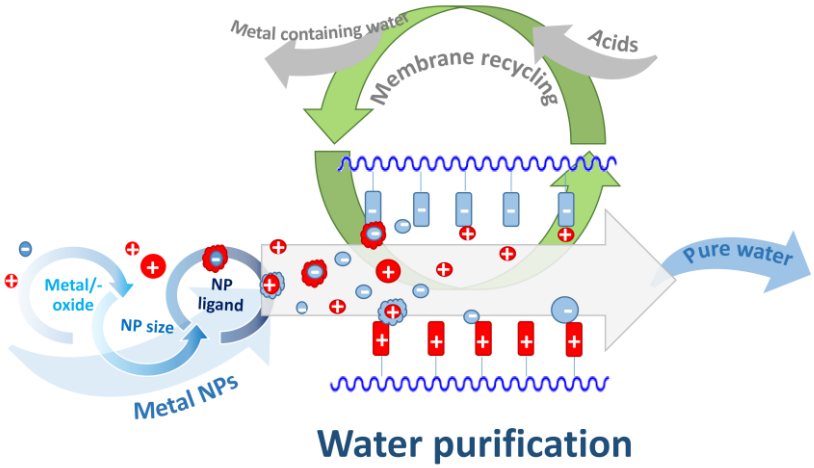

Figure 13. *Table of contents image of publication (2).*

2.4.1 Contribution to Joint Publications

I synthesized and characterized the gold, silver, titanium dioxide, copper oxide, zinc oxide, and iron oxide nanoparticles (DLS, AF-FFF). I also executed the filtration and regeneration experiments. I analyzed the filtrates by AF-FFF and UV/Vis and took the SEM images of the filter materials. The zeta sizer for zeta potential measurements was provided by Physical Chemistry II from the University of Bayreuth. TEM images and ICP-OES measurements of the nanoparticles were done by Carmen Kunert (Technician, Macromolecular Chemistry II, University of Bayreuth).

I wrote the manuscript and prepared all figures. Prof. Greiner supervised the project and supported writing the manuscript. Prof. Greiner and Prof. Xu (Professor, University of Zhejiang) reviewed and corrected the manuscript.

2.4.2 Summary and Discussion

In the publication (1) (**chapter 2.3**) the successful filtration of gold nanoparticles was demonstrated. However, metal oxide nanoparticles are produced in much higher amounts than gold nanoparticles, and show a greater relevance for escape into the environment. Thus, publication (2) focused on the filtration of metal oxide nanoparticles. To improve the in-depth understanding of filtration, the impact of parameters, such as the functional group, particle size, and particle ligands, on the filtration efficiency were investigated. Since it can be expected, that nanoparticles might appear as mixtures in the environment, a combi membrane was provided, which was able to filter the different nanoparticles in one step. Additionally, I was aiming to increase the membrane lifetime and, thus, increase the sustainability of the filtration process by membrane regeneration (**chapter 1.3.1**). A short overview of the content of publication (2) is given in **Figure 13**.

Impact of Nanoparticle Size

Gold nanoparticles with different sizes were prepared by the particle growth mechanism in the size range of 26–159 nm. The filtration was successfully performed with the Pyr and Nplus membrane, which evidenced lower filtration efficiencies for nanoparticles below 30 nm. A lower filtration efficiency might be a consequence of a higher particle number but also a higher ratio between the particle and pore size. Since nanoparticles especially in the size range below 20 nm are expected to impact biological systems, the focus of all following experiments were on nanoparticles under 20 nm.

Filtration of Metal Oxide Nanoparticles

Metal oxide nanoparticles, such as copper oxide, zinc oxide, iron oxide, and titanium dioxide, were synthesized for example, by co-precipitation and sol-gel methods (**chapter 1.1.1**) with particle sizes below 20 nm. The filtration was conducted with the four different membrane functional groups but only the NIPAM and AA membrane were able to adsorb the metal oxide nanoparticles.

The nanoparticle behavior is significantly influenced in the environment by different factors for example, ligands. Polyvinyl pyrrolidone (PVP), trisodium pyrophosphate, or sodium citrate were chosen to represent model ligands for typical natural organic or inorganic matter. These ligands interact with the nanoparticle surface and change their particle size and zeta potential. The change in zeta potential was reflected by a different filtration behavior.

Filtration Principles

Gold or silver nanoparticles possess negative zeta potentials and can both be filtered by the positively charged Nplus membrane (**Figure 14A**). The metal oxide nanoparticles featured a positive zeta potential and were filtered by the NIPAM and AA membrane. By the addition of model ligands, such as pyrophosphate or citrate, to the metal oxide nanoparticles the zeta potential was changed to negative, resulting in a relieved nanoparticle filtration by the Nplus membrane (**Figure 14B**).

Thus, two combinations showed potential in nanoparticle filtration: negative charged nanoparticles/ Nplus membrane, positively charged nanoparticles/ AA membrane.

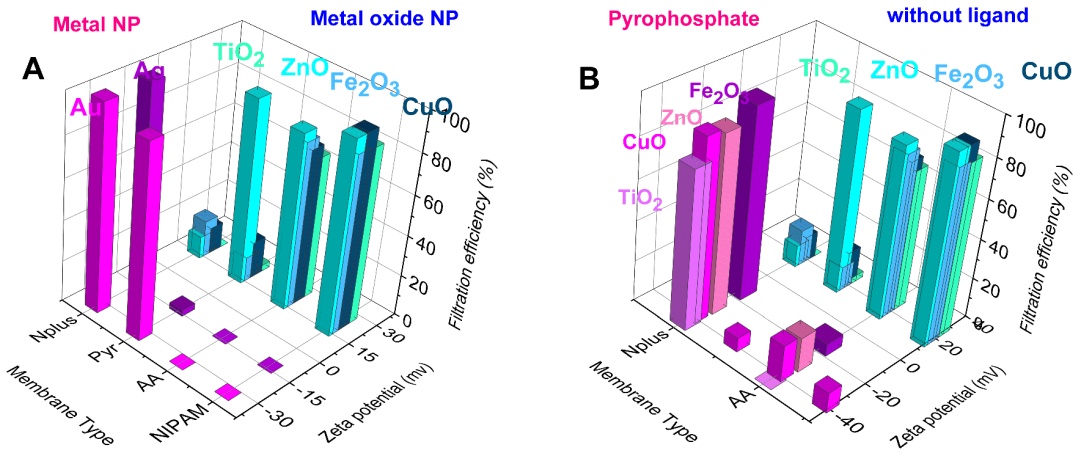

Figure 14. *Filtration efficiency dependent on the membrane type and zeta potential of the A) metal and metal oxide nanoparticles and B) the ligand.*

Filtration of Nanoparticle Mixtures and Membrane Regeneration

The suitability of the membranes prepared for applications in systems in daily life was evidenced by the filtration of nanoparticle mixtures and membrane regeneration. The metal and metal oxide nanoparticles were combined in a mixture and filtered by a membrane combining the Nplus and AA functional groups in one membrane. The Janus-type membrane successfully filtered the nanoparticles without preferring any nanoparticle material. The nanoparticle-loaded membranes were easily regenerated by rinsing with low concentrated acids without any relevant loss in filtration efficiency over three cycles.

2.5 Disentangling biological effects of primary nanoplastics from dispersion paint's additional compounds

A.-K. Müller[1], J. Brehm[2], M. Völkl[3], V. Jèrôme[3], C. Laforsch[2]*, R. Freitag[3]*, A. Greiner[1]*,
Ecotoxicol. Environ. Saf., **2022**, 242, 113877.

Full article (**chapter 3.3**) and figures printed with permission of *Ecotoxicol. Environ. Saf.*

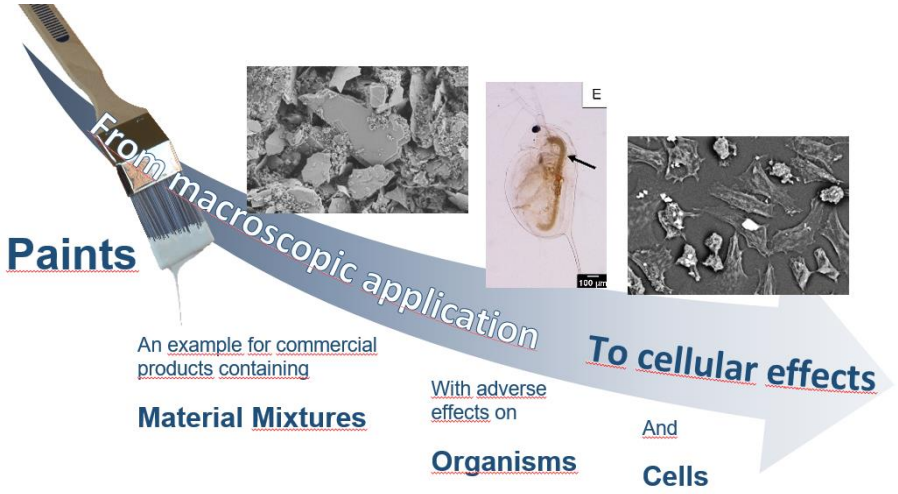

Figure 15. *Table of contents image of publication (3).*

2.5.1 Contribution to Joint Publication

I analyzed the paints and developed separation procedures. I also analyzed the paint fractions received with AF-FFF, DLS, zeta sizer, and SEM. I prepared batches of paint fractions for the biological tests and discussed with Julian Brehm (PhD, Animal Ecology I, University of Bayreuth) and Dr. Valérie Jèrôme (Process Biotechnology, University of Bayreuth) which biological tests needed to be done.

Julian Brehm executed the biological tests with *Daphnia magna* and calculated the EC_{50} values. Matthias Völkl (PhD, Process Biotechnology, University of Bayreuth) executed the biological tests with L929 cells and provided data for the cell metabolic activity.

I wrote the manuscript and received help from Julian Brehm and Matthias Völkl for the biological part. Dr. Valérie Jèrôme, Prof. Laforsch (Animal Ecology I, University of Bayreuth), Prof. Freitag (Process Biotechnology, University of Bayreuth), and Prof. Greiner corrected the manuscript.

2.5.2 Summary and Discussion

Publication (2) (**chapter 2.4**) demonstrated the model filtration of different nanoparticles and contributed to the in-depth understanding of filtration principles. However, those principles needed to be tested for a successful transfer to the filtration of nanoparticle sources in daily life. Since commercial nanoparticle sources might feature different properties than the model nanoparticles, also different behavior in the filtration process might be expected. Paints are known to be a source of nanoparticles and nanoplastics, therefore, these were chosen as nanoparticle source in daily life (**chapter 1.1.4**). The potential impact on biological systems in the environment was investigated in publication (3) to prove the significance of this research. *Daphnia magna* and L929 cells were used as test systems to evaluate the impact on organisms and at a cellular level. A short overview of the content of publication (3) is given in **Figure 15**.

Paint Composition and Properties

Two paints were chosen which can be classified as water-based wall and ceiling paint dispersions. Both paints consist of different compounds (**Figure 16A**), which were separated by centrifugation. These compounds were analyzed and can be briefly described as: polyacrylate nanoparticles, titanium dioxide nanoparticles, dispersed copolymer, and calcium carbonate micro fragments. In addition to centrifugation, sedimentation over time also led to paint separation. The titanium dioxide nanoparticles and the calcium carbonate micro fragments sedimented over time, leaving a supernatant behind which consisted of either polyacrylate nanoparticles or dispersed copolymer. The stability of the paint dispersions can also be manipulated by adjusting the pH value or the salt concentration. Both parameters affect the zeta potential, which is reasonable for dispersion stability and, thus, is an essential parameter for estimating the probability of distribution of those compounds in the environment.

Biological Tests with *Daphnia magna*

The paints were fractionated by centrifugation and those fractions were used for biological tests with *daphnia magna*. The daphnids were exposed to the paint fractions at different concentrations and the immobility of the daphnids was detected. The measurement of daphnid immobility was used as a parameter to determine any adverse effects on the daphnids' vitality. The immobility was checked after multiple time intervals but no changes could be detected before 96 h. The EC_{50} values were calculated to compare the paint components' adverse effects

with literature. These values evidenced that the strongest impact resulted from the dispersed copolymer with 78.2 µg/mL, followed by the polyacrylate and calcium carbonate microparticles (~160 µg/mL). The paint fractions interfered with the daphnids because the paint compounds were accidentally ingested or adsorbed onto the daphnids carapace (**Figure 16B**).

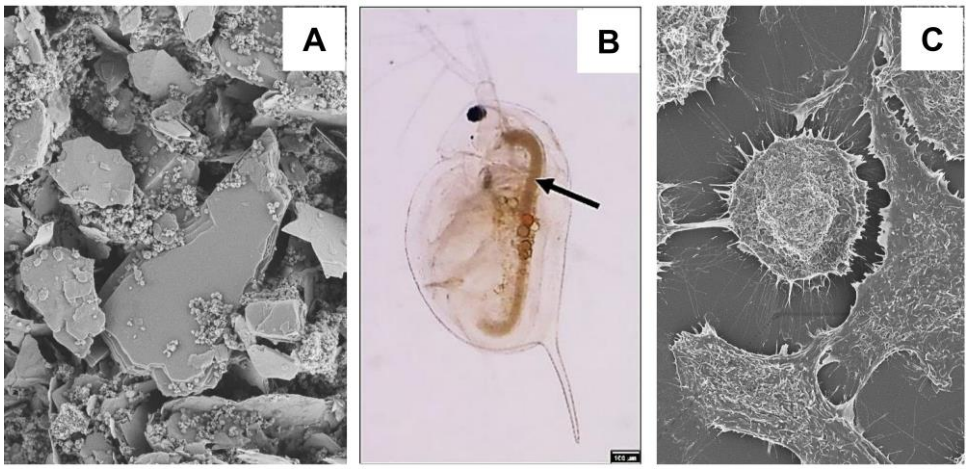

Figure 16. *Paints, as an example for daily life nanoparticle sources were A) analyzed, and tested for potential toxicity on b) Daphnia magna and c) L929-cells.*

Biological Tests with L929 cells

The biological tests with L929 cells were performed with the paint fractions, separated by centrifugation (**Figure 16C**). The cells were exposed to the paint fractions at different concentrations and their metabolic activity was monitored. A decreasing metabolic activity reflects a decreasing cell vitality and is expected to result from a negative impairment by the paint fractions. The test illustrated a dose-dependent impact of paint fractions on the cell vitality. The strongest impact resulted from the titanium dioxide (LD_{50} = 1.1 µg/mL) and the polyacrylate nanoparticles (LD_{50} = 3.1 µg/mL).

The paint fractions demonstrated potentially adverse effects on microorganisms and the cellular level. However, the extent of response to the paint components differed for the two model systems. No general trend in toxicity can be drawn for titanium dioxide nanoparticles, dispersed polyacrylate, and calcium carbonate microparticles, except for the polyacrylate nanoparticles. These have been one of the components with a tremendous effect on the vitality in both systems. Thus, the adverse effects of paint components are strongly dependent on the species observed and no general toxicity on living systems can be concluded from the experiments performed.

2.6 Filtration of Paint-contaminated Water by Electrospun Membranes

A.-K. Müller, Z.-K. Xu, A. Greiner, *Macromol. Mater. Eng.*, **2022**, 2200238.

Full article (**chapter 3.4**) and figures printed with permission of *Macromol. Mater. Eng.*

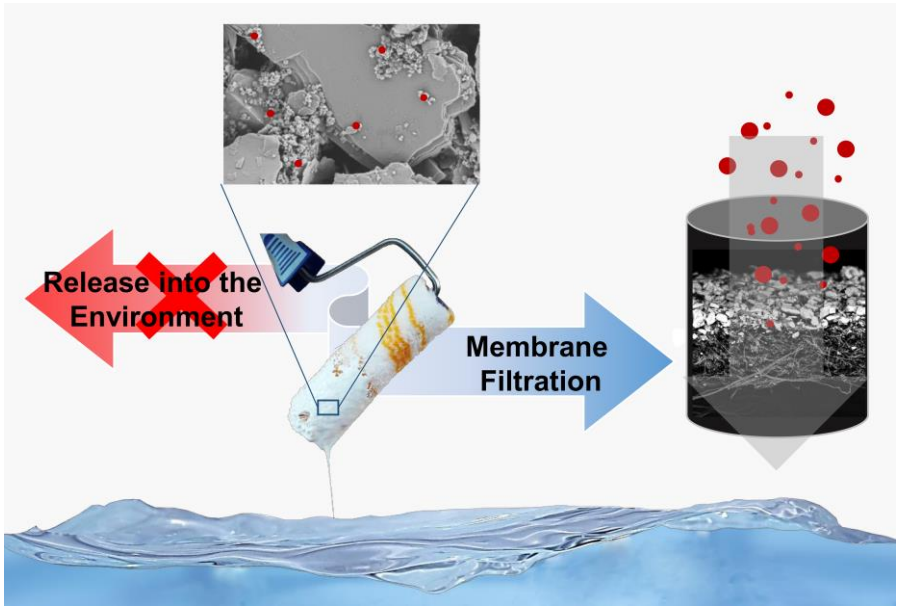

Figure 17. *Table of content image of publication (4).*

2.6.1 Contribution to Joint Publication

I did the filtration of paint and the pressure-drop measurements. I analyzed the paint filtrates utilizing UV/Vis and AF-FFF methods, and performed SEM measurements of the membranes after filtration. I prepared the photographic documentation of the filtrates and the membranes after filtration.

I analyzed and evaluated the data, prepared all images and graphs, and wrote the manuscript with the support of Prof. Greiner and Prof. Xu. Both corrected the manuscript.

2.6.2 Summary and Discussion

Publication (3) (**chapter 2.5**) demonstrated the adverse effects of paint components on biological test systems and emphasized the importance of purification methods for paint-contaminated environmental media. Thus, the filtration of paint dispersion and paint components was investigated in the publication (4). In contrast to the former publications, not only the filtration of metal nanoparticles is tested but also that of nanoplastics and dispersed

polymers, which both appeared as emerging contaminants (**chapter 1.1.4**, **chapter 1.3.4**). The filtration principles stated previously were conformed and the filtration mechanisms were discussed (**chapter 1.3.1**). The filtration mechanism for the metal and plastic nanoparticles can be described as affinity-based, but filtration of the dispersed polymers demonstrated other phenomena. The dispersed polymer possessed a negative zeta potential and might be adsorbed on the membrane by electrostatic charges. However, a simultaneous increasing drop in pressure was observed which can be explained by pore gluing to the dispersed polymer. Thus, the filtration of dispersed polymers might raise other problems. A short overview of the content of publication (4) is given in **Figure 17**.

Filtration of Paint 1

Paint 1 was filtered with high efficiencies, but was accompanied with a rising pressure drop on the membrane. The microparticles block the upper membrane surfaces and hinder the water flow, resulting in a growing drop in pressure. The microparticles were separated according to the size-exclusion mechanism on the top of the membrane surface, but the titanium dioxide and polyacrylate nanoparticles entered the membrane volume. The nanoparticles were adsorbed on the fiber surface in the membrane volume by electrostatic interaction, leading to high filtration efficiencies (**Figure 18**).

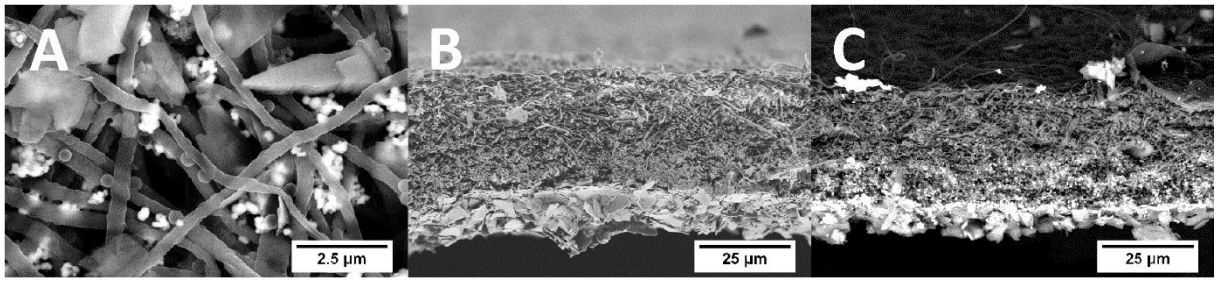

Figure 18. *Paint 1 was filtered by the Nplus membrane and was investigated with SEM. The SEM images illustrate A) the adsorption of different paint compounds on the membrane, B) the cake formation on the membrane surface, and C) nanoparticles, which were adsorbed in the membrane volume.*

Filtration of Paint 2

Similar to the increasing pressure drop during the filtration of paint 1, a comparable phenomenon could be detected for the filtration of paint 2. Here, the microparticles blocked the membrane surface and the dispersed copolymer exhibited a pore-blocking mechanism. It was demonstrated by SEM images that the dispersed copolymer can enter the membrane volume in contrast to the microparticles. Thus, the pores are glued by the dispersed polymer throughout

the membrane volume. The filtration step is followed by a drying procedure, resulting in the shrinkage of the dispersed polymer. Thus, the formerly glued membrane pores are reopened again. This filtration mechanism can be described as an electrostatic interaction-based mechanism occurring with the phenomenon of an increasing pressure drop, which is normally attributed to size-exclusion mechanisms.

3. Publications

3.1 Publication (1)

ACS APPLIED MATERIALS & INTERFACES

www.acsami.org Research Article

Preparation and Performance Assessment of Low-Pressure Affinity Membranes Based on Functionalized, Electrospun Polyacrylates for Gold Nanoparticle Filtration

Ann-Kathrin Müller, Zhi-Kang Xu,* and Andreas Greiner*

Cite This: *ACS Appl. Mater. Interfaces* 2021, 13, 15659−15667 Read Online

ACCESS | Metrics & More | Article Recommendations | Supporting Information

ABSTRACT: Electrospun nanofibrous membranes (ENM) possess many advantages over commonly utilized water purification systems. They provide high porosity with interconnected pores and a high surface to volume ratio, facilitating particle adsorption. Affinity separation moves into a promising future for application, for example, nanoparticle adsorption with excellent filtration efficiency, because of its highly specific adsorption mechanism. However, not all effects on filtration performance are entirely understood. In this paper, we investigate significant filtration parameters, such as pore size, mechanical stability, and hydrophilicity, and determine a sequence of importance for an optimal pressure drop. Copolymers with various hydrophilic functional groups such as acid, amide, pyridine, and quaternary amine were utilized. Effects on the pressure drop or nanoparticle filtration efficiency can then easily be attributed to the corresponding functional group. UV-light was used to induce cross-linking in the membranes, which subsequently surpassed the mechanical stability of commonly used hydrophobic membranes. A maximum tensile-stress of up to 11.6 MPa was obtained, whereby an optimization of at least 22% was achieved. Moreover, these cross-links reduce fiber swelling by a maximum of 26%. The membrane potential depends on the different functional groups and their incorporation number from 10 to 50 mol %. Successful gold nanoparticle (AuNP) filtration in flow mode was demonstrated and highlighted the outstanding membrane properties and selectivity. The Nplus membrane achieved 100% filtration efficiency over a duration of 6 min, surpassing the Pyr membrane's performance. This was attributed to the ionic interaction of the Nplus membrane, in contrast with the physical adsorption of the Pyr membrane.

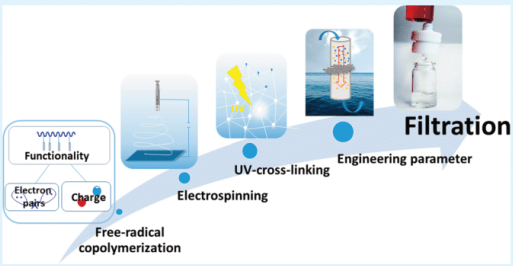

KEYWORDS: *electrospun nanofibrous membranes (ENM), affinity separation, gold nanoparticle filtration, membrane properties, photo-cross-linking*

INTRODUCTION

Pollution due to urbanization and industrialization leaves human beings and their ecosystem with unresolved problems.[1] The rising demand for engineered nanomaterials led to higher production quantities,[2] and thus to the emergence of emissions during the production process and the unintentional release or the improper disposal of industrial wastewater.[3] This reinforces the worldwide distribution, accumulation, and long-term effect of the released nanomaterials.[4] However, for many nanomaterials, the long-term consequences on human health[5] and the environment[6] cannot yet be estimated. Hence, a rising need for the development of efficient filtration methods is apparent.[7]

Conventional methods for purification of wastewater[8,9] are progressively replaced by new membrane technologies, offering advantages over customary systems by easy scalability,[10] low energy consumption,[11] and no need for added chemicals.[12] In the future, membrane technologies will be utilized for solving more complex problems in specific applications whereby rising demands will be made on membrane properties.[13] Thus, the drawback of low selectivity or efficiency must be overcome.[9] Electrospun nanofibrous membranes (ENM) are an excellent solution if a high degree of functional performance and flexible properties are required.[14−16] However, membrane technology still faces challenges, such as reducing the pressure drop for usage under high flux applications meanwhile maintaining high filtration efficiencies. Therefore, impacts on the pressure drop are under investigation.

Standard techniques[17−20] are limited to size-based separation[21] without differentiating chemically different particles and often face high-pressure drops. Consequentially, a new branch

Received: January 19, 2021
Accepted: March 4, 2021
Published: March 24, 2021

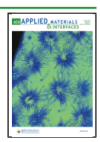

Scheme 1. Reaction Scheme for Copolymerization of MMA with UV-Cross-Linker (MABP) and Different Comonomers[a]

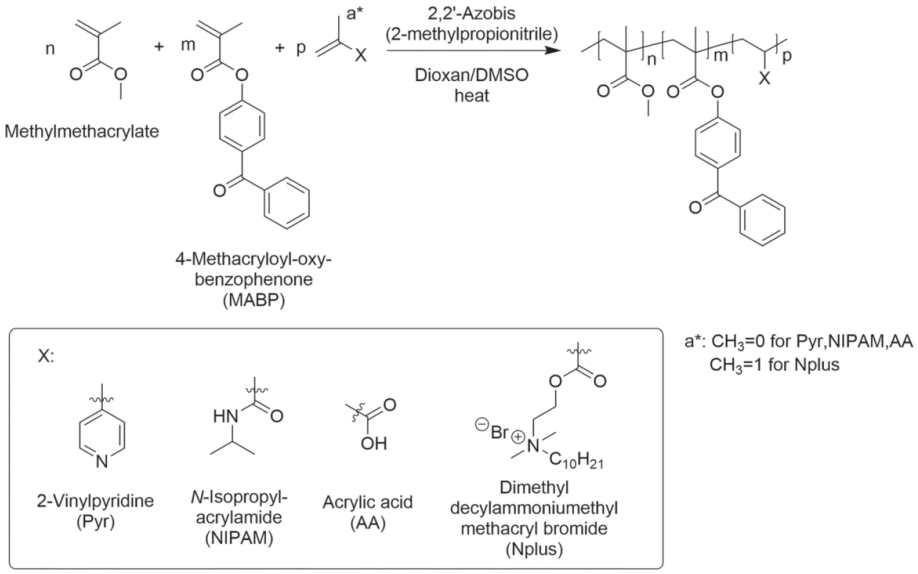

[a]The comonomers NIPAM, AA, Pyr, and Nplus provide functional groups for affinity separation.

of research was established, in which substances are segregated by their physical/chemical properties or their biological function: affinity separation.[22,23] Affinity membranes feature very high filtration efficiencies and are created by integrating functional groups, such as ionic dyes,[24] oligosaccharides,[25] and proteins.[26] Often, a hydrophobic core-polymer is selected due to its superior mechanical properties, and a more hydrophilic or functionalized surface is designed afterward by different methods.[27−29] Either filter support can be adopted[30] or the fiber contact points can be melted together[27] to further improve the ENM mechanical stability enabling high flux applications. However, these approaches are limited because the process of fiber functionalization can lead to inhomogeneous membrane properties and a reduction in pore size,[31] which can also be triggered by melt processing.[32] Furthermore, these additional steps increase the effort required to produce these membranes. Affinity membranes utilized in batch process management exhibit long adsorption times and result in inhomogeneous particle distribution on the membrane compared to the continuous flow mode.[33] In contrast to the dynamic mode possessing great advantages: the material output can be enhanced, as well as opening the possibility for scale-up and reasonable control over the continuous adsorption process.[34]

This paper demonstrates a method to maintain the desired hydrophilic membrane character for nanoparticle filtration using polymers with functional groups, such as acid, amide, pyridine, and quaternary amine, for electrospinning. By choosing these monomers, membrane properties can easily be attributed to specific functionalities. Excellent mechanical fiber properties were obtained by UV-light-induced cross-linking. The relationship between mechanical strength, contact angle, pore size, and pressure drop was studied because a low-pressure drop is favorable. In addition, the filtration of AuNP in the dynamic mode was analyzed, and the impact of the various functional groups on AuNP filtration capacity was studied.

RESULTS AND DISCUSSION

Polymer Synthesis. Copolymers of methyl methacrylate (MMA), 4-methacryloyl-oxy-benzophenone (MABP), and four functional comonomers—acrylic acid (AA), *n*-isopropylacrylamide (NIPAM), 4-vinylpyridine (Pyr), and dimethyldecyl ammoniumethyl methacryl bromide (Nplus)—were synthesized with varying compositions (Scheme 1). The effect of increased functional group incorporation in the membrane on the filtration efficiency was investigated. MABP was used as a photo cross-linker, with a higher molar ratio for more hydrophilic membranes to reduce membrane swelling. The functional group's molar ratio was raised from 10 up to 30, 50, or 70%, whereas the MABP content was set to 5, 10, or 30%. The copolymers produced show minor deviations from the target compositions, exhibiting high molecular weight in the range of 120−260 kDa with a dispersity of 1.4−2.3. The copolymers were recovered in high yields, except for the Nplus copolymer (Table S2). For this monomer, the copolymerization was terminated after 30 min at low monomer conversions. At longer reaction times, stable monomer conformations are produced as side reactions. These are shielding the polymerizable vinyl group and are preventing further polymerization.[35]

The kinetics were investigated to prove the statistical character of all copolymers, which was confirmed by the equal turnover frequency of all monomers in the polymerization. The calculation was done from the ratio of the monomer to polymer NMR peaks (Figures S1−S5) and the peak ratio of the remaining monomers in the solution (Figure S6). Furthermore, the copolymerization parameters are all in the same range, with a deviation of ±0.1 (Figure S7). In the following discussion, the copolymers will be termed as, for example, AA10%, corresponding to the target functional group

https://dx.doi.org/10.1021/acsami.1c01217
ACS Appl. Mater. Interfaces 2021, 13, 15659−15667

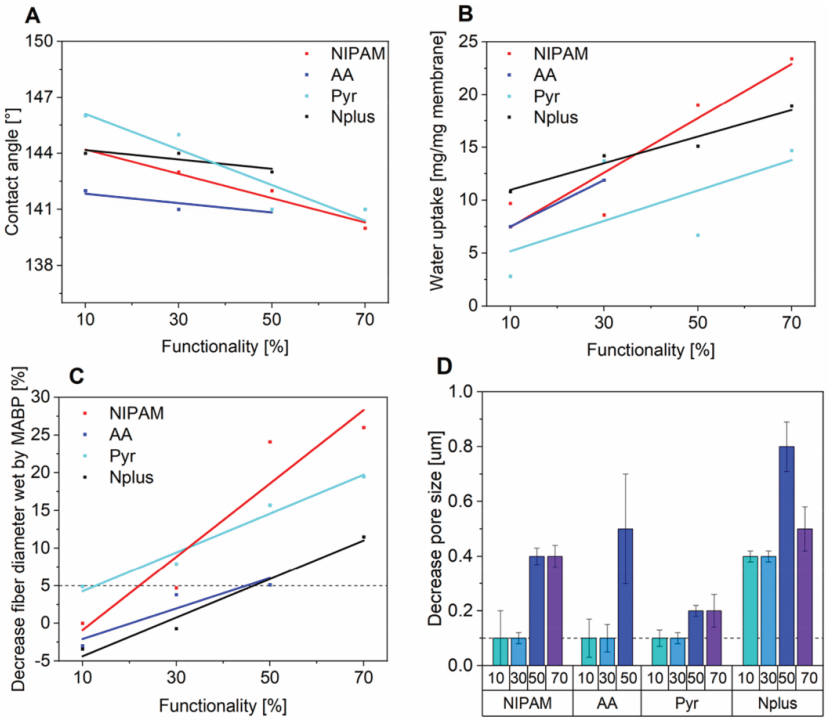

Figure 1. Parameters correlating to swelling behavior for the membranes depending on the monomers NIPAM, AA, Pyr, and Nplus and its copolymer composition: (A) contact angle of all cross-linked membranes with deviations of ±5°, (B) water uptake of cross-linked membranes with deviations of ±2%, (C) decrease in wet fiber diameter by MABP (mean deviation for fiber diameters is ±17.5 nm or ±5%), (D) decrease in pore size after wetting.

Table 1. Increase in Fiber Diameter (%) for Non-Cross-Linked Membranes Depending on the Amount of Functional Group[a]

	amount of functional group (%)			
fiber diameter increase (%)	10	30	50	70
NIPAM	10	5	41	23
AA	0	3	30	-
Pyr	15	5	26	30
Nplus	10	2	49	19

[a]MABP content is 5, 10, 10, and 30 mol %.

incorporation in the respective copolymer. Because we aimed to investigate these functional groups' influences on the filtration performance, membranes were produced from the synthesized copolymers. The copolymers were electrospun with 25 wt % from DMF on a rotating disc collector (parameters are given in the Supporting Information). Afterward, the membranes were UV-cross-linked, whereby the cross-linking progress was monitored with IR spectroscopy. The resulting fibers were characterized with scanning electron microscopy (SEM) (Figure S8).

Membrane Properties. Filtration performance in water is strongly dependent on membrane properties such as swelling behavior, pressure drop, and stress−strain properties. The swelling behavior can be evaluated by measuring the water uptake, water contact angle, change of pore size, and fiber diameter of the membranes to compare properties from the dry and the wet states (Figure 1, Figure S9, Tables S3−S6). For these experiments, whole membranes were used instead of individual fibers. Figure 1A shows the change in contact angle with the number of functional groups. Similar contact angles between 140 and 146° were determined for all ENMs. The contact angle did not change over 50 min for the 10 and 30% functional groups. However, it decreased for 50 and 70% functional groups to 0° in-between 30 s (Nplus) up to 5 min (NIPAM), indicating high water adsorption capacity. Therefore, the water uptake was measured over 24 h for the cross-linked membranes. In Figure 1B, it is demonstrated that NIPAM and Nplus can take-up the highest amount of water per gram of membrane. For example, water uptake of 23.4 mg/mg membrane was recorded for NIPAM70% in contrast to 2.8 mg/mg membrane for Pyr10%. The water uptake also caused an increase in the fiber diameter due to fiber swelling in the membrane. The most prominent effect becomes apparent for the NIPAM50% and Nplus50% membranes, showing swelling of 41 and 49%, respectively, for non-cross-linked membranes (Table 1).

The fiber swelling also depended on the amount of functional group, creating a hydrophilic effect. However, fiber swelling declines even without cross-linking when compared to membranes with 10 and 30% functional groups. This effect could be explained by the increase in MABP from 5 to 10% as MABP might have a hydrophobic effect due to its chemical

https://dx.doi.org/10.1021/acsami.1c01217
ACS Appl. Mater. Interfaces 2021, 13, 15659−15667

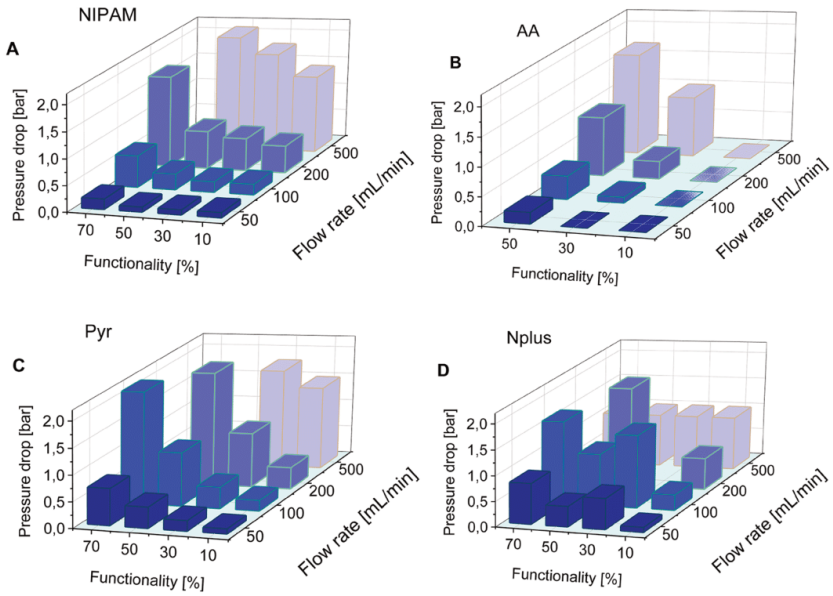

Figure 2. Pressure drop depending on the flow rate and the functional group ratio for (A) NIPAM, (B) AA, (C) Pyr, and (D) Nplus.

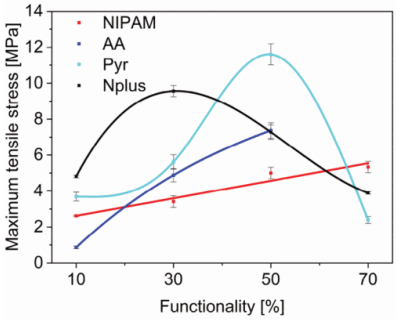

Figure 3. Maximum tensile stress for all membranes depending on their functional groups such as NIPAM, AA, Pyr, and Nplus and the functional group ratio.

Table 2. Increase in Maximum Tensile Stress (%) after Cross-Linking the Membranes

	amount of functional group (%)			
increase in max. tensile stress (%)	10	30	50	70
NIPAM	51	62	90	91
acid	28	55	89	-
pyridin	70	54	53	22
Nplus	49	64	70	75

structure. Thereby, the hydrophilic impact of the functional groups is surpassed, and the fiber swelling declines. The copolymers with 30 and 50% functional groups both contain 10% MABP. A substantial increase in the fiber diameter becomes apparent here. As we expected, the fiber swelling is more pronounced with increasing functional group ratio when keeping the MABP amount constant. Thus, it is important to mention that not only the amount of functional group or the cross-linking is influencing the fiber swelling but also MABP's hydrophobic character.

We intended to limit fiber swelling by introducing MABP as UV-cross-linker. The fiber swelling could be reduced after cross-linking by up to 26% for NIPAM70% (Figure 1C). All values below ±5% for the decrease of fiber diameter are not significant due to measurement precision. Therefore, only the fibers containing 50% and more functional group incorporation in the membrane demonstrate substantial fiber swelling.

The pore size is reduced by fiber swelling, as measured with a porometer. This effect is evident for the membranes with a high amount of functional group and is most pronounced for Nplus50%, where the pore size is decreased by 0.8 μm (Figure 1D). Nplus50% might experience the most distinctive decline in pore size because, even with cross-linking, the fiber swelling could not be suppressed significantly (Figure 1C). Similar behavior was monitored for AA50%. Also the NIPAM 50 and 70% membranes exhibit high values for the pore size decline. For example, the NIPAM50% membrane passes through extensive fiber swelling (Table 1), but this can be substantially declined by cross-linking (Figure 1C). Therefore, the decrease in pore size is less dominant compared to the Nplus50% and AA50% membrane. Furthermore, the decline in pore size is less pronounced for Nplus70% membranes compared to the Nplus50%. Here the hydrophobic effect of the MABP outbalances the swelling, which might occur due to the increasing functional group ratio (Table 1).

The next most essential factor for good filtration performance, after the filtration efficiency, is the pressure drop over the membrane. The pressure drop was tested for all cross-linked membranes. In general, the pressure drop increases with flow rate from 50 mL/min up to 500 mL/min in the range of 0.1 bar up to 2 bar. In the process, a measurement error is present of ±0.1 bar (Figure 2A–D, Table S8). The polymer functionality itself seems to impact the pressure drop. This is indicated by the increase in pressure drop on increasing the

https://dx.doi.org/10.1021/acsami.1c01217
ACS Appl. Mater. Interfaces 2021, 13, 15659−15667

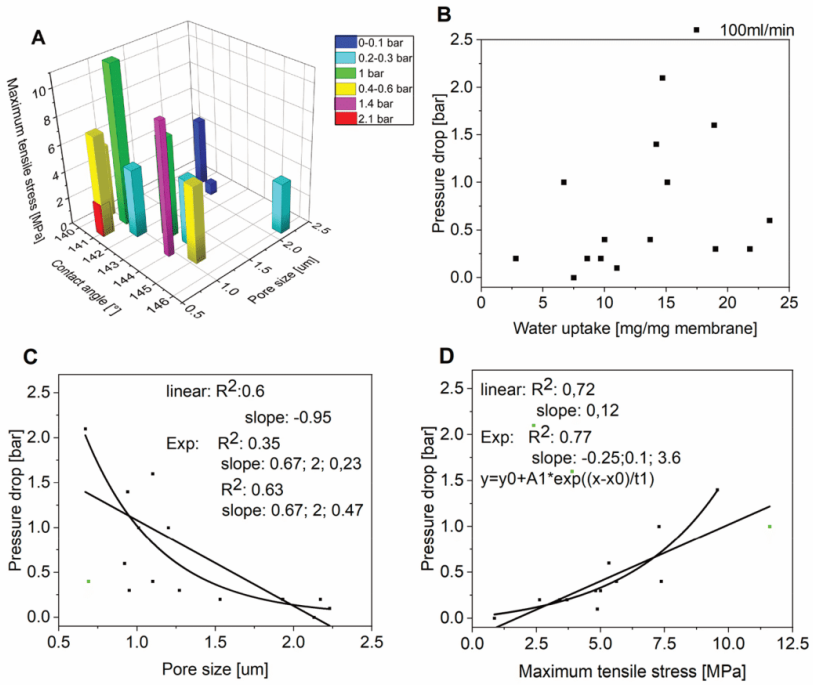

Figure 4. (A) 3D plot for all parameters (pressure drop measured at flow rates of 100 mL/min) and exponential data fit for (B) pressure drop depending on the water uptake for cross-linked membranes; (C) pressure drop depending on pore size; (D) pressure drop depending on maximum tensile stress.

number of functional groups for each type. Here the pressure rises, for example, from 0.2 bar for Pyr10% up to 2.1 bar for Pyr70% at a flow rate of 100 mL/min. The pressure drop at all flow rates and the amount of functional groups was lowest for the AA functional group membranes. The pressure drop also strongly depends on the membrane design and application. Membranes for ultrafiltration or ion adsorption under operation show fluxes, for example, from 45 up to 6000 L/(m^2 h) bar.[36−40] Membranes such as the Pyr or Nplus membranes possess comparable fluxes outperformed by the NIPAM and AA membranes.

In this context, the pore size must be considered as another critical variable that is susceptible to manipulation by the pressure. Flexible pores can be forced open with rising pressure and thus change their size. This phenomenon has already been reported by Bjorge et al.[41]

To calculate the tendency of the pore size to expand, we measured the stress−strain properties. Measurements were done with dried membranes, which had been previously used for filtration tests. The measured curves show no distinct maximum for any membrane because the fibers are randomly orientated (Figure S10). The first fibers started to break, whereas others are not stressed at that moment because they do not share the same alignment. Thus, extensive elongation values up to 200% are reached (Figure 3, Tables S9 and S10). As expected, the cross-linking improved the tensile properties by up to 91% because the movement of the polymer chains was restricted (Table 2). The maximum tensile stress for the cross-linked membranes reached values of up to 11.6 MPa (Pyr70%). The Pyr membranes showed the highest mechanical stability at each membrane composition because of their aromatic chemical polymer structure.

The trends observed in the maximum tensile stress curves for all functional groups are also reflected in the pressure drop curves, leading to the assumption of a distinct correlation between both parameters. For example, the copolymers with 10% functional groups possess maximum tensile stress values rising in the order of AA to NIPAM, Pyr, and Nplus. The pressure drop for those copolymers increases from AA to NIPAM, Pyr, and Nplus in the range of 0−0.3 bar. Therefore, it can be assumed that membranes with low mechanical stability like the AA10% membrane have a high tendency to widen their pores.

However, Pyr and Nplus both exhibit a substantial decline in maximum tensile stress at 70% functional groups. The lack of MMA as a soft segment might lead to a brittle polymer[42] already before the UV-cross-linking, which might have been problematic in this case. Both polymers have a hard chain structure in the solid state, resulting in low flexibility; therefore, the lower max tensile stress of the 70% copolymers can be explained by less effective cross-linking between different polymer chains. According to the literature, good tensile properties are necessary for outstanding filtration performance, gained here without using a hydrophobic polymer. Hydrophobic polymers provide high mechanical stability without the disadvantage of swelling.[43] In the literature, several studies have intended to increase membrane mechanical strength by utilizing a core polymer, for example, polyvinylidene fluoride (PVDF), resulting in a maximum force of 2.88 MPa[44] and for polyphenyl sulfone of 4 MPa.[45] The implementation of UV-

https://dx.doi.org/10.1021/acsami.1c01217
ACS Appl. Mater. Interfaces 2021, 13, 15659−15667

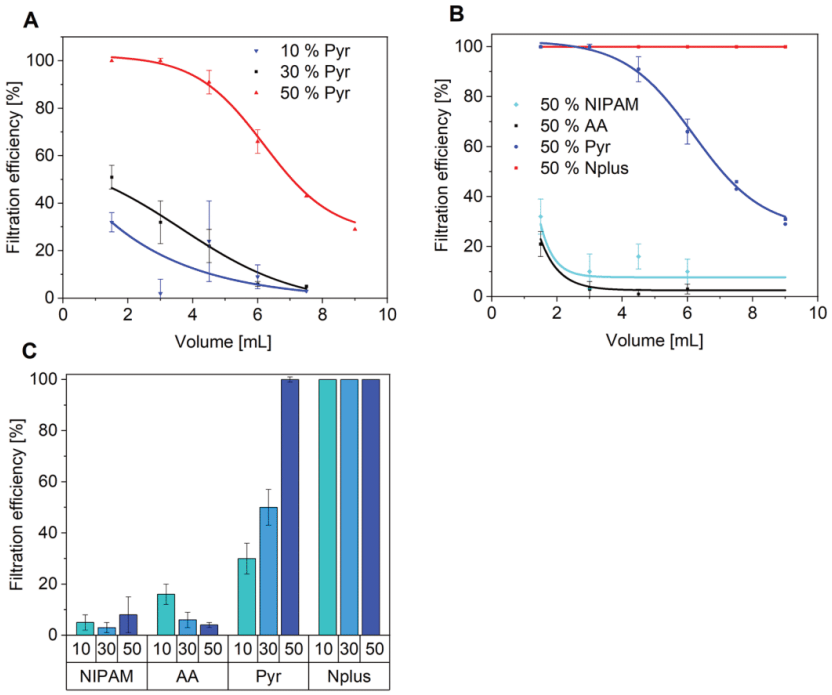

Figure 5. AuNP filtration efficiencies determined by UV/vis, AFFFF, and ICP-OES, (A) time-dependent for different amounts of Pyr in the membrane, (B) time-dependent for different functional groups with 50% of functionality incorporated in the membrane, and (C) for all membranes after 1.5 mL of AuNP filtration.

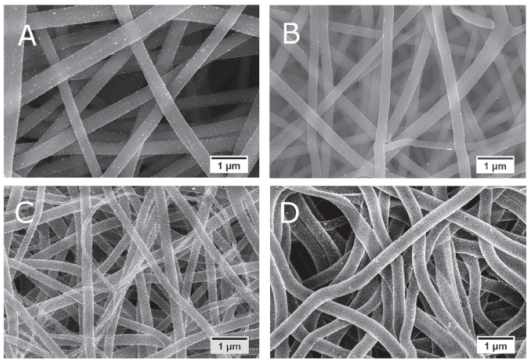

Figure 6. SEM measurement after AuNP filtration, with back-scattering detector, of all membranes containing 50% functional groups of (A) NIPAM, (B) AA, (C) Pyr, and (D) Nplus.

cross-linkable MABP monomers outperforms the maximum forces of the referenced polymers by up to three times. Furthermore, no postpolymerization steps are necessary. Instead, by increasing hydrophilicity, the maximum force reaches higher values.

Correlation of Essential Influences on Filtration Performance. the correlation between pressure drop, pore size, maximum tensile stress, and hydrophilicity is demonstrated in Figure 4A. Here the properties of all produced membranes are summarized. The data evaluation was conducted regardless of the membrane material but only its properties. And the mentioned pore size is interpreted as the pore size in the wet state, including the swelling. It becomes apparent that a smaller pore size (Figure 4C) and a higher maximum tensile stress (Figure 4D) causes an increased pressure drop. On the contrary, the hydrophilicity, represented by the water uptake, does not directly relate to the pressure drop in the investigated contact angle range (Figure 4B). A large pore size enables unhindered solvent flow, high mechanical stability prevents pore size bending, and a more hydrophilic membrane character results in enhanced membrane–water interaction. This phenomenon has already been discussed in the literature; often, a direct relationship between pressure drop and hydrophilicity is hypothesized,[46] but no definite answer has yet been found.[47] However, increased hydrophilicity has an impact on mechanical properties,[43] as hydrophilic polymers possess lower mechanical stability and reduce the pore size because of swelling. For example, the maximum tensile stress for AA-containing copolymers is weaker than that for the Pyr and Nplus copolymers. In this case, the hydrophilicity might also be a core parameter that has no crucial influence. However, it is important to consider that the maximum tensile stress and pore size are key parameters for the pressure drop.

To identify a sequence of importance for these parameters, we fitted the data by exponential functions, and the slope was used to determine the extent of correlation to the pressure drop (Figure 4). With a slope of 0.67/2/0.47, the pore size is

https://dx.doi.org/10.1021/acsami.1c01217
ACS Appl. Mater. Interfaces 2021, 13, 15659–15667

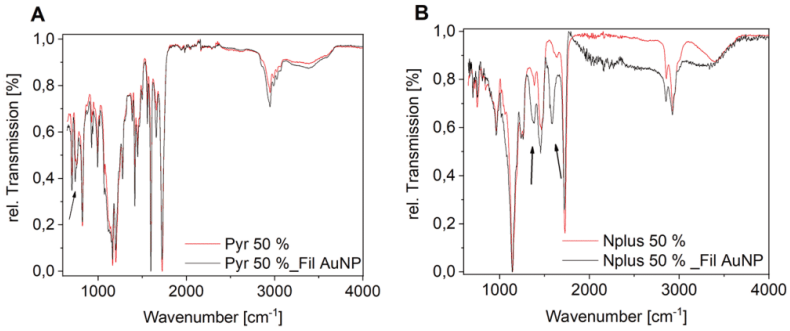

Figure 7. IR spectra of membrane before, and after filtration of AuNP with (A) Pyr50% and (B) Nplus50% as the functional group of the membrane.

the most important influence, followed by the maximum tensile stress, and the hydrophilicity plays a minor role.

Nanoparticle Filtration. After investigating the membrane properties, the filtration performance was tested with the membranes containing 10, 30, and 50% functional groups (see Video S1 for Nplus50% AuNP filtration). We intended to explore the impact of the functional groups and their amount on the filtration efficiency. The 70% membranes were not tested as the AA copolymer with 70% could not be electrospun because of poor solubility. Moreover, the membrane swelling would further increase, leading to a high-pressure drop, which is not desired for filtration. The overall filtration performance was investigated by self-synthesized spherical AuNP with a 16.5 ± 1.6 nm diameter of gyration (TEM), a hydrodynamic radius of 9 nm (DLS), and a zeta potential of −37 mV (AFFFF) (Figures S11−14, Table S11). Initially, experimental parameters were evaluated, resulting in the selection of a flow rate of 1 mL/min and a double layer of the membrane (2.4 mg ±0.5/1.5 cm^2) as standard conditions (Figure S15). ENMs were tested, and the filtrate was analyzed for unfiltered AuNP with UV/vis, AFFFF, and ICP-OES (Tables S12−S29). The data were highly consistent (max. 9% average concentration deviation between measurements), and an average efficiency value was calculated. The efficiency declines with time because adsorption sites at functional groups were cumulatively blocked with nanoparticles. For the Pyr copolymer, the efficiency correlates with the number of functional groups (Figure 5A, Figure S16A) because more adsorption sites are available. When comparing the efficiency of the different functional groups, the Nplus copolymer was the best and achieved 100% efficiency over the measurement duration (Figure 5B, Figure S16B). On the contrary, no adsorption occurs with the NIPAM and AA copolymers. Apparently, these functional groups cannot interact with the AuNPs, and this effect was also unchanged depending on the functional group ratio (Figure 5C). Evidently, the acid functional group cannot interact with AuNPs by hydrogen bonding or its possible negative charge: the latter might even lead to AuNP repulsion. In addition, the amide functional group of NIPAM is not able to attract AuNPs in contrast to the aromatic, electron-rich Pyr's and the positively charged Nplus membrane, which also both possess nitrogen atoms. Thus, it cannot be assumed that every functional group containing a nitrogen atom can bind AuNPs, but instead that it strongly depends on the surrounding groups. For the Nplus containing membrane, 100% efficiency was achieved independently of the functional group ratio because the maximum membrane capacity was not reached. The capacity is here defined as the ratio of maximum loading of nanoparticles (mg) which can be adsorbed on a membrane (mg). Finally, we conclude the 50 mol %-containing membranes are the most suitable for NP filtration, as they exhibit the largest adsorption capacity.

The binding mechanism of AuNP with Pyr has already been well investigated by Stolberg et al.[48] If the surface charge of AuNP is negative from the point-of-zero-charge (PZC), the π-orbital of the aromatic ring interacts in a horizontal position with the AuNP. The nitrogen atom provides a free-electron pair from a vertical position toward the AuNP for a positive surface charge.[49] The Nplus functionality adsorbs to the AuNP based on ionic interactions. The fiber surface contains a positive charge, whereas the zeta potential of the AuNPs was determined to be negative. When comparing the type of interaction with the AuNP, the different filtration efficiencies of Pyr and Nplus can be explained. Ionic interaction is much stronger than physical; therefore, adsorption is relieved. It can be concluded that the functional group choice is the most critical factor for affinity separation, but the functional group ratio can optimize the filtration efficiency. The existence of gold NPs on the fiber was also proven by SEM (Figure 6), revealing minor deposition of AuNPs on NIPAM and AA fibers (Figure 6A, B) in contrast to a higher AuNP loading on Pyr and Nplus fibers (Figure 6C, D). Furthermore, changes in the IR spectra (Figure 7) confirm successful affinity filtration.

Other papers already reported successful AuNP filtration by testing different functional groups such as thiols or primary amines.[50] However, in this paper, the new functional group Nplus was found to be highly active for filtration and showed high reactivity and capacity in flow-mode filtration. Executing the filtration in flow-mode facilitates fast water purification and provides opportunities for scale-up and wide-ranging applications.

■ CONCLUSION

In this paper, straightforward synthesis and preparation of ENMs with different functional groups, such as acid, amide, pyridine, and quaternary amine in various compositions, are reported. The UV-light-induced cross-links improve mechanical stability by 20−90%. They successfully outperform the mechanical stability of comparable filtration membranes by an order of at least two with a maximum value of 11.6 MPa for Pyr50%. Furthermore, fiber swelling was suppressed by a

https://dx.doi.org/10.1021/acsami.1c01217
ACS Appl. Mater. Interfaces 2021, 13, 15659−15667

maximum of 26%. The membrane properties were investigated, and it can be concluded that the pressure drop is primarily controlled by the pore size, followed by the ENM's maximum tensile stress.

Furthermore, AuNP filtration tests were successfully conducted with filtration efficiencies up to 100%. As a proof of concept, a higher functional group ratio of up to 50 mol % increases the efficiency. However, correct functionality choice is the most important factor for affinity filtration, which is explicitly demonstrated by the Nplus membrane. The results present in this manuscript indicate that no specific atom appeared to be favored for AuNP adsorption, but instead its properties such as electron density or charge. Moreover, the Pyr membrane's filtration efficiency, based on physical adsorption, was outperformed by the Nplus membrane, which attracts particles by its ionic charge. Further investigation of the membrane−nanoparticle interaction is started to deeply understand its mechanism and to expand membrane technology to a broader field of nanoparticles.

■ ASSOCIATED CONTENT

Supporting Information

The Supporting Information is available free of charge at https://pubs.acs.org/doi/10.1021/acsami.1c01217.

Materials, measurements, and experimental procedures. Copolymer composition, molecular weight, dispersity and yield for all copolymers (Table S2); copolymerization kinetics (Figures S1−S7); SEM image of electrospun membranes (Figure S8); data for water uptake (Table S3), pore size (Table S4), fiber diameter (Table S5), contact angle (Table S6, Figure S9), membrane thickness (Table S7), pressure drop (Table S8), stress−strain (Table S9), elongation at break (Table S10); stress−strain curves (Figure S10); AF-FFF measurements (Figure S11), TEM measurements (Figure S12), DLS measurement (Figure S13), EAF-FFF measurements (Figure S14, Table S11); filtration efficiencies and pictures of membranes after filtration (Figures S15−S16, Tables S12−29) (PDF)

Video S1 showing test of filtration performance with the membranes containing 50% functional groups (MP4)

■ AUTHOR INFORMATION

Corresponding Authors

Andreas Greiner − *Macromolecular Chemistry and Bavarian Polymer Institute, University of Bayreuth, Bayreuth 95440, Germany;* orcid.org/0000-0002-5310-3850; Email: greiner@uni-bayreuth.de

Zhi-Kang Xu − *MOE Key Laboratory of Macromolecular Synthesis and Functionalization, and Key Laboratory of Adsorption and Separation Materials & Technologies of Zhejiang Province, Department of Polymer Science and Engineering, Zhejiang University, Hangzhou 310027, China;* Email: xuzk@zju.edu.cn

Author

Ann-Kathrin Müller − *Macromolecular Chemistry and Bavarian Polymer Institute, University of Bayreuth, Bayreuth 95440, Germany*

Complete contact information is available at: https://pubs.acs.org/10.1021/acsami.1c01217

Author Contributions

The manuscript was written through the contributions of all authors. All authors have given approval to the final version of the manuscript.

Notes

The authors declare no competing financial interest.

■ ACKNOWLEDGMENTS

The authors gratefully acknowledge financial support from the Bavarian State Ministry of the Environment and Consumer Protection (funding code TNT01NaT-72524). Furthermore, the authors thank David Nardini from the MC I (University of Bayreuth) for providing the filtration test facility and his support, as well as Carmen Kunert for ICP-OES and TEM measurements.

■ REFERENCES

(1) Thiagarajan, V.; Alex, S. A.; Seenivasan, R.; Chandrasekaran, N.; Mukherjee, A. Interactive Effects of Micro/Nanoplastics and Nanomaterials/Pharmaceuticals: Their Ecotoxicological Consequences in the Aquatic Systems. *Aquat. Toxicol.* **2021**, *232*, 105747.

(2) Vance, M. E; Kuiken, T.; Vejerano, E. P; McGinnis, S. P; Hochella, M. F; Rejeski, D.; Hull, M. S Nanotechnology in the Real World: Redeveloping the Nanomaterial Consumer Products Inventory. *Beilstein J. Nanotechnol.* **2015**, *6*, 1769−1780.

(3) Koivisto, A. J.; Jensen, A. C. Øs.; Kling, K. I.; Nørgaard, A.; Brinch, A.; Christensen, F.; Jensen, K. A. Quantitative Material Releases from Products and Articles Containing Manufactured Nanomaterials: Towards a Release Library. *NanoImpact* **2017**, *5*, 119−132.

(4) Garner, K. L.; Suh, S.; Keller, A. A. Assessing the Risk of Engineered Nanomaterials in the Environment: Development and Application of the NanoFate Model. *Environ. Sci. Technol.* **2017**, *51*, 5541−5551.

(5) Boyes, W. K.; van Thriel, C. Neurotoxicology of Nanomaterials. *Chem. Res. Toxicol.* **2020**, *33*, 1121−1144.

(6) Kabir, E.; Kumar, V.; Kim, K.-H.; Yip, A. C.K.; Sohn, J.R. Environmental Impacts of Nanomaterials. *J. Environ. Manage.* **2018**, *225*, 261−271.

(7) Yoon, K.; Hsiao, B. S.; Chu, B. Functional Nanofibers for Environmental Applications. *J. Mater. Chem.* **2008**, *18*, 5326−5334.

(8) Brennan, M. B. Research Accelerates on Advanced Water-Treatment Technologies as Their Use in Purification Grows. *Chem. Eng. News* **2001**, *79*, 32−38.

(9) Kurniawan, T. A.; Chan, G. Y.S.; Lo, W.-H.; Babel, S. Physico−Chemical Treatment Techniques for Wastewater Laden with Heavy Metals. *Chem. Eng. J.* **2006**, *118*, 83−98.

(10) Aruchamy, K.; Mahto, A.; Nataraj, S. K. Electrospun Nanofibers, Nanocomposites and Characterization of Art: Insight on Establishing Fibers as Product. *Nano-Structures & Nano-Objects* **2018**, *16*, 45−58.

(11) Le, N. L.; Nunes, S. P. Materials and Membrane Technologies for Water and Energy Sustainability. *Mater. Sci. Technol.* **2016**, *7*, 1−28.

(12) Ramakrishna, S.; Jose, R.; Archana, P. S.; Nair, A. S.; Balamurugan, R.; Venugopal, J.; Teo, W. E. Science and Engineering of Electrospun Nanofibers for Advances in Clean Energy, Water Filtration, and Regenerative Medicine. *J. Mater. Sci.* **2010**, *45*, 6283−6312.

(13) Chen, H.; Huang, M.; Liu, Y.; Meng, L.; Ma, M. Functionalized Electrospun Nanofiber Membranes for Water Treatment: A Review. *Sci. Total Environ.* **2020**, *739*, 139944.

(14) Kaur, S.; Sundarrajan, S.; Rana, D.; Sridhar, R.; Gopal, R.; Matsuura, T.; Ramakrishna, S. Review: The Characterization of Electrospun Nanofibrous Liquid Filtration Membranes. *J. Mater. Sci.* **2014**, *49*, 6143−6159.

(15) Ding, B.; Yu, J. Electrospun Nanofibers for Energy and Environmental Applications; *Nanostructure science and technology*; Springer: Berlin, 2014.
(16) Firouzjaei, M. D.; Seyedpour, S. F.; Aktij, S. A.; Giagnorio, M.; Bazrafshan, N.; Mollahosseini, A.; Samadi, F.; Ahmadalipour, S.; Firouzjaei, F. D.; Esfahani, M. R.; et al. Recent Advances in Functionalized Polymer Membranes for Biofouling Control and Mitigation in Forward Osmosis. *J. Membr. Sci.* **2020**, *596*, 117604.
(17) Qasim, M.; Badrelzaman, M.; Darwish, N. N.; Darwish, N. A.; Hilal, N. Reverse Osmosis Desalination: A State-of-the-Art Review. *Desalination* **2019**, *459*, 59−104.
(18) Kaur, S.; Barhate, R.; Sundarrajan, S.; Matsuura, T.; Ramakrishna, S. Hot Pressing of Electrospun Membrane Composite and its Influence on Separation Performance on Thin Film Composite Nanofiltration Membrane. *Desalination* **2011**, *279*, 201−209.
(19) Bae, J.; Baek, I.; Choi, H. Mechanically Enhanced PES Electrospun Nanofiber Membranes (ENMs) for Microfiltration: The Effects of ENM Properties on Membrane Performance. *Water Res.* **2016**, *105*, 406−412.
(20) Al Aani, S.; Mustafa, T. N.; Hilal, N. Ultrafiltration Membranes for Wastewater and Water Process Engineering: A Comprehensive Statistical Review over the Past Decade. *J. Water Process Eng.* **2020**, *35*, 101241.
(21) Ray, S. S.; Chen, S.-S.; Li, C.-W.; Nguyen, N. C.; Nguyen, H. T. A Comprehensive Review: Electrospinning Technique for Fabrication and Surface Modification of Membranes for Water Treatment Application. *RSC Adv.* **2016**, *6*, 85495−85514.
(22) Chen, W.; Mo, J.; Du, X.; Zhang, Z.; Zhang, W. Biomimetic Dynamic Membrane for Aquatic Dye Removal. *Water Res.* **2019**, *151*, 243−251.
(23) Managheb, M.; Zarghami, S.; Mohammadi, T.; Asadi, A. A.; Sahebi, S. Enhanced Dynamic Cu(II) Ion Removal Using Hot-Pressed Chitosan/Poly (vinyl alcohol) Electrospun Nanofibrous Affinity Membrane (ENAM). *Process Saf. Environ. Prot.* **2021**, *146*, 329−337.
(24) Hosseini, S. A.; Vossoughi, M.; Mahmoodi, N. M. Preparation of Electrospun Affinity Membrane and Cross Flow System for Dynamic Removal of Anionic Dye from Colored Wastewater. *Fibers Polym.* **2017**, *18*, 2387−2399.
(25) Kaur, S.; Kotaki, M.; Ma, Z.; Gopal, R.; Ramakrishna, S.; Ng, S. C. Oligosaccharide Functionalized Nanofibrous Membrane. *Int. J. Nanosci.* **2006**, *5*, 1−11.
(26) Homaeigohar, S.; Dai, T.; Elbahri, M. Biofunctionalized Nanofibrous Membranes as Super Separators of Protein and Enzyme from Water. *J. Colloid Interface Sci.* **2013**, *406*, 86−93.
(27) Homaeigohar, S.; Elbahri, M. Nanocomposite Electrospun Nanofiber Membranes for Environmental Remediation. *Materials* **2014**, *7*, 1017−1045.
(28) Miller, D. J.; Dreyer, D. R.; Bielawski, C. W.; Paul, D. R.; Freeman, B. D. Surface Modification of Water Purification Membranes. *Angew. Chem., Int. Ed.* **2017**, *56*, 4662−4711.
(29) Yan, X.; Li, J.; Yi, L. Fabrication of pH-Responsive Hydrophilic/Hydrophobic Janus Cotton Fabric via Plasma-Induced Graft Polymerization. *Mater. Lett.* **2017**, *208*, 46−49.
(30) Hutten, I. M. *Handbook of Nonwoven Filter Media*; Elsevier/BH: Amsterdam, 2007.
(31) Karim, Z.; Hakalahti, M.; Tammelin, T.; Mathew, A. P. In Situ TEMPO Surface Functionalization of Nanocellulose Membranes for Enhanced Adsorption of Metal Ions from Aqueous Medium. *RSC Adv.* **2017**, *7*, 5232−5241.
(32) Wang, Z.; Sahadevan, R.; Crandall, C.; Menkhaus, T. J.; Fong, H. Hot-Pressed PAN/PVDF Hybrid Electrospun Nanofiber Membranes for Ultrafiltration. *J. Membr. Sci.* **2020**, *611*, 118327.
(33) Khajavian, M.; Salehi, E.; Vatanpour, V. Chitosan/Polyvinyl Alcohol Thin Membrane Adsorbents Modified with Zeolitic Imidazolate Framework (ZIF-8) Nanostructures: Batch Adsorption and Optimization. *Sep. Purif. Technol.* **2020**, *241*, 116759.
(34) Li, L.; Li, Y.; Yang, C. Chemical Filtration of Cr (VI) with Electrospun Chitosan Nanofiber Membranes. *Carbohydr. Polym.* **2016**, *140*, 299−307.
(35) Hamid, S. M.; Sherrington, D. C. Novel Quaternary Ammonium Amphiphilic (Meth)acrylates: 2. Thermally and Photochemically Initiated Polymerizations. *Polymer* **1987**, *28*, 332−339.
(36) Gandhimathi, C.; Sundarrajan, S.; Matsuura, T.; Srinivasan, D. K.; Wei, H.; Xuecheng, D.; Ramakrishna, S. Fabrication and Characterization of High Flux Poly(vinylidene fluoride) Electrospun Nanofibrous Membrane Using Amphiphilic Polyethylene-block-poly-(ethylene glycol) Copolymer. *J. Appl. Polym. Sci.* **2021**, *138*, 50296.
(37) Li, L.; Zhang, J.; Li, Y.; Yang, C. Removal of Cr (VI) with a Spiral Wound Chitosan Nanofiber Membrane Module via Dead-End Filtration. *J. Membr. Sci.* **2017**, *544*, 333−341.
(38) Kiani, S.; Mousavi, S. M.; Saljoughi, E.; Shahtahmassebi, N. Novel High Flux Nanofibrous Composite Membrane based on Polyphenylsulfone Thin Barrier Layer on Nanofibrous Support. *Fibers Polym.* **2017**, *18*, 1531−1544.
(39) Dobosz, K. M.; Kuo-Leblanc, C. A.; Martin, T. J.; Schiffman, J. D. Ultrafiltration Membranes Enhanced with Electrospun Nanofibers Exhibit Improved Flux and Fouling Resistance. *Ind. Eng. Chem. Res.* **2017**, *56*, 5724−5733.
(40) Shi, X.; Xu, Z.; Huang, C.; Wang, Y.; Cui, Z. Selective Swelling of Electrospun Block Copolymers: From Perforated Nanofibers to High Flux and Responsive Ultrafiltration Membranes. *Macromolecules* **2018**, *51*, 2283−2292.
(41) Bjorge, D.; Daels, N.; van Hulle, S. Initial Testing of Electrospun Nanofibre Filters in Water Filtration Applications. *WSA* **2010**, *36*, 151−156.
(42) Li, X.-G.; Kresse, I.; Springer, J.; Nissen, J.; Yang, Y.-L. Morphology and Gas Permselectivity of Blend Membranes of Polyvinylpyridine with Ethylcellulose. *Polymer* **2001**, *42*, 6859−6869.
(43) Tlili, I.; Alkanhal, T. A. Nanotechnology for Water Purification: Electrospun Nanofibrous Membrane in Water and Wastewater Treatment. *J. W. Reuse Des.* **2019**, *9*, 232−248.
(44) Huang, L.; Arena, J. T.; McCutcheon, J. R. Surface Modified PVDF Nanofiber Supported Thin Film Composite Membranes for Forward Osmosis. *J. Membr. Sci.* **2016**, *499*, 352−360.
(45) Wang, Y.; Gorecki, R. P.; Stamate, E.; Norrman, K.; Aili, D.; Zuo, M.; Guo, W.; Helix-Nielsen, C.; Zhang, W. Preparation of Super-Hydrophilic Polyphenylsulfone Nanofiber Membranes for Water Treatment. *RSC Adv.* **2019**, *9*, 278−286.
(46) Wang, X.; Chen, X.; Yoon, K.; Fang, D.; Hsiao, B. S.; Chu, B. High Flux Filtration Medium Based on Nanofibrous Substrate with Hydrophilic Nanocomposite Coating. *Environ. Sci. Technol.* **2005**, *39*, 7684−7691.
(47) Ma, Z.; Kotaki, M.; Ramakrishna, S. Surface Modified Nonwoven Polysulphone (PSU) Fiber Mesh by Electrospinning: A Novel Affinity Membrane. *J. Membr. Sci.* **2006**, *272*, 179−187.
(48) Stolberg, L.; Richer, J.; Lipkowski, J.; Irish, D.E. Adsorption of Pyridine at the Polycrystalline Gold-Solution Interface. *J. Electroanal. Chem. Interfacial Electrochem.* **1986**, *207*, 213−234.
(49) Gandubert, V. J.; Lennox, R. B. Assessment of 4-(Dimethylamino)pyridine as a Capping Agent for Gold Nanoparticles. *Langmuir* **2005**, *21*, 6532−6539.
(50) Mahanta, N.; Valiyaveettil, S. Surface Modified Electrospun Poly(vinyl alcohol) Membranes for Extracting Nanoparticles from Water. *Nanoscale* **2011**, *3*, 4625−4631.

https://dx.doi.org/10.1021/acsami.1c01217
ACS Appl. Mater. Interfaces 2021, 13, 15659−15667

Supporting Information for

Preparation and Performance Assessment of Low-Pressure Affinity Membranes based on Functionalized, Electrospun Polyacrylates for Gold Nanoparticle Filtration

Ann-Kathrin Müller[a)], Zhi-Kang Xu[b)],Andreas Greiner[a)]**

[a)] Macromolecular Chemistry and Bavarian Polymer Institute, University of Bayreuth, Universitätsstraße 30,95440 Bayreuth, Germany; E-mail: greiner@uni-bayreuth.de

[b)] MOE Key Laboratory of Macromolecular Synthesis and Functionalization, and Key Laboratory of Adsorption and Separation Materials & Technologies of Zhejiang Province, Department of Polymer Science and Engineering, Zhejiang University, Hangzhou 310027, China; E-mail: xuzk@zju.edu.cn

This PDF-file includes:

Materials, measurements, and experimental procedures

Fig. S1-S16, Table S1-S29, video

Experimental Section

Materials

4-Vinylpyridine (Acros Organics, 95 %), acrylic acid (Alfa Aesar, >99 %) and methyl methacrylate (Aldrich, 99 %) were recondensed, N-isopropylacrylamid (TCI, 98 %) and azobis(isobutyronitrile) (Sigma Aldrich, 98 %) were recrystallized before use. 2-Dimethylaminoethylmethacrylate (Acros Organics, 99 %), 1-bromodecane (Aldrich, 98 %), sodium borohydride (Acros Organics, 99 %), citric acid trisodium trihydrate (Acros Organics, 99 %), tetrachloroauro(III)acid trihydrate (Alfa Aesar, 99,99 %) was used without further purification. Acetonitrile (Alfa Aesar, >99 %), chloroform (Fisher Chemical, 99 %), dimethyl sulfoxide (Fisher Chemical, >99 %), dimethyl formamide (Fisher Chemical, >99 %). 4-Methacryloyl-oxy-benzophenone (MABP) was synthesized according to literature elsewhere. [1]

Measurements

Nuclear Magnetic resonance (NMR)

1H and 13C NMR were recorded using Bruker Ultra-Shield using 300 MHz and 75 MHz. Dimethylsulfoxide-d6 was used as solvent for NMR measurements, and MestreNova software utilized for data evaluation.

Attenuated total reflection-Fourier transformed infrared spectra (ATR-FTIR)

ATR-FTIR was recorded on Spectrum 100 FT-IR (Perkin Elmer). All samples were measured in the wavenumber region between 400- 4000 cm-1 with data points in the interval of 1 cm-1 four times and were evaluated with software Spectrum (Version 6.3.5).

Size exclusion chromatography (SEC)

Polymer molar masses and dispersities were measured with a size-exclusion-system equipped with a pre-column (Gram 10 µm) and two columns Gram 10 µm 100/ 3000 Å. Polymers were detected with a refraction index detector (RI, Agilent Technologies 1260 Infinity) and a diode array detector (DAD, UV-vis, Agilent Technologies 1260 Infinity). The system was operated at a 0.5 mL/min flow rate, controlled by Agilent Technologies 1260 Infinity Pump and with DMF, lithium bromide (5 g/L), and toluene solvent as an internal standard. Narrowly distributed polystyrene (PSS-Polymer standards) was used as standard. The polymer samples were prepared with 2 mg/mL in DMF with lithium bromide and toluene and were filtered through a 0.22 µm syringe.

UV-Cross-linking

Cross-linking reactions were performed using UVHand 250 GS from the Hönle group, with a light source emitting wavelength from 320-400 nm and at 15 cm sample distance with a power of 60 mW/cm2.

Tensile Test

Tensile elongation was conducted using a machine from Zwick Roell, containing a load cell of 20 N (XForce HP) and as test speed 2 mm/min. Membranes were cut with a razor blade into samples with a dimension of 2 cm x 4 mm, and the sample thickness was in the range of roughly 20-40 µm. A minimum of three samples were examined, and evaluation was done using test Xpert II software.

Contact angle measurement

The contact angle for all nonwovens was investigated with a drop shape analyzer from Krüss, using the software Advanced Version 1.4.0.1. The polymeric films were located on an object holder and a drop of 4 µL was produced and placed on the film.

Pore size measurement

The membrane pore sizes were measured with the porometer Topas PSM165 utilizing the PSMWin software. The membrane sample was clamped into a measuring adapter, which has a flow cross-section of 11 mm, and for the bubble point, Topor liquid was dropped onto the membrane (surface tension 16.0 mN/m). The airflow rate was adjusted in the range of 3.6 - 4200 L/h.

Pressure drop test

Membrane pressure drop was investigated on a specifically designed apparatus. An HPLC pump (Preparative Pump 1800, Knauer) secures the correct flow rate through the filter (1.1 cm radius), which was placed in a cylindrical metal cartridge. Before and after the membrane, a pressure sensor (Omega, PAA33x-V-10) was installed to determine the pressure drop by software.

Ultraviolet/visible light (UV/Vis)

UV/Vis spectra were recorded on V-630 spectrometer from Jasco with spectra manager CFR software. All spectra were measured in the wavelength region between 200-800 nm, collecting data points at a distance of 2 nm. Samples were prepared by diluting nanoparticle dispersions with water, with concentrations 0.05- 0.025 mg/mL, and measurement were executed in a quartz cuvette (1 cm x 1 cm). A calibration was done for concentration determination. Each measurement has an error of at least ± 0.00046 mg/mL and an average error of ±5 %.

Asymmetric flow-field flow fractionation (AFFFF)

AFFFF was performed on an AF2000 system from Postnova Analytics (Landsberg am Lech, Germany). Samples were separated on a NovaRC 10 kDa membrane in a 295x30 mm channel with 350 µm spacer with Milli-Q water as eluent. UV detector (253 nm) and Multiple angle light scattering (MALS) detector (532 nm) were used for analysis, and Postnova AF2000 Control software was applied for size evaluation. The electrical EFFFF was applied for measuring the zeta potential of the AuNPs in Milli-Q water with potassium nitrate (1 mM) as eluent at various applied currents: neutral, -0.7 mA, -1.5 mA, -3 mA.

The UV detector signal for measurements without separation was used for concentration determination, and the recovery rate was calculated for measurements with separation. The particle size was analyzed in separation experiments. A calibration was done for concentration determination inducing an error of ±0.00525 mg/mL for each sample, and an averaged total error of ±12 %.

Samples were measured with and without separation, according to the following methods:

Table S 1. AFFFF and EFFFF method for measuring AuNPs.

Step	Parameter		With separation	Without separation	Zeta potential
	Injection volume [µL]		20	20	20
	Detector flow [mL/min]		0.5	0.5	0.5
Focusing	Injection flow [mL/min]		0.2	0.2	0.2
	Injection time [min]		5	1	6
	Crossflow		0.7	0	0.7
	Transition time		0.5	0.5	0.5
Elution	Step 1	Elution time [min]	2	10	1
		From [mL/min]	0.7	0	0.7
		To [mL/min]	0.7	0	0.5
		Type	Const.	Const.	Linear
	Step 2	Elution time [min]	20	None	40
		From [mL/min]	0.7		0.5
		To [mL/min]	0.0		0.5
		Type	0.05 Power		Const.
	Step 3	Elution time [min]	None		1
		From [mL/min]			0.5
		To [mL/min]			0
		Type			Linear
Rinsing	Time [min]		5	5	5

Transmission electron microscope (TEM)

Samples for TEM measurement were prepared by adding 2 µL of nanoparticle dispersion on top of carbon-coated copper grid (Carbon support film, 16 200 mesh, copper) and dried at room temperature. Measurement was executed on Leo 922 from Zeiss at an acceleration voltage of 200 kV, with a LuS6 crystal as the cathode. At least 70 nanoparticles were gauged with ImageJ software for mean particle diameter.

Scanning electron microscope (SEM)

Membranes were placed onto a coal film and sputtered with 1.3 nm platinum by the Cressington platinum-sputter coater 208HR. Measurements were done with the Leo 1530 from Zeiss at an acceleration voltage of 3 kV and at a pressure of 2.0 x 10^{-5} bar for pictures with inlense and secondary electron (Everhart Thornley) detector. The backscattering detector from Centaurus was used at 10 kV acceleration voltage and the same pressure.

Dynamic light scattering (DLS)

DLS measurements were done using a system ALV/ DLS/ SLS-5022GF. A photon-counting module for pseudo-cross correlation measurements with the ALV compact goniometer system, consisting of two high QE APDs. As adjustment was set, the cylindrical HeNe-laser wavelength at 632 nm (22 mW) with a detector angle of 90° and a temperature of 294 K. Samples were all prepared in water with a viscosity of 0.9711 cp. The data was analyzed with WINDOWS-95/98/NT-4.0 control and data reduction software.

Inductively coupled plasma-optical emission spectroscopy (ICP-OES)

Measurements were performed on an Avio 200, Perkin Elmer in radial viewed plasma with purged polychromator configurations. The measurement was calibrated with five standard solutions at concentrations of 0.05, 0.1, 0.5, 1, and 10 mg L-1. AuNP samples were prepared

by diluting the dispersions with aqua regia (HNO3:HCl 1:3) and Milli-Q water. The measurements possess an averaged error of ±10 % and at least ±0.00272 mg/mL due to the calibration.

Experimental procedure

Dimethyl decylammoniumethyl methacryl bromide (Nplus)

This acrylate monomer was synthesized according to Elisabeth Giebel.[2] To a mixture of acetonitrile (50 mL) and chloroform (25 mL) the reactants 2-dimethylamino-ethylmethacrylate (10.7 mL, 63.6 mmol) and 1 – bromodecane (17.5 mL, 70.0 mmol) were added and stirred for 24 h at 40°C. The solvent was removed under reduced vacuum, and the solid was washed with diethyl ether. After drying under high vacuum, white crystals were observed (13.98 g, 53.8 % yield).

^{1}H-NMR (300 MHz, DMSO-d$_6$) δ 0.85 (s, 3 H, H^{18}); 1.24 (s, 16 H, H^{10}-H^{17}); 1.67 (b, 2 H, H^{9}); 1.90 (s, 3 H, H^{3}); 3.13 (s, 6 H, H^{7} u H^{8}); 3.74 (b, 2 H, H^{5}), 4.52 (b, 2 H, H^{6}); 5.76 (b, 1 H, H^{1}); 6.08 (b, 1 H, H^{1})

^{13}C-NMR (75 MHz, DMSO-d$_6$) δ 14.4 (C^{18}); 18.4 (C^{3}); 22.2 (C^{9}); 22.6 u 26.2 u 29.1 u 31.7 u 35.7 (C^{10}-C^{17}); 50.8 u 51.1 (C^{7} u C^{8}); 58.6 (C^{6}); 62.1 (C^{5}); 126.9 (C^{1}); 135.8 (C^{2}); 166.3 (C^{4})

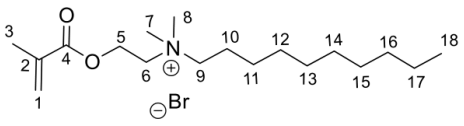

Free-radical copolymerization

Under Schlenk-conditions, monomers and solvent were mixed, and the solution was degassed by three freeze-thaw cycles. In a separate flask, 2,2'azobis(2-methylpropionitrile) (AIBN) was dissolved in solvent (3 mL), and also three freeze-thaw cycles were executed. The AIBN was then quickly injected into the monomer mixture. The polymerization was then carried out under rapid stirring for 24 h at 80°C. The polymerization was stopped by freezing in liquid nitrogen and afterward diluted with THF and slowly poured into hexane (respectively mixture with acetone (for AA copolymers) or ethyl acetate (for Nplus copolymers)), filtered off the polymer, and dried under high vacuum.

Gold nanoparticles

Gold nanoparticles (AuNP) were synthesized according to the procedure of Neus G. Bastus.[3] The aqueous solution of $HAuCl_4$ dihydrate (39.36 mg; 2.5 x 10^{-4} M) was heated to the boiling point, followed by the dropwise addition of trisodium citrate (105.12 mg; 39.17 mM). In the next 5 min, the solution color changed from yellow to white, grey, faint blue, and finally purple/red, indicating the formation of AuNP. After another 30 min of reaction time, the solution was cooled down to room temperature and was stored at 4°C. The nanoparticle dispersion is stable for more than a half year.

Electrospinning and UV-cross-linking

All copolymers were dissolved with 25 wt% in dimethyl formamide (DMF) and were electrospun with 17/-1 kV onto a rotating disc collector. This copolymer could not be electrospun because of poor solubility in any solvent. Afterward, all nonwovens were UV-cross-linked. The cross-linking was tracked with FTIR-spectroscopy. Before and after cross-linking, the spectra showed the disappearance of the two peaks at 1600 and 1651 cm^{-1} from the

MABP carboxyl group. With the rising amount of MABP, the UV-irradiation time needed to be increased from 2, 3 up to 5 hours.

Water uptake, pore size, and fiber diameter

The mass of the membrane was measured before it was placed in water. With a different piece of the same membrane the pore size (porometer) and the fiber diameter (SEM) were determined. After 24 hours, the membrane was taken out, and after the water dropped off, the membrane was weight again. The membrane was dried under room temperature and the pore size and the fiber diameter were measured, too.

Nanoparticle filtration

The membranes were cut into pieces with a razor have a diameter of 14 mm. These were deposit on top of a sheet of PET mesh with a pore size of 50 μm and were placed into a reusable filtering apparatus from Satorius AG. The used membrane area for filtration is limited by the apparatus to 0.95 cm^2. The solution flow rate is adjusted by a syringe pump (Landgraf Laborsysteme, model no. LA 30), and the filtrate is collected in vials. Main filtration tests were carried out with 1 mL/min flow rate and a double layer of nonwoven. The filtrate was collected for 1.5 min in one batch; total collection time was 6 min. Each batch was then further analyzed by UV/Vis, AFFFF, and ICP-OES.

Polymer Synthesis

Table S 2. Composition, molecular weight, dispersity and yield for all copolymers.

Functional group	Feed composition MMA:MABP: X	Copolymer composition (NMR)*[a]	Molecular Weight (cal.) [kDa]	Molecular Weight *[b]/*[c] (GPC) [kDa]	Dispersity Đ	Yield [%]
Pyr	85:5:10	87:4:9	108	123	1.48	96
NIPAM		83:6:11	109	164	1.74	97
AA		86:4:10	104	43	1.97	98
Nplus		79:8:13	135	30	1.96	60
Pyr	60:10:30	55:13:32	257	171	1.67	60
NIPAM		57:13:30	263	221	1.73	98
AA		72:11:17	230	-	-	91
Nplus		65:11:24	474	-	-	45
Pyr	40:10:50	42:8:50	235	170	1.68	44
NIPAM		37:11:52	243	233	1.67	98
AA		65:7:28	202	-	-	92
Nplus		55:14:30	510	-	-	52
Pyr	30:70	31:69	306	150	1.62	95
NIPAM		30:70	320	260	2.30	93
AA		30:70	260	-	-	105
Nplus		-	687	-	-	87

*a NMR: 300 MHz in DMSO-d6. The copolymer composition is determined by the ratio of the polymer integrals: NIPAM (3.7-3.95 ppm; 1 proton), acid (12.2-12.6 ppm; 1 proton), pyridine (8.2-8.6 ppm; 2 protons), Nplus (4.1-4.7 ppm, 2 protons), MABP (7.1-8.1 ppm; 9

protons), MMA (3.4-3.7 ppm, 3 protons). If signals are overlapping with signals from other groups, the integral of the overlapping signal is substracted.

*b The polymers were measured in DMF with lithium bromide against polystyrene standard.

*c The copolymers with AA and Nplus 30-70 % could be not measured by GPC because of too many interactions between the acid or the quaternary amine group with the column material.

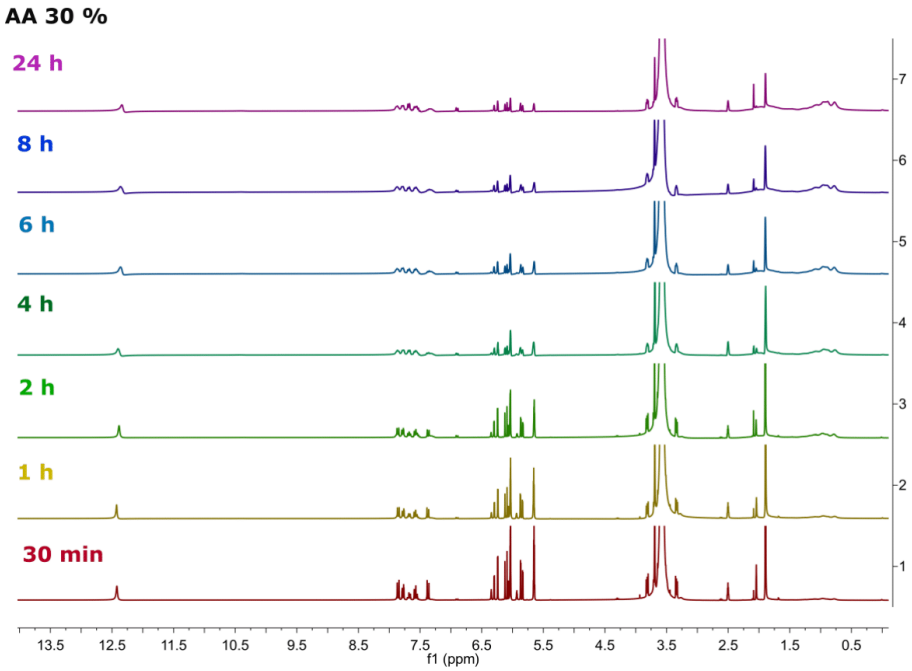

Figure S 1. ^{1}H-NMR data for kinetic of AA30% copolymer.

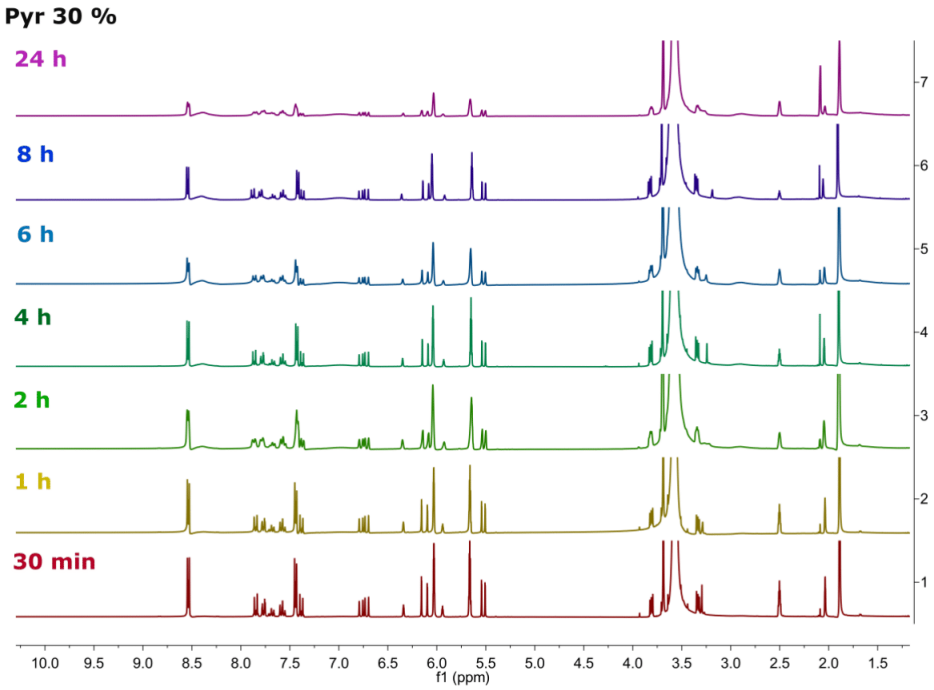

Figure S 2. [1]H-NMR data for kinetic of Pyr30% copolymer.

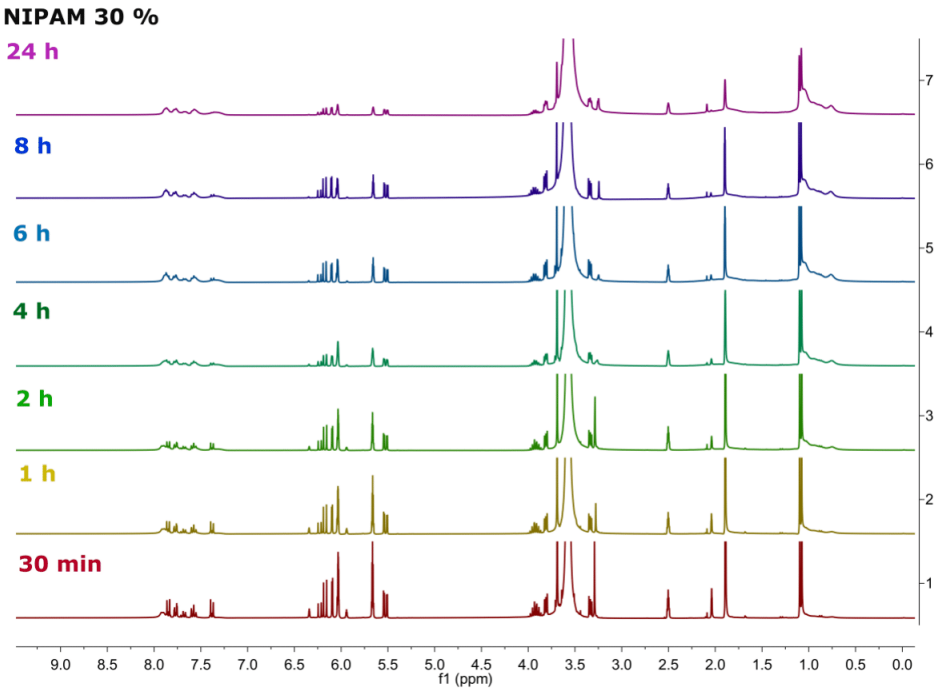

Figure S 3. [1]H-NMR data for kinetic of NIPAM30% copolymer.

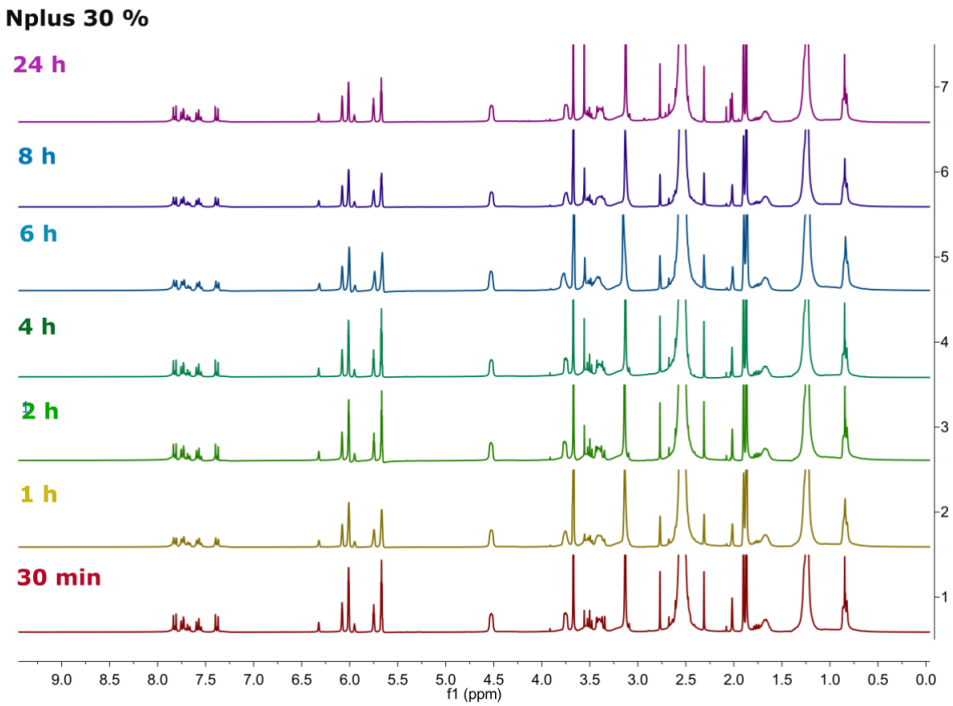

Figure S 4. ^{1}H-NMR data for kinetic of Nplus30% copolymer.

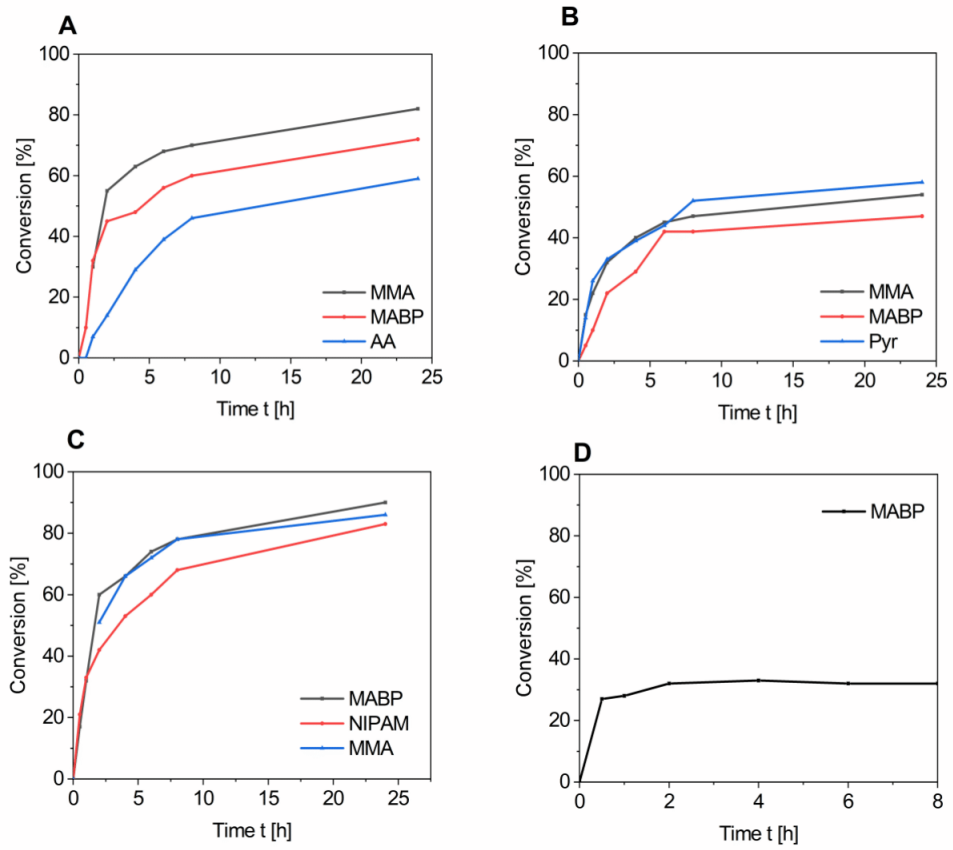

Figure S 5. Monomer conversion in dependence on time for A) AA; B) Pyr; C) NIPAM and D) Nplus. For the copolymerization with Nplus, only the MABP monomer and polymer peaks can be integrated, for all other substances the peaks overlap and therefore, no conversion curve can be calculated.

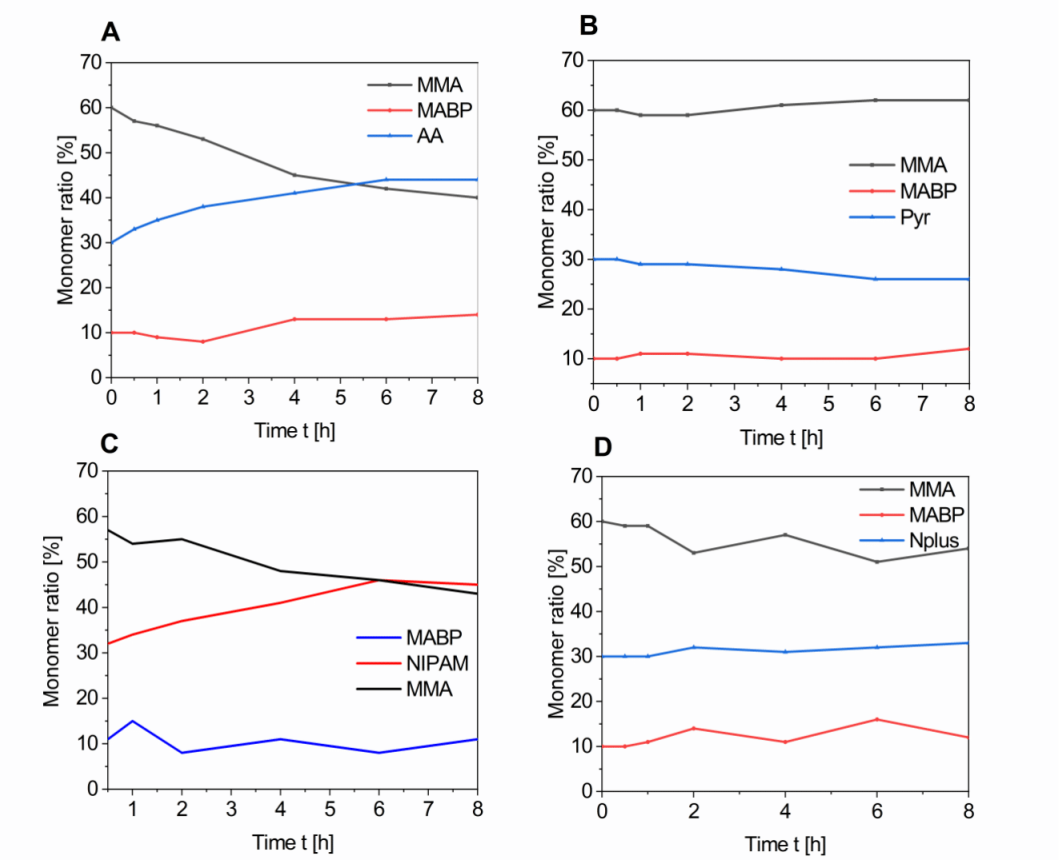

Figure S 6. Monomer ratio in dependence on time for A) AA; B) Pyr; C) NIPAM and D) Nplus.

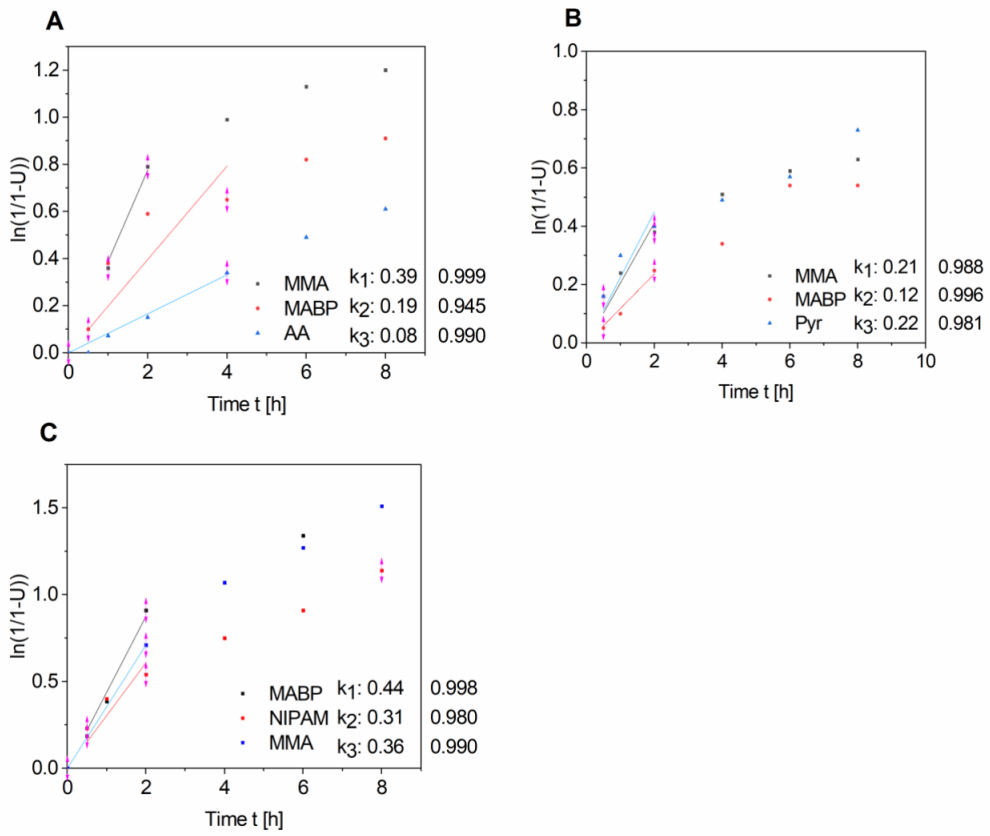

Figure S 7. Determination of copolymerization parameters for A) AA; B) Pyr and C) NIPAM. For the Nplus-copolymer no copolymerization parameters can be determined because the conversion of the monomers to polymers cannot be calculated due to overlapping peaks.

Membrane Properties

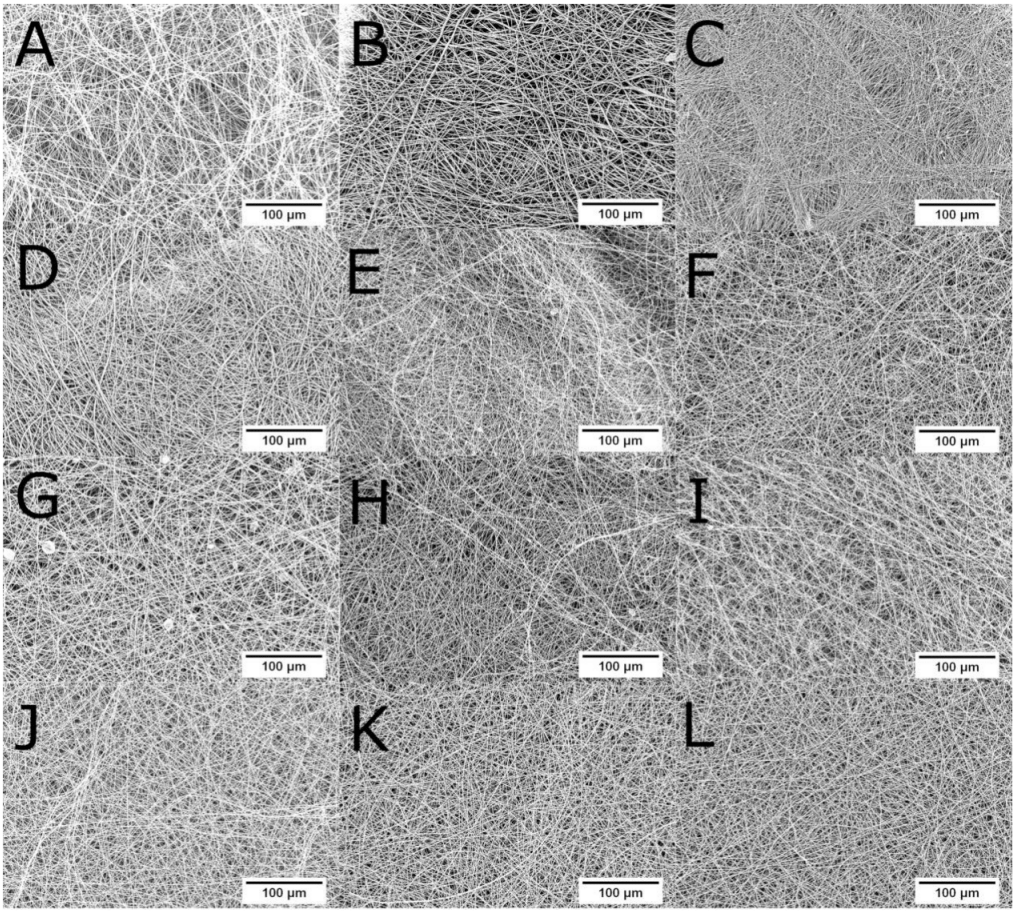

Figure S 8. SEM images of the electrospun membranes in the order of A) AA10%, B) AA30%, C) AA50%, D) NIPAM10%, E) NIPAM30%, F) NIPAM50%, G) Pyr10%, H) Pyr30%, I) Pyr50%, J) Nplus10%, K) Nplus30%, and L) Nplus50%.

Table S 3. Water uptake of the electrospun nanofibrous membranes.

Functional group	Amount [%]		Water uptake [mg/mg membrane]		Reduction of water uptake [%] *
	Functional group	MABP	Cross-linked	Non-cross-linked	
NIPAM	10	5	9.7	26.9	63
	30	10	8.6	19.1	54
	50	10	19.0	42.6	55
	70	30	23.4	52.3	55
AA	10	5	7.5	12.5	40
	30	10	11.9	14.8	20
	50	10	10.0	27.7	64
	70	30			
Pyr	10	5	2.8	3.5	20
	30	10	13.7	22.3	40
	50	10	6.7	15.1	56
	70	30	14.7	42.4	63
Nplus	10	5	21.8	25.4	15
	30	10	14.2	19.2	26
	50	10	15.1	57.1	74
	70	30	18.9	15.7	

*Ratio is calculated for water uptake of cross-linked and non-cross-linked fibers.

Table S 4. Pore size [µm] for electrospun nanofibrous nonwoven before and after water contact, non-cross-linked and cross-linked.

Functional group	Amount [%]		Pore size [um]				Bandwidht of pore size *
	Functional group	MABP	Cross-linked		Non-cross-linked		
			dry	wet	dry	wet	
NIPAM	10	5	2.13	1.93	2.21	2.09	0.1
	30	10	1.61	1.53	1.51	1.62	0.1
	50	10	1.40	0.95	1.16	0.77	0.4
	70	30	1.28	0.92	1.21	0.77	0.4
AA	10	5	2.14	2.13	2.11	2.30	0.1
	30	10	2.38	2.23	2.18	2.24	0.1
	50	10	1.38	0.69	1.28	0.99	0.5
	70	30					
Pyr	10	5	2.08	2.17	2.18	2.15	0.1
	30	10	1.19	1.10	1.21	1.17	0.1
	50	10	1.19	1.01	1.17	0.97	0.2
	70	30	0.88	0.67	0.82	0.70	0.2
Nplus	10	5	1.74	1.27	1.72	1.21	0.5
	30	10	1.55	0.94	1.32	1.17	0.4
	50	10	1.43	0.51	1.28	-	0.8
	70	30	1.62	1.10	1.49	-	0.4

*The difference of pore sizes in the dry and wet state is calculated both for the cross-linked and the non-cross-linked nonwoven and an average value was determined.

Table S 5. Fiber diameter [nm] for the electrospun nanofibrous membranes before and after water contact, as well as cross-linked and non-cross-linked.

Amount [%]			Fiber diameter [nm]				
Functional group	Functional group	MABP	Cross-linked		Non-cross-linked	Percentage difference [%] *	Swelling of non cross-linked fibers [%]
			dry	Wet	wet		
NIPAM	10	5	388 ±53	434 ±15	430 ±12	-0.07	10
	30	10	364 ±20	365 ±13	383 ±12	+4.7	5
	50	10	267 ±10	344 ±23	454 ±25	+24.1	41
	70	30	307 ±12	297 ±7	401 ±18	+26.0	23
AA	10	5	377 ±28	384 ±17	362 ±19	-3.0	-4
	30	10	568 ±14	575 ±21	587 ±12	+2.1	3
	50	10	219 ±17	303 ±18	317 ±16	+5.1	30
	70	30					
Pyr	10	5	401 ±10	449 ±23	472 ±20	+4.9	15
	30	10	317 ±15	305 ±12	331 ±9	+7.9	5
	50	10	320 ±18	350 ±22	415 ±19	+15.7	26
	70	30	147 ±13	170 ±12	210 ±8	+19.5	30
Nplus	10	5	339 ±12	389 ±10	376 ±14	-3.4	10
	30	10	371 ±15	382 ±22	379 ±13	-0.7	2
	50	10	247 ±22	367 ±11	-	-	49
	70	30	401 ±31	434 ±22	490 ±31	+11.5	19

*The ratio of fiber diameter was determined for cross-linked and non-cross-linked fibers and hence the reduction of swelling by cross-linking was identified.

Table S 6. Contact angle of electrospun nanofibrous membranes.

Functional group	Contact angle [°]*			
	10 %	30 %	50 %	70 %
NIPAM	144	143	142 → 0	140 → 0
AA	142	141	141 → 0	
Pyr	146	145	141 → 0	141 → 0
Nplus	144	144	143 → 0	113 → 0

* The contact angle decreased for membranes with 50 mol% and 70 mol% in-between 30 sec. up to 5 min to 0°. This property is marked by: →0.

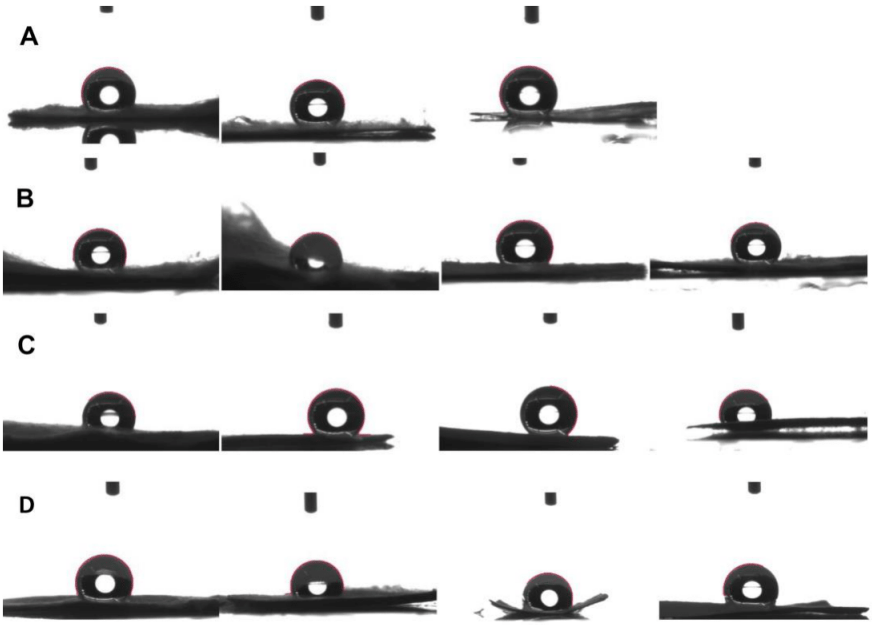

Figure S 9. Picture of contact angle measurements directly after placing the drop on the membrane. Membranes contain rising amounts of functional group from 10 %, 30 %, 50 %, and 70 % functional group A) AA, B) NIPAM, C) Nplus, and D) Pyr.

Table S 7. Membrane thickness [calculated with mikrotom [µm]].

Functional group	Membrane thickness [µm]			
	10 %	30 %	50 %	70 %
NIPAM	42 - 55	35 – 40	50 – 68	46 – 54
AA	43 - 53	43 – 50	25 – 34	
Pyr	50 - 60	35 – 45	37 – 55	30 – 49
Nplus	58 - 68	53 – 60	48 – 68	33 – 42

Table S 8. Pressure drop of all electrospun nanofibrous membranes at different flow rates. *

Functional group	Amount [%]	Membrane weight m [mg]	Pressure drop for different flow rates [mL/min] [bar]			
			50	100	200	500
NIPAM	10	9.7	0.1	0.2	0.5	2.0
	30	5.8	0.1	0.2	0.6	1.8
	50	7.5	0.1	0.3	0.7	2.1
	70	5.9	0.2	0.6	1.7	-
AA	10	4.6	0.0	0.0	0.0	0.04
	30	7.1	0.0	0.1	0.3	1.0
	50	5.8	0.2	0.4	1.0	1.7
	70					
Pyr	10	6.2	0.1	0.2	0.4	1.5
	30	4.0	0.2	0.4	1.0	1.8
	50	7.6	0.4	1.0	2.1	-
	70	4.4	0.7	2.1	-	-
Nplus	10	6.9	0.1	0.3	0.6	-
	30	11.6	0.6	1.4	-	-
	50	7.0	0.4	1.0	1.9	-
	70	5.0	0.8	1.6	-	-

*The pressure drop apparatus could just withstand a total pressure drop of 3 bar. Therefore, measurements were stopped, which probably exceed those values. Those tests are marked in the table with -.

Table S 9. Maximum tensile strength [MPa] investigated in tensile-testing of all cross-linked membranes after water contact.

Functional group	Maximum tensile strength [MPa]			
	10 %	30 %	50 %	70 %
NIPAM	2.6 ±0,0	3.4 ±0,3	5.0 ±0,3	5.3 ±0,3
AA	0.9 ±0,1	4.9 ±0,4	7.4 ±0,4	-
Pyr	3.7 ±0,2	5.6 ±0,4	11.6 ±0,6	2.4 ±0,2
Nplus	4.8 ±0,1	9.6 ±0,3	7.3 ±0,4	3.9 ±0,1

Table S 10. Elongation [%] of membranes at break.

Functional group	Elongation [%]			
	10 %	30 %	50 %	70 %
NIPAM	206 ± 6	118 ± 5	116 ± 2	78 ± 9
AA	104 ± 5	73 ± 31	8 ± 2	-
Pyr	152 ± 5	95 ± 12	41 ± 3	19 ± 5
Nplus	77 ± 9	59 ± 5	12 ± 4	24 ± 5

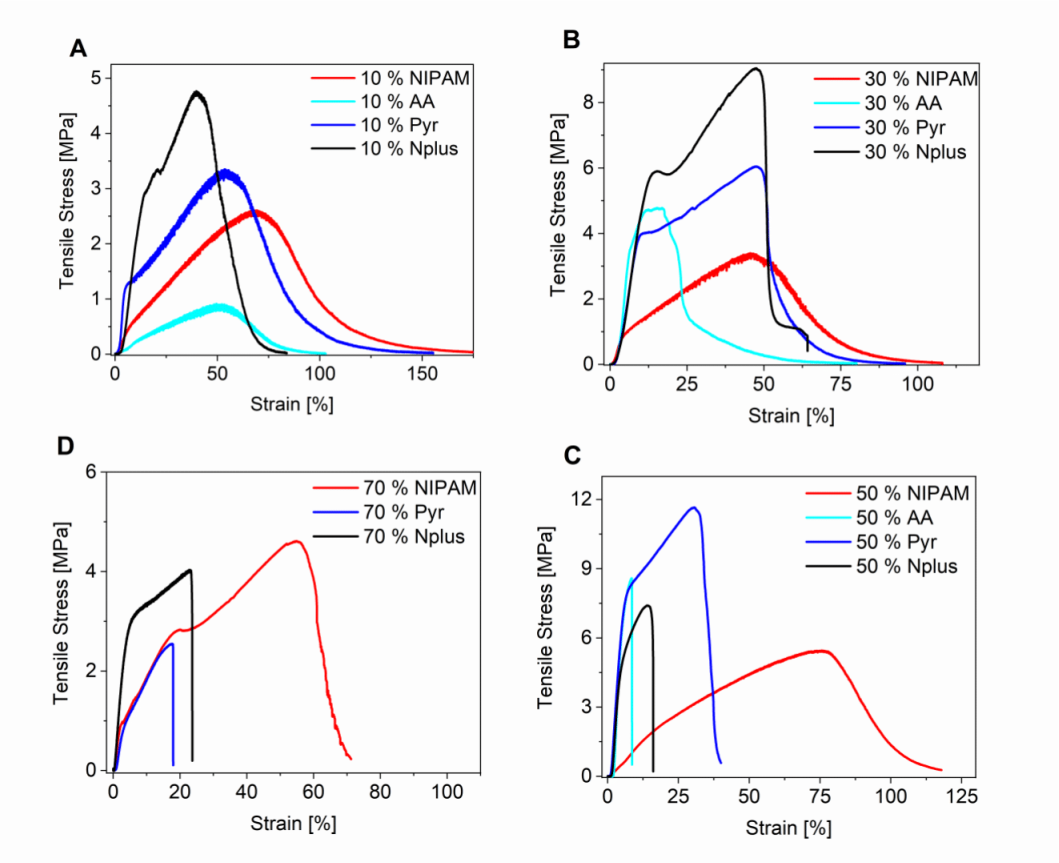

Figure S 10. Tensile test stress-strain curves for all membranes.

AuNP adsorption

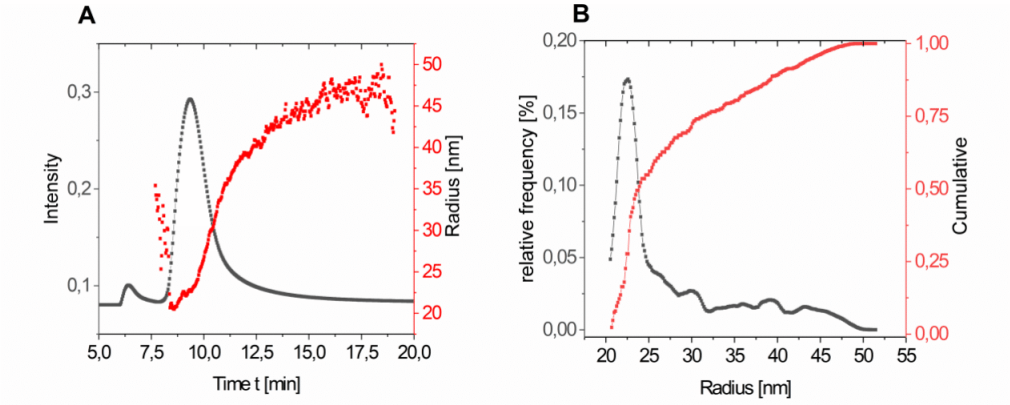

Figure S 11. AFFFF measurements of AuNPs and its A) flow diagram as well as its B) particle size distribution.

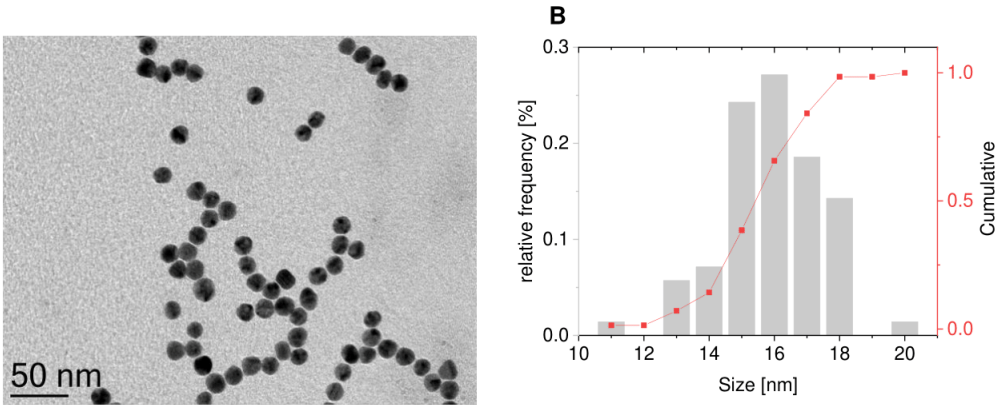

Figure S 12. TEM measurements and particle size distribution for 70 NP with mean diameter of 16.4 nm and size distribution of ±1.6 nm.

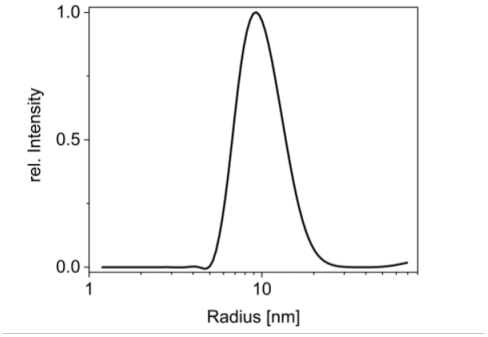

Figure S 13. DLS measurement of AuNPs with a radius of 9 nm.

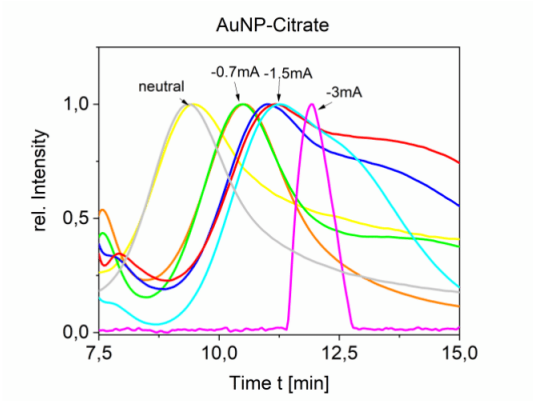

Figure S 14. Time-dependent measuring curves of UV-detector (253 nm) for determination of zeta potential with AFFFF and with the application of different electrical fields in the range of 0/-3 mA.

Table S 11. Calculated average electrophoretic mobility of -3.03 µm cm/Vs (R^2 0.98) and a zeta potential of -38.80 mV according to Smoluchowski.[4]

Applied current [mA]	Electrical field [V/m]	Conductivity [mS/cm]	Ratio net retention time
Neutral	0	0.147	1.00
Neutral	0	0.150	1.01
-0.7	-0.113	0.190	1.12
-0.7	-0.126	0.170	1.12
-1.5	-0.205	0.223	1.19
-1.5	-0.215	0.213	1.20
-1.5	-0.209	0.219	1.19
-3.0	-0.330	0.277	1.25

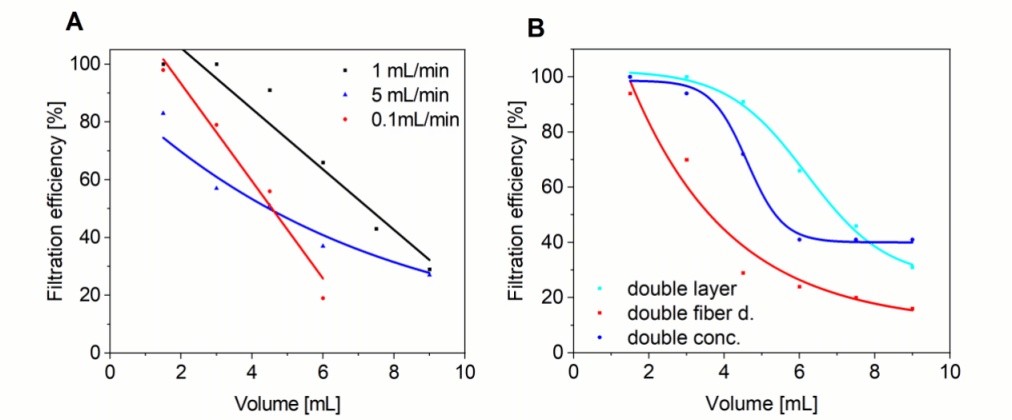

Figure S 15. AuNP filtration efficiency over filtered volume with Pyr 50 % membrane in dependence on A) the flow rate, B) nanoparticle concentration (1.8 mg membrane, 0.05 mg/mL NP conc., 300 nm fiber diam.) and double layer (1.8 mg membrane, 0.025 mg/mL NP conc., 300 nm fiber diam.), respectively, double fiber diameter (1.8 mg membrane, 0.025 mg/mL NP conc., 800 nm fiber diam.)

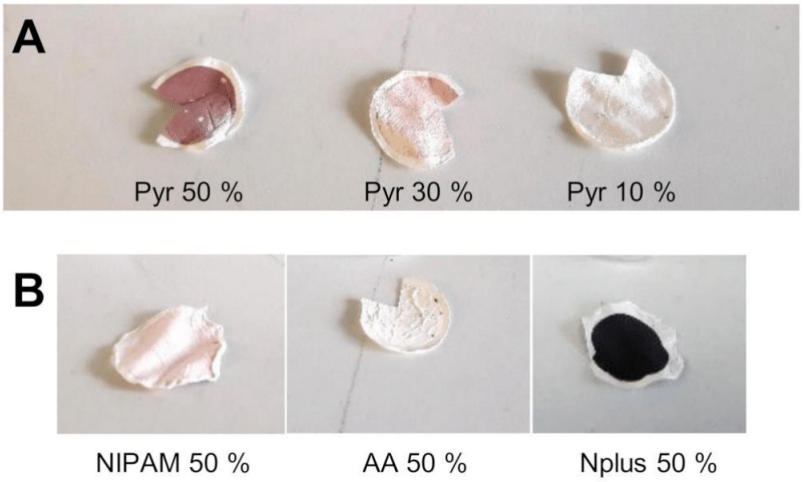

Figure S 16. Pictures taken after AuNP filtration with A) Pyr membranes and B) NIPAM, AA, and Nplus membranes with 50 % functional group.

Table S 12. Filtration experiment of AuNP (0.025 mg/mL) with the Pyr 50 membrane and a flowrate of 1mL/min. The averaged concentration deviation between UV/Vis, AFFFF, and ICP-OES is up to 9 %.

Time t [min]	Efficiency [%]	Concentration of gold in filtrate [mg/mL]			
		UV/VIS	AFFFF	ICP-OES	Average
1.5	100	0.0000	0.0000	0.0000	0.0000
3	94	0.0013	0.0000	0.0014	0.0013
4.5	79	0.0055	0.0044	0.0057	0.0052
6	66	0.0077	0.0117	0.0122	0.0086
7.5	49	0.0118	0.0108	0.0139	0.0122
9	38	0.0146	0.0129	0.0175	0.0150

Table S 13. Filtration experiment of AuNP (0.025 mg/mL) with the Pyr 50 membrane (0.8 mg) and a flowrate of 1mL/min.

Time t [min]	Concentration [mg/mL] of gold in filtrate				Efficiency [%]
	UV/VIS	AFFFF	ICP-OES	Average	
1.5	0.0014	0.0008	0.0009	0.0010	96
3	0.0065	0.0044	0.0073	0.0061	75
4.5	0.0066	0.0086	0.0131	0.0094	61
6	0.0128	0.0106	0.0170	0.0135	43
7.5	0.0164	0.0096	0.0196	0.0179	25

Table S 14. Filtration experiment of AuNP (0.025 mg/mL) with the Pyr 50 membrane (0.8 mg) at a flowrate of 0.1 mL/min.

Time t [min]	Concentration [mg/mL] of gold in filtrate				Efficiency [%]
	UV/VIS	AFFFF	ICP-OES	Average	
15	0.0011	0.0000	0.0000	0.0004	98
30	0.0063	0.0045	0.0048	0.0052	79
45	0.0118	0.0072	0.0129	0.0107	56
60	0.0211	0.0196	0.0180	0.0196	19

Table S 15. Filtration experiment of AuNP (0.025 mg/mL) with the Pyr 50 membrane (0.8 mg) at a flowrate of 5 mL/min.

Time t [sec]	Concentration [mg/mL] of gold in filtrate				Efficiency [%]
	UV/VIS	AFFFF	ICP-OES	Average	
18	0.0062	0.0066	0.0065	0.0064	83
36	0.0081	0.0000	0.0122	0.0102	57
54	0.0088	0.0091	0.0173	0.0117	51
72	0.0149	0.0115	0.0187	0.0151	37
90	0.0073	0.0089	0.0199	0.0121	49
108	0.0175	0.0160	0.0195	0.0177	27

Table S 16. Filtration experiment of AuNP (0.025 mg/mL) with a double layer of the Pyr 50 membrane (1.8 mg) at a flowrate of 1 mL/min.

Time t [min]	Concentration [mg/mL] of gold in filtrate				Efficiency [%]
	UV/Vis	AFFFF	ICP-OES	Average	
1.5	0.0000	0.0000	0.0000	0.0000	100
3	0.0000	0.0000	0.0004	0.0000	100
4.5	0.0032	0.0003	0.0032	0.0022	91
6	0.0083	0.0066	0.0096	0.0082	66
7.5	0.0146	0.0111	0.0148	0.0135	43
9	0.0192	0.0137	0.0183	0.0170	29

Table S 17. Filtration experiment of AuNP (0.05 mg/mL) at double NP concentration with a double layer of Pyr 50 membrane at a flowrate of 1 mL/min (1.8 mg).

Time t [min]	Concentration [mg/mL] of gold in filtrate				Efficiency [%]
	UV/Vis	AFFFF	ICP-OES	Average	
1.5	0.0000	0.0000	0.0001	0.0000	100
3	0.0031	0.0023	0.0027	0.0027	89
4.5	0.0139	0.0048	0.0146	0.0135	43
6	0.0329	0.0236	0.0029	0.0286	38
7.5	0.0253	0.0253	0.0364	0.0289	37
9	0.0264	0.0195	0.0401	0.0286	37

Table S 18. Filtration experiment of AuNP (0.025 mg/mL) with a double layer of Pyr 50 membrane with double fiber diameters and at a flowrate of 1 mL/min (1.8mg).

Time t [min]	Concentration [mg/mL] of gold in filtrate				Efficiency [%]
	UV/Vis	AFFFF	ICP-OES	Average	
1.5	0.0011	0.0017	0.0013	0.0014	94
3	0.0073	0.0053	0.0094	0.0073	70
4.5	0.0164	0.0177	0.0173	0.0172	29
6	0.0194	0.0152	0.0208	0.0184	24
7.5	0.0224	0.0146	0.0212	0.0194	20
9	0.0191	0.0139	0.0209	0.0200	16

Table S 19. Filtration experiment of AuNP (0.025 mg/mL) with a double layer of Pyr 10 membrane at a flow rate of 1mL/min (2.2 mg).

Time t [min]	Concentration [mg/mL] of gold in filtrate				Efficiency [%]
	UV/Vis	AFFFF	ICP-OES	Average	
1.5	0.0172	0.0165	0.0150	0.0162	32
3	0.0239	0.0025	0.0219	0.0237	2
4.5	0.0157	0.0183	0.0219	0.0186	26
6	0.0224	0.0203	0.0225	0.0217	9

Table S 20. Filtration experiment of AuNP (0.025 mg/mL) with a double layer of Pyr 30 membrane at a flowrate of 1mL/min (2.1 mg).

Time t [min]	Concentration [mg/mL] of gold in filtrate				Efficiency [%]
	UV/Vis	AFFFF	ICP-OES	Average	
1.5	0.0131	0.0099	0.0122	0.0117	51
3	0.0167	0.0127	0.0196	0.0163	32
4.5	0.0209	0.0123	0.0225	0.0186	22
6	0.0227	0.0092	0.0222	0.0224	6

Table S 21. Filtration experiment of AuNP (0.025 mg/mL) with a double layer of NIPAM 50 membrane at a flowrate of 1mL/min (2.3 mg).

Time t [min]	Concentration [mg/mL] of gold in filtrate				Efficiency [%]
	UV/Vis	AFFFF	ICP-OES	Average	
1.5	0.0167	0.0181	0.0141	0.0163	32
3	0.0232	0.0088	0.0201	0.0174	27
4.5	0.0188	0.0024	0.0209	0.0212	11
6	0.0232	0.0214	0.0197	0.0214	10

Table S 22. Filtration experiment of AuNP (0.025 mg/mL) with a double layer of NIPAM 10 membrane (2.1 mg) at a flowrate of 1mL/min.

Time t [min]	Concentration [mg/mL] of gold in filtrate				Efficiency [%]
	UV/Vis	AFFFF	ICP-OES	Average	
1.5	0.0178	0.0205	0.0167	0.0183	24
3	0.0237	0.0228	0.0218	0.0227	5
4.5	0.0225	0.0237	0.0227	0.0229	4
6	0.0247	0.0234	0	0.0241	0

Table S 23. Filtration experiment of AuNP (0.025 mg/mL) with a double layer of NIPAM 30 membrane (2.4 mg) at a flowrate of 1mL/min.

Time t [min]	Concentration [mg/mL] of gold in filtrate				Efficiency [%]
	UV/Vis	AFFFF	ICP-OES	Average	
1.5	0.0179	0.0210	0.0172	0.0187	24
3	0.0245	0.0232	0.0226	0.0234	2
4.5	0.0245	0.0235	0.0226	0.0235	2
6	0.0245	0.0181	0.0223	0.0234	2

Table S 24. Filtration experiment of AuNP (0.025 mg/mL) with a double layer of AA10 membrane (1.1 mg) at a flowrate of 1mL/min.

Time t [min]	Concentration [mg/mL] of gold in filtrate				Efficiency [%]
	UV/Vis	AFFFF	ICP-OES	Average	
1.5	0.0187	0.0208	0.0203	0.0193	27
3	0.0159	0.0226	0.0193	0.0209	16
4.5	0.0222	0.0241	0.0241	0.0235	6
6	0.0210	0.0226	0.0237	0.0224	10

Table S 25. Filtration experiment of AuNP (0.025 mg/mL) with a double layer of AA30 membrane (2.3 mg) at a flowrate of 1mL/min.

Time t [min]	Concentration [mg/mL] of gold in filtrate				Efficiency [%]
	UV/Vis	AFFFF	ICP-OES	Average	
1.5	0.0172	0.0221	0.0180	0.0191	23
3	0.0210	0.0253	0.0237	0.0233	6
4.5	0.0209	0.0256	0.0205	0.0223	10
6	0.0246	0.0242	0.0224	0.0237	5

Table S 26. Filtration experiment of AuNP (0.025 mg/mL) with a double layer of AA 50 membrane at a flowrate of 1mL/min (1.4 mg).

Time t [min]	Concentration [mg/mL] of gold in filtrate				Efficiency [%]
	UV/Vis	AFFFF	ICP-OES	Average	
1.5	0.0176	0.0200	0.0231	0.0202	19
3	0.0225	0.0245	0.0228	0.0233	3
4.5	0.0234	0.0245	0.0159	0.0239	1
6	0.0228	0.0245	0.0227	0.0233	3

Table S 27. Filtration experiment of AuNP (0.025 mg/mL) with a double layer of Nplus 50 membrane at a flowrate of 1mL/min (4.6 mg).

Time t [min]	Concentration [mg/mL] of gold in filtrate			Efficiency [%]
	UV/Vis	AFFFF	ICP-OES	
1.5	0.0000	0.0000	0.0001	100
3	0.0000	0.0000	0.0000	100
4.5	0.0000	0.0000	0.0000	100
6	0.0000	0.0000	0.0000	100

Table S 28. Filtration experiment of AuNP (0.025 mg/mL) with a double layer of Nplus 30 membrane at a flowrate of 1mL/min (1.8 mg).

Time t [min]	Concentration [mg/mL] of gold in filtrate			Efficiency [%]
	UV/Vis	AFFFF	ICP-OES	
1.5	0.0000	0.0000	0.0000	100
3	0.0000	0.0000	0.0000	100
4.5	0.0000	0.0000	0.0000	100
6	0.0000	0.0000	0.0000	100

Table S 29. Filtration experiment of AuNP (0.025 mg/mL) with a double layer of Nplus 10 membrane at a flowrate of 1mL/min (2.6 mg).

Time t [min]	Concentration [mg/mL] of gold in filtrate			Efficiency [%]
	UV/Vis	AFFFF	ICP-OES	
1.5	0.0000	0.0000	0.0000	100
3	0.0000	0.0000	0.0000	100
4.5	0.0000	0.0000	0.0000	100
6	0.0000	0.0000	0.0000	100

References

(1) Du, F.-S.; Zhang, P.; Li, F.-M. A Polymerizable Photoredox Initiation System for Vinyl Photopolymerization. *J. Appl. Polym. Sci.* **1994**, *51*, 2139–2144.

(2) Elisabeth Giebel. *Stabilisierung und Funktionalisierung von Submikrometerfasern hergestellt durch "Green Electrospinning": Dissertation*, 2012.

(3) Bastús, N. G.; Comenge, J.; Puntes, V. Kinetically Controlled Seeded Growth Synthesis of Citrate-Stabilized Gold Nanoparticles of up to 200 nm: Size Focusing versus Ostwald Ripening. *Langmuir* **2011**, *27*, 11098–11105.

(4) *Handbuch der Elektrizität und des Magnetismus;* Smoluchowski, M. V., Ed. 3; Joh. Ambr. Barth: Leipzig, 1921.

3.2 Publication (2)

ACS APPLIED POLYMER MATERIALS

pubs.acs.org/acsapm Article

Sustainable Electrospun Affinity Membranes for Water Remediation by Removing Metal and Metal Oxide Nanoparticles

Ann-Kathrin Müller, Zhi-Kang Xu,* and Andreas Greiner*

Cite This: https://doi.org/10.1021/acsapm.1c00990 Read Online

ACCESS | Metrics & More | Article Recommendations | Supporting Information

ABSTRACT: Nanoparticles (NPs) as part of engineered nanomaterials (ENMs) possess outstanding properties. Thus, they are more frequently integrated into various products resulting in high annual production quantities. The consequence can be the unintentional release into the environment where NPs could accumulate and pose a threat to human health. Therefore, the strong need becomes apparent for the remediation of environmental media. Electrospun nonwovens, which are defined here as membranes, could efficiently remove these released NPs. In this paper, electrospun membranes are utilized to flow filtration of metal and metal oxide NP, such as gold, silver, copper oxide, zinc oxide, iron oxide, and titanium dioxide. The membrane−NP interaction was analyzed and the correlation between NP size, NP ligand, ligand concentration, and the membrane surface functional group was investigated systematically. Finally, a membrane combining two functional groups was designed, which is able to adsorb up to 100% of the filtered NPs. The highest adsorption capacity was provided by AuNPs with 0.14 mg NP/mg membrane. To enhance their lifetime and gain sustainability, the membranes were then regenerated three times by rinsing with low concentrated acids. No significant efficiency loss was recorded, which allowed reusability of the electrospun membranes. We believe that the results shown here are of general relevance for other metals, metal oxides, and microplastic particles as well.

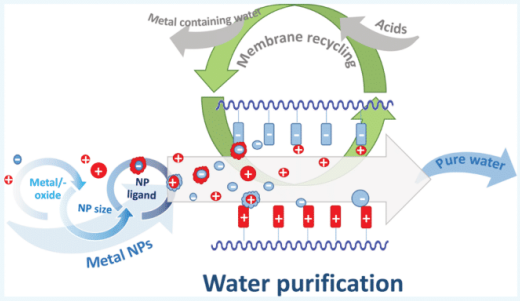

KEYWORDS: *electrospun membrane, affinity separation, ligands, metal nanoparticles, membrane regeneration*

INTRODUCTION

In the field of engineered nanomaterials (ENMs), extensive developments have been achieved in the last decades.[1] Due to their unique features and properties, ENMs are incorporated into more and more products.[2] Therefore, the economic sector has experienced incredible growth and has a potential market value of USD 55 billion in 2022.[3] In view of the high production volume and the widespread use of ENMs, these materials will enter the environment in manifold ways and will be distributed gradually worldwide.[4,5] Nanoparticle (NP) release can occur during production, transportation, usage, and/or disposal.[6] In addition to that, it can occur through intentional release for water remediation[7] and agricultural[8,9] or water purification processes.[10,11] In addition, NPs escape at nonpoint sources such as sunscreen,[12] cosmetics, and textiles.[13]

The highest worldwide production quantity of NPs is based on SiO_2 followed by TiO_2, ZnO, FeOx, and Ag,[14] resulting in high water, air, soil, and sediment concentrations.[15] These nanomaterials can accumulate over longer time periods, creating prerequisites for various studies that are investigating the impact on human health and the environment.[16] The current state of research suggests that NPs may pose a risk to human health. The NP small dimensions lead to enhanced surface reactivity.[17] Furthermore, metal oxide NPs can enter the human body and exhibit toxicity[18] by releasing reactive oxygen species (ROS) and metal ions or by attaching to the cell surface of an organism.[19] Even DNA damage is reported.[20] NPs, such as TiO_2 and ZnO, have been considered nontoxic to human beings due to their bulk material behavior but move again into public interest. Since many nanomaterials exhibit toxicity to microbes, concerns about the ecotoxicity effects arise.[20] To appropriately determine the toxicity, environmentally induced changes in the nanomaterials' chemistry also need to be taken into account:[21] dissolution,[22] oxidization, photodegradation,[23] surface coating,[24] or passivation.[25] The NP fate is thereby strongly affected by the pH value, ionic strength (IS),[26] and natural organic matter (NOM).[27,28] The metal NPs containing Zn, Cu, and Ag show high tendencies for

Received: August 9, 2021
Accepted: September 27, 2021

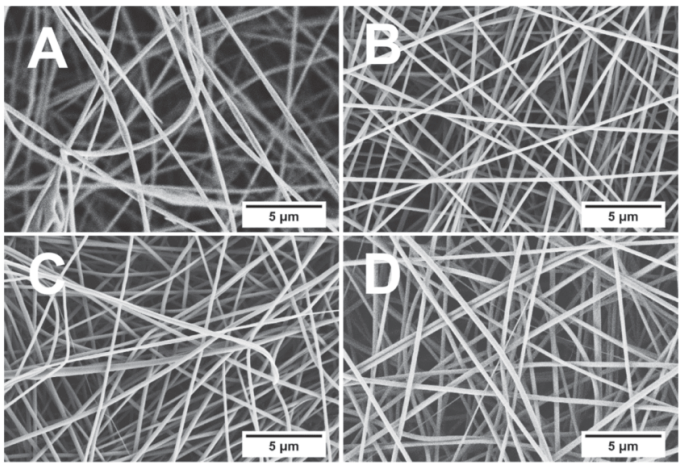

Figure 1. SEM images of fibers with (A) NIPAM, (B) AA, (C) Pyr, and (D) Nplus functional groups.

partial dissolution, releasing metal ions that are known to be highly toxic.[29]

Due to the environmental concern about metal NPs and heavy-metal ions, water remediation by filtration has gained significant attention.[30,31] In the filtration of NPs and metal ions, batch[32,33] and flow[34,35] filtration have to be distinguished. Heavy-metal-ion flow filtration was mostly based on the attraction by filter media equipped with functional groups[36] or metal NP.[37] Here, the filtration occurs by adsorption of the metal ions to the filter media. It has already been identified for heavy-metal-ion adsorption that the efficiency declines with time.[38] The filtration efficiency decreases at a higher initial metal ion concentration,[39] as well as a higher filtration flow rate.[40] Similar phenomena were observed in the flow filtration of metal NPs with electrospun nonwovens. For example, AuNPs, AgNPs, and TiO_2 NPs were filtered from aqueous systems by electrospun carbon nanofiber nonwovens.[41] AuNPs (20 nm) were filtered with efficiencies up to 95%, AgNPs (20 nm) up to 98%, and TiO_2 NPs (10−15 nm) up to 94%. The batch filtration has been also applied for AuNPs and AgNPs using electrospun poly(vinyl alcohol) membranes with chemically modified surface hydroxyl groups (thiols and amines).[42]

To fully exploit the large potential of electrospun nonwovens for the filtration of metal NPs, it is essential to understand the filtration performance in terms of efficiency, pressure drop, and recyclability. In addition, further filtration-influencing parameters such as NP size, ligands, and ligand concentration have to be considered.

This contribution explores the flow filtration of metal NPs and metal oxide NPs with polymeric electrospun membranes containing four different functional groups: acid, pyridine, amine, and quaternary amine. These functional groups are well known for interaction with NP.[43] Based on our previous work[44] on the filtration of AuNPs using the above mentioned functional groups in electrospun nonwovens, we have expanded our investigation to the filtration of environmentally highly relevant metal NP and metal oxide NPs (AgNPs, CuO NPs, ZnO NPs, Fe_2O_3 NPs, TiO_2 NPs). The filtration efficiency and adsorption capacity of the electrospun nonwovens with the different functional groups were investigated in detail as a function of particle size in the range of 26−156 nm and various particle ligands. Furthermore, we examined the recyclability of the membranes for filtration. With these investigations, we can show general concepts for the efficient flow filtration of metal NPs and metal oxide NPs from aqueous media by electrospun nonwovens, which will help to exploit the full potential of such advanced filter media.

RESULTS AND DISCUSSION

Copolymers containing different functional groups for NP attraction were prepared by free-radical copolymerization. We chose four different functional groups, which are known to interact with metal NP: acid, pyridine, amide, and quaternary amine. These groups were implemented with the monomers: acrylic acid (AA), 4-vinyl pyridine (Pyr), *N*-isopropyl acrylamide (NIPAM), and dimethyldecyl ammonium ethyl methacryl bromide (Nplus). In addition to these monomers, we integrated methyl methacrylate (MMA) as a flexible part and 4-methacryloyl-oxy-benzophenone (MABP) as a UV cross-linker to improve membrane stability and avoid fiber swelling in aqueous media. The monomer molar ratios were set to 50% functional group, 10% MABP, and 40% MMA. The resulting copolymers were electrospun from dimethylformamide (DMF) (25 wt %) and cross-linked for 4 h under UV light. The membrane properties, such as fiber diameter, pore size, tensile strength, and pressure drop were investigated. Procedures for copolymerization, electrospinning, cross-linking, as well as membrane properties were already published in our previous paper.[44] Scanning electron microscopy (SEM) images of membranes are visualized in Figure 1.

Characterization of Nanoparticles for Filtration. Different nanoparticles, such as AuNPs, AgNPs, CuO NPs, ZnO NPs, Fe_2O_3 NPs, and TiO_2 NPs, were synthesized according to literature procedures.[45−53] The size and ζ-potential of NP (Ag, CuO, ZnO, Fe_2O_3, TiO_2) were analyzed in detail by transmission electron microscopy (TEM), dynamic light scattering (DLS), asymmetric flow field-flow fractionation (AF-FFF), and ζ sizer (Table 1) as they might influence the filtration performance of electrospun nonwovens significantly. The diameters of the NP are in the range of 7−15 nm according to TEM analysis (Figures S1−S5). The hydrodynamic radii are between 16 and 47 nm, as measured by DLS

https://doi.org/10.1021/acsapm.1c00990
ACS Appl. Polym. Mater. XXXX, XXX, XXX−XXX

Table 1. Properties of NP, Such as the Gyration Radius, the Hydrodynamic Radius, the ζ-Potential, and the pH Value of the Dispersion

nanoparticle	size (TEM) (nm)	hydrodyn. radius (DLS) (nm)	hydrodyn. radius (A4F) (nm)	ζ-potential (mV)[a]	pH value
Ag	11 ± 2	33 ± 14	16 ± 2	−13 ± 2	5
CuO	8 ± 1	47 ± 15	50 ± 3	+21 ± 1	5
ZnO	15 ± 3	27 ± 8	50 ± 12	+16 ± 1	6
Fe_2O_3	13 ± 2	25 ± 11	40 ± 4	+18 ± 1	4
TiO_2	7 ± 1	16 ± 9	27 ± 7	+25 ± 4	4

[a]ζ-Potential of NP dispersion measured using the ζ sizer.

(Figure S6). The hydrodynamic radii of AgNPs measured by AF-FFF (measuring parameters Tables S1 and S2) are smaller compared to those measured by DLS. The values for the hydrodynamic radii of the metal oxides measured by AF-FFF (Figures S7−S11) are higher than measured with DLS, which is due to the dispersion agents poly(vinylpyrrolidone) (PVP) and Novachem (Postnova dispersing agent). The ζ-potential of AgNPs was determined to be negative by electrical asymmetrical flow field flow fractionation (EAF-FFF) (Figure S12) and a ζ sizer. In contrast, the ζ-potential of CuO NPs, ZnO NPs, Fe_2O_3 NPs, and TiO_2 NPs is positive, which could be only determined by the ζ sizer due to the ligands.

General Settings for Filtration Experiments. Filtration experiments were done by filtering a certain volume of NP dispersion with a defined concentration at a flow rate of 1 mL/min through a membrane. Samples were collected for 1.5 min followed by investigation with UV/vis, AF-FFF, and inductively coupled plasma-optical emission spectrometry (ICP-OES). The filtration efficiency is calculated from the concentration ratio before and after filtration.

Influence of NP Size and NP Ligands on Metal Nanoparticle Filtration. The NP size and ligand might have a significant impact on the particle−membrane interaction. To investigate these influences, AuNPs with different ligands such as trisodium citrate, 1-mercapto undecanoic acid (MUA), and poly(vinylpyrrolidone)-360 (PVP) were synthesized by ligand-exchange reactions. Their ζ-potential was determined using a ζ sizer (Table S3) and EAF-FFF (Figure S13). The advantage of the ligand-exchange method is to keep the size and the character of the AuNP constant while changing the ligand.

The filtration efficiency of AuNP with different ligands was analyzed with the membranes containing Pyr and Nplus as functional groups. The efficiency decreases for MUA and PVP ligands when using the Pyr membrane but reached 100% with the citrate ligand (Figure 2A). The ζ-potential of the AuNP can explain this result. With the higher steric demand of the ligands, the NP core is shielded, resulting in a decreasing ζ-potential. The lower the ζ-potential of the NP dispersion, the less interaction appears between the membrane and NP. However, the Nplus membrane did not show any significant differences in filtration efficiencies between the AuNPs with various ligands (Figure 2B). A reason might be the positive charges on the membrane surface, which can adsorb all NPs when they are negatively charged.

Citrate-capped AuNPs with different NP sizes (Table S4, Figures S14, and S15) but equal ζ-potentials (Table S5) were synthesized by a particle growth mechanism and tested for filtration with Pyr- and Nplus-containing membranes.

NPs from growth step 2 were excluded from filtration tests because the size gap to growth 1 and 3 is very low. Therefore, no differing results can be expected. For both membranes, the filtration efficiency amounts to 100% except for the NP sizes of 26 and 38 nm (Figure 3A,B). These achieved a slightly lower efficiency, which can be explained by the depth of membrane penetration.

The SEM images (Figure 4) demonstrate that smaller NPs can more easily pass into deeper layers of the membrane than bigger NPs. The penetration depth decreased from 13 μm for 26 nm NPs to 4 μm for 156 nm NPs (Table S3). The filtration character does not change with the particle size; all NPs are adsorbed homogeneously over the fiber surface showing no aggregation (Figure S16).

One reason for the varying penetration depths is the use of equally concentrated (wt %) AuNP dispersions. This results in a higher AuNP number for smaller AuNP. Therefore, more adsorption sites get blocked by smaller NPs, which leads to deeper membrane penetration. Another reason might be that the ratio of the NPs to the pore size (~1 μm) changes from small (26 nm) to big (156 nm) NPs. Thus, collisions between the membrane and the particle become more likely with increasing particle size.

Since NPs with sizes below 20 nm are particularly difficult to filter, we decided to utilize only small NPs for all following filtration tests. We assume that successful filtration can then be

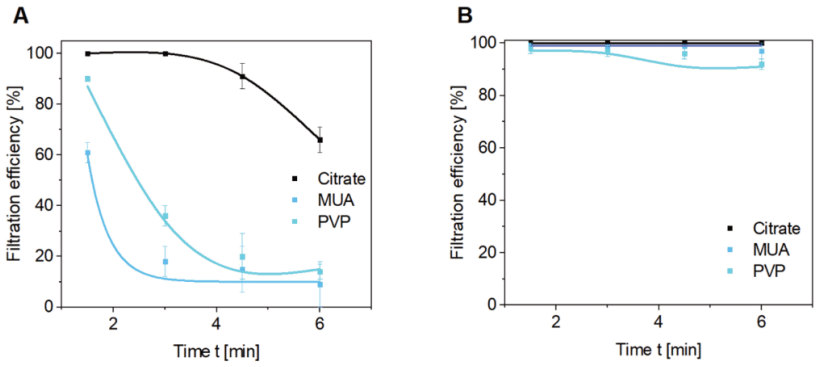

Figure 2. Filtration efficiency of AuNPs with citrate, MUA, or PVP as ligands for the (A) Pyr and (B) Nplus membranes, respectively. Standard deviations were calculated from the different analysis methods.

https://doi.org/10.1021/acsapm.1c00990
ACS Appl. Polym. Mater. XXXX, XXX, XXX−XXX

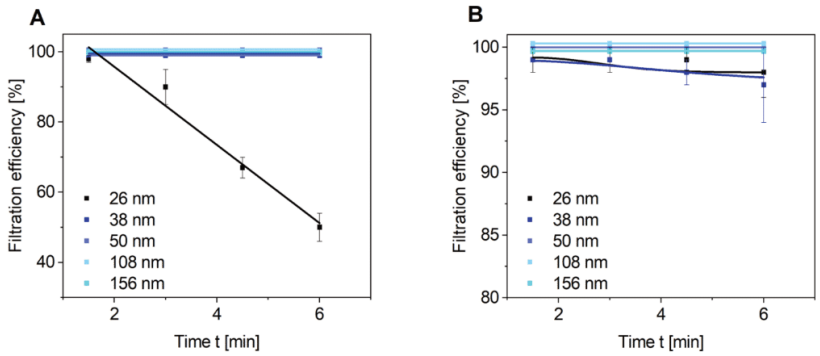

Figure 3. Filtration efficiency of AuNPs with different particle sizes (measured by TEM) for (A) Pyr and (B) Nplus membranes. Standard deviations were calculated from the different analysis methods.

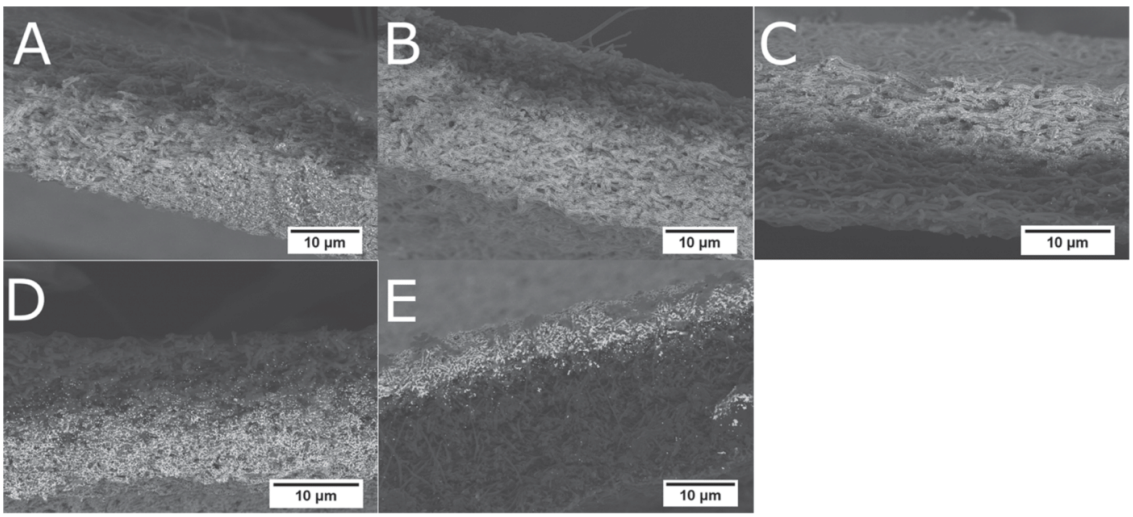

Figure 4. SEM image of the Nplus membranes after filtration of AuNP with different sizes. (A) 26 nm, (B) 38 nm, (C) 50 nm, (D) 108 nm, and (E) 156 nm. Here, given AuNP sizes were measured by TEM.

secured for all particle sizes. The decreasing filtration efficiency for smaller AuNP sizes was also found before by Faccini et al.[41]

We wondered if the observed filtration behavior of the AuNPs would be comparable to other metal NPs. Therefore, AgNP filtration efficiencies were tested with different membranes. The results demonstrated that the NIPAM, AA, or Pyr-containing membranes could not filter the AgNPs in contrast to the Nplus membranes (Figure S17). The finding can be underlined from the photographs too (Figures S18 and S19). To further investigate the interdependence between the membrane material and high nanoparticle filtration efficiency, we expand our filtration tests to metal oxide NPs.

Filtration of Metal Oxide Nanoparticles and Influence of Ligands. The filtration efficiency of the membranes was also investigated for metal oxide NPs. High efficiencies up to 100% were found only for the NIPAM and AA membranes in the first 1.5 min filtering CuO NPs, ZnO NPs, Fe_2O_3 NPs, and TiO_2 NPs (Figure 5). However, also Pyr was able to adsorb to some extent ZnO NPs, and thereby achieved a considerable filtration effect. The filtration efficiency declines within 6 min because adsorption places get blocked (Figure S20). The

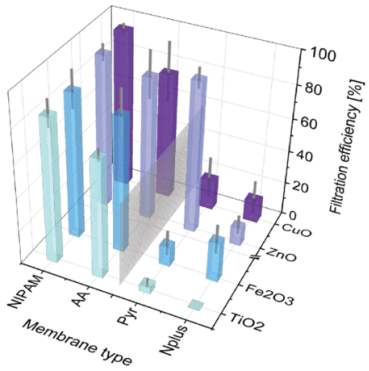

Figure 5. Filtration efficiency in the first 1.5−3 min for CuO NPs, ZnO NPs, Fe_2O_3 NPs, and TiO_2 NPs. Filtration tests were repeated with new membranes. For CuO NPs and ZnO NPs, a new batch of NPs was used. Standard deviation was calculated from both tests and the different analysis methods.

https://doi.org/10.1021/acsapm.1c00990
ACS Appl. Polym. Mater. XXXX, XXX, XXX−XXX

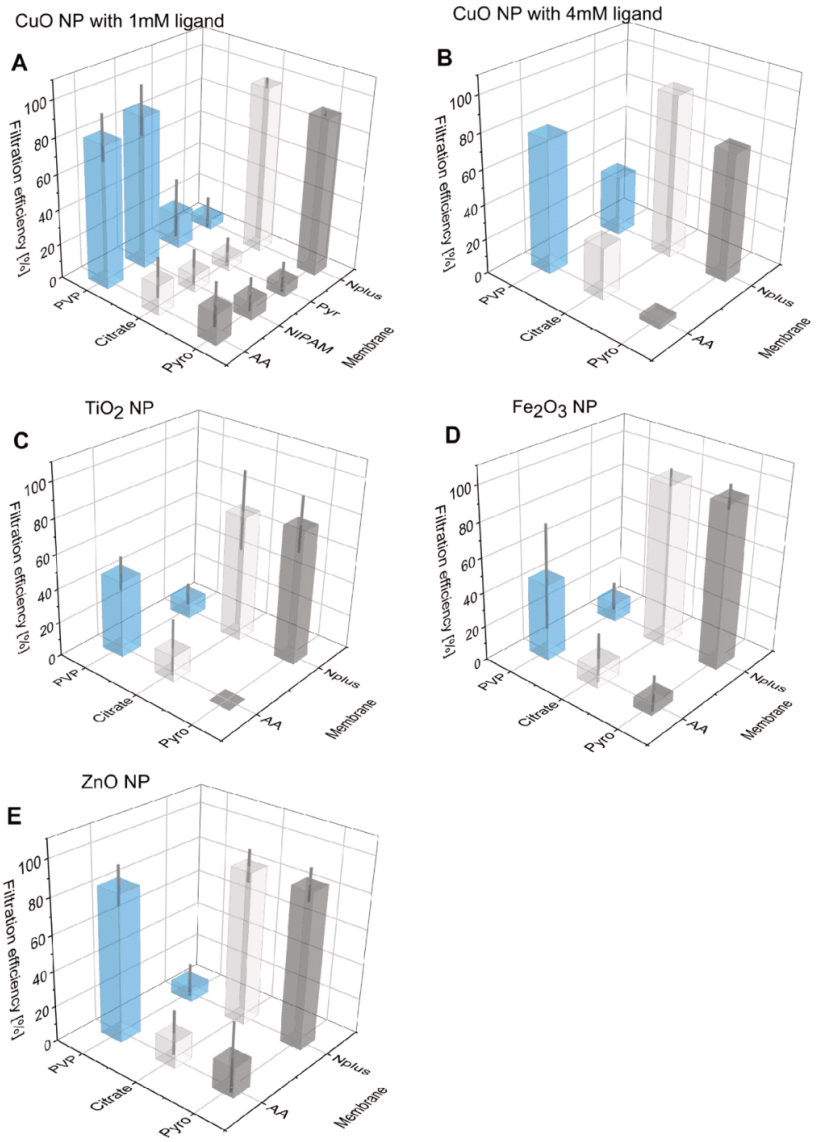

Figure 6. CuO NP filtration efficiency with AA and Nplus membranes and the ligands PVP, citrate, and pyrophosphate for the concentrations (A) 1 mM and (B) 4 mM and filtration efficiencies of (C) TiO_2 NPs, (D) Fe_2O_3 NPs, and (E) ZnO NPs at 1 mM ligand concentrations. Filtration tests were repeated with new membranes and a new batch of CuO NPs and ZnO NPs. Standard deviations were calculated from both tests and the analysis methods.

adsorption of CuO NPs and Fe_2O_3 NPs is also visible by color change of the membranes (Figures S21 and S22).

We have also investigated the impact of different oxide NP ligands (trisodium citrate, sodium pyrophosphate, and PVP) on the filtration efficiency of different membranes. These ligands are chosen because they do not change the pH of the NP dispersion but significantly impact particle stability and membrane interaction. The hydrodynamic radius and the ζ-potential of the oxide NPs are controlled by the nature of the ligands. It becomes apparent from the DLS measurement of the hydrodynamic radius of all metal oxide NPs that PVP increases the solvation shell, whereas the citrate and pyrophosphate ligands decrease the particle size due to breaking up agglomerates (Figure S23). For ZnO NPs, no distinct correlation between the hydrodynamic radius and the ligand concentration can be determined. A reason might be a slow dissolution of ZnO NPs, which are well known for low stability in specific environments.[54]

The ligands also affect the ζ-potential (Figure S24). Usually, the ζ-potential is determined by surface functional groups on metal oxide NPs. These can be de/protonated depending on the pH value. Under a neutral to acidic environment, metal

https://doi.org/10.1021/acsapm.1c00990
ACS Appl. Polym. Mater. XXXX, XXX, XXX−XXX

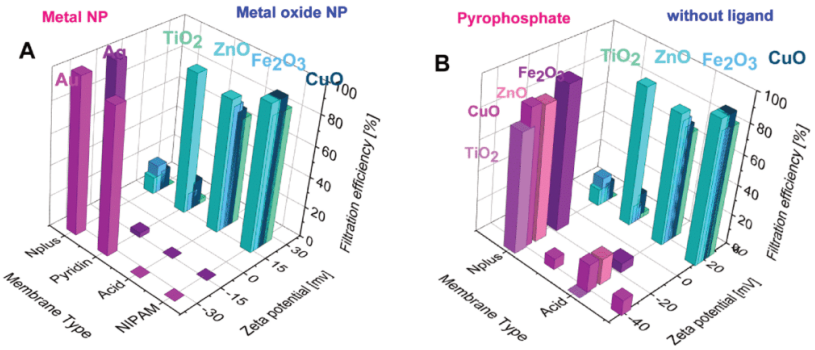

Figure 7. Three-dimensional (3D) plot of NP filtration efficiency dependent on the applied membrane type and the NP ζ-potential. Filtration efficiency is compared for (A) metal and metal oxide NP and (B) metal oxide NPs with and without the pyrophosphate ligand (for the comparison of filtration efficiencies for metal and metal oxide NPs, values for AuNP adsorption are taken from our previous publication).

oxide NPs are stabilized by positive charges on the particle surface.[55] On the contrary, the ζ-potential of the oxide NPs becomes negative by the negatively charged citrate and pyrophosphate ligands. The neutral PVP ligand reduces the positive ζ-potential by a shielding effect.

The impact on the hydrodynamic radius and the ζ-potential correlates with the ligand concentration. Consequently, the ζ-potential increases close to zero with increasing amounts of citrate and pyrophosphate because the total ionic strength in the dispersion starts to increase as well. This results in a reduced potential difference between the particle and the solvent. However, the strongest change in the ζ-potential from the original particle character is already detected at a 1 mM ligand concentration. The particle surface seems to be already saturated at 1 mM because the ζ-potential starts to increase with a higher ligand concentration. In addition, small ligand concentrations are more likely to appear in the environment. Hence, filtration tests were conducted once for CuO NP at 1 mM and 4 mM ligand concentrations to show the impact of the ligand concentration on the filtration efficiency, but for the remaining metal oxide NPs, filtration tests were only executed at a 1 mM ligand concentration.

CuO NPs were tested for membrane filtration with citrate, pyrophosphate, and PVP ligands. CuO NPs can be successfully filtered in the combination of a PVP ligand and an AA membrane, in contrast to CuO NPs with a citrate or pyrophosphate ligand, which can be filtered by the Nplus membrane with high filtration efficiencies (Figure 6A). These favorable combinations of the PVP ligand/AA membrane or the citrate ligand/Nplus membrane do not change when increasing the ligand concentration. However, the filtration efficiency decreases (Figure 6B).

If a higher concentration of 4 mM PVP is utilized, the NP's solvation shell increases, and ζ-potential decreases close to zero. Thus, the particle−membrane interaction is reduced, resulting in lower filtration efficiency. The filtration efficiency also declines at 4 mM for a citrate and pyrophosphate ligand. At higher concentrations of 4 mM, both ligands cause a ζ-potential close to zero, leading to a reduced membrane−particle attraction.

We studied filtration efficiencies at a standard concentration of 1 mM for the other metal oxide NPs. The same membrane−NP combinations of the PVP ligand/AA membrane and the citrate ligand/Nplus membrane are valid for the Fe_2O_3 NPs (Figure 6C), TiO_2 NPs (Figure 6D), and ZnO NPs (Figure 6E). Photographs of the AA and Nplus membranes after filtration are given for CuO NPs and Fe_2O_3 NPs in Figures S25 and S26.

Comparing the filtration efficiencies for the citrate and pyrophosphate ligand, it becomes evident that NPs seem to be filtered nearly at the same efficiency level with both ligands. However, for CuO NPs and ZnO NPs, the citrate ligands achieved a slightly higher efficiency than the pyrophosphate ligand. For the TiO_2 NPs, an opposite behavior is apparent. One reason might be a preferred interaction between some ligands with metal oxide NPs. For example, CuO NPs interact stronger with citrate than with pyrophosphate ligands, resulting in the relieved adsorption of citrate NPs on the Nplus membrane. This effect might also be reflected in the total filtration efficiency.

Comparison of Metal and Metal Oxide Nanoparticles. We studied the filtration efficiency of metal and metal oxide NPs with different ligands and membranes. In this section, we want to consolidate our results to deeply conclude the main correlations between high filtration efficiencies and NP characteristics.

The filtration results are summarized in Figure 7. The filtration efficiency of the metal and metal oxide NPs is demonstrated (Figure 7A) with and without ligands (Figure 7B) dependent on the ζ-potential. It is evident that, based on distinct interactions, membranes adsorb specific NPs. Metal NPs possess negative charges and can only be absorbed by the positively charged Nplus membrane, in contrast to metal oxide NPs, which possess positive ζ-potentials and can thus be attracted by the AA and NIPAM membranes. Applying ligands such as citrate or pyrophosphate, the metal oxide NP's ζ-potential can be turned negative, leading to an attraction of the metal oxide NPs by the Nplus membrane.

Hence, it can be concluded that the adsorption mechanism is only based on the ζ-potential. If the ζ-potential of the NPs and the membrane does not fit, no adsorption occurs at all. What all membrane−particle interactions have in common is the same, positive versus negative, ζ-potential, which explains why only electrostatic interaction between the particle (NP + ligand) and the membrane is so crucial for successful adsorption filtration. The particle size influences the filtration efficiency but is not responsible for the occurrence of successful NP adsorption.

https://doi.org/10.1021/acsapm.1c00990
ACS Appl. Polym. Mater. XXXX, XXX, XXX−XXX

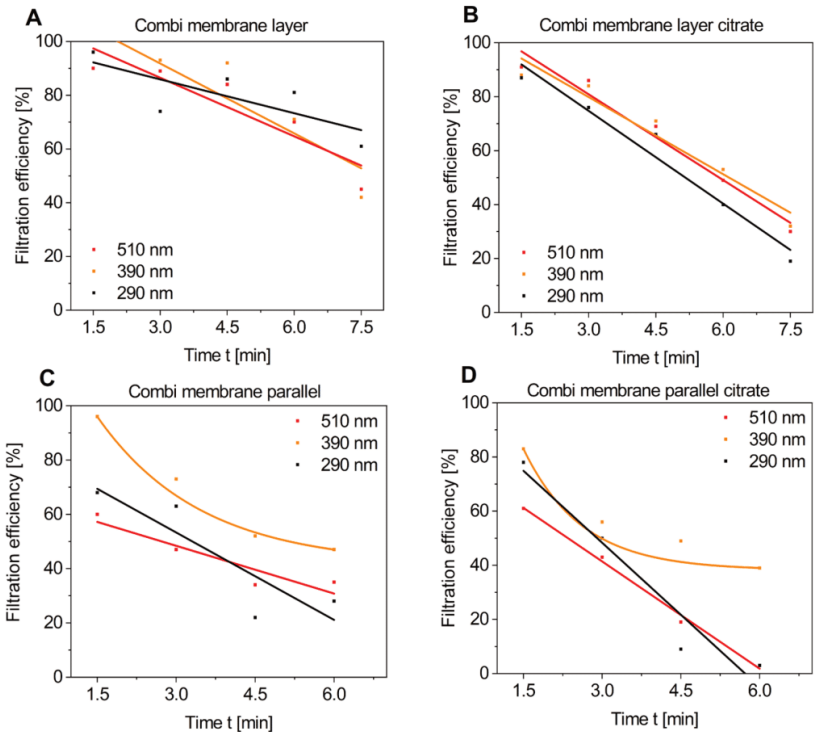

Figure 8. Filtration efficiencies of NP mixtures containing AuNPs, AgNPs, CuO NPs, Fe_2O_3 NPs, and TiO_2 NPs for (A) layer combi membrane, (B) layer combi membrane with citrate as an NP ligand, (C) parallel electrospun combi membrane, and (D) parallel electrospun combi membrane with citrate as a ligand.

Membrane Combinations. To create a highly versatile filter membrane for different metal and metal oxide NPs with different ligands, we have combined the membranes with AA and Nplus functional groups. The AA membrane should attract positively charged NPs, while the Nplus membrane should adsorb negatively charged NPs. Two routes were probed for the combination of the membranes. The first route is to electrospin copolymers with AA and Nplus functional groups simultaneously from two syringes. The second route is the Janus-type combination of both membranes. For these two types of combined (combi) membranes, the adsorption capacity was determined (Table S6). For the Janus-type combination, the membrane was placed into an apparatus with the nonfiltering section upside so that the NP dispersion first passed through the nonfiltering part.

The highest adsorption capacity was reached by the AuNPs with up to 0.14 mg NP/mg membrane. The Janus-type membrane exhibited a higher filtration capacity for AuNPs than the parallel electrospun membrane.

The combi membranes possess a lower adsorption capacity for CuO NPs than for AuNPs. One reason might be less attraction between CuO NPs and the membrane. However, it seems to be more likely that less CuO NPs can be adsorbed on the membrane due to their smaller size. For the other metal or metal oxide NPs, the capacity was only determined for the layer combi membranes.

Overall, the adsorption capacity for all NPs is around 0.06 mg NP/mg membrane. With respect to the standard deviations, no significant differences between the capacity values for the different NP become obvious.

The distribution of AuNPs and CuO NPs on the combined membranes can be observed in Figure S27. Images were taken from scanning electron microscopy−energy dispersive X-ray analysis (SEM−EDX) measurements. In the Janus-type membrane, the transition between the AA and Nplus membrane can be proven by EDX signals from Brom-counter ions of the Nplus copolymer. It becomes obvious that the AuNPs are located in the section containing Brom ions in contrast to the CuO NPs, which were located on the AA membrane part—when used without ligand—and in the Nplus membrane part with the citrate ligand.

Finally, the NP dispersion was combined containing AuNPs, AgNPs, CuO NPs, Fe_2O_3 NPs, and TiO_2 NPs at their standard solution concentrations. The NP mixture was filtered with the combined membranes, and the filtrate was analyzed with UV/vis and AF-FFF (Figure S28). Only three peaks could be observed at 518, 390, and 290 nm, representing AuNPs, AgNPs, and a mixture of CuO NPs and Fe_2O_3 NPs. The TiO_2 NPs cannot undoubtedly be attributed to other peaks. However, from these three peaks, the filtration efficiency was evaluated for combi membranes as Janus-type (Figure 8A), as Janus-type with a citrate ligand (Figure 8B), for combi membranes with a parallel type (Figure 8C), and parallel type with a citrate ligand (Figure 8D). The results show similar filtration efficiencies for AuNPs, AgNPs, CuO NPs, and Fe_2O_3 NPs respectively. The filtration efficiencies indicate that none of these NPs is preferentially attracted.

https://doi.org/10.1021/acsapm.1c00990
ACS Appl. Polym. Mater. XXXX, XXX, XXX−XXX

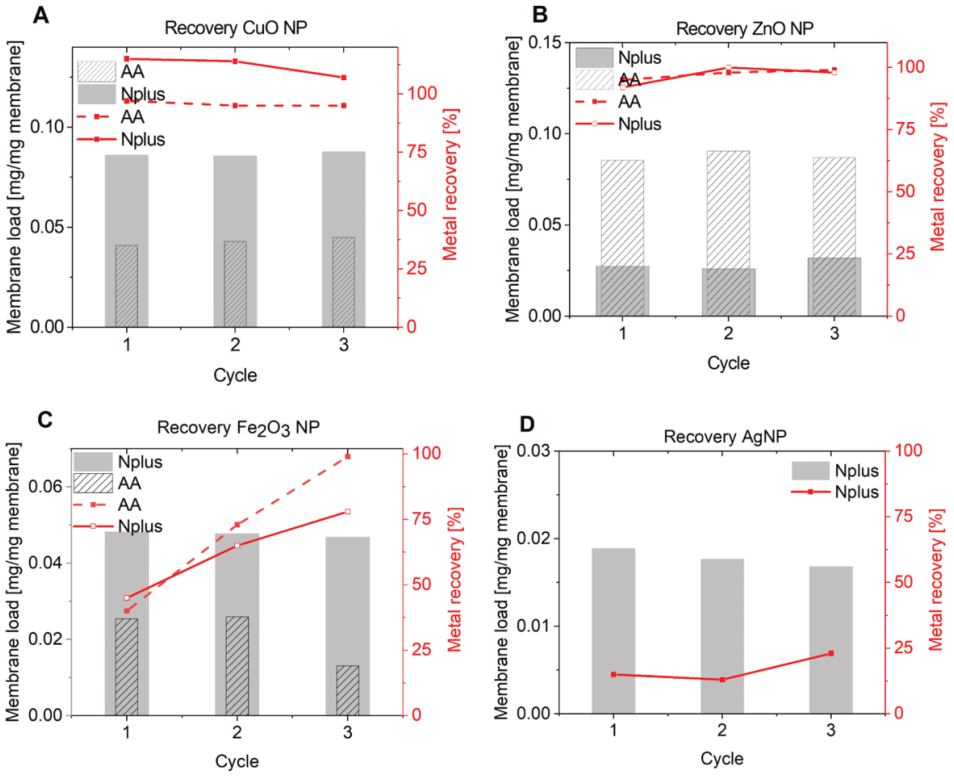

Figure 9. Membrane regeneration with membrane capacity and metal recovery values for (A) CuO NPs, (B) ZnO NPs, (C) Fe_2O_3 NPs, and (D) AgNPs.

Membrane Regeneration. The regeneration of membranes is an essential issue since it can expand the membrane lifetime. Therefore, AA or Nplus membranes were loaded with NPs, followed by rinsing with nitric acid or orthophosphoric acid. For all NPs, except for TiO_2 NPs, the membranes could be successfully regenerated. The membrane load was insignificantly lowered in the first three cycles (Figure 9A–D). Even though the metal recovery of Ag and Fe proved by ICP is low, no color could be observed on the membranes after the rinsing step. Most probably, the NPs are not completely dissolved or the ions stick to the membrane. Hence, metal recovery of Ag and Fe should be enhanced by a longer exposure time to acid.

■ CONCLUSIONS

In this paper, various NPs were synthesized and removed with high filtration efficiencies from aqueous samples. This includes AuNPs, AgNPs, CuO NPs, ZnO NPs, Fe_2O_3 NPs, and TiO_2 NPs. NP filtration efficiencies were tested with four different membrane surface functional groups: acid, pyridine, amide, and quaternary amine. From these four functional groups, we identified two NP–membrane pairs for high filtration efficiencies: a positively charged NP/acid membrane or a negatively charged NP/quaternary amine membrane. The NP charge is dependent on the NP material. The prepared metal NPs possess negative surface charges in contrast to metal oxide NPs, exhibiting a positive surface charge. The NP charge can be adjusted by the addition of ligands, which also changed the hydrodynamic radius of the NP. The strength of NP–ligand interaction affected the filtration efficiency. For weak NP–ligand interaction, the surface charge is not completely determined by the ligand deteriorating membrane attraction. Filtration efficiency is further influenced by the NP size. NPs with sizes below 20 nm are especially difficult to remove from water.

We propose a mechanism for the membrane–particle interaction based on the NP ζ-potential. This knowledge was implemented by designing a membrane combining two suitable membrane functional groups. The combi membrane can be used as a platform for filtration of NP mixtures. It opens up the possibility for successful broad-spectrum NP adsorption. To fulfill the requirement of long membrane lifetimes, our membranes were regenerated after filtration. Membrane regenerated could be repeated for at least three cycles with no significant loss in filtration efficiency.

We postulate that the results presented here regarding the relevant parameters could be transferred to other metal and metal oxide particles as well as to microplastic particles.

■ ASSOCIATED CONTENT

Supporting Information

The Supporting Information is available free of charge at https://pubs.acs.org/doi/10.1021/acsapm.1c00990.

Materials, equipment information, synthesis procedures, filtration procedures, TEM (Figures S1–S5), DLS (Figure S6), AF-FFF (Figures S7–S11), EAF-FFF

https://doi.org/10.1021/acsapm.1c00990
ACS Appl. Polym. Mater. XXXX, XXX, XXX–XXX

(Figures S12 and S13), ζ-sizer (Table S3) measurements, particle size and penetration depth (Table S4), DLS measurements (Figure S14), TEM images (Figure S15), table for ζ-potential (Table S5) of AuNPs, SEM of AuNP-loaded fibers (Figure S16), filtration efficiency of AgNPs (Figure S17), photos of the AgNP filtrate (Figure S18), photos of membranes after filtration for AgNPs (Figure S19), time-dependent filtration efficiency for metal oxide NPs (Figure S20), picture of membranes after filtration of CuO NPs and Fe_2O_3 NPs (Figures S21 and S22), DLS (Figure S23), ζ-potential (Figure S24) measurement for metal oxide NPs with ligands, photos of membranes after filtration with ligands for CuO NPs and Fe_2O_3 NPs (Figures S25 and S26), SEM−EDX measurements for combi membranes (Figure S27), and photos of the filtrate (Figure S28) (PDF)

AUTHOR INFORMATION

Corresponding Authors

Zhi-Kang Xu − *MOE Key Laboratory of Macromolecular Synthesis and Functionalization, and Key Laboratory of Adsorption and Separation Materials & Technologies of Zhejiang Province, Department of Polymer Science and Engineering, Zhejiang University, Hangzhou 310027, China*; Email: xuzk@zju.edu.cn

Andreas Greiner − *Macromolecular Chemistry and Bavarian Polymer Institute, University of Bayreuth, Bayreuth 95440, Germany*; orcid.org/0000-0002-5310-3850; Email: greiner@uni-bayreuth.de

Author

Ann-Kathrin Müller − *Macromolecular Chemistry and Bavarian Polymer Institute, University of Bayreuth, Bayreuth 95440, Germany*

Complete contact information is available at: https://pubs.acs.org/10.1021/acsapm.1c00990

Author Contributions

A.-K.M. and A.G. conceived the project and discussed all results. A.-K.M. performed the experiments. The manuscript was written by A.-K.M., Z.-K.X., and A.G. All authors have given approval to the final version of the manuscript.

Notes

The authors declare no competing financial interest.

ACKNOWLEDGMENTS

The authors gratefully acknowledge financial support from the Bavarian State Ministry of the Environment and Consumer Protection (funding code TNT01NaT-72524) and the German Research Foundation, CRC 1357—"Mikroplastik" 391977956. Further, they thank the KeyLab Electron and Optical Microscopy of the Bavarian Polymer Institute (BPI) for providing support and equipment for SEM and TEM measurements. They also thank PC2 from the University Bayreuth for enabling ζ-potential measurements at their ζ-sizer device.

REFERENCES

(1) Palit, S.; Hussain, C. M. Nanomaterials for Environmental Engineering and Energy Applications. In *Handbook of Nanomaterials and Nanocomposites for Energy and Environmental Applications*; Kharissova, O. V.; Martínez, L. M. T.; Kharisov, B. I., Eds.; Springer International Publishing: Cham, 2020; pp 1−24.

(2) Mohajerani, A.; Burnett, L.; Abdul Kadir, A. Nanoparticles in Construction Materials and Other Applications, and Implications of Nanoparticle Use. *Materials* **2019**, *12*, No. 3052.

(3) Inshakova, E.; Inshakov, O.; Roshchupkin, S. In *World Market for Nanomaterials: Structure and Trends*, MATEC Web of Conferences; EDP Sciences, 2017; pp 1−5.

(4) Suhendra, E.; Chang, C.-H.; Hsieh, Y.-C. A Review on the Environmental Fate Models for Predicting the Distribution of Engineered Nanomaterials in Surface Waters. *Int. J. Mol. Sci.* **2020**, *21*, No. 4554.

(5) Uddin, M. N.; Desai, F.; Asmatulu, E. Engineered Nanomaterials in the Environment: Bioaccumulation, Biomagnification and Biotransformation. *Environ. Chem. Lett.* **2020**, *18*, 1073−1083.

(6) Oliveira, M. L. S.; Izquierdo, M.; Silva, L. F. O. Nanoparticles from Construction Wastes: A Problem to Health and the Environment. *J. Cleaner Prod.* **2019**, *219*, 236−243.

(7) Zhu, Y.; Liu, X.; Zhu, M. Behavior, Remediation Effect and Toxicity of Nanomaterials in Water Environments. *Environ. Res.* **2019**, *174*, 54−60.

(8) Bandala, E. R.; Berli, M. Engineered Nanomaterials (ENMs) and their Role at the Nexus of Food, Energy, and Water. *Mater. Sci. Technol.* **2019**, *2*, 29−40.

(9) He, X.; Deng, H.; Hwang, H.-M. The Current Application of Nanotechnology in Food and Agriculture. *J. Food Drug Anal.* **2019**, *27*, 1−21.

(10) Simeonidis, K.; Martinez-Boubeta, C.; Mitrakas, M. Implementing Nanoparticles for Competitive Drinking Water Purification. *Environ. Chem. Lett.* **2019**, *17*, 705−719.

(11) Ghadimi, M.; Zangenehtabar, S.; Homaeigohar, S. An Overview of the Water Remediation Potential of Nanomaterials and Their Ecotoxicological Impacts. *Water* **2020**, *12*, No. 1150.

(12) Slomberg, D. L.; Catalano, R.; Labille, J. Release and Fate of Nanoparticulate TiO2 UV Filters from Sunscreen: Effects of Particle Coating and Formulation Type. *Environ. Pollut.* **2021**, *260*, No. 116263.

(13) Pakdel, E.; Wang, J.; Wang, X. Advances in Photocatalytic Self-cleaning, Superhydrophobic and Electromagnetic Interference Shielding Textile Treatments. *Adv. Colloid Interface Sci.* **2020**, *277*, No. 102116.

(14) Piccinno, F.; Gottschalk, F.; Nowack, B. Industrial Production Quantities and Uses of Ten Engineered Nanomaterials in Europe and the World. *J. Nanopart. Res.* **2012**, *14*, No. 1109.

(15) Abbas, Q.; Yousaf, B.; Naushad, M. Transformation Pathways and Fate of Engineered Nanoparticles (ENPs) in Distinct Interactive Environmental Compartments: A Review. *Environ. Int.* **2020**, *138*, No. 105646.

(16) Xu, L.; Wang, Z.; Xing, B. Accumulation of Metal-based Nanoparticles in Marine Bivalve Mollusks from Offshore Aquaculture as Detected by Single Particle ICP-MS. *Environ. Pollut.* **2020**, *260*, No. 114043.

(17) Saleh, T. A. Nanomaterials: Classification, Properties, and Environmental Toxicities. *Environ. Technol. Innov.* **2020**, *20*, No. 101067.

(18) Ahmad, F.; Wang, X.; Li, W. Toxico-Metabolomics of Engineered Nanomaterials: Progress and Challenges. *Adv. Funct. Mater.* **2019**, *29*, No. 1904268.

(19) Buchman, J. T.; Hudson-Smith, N. V.; Haynes, C. L. Understanding Nanoparticle Toxicity Mechanisms to Inform Redesign Strategies to Reduce Environmental Impact. *Acc. Chem. Res.* **2019**, *52*, 1632−1642.

(20) Djurišić, A. B.; Leung, Y. H.; Wu, R. S. Toxicity of Metal Oxide Nanoparticles: Mechanisms, Characterization, and Avoiding Experimental Artefacts. *Small* **2015**, *11*, 26−44.

(21) Svendsen, C.; Walker, L. A.; Spurgeon, D. J. Key Principles and Operational Practices for Improved Nanotechnology Environmental Exposure Assessment. *Nat. Nanotechnol.* **2020**, *15*, 731−742.

https://doi.org/10.1021/acsapm.1c00990
ACS Appl. Polym. Mater. XXXX, XXX, XXX−XXX

(22) Hedberg, J.; Blomberg, E.; Odnevall Wallinder, I. In the Search for Nanospecific Effects of Dissolution of Metallic Nanoparticles at Freshwater-Like Conditions: A Critical Review. *Environ. Sci. Technol.* **2019**, *53*, 4030−4044.
(23) Sobhanan, J.; Jones, P.; Biju, V. Toxicity of Nanomaterials due to Photochemical Degradation and the Release of Heavy Metal Ions. *Nanoscale* **2020**, *12*, 22049−22058.
(24) Surette, M. C.; Nason, J. A. Nanoparticle Aggregation in a Freshwater River: The Role of Engineered Surface Coatings. *Environ. Sci. Nano* **2019**, *6*, 540−553.
(25) Lin, D.; Tian, X.; Xing, B. Fate and Transport of Engineered Nanomaterials in the Environment. *J. Environ. Qual.* **2010**, *39*, 1896−1908.
(26) Zhou, W.; Liu, Y.-L.; Lenhart, J. J. Effects of pH, Electrolyte, Humic Acid, and Light Exposure on the Long-Term Fate of Silver Nanoparticles. *Environ. Sci. Technol.* **2016**, *50*, 12214−12224.
(27) Slomberg, D. L.; Ollivier, P.; Labille, J. Nanoparticle Stability in Lake Water Shaped by Natural Organic Matter Properties and Presence of Particulate Matter. *Sci. Total Environ.* **2019**, *656*, 338−346.
(28) Zhang, J.; Guo, W.; Liu, S. The Effects and the Potential Mechanism of Environmental Transformation of Metal Nanoparticles on their Toxicity in Organisms. *Environ. Sci. Nano* **2018**, *5*, 2482−2499.
(29) Jośko, I.; Dobrzyńska, J.; Terpiłowski, K. The Effect of pH and Ageing on the Fate of CuO and ZnO Nanoparticles in Soils. *Sci. Total Environ.* **2020**, *721*, No. 137771.
(30) Kugarajah, V.; Ojha, A. K.; Mishra, N. M. Future Applications of Electrospun Nanofibers in Pressure Driven Water Treatment: A Brief Review and Research Update. *J. Environ. Chem. Eng.* **2021**, No. 105107.
(31) Zhu, F.; Zheng, Y.; Dai, Y. A Critical Review on the Electrospun Nanofibrous Membranes for the Adsorption of Heavy Metals in Water Treatment. *J. Hazard. Mater.* **2021**, *401*, No. 123608.
(32) Feng, Q.; Wu, D.; Fong, H. Electrospun AOPAN/RC Blend Nanofiber Membrane for Efficient Removal of Heavy Metal Ions from Water. *J. Hazard. Mater.* **2018**, *344*, 819−828.
(33) Aliahmadipoor, P.; Ghazanfari, D.; Akhgar, M. R. Preparation of PVDF/FMBO Composite Electrospun Nanofiber for Effective Arsenate Removal from Water. *RSC Adv.* **2020**, *10*, 24653−24662.
(34) Almasian, A.; Giahi, M.; Maleknia, L. Removal of Heavy Metal Ions by Modified PAN/PANI-Nylon Core-shell Nanofibers Membrane: Filtration Performance, Antifouling and Regeneration Behavior. *Chem. Eng. J.* **2018**, *351*, 1166−1178.
(35) Manirethan, V.; Gupta, N.; Raval, K. Batch and Continuous Studies on the Removal of Heavy Metals from Aqueous Solution Using Biosynthesised Melanin-coated PVDF Membranes. *Environ. Sci. Pollut. Res.* **2020**, *27*, 24723−24737.
(36) Chen, Q.; Zheng, J.; Zhang, L. A Multi-Functional-Group Modified Cellulose for Enhanced Heavy Metal Cadmium Adsorption: Performance and Quantum Chemical Mechanism. *Chemosphere* **2019**, *224*, 509−518.
(37) Bahmani, P.; Maleki, A.; McKay, G. Application of Modified Electrospun Nanofiber Membranes with α-Fe2O3 Nanoparticles in Arsenate Removal from Aqueous Media. *Environ. Sci. Pollut. Res.* **2019**, *26*, 21993−22009.
(38) Mautner, A.; Kwaw, Y.; Bismarck, A. Natural Fibre-Nanocellulose Composite Filters for the Removal of Heavy Metal Ions from Water. *Ind. Crops Prod.* **2019**, *133*, 325−332.
(39) Hezarjaribi, M.; Bakeri, G.; Akbari, S. Novel Adsorptive Membrane Through Embedding Thiol-Functionalized Hydrous Manganese Oxide into PVC Electrospun Nanofiber for Dynamic Removal of Cu(II) and Ni(II) Ions from Aqueous Solution. *J. Water Process Eng.* **2020**, *37*, No. 101401.
(40) Efome, J. E.; Rana, D.; Lan, C. Q. Effects of Operating Parameters and Coexisting Ions on the Efficiency of Heavy Metal Ions Removal by Nano-Fibrous Metal-Organic Framework Membrane Filtration Process. *Sci. Total Environ.* **2019**, *674*, 355−362.
(41) Faccini, M.; Borja, G.; Amantia, D. Electrospun Carbon Nanofiber Membranes for Filtration of Nanoparticles from Water. *J. Nanomater.* **2015**, *2015*, No. 247471.
(42) Mahanta, N.; Valiyaveettil, S. Surface Modified Electrospun Poly(vinyl alcohol) Membranes for Extracting Nanoparticles from Water. *Nanoscale* **2011**, *3*, 4625−4631.
(43) Heuer-Jungemann, A.; Feliu, N.; Kanaras, A. G. The Role of Ligands in the Chemical Synthesis and Applications of Inorganic Nanoparticles. *Chem. Rev.* **2019**, *119*, 4819−4880.
(44) Müller, A.-K.; Xu, Z.-K.; Greiner, A. Preparation and Performance Assessment of Low-Pressure Affinity Membranes Based on Functionalized, Electrospun Polyacrylates for Gold Nanoparticle Filtration. *ACS Appl. Mater. Interfaces* **2021**, *13*, 15659−15667.
(45) Rostek, A.; Mahl, D.; Epple, M. Chemical Composition of Surface-functionalized Gold Nanoparticles. *J. Nanopart. Res.* **2011**, *13*, 4809−4814.
(46) Smith, A. M.; Marbella, L. E.; Millstone, J. E. Quantitative Analysis of Thiolated Ligand Exchange on Gold Nanoparticles Monitored by 1H NMR Spectroscopy. *Anal. Chem.* **2015**, *87*, 2771−2778.
(47) Mirzaei, A.; Janghorban, K.; Neri, G. Characterization and Optical Studies of PVP-Capped Silver Nanoparticles. *J. Nanostruct. Chem.* **2017**, *7*, 37−46.
(48) Ahamed, M.; Alhadlaq, H. A.; Al-Dhabi, N. A. Synthesis, Characterization, and Antimicrobial Activity of Copper Oxide Nanoparticles. *J. Nanomater.* **2014**, *2014*, No. 637858.
(49) Amde, M.; Tan, Z.-Q.; Liu, J. Separation and Size Characterization of Zinc Oxide Nanoparticles in Environmental Waters Using Asymmetrical Flow Field-Flow Fractionation. *Talanta* **2019**, *200*, 357−365.
(50) Lucas, I. T.; Durand-Vidal, S.; Turq, P. Surface Charge Density of Maghemite Nanoparticles: Role of Electrostatics in the Proton Exchange. *J. Phys. Chem. C* **2007**, *111*, 18568−18576.
(51) Mahshid, S.; Askari, M.; Ghamsari, M. S. Synthesis of TiO2 Nanoparticles by Hydrolysis and Peptization of Titanium Isopropoxide Solution. *J. Mater. Process. Technol.* **2007**, *189*, 296−300.
(52) Bastús, N. G.; Comenge, J.; Puntes, V. Kinetically Controlled Seeded Growth Synthesis of Citrate-Stabilized Gold Nanoparticles of up to 200 nm: Size Focusing versus Ostwald Ripening. *Langmuir* **2011**, *27*, 11098−11105.
(53) Piella, J.; Bastús, N. G.; Puntes, V. Size-Controlled Synthesis of Sub-10-nanometer Citrate-Stabilized Gold Nanoparticles and Related Optical Properties. *Chem. Mater.* **2016**, *28*, 1066−1075.
(54) Fatehah, M. O.; Aziz, H. A.; Stoll, S. Stability of ZnO Nanoparticles in Solution. Influence of pH, Dissolution, Aggregation and Disaggregation Effects. *J. Colloid Sci. Biotechnol.* **2014**, *3*, 75−84.
(55) Wang, X.; Sun, T.; Dai, H. Roles of pH, Cation Valence, and Ionic Strength in the Stability and Aggregation Behavior of Zinc Oxide Nanoparticles. *J. Environ. Manage.* **2020**, *267*, No. 110656.

https://doi.org/10.1021/acsapm.1c00990
ACS Appl. Polym. Mater. XXXX, XXX, XXX−XXX

Supporting Information for

Sustainable Electrospun Affinity Membranes for Water Remediation by Removing Metal and Metal Oxide Nanoparticles

Ann-Kathrin Müller,[a)] Zhi-Kang Xu[b)], Andreas Greiner[a)]**

a) Macromolecular Chemistry and Bavarian Polymer Institute, University of Bayreuth, Universitätsstraße 30, Bayreuth 95440, Germany

b) MOE Key Laboratory of Macromolecular Synthesis and Functionalization, and Key Laboratory of Adsorption and Separation Materials & Technologies of Zhejiang Province, Department of Polymer Science and Engineering, Zhejiang University, Hangzhou 310027, China

*Correspondence should be addressed to greiner@uni-bayreuth.de or xuzk@zju.edu.cn

This PDF file includes:

Materials and Methods

Fig. S1-28

Table S1-6

Experimental Section

Materials

Sodium borohydride (Acros Organics, 99%), copper acetate monohydrate (Grüss, 99%), zinc acetate dehydrate (Fisher Chemical, >99,5%), iron (II) chloride tetrahydrate (Aldrich, >99%), iron (III) chloride (Aldrich, >99%), titanium isopropoxide (Aldrich Chemistry, >97%), silver nitrate (Alfa Aesar, >99.9%), Polyvinylpyrrolidone 360 (Sigma life Science), 11-mercaptoundecanoic acid (Aldrich, 98%), sodium pyrophosphate (Alfa Aesar, 98%), citric acid trisodium trihydrate (Acros Organics, 99%), and sodium hydroxide (Merck, >98%) were used without further purification. Ammonia (VWR, 25%), methanol (Fisher Scientific, >99.9%), hydrochloric acid (35%) (VWR-Prolab, Ph.Eur.), nitric acid (65%) (B. Kraft, analysis), orthophosphoric acid (85%) (Fisher Scientific, analysis), and glacial acetic acid (Fisher Scientific, 99.7%) were used as received. Postnova GmbH supplied the special tenside novachem for AF-FFF measurements.

Filtration tests were done with membranes containing 50 mol% of the functional groups- AA, Pyr, NIPAM, or Nplus-, 10 mol% of MABP, and 40 mol% MMA. Polymer synthesis and membrane preparation were done according to the procedure in the previous paper.[1]

Measurements

Ultraviolet/visible light (UV/Vis)

V-630 spectrometer from Jasco with spectra manager CFR software was used for recording UV/Vis spectra. The measured wavelength region was set to 200-800 nm, and data points were collected in a distance of 2 nm. Aqueous samples were prepared with concentrations between

0.009 up to 0.5 mg/mL. The measurements were executed in a quartz cuvette (1 cm x 1cm). The standard measurement error was determined to be ±10%.

Asymmetric flow-field flow fractionation (AF-FFF)

AF-FFF was performed on an AF2000 system from Postnova Analytics (Landsberg am Lech, Germany). The channel (295x30 mm) was equipped with a NovaRC 10 kDa membrane and with a 350 µm spacer. Analysis was done with a UV detector and multiple angle light scattering (MALS) detector (532 nm). Postnova AF2000 Control software was applied for size evaluation.

The UV detector signal for measurements without separation was used for concentration determination, and the recovery rate was calculated for measurements with separation. The following wavelengths were set for detection: AuNP (253 nm), AgNP (350 nm), CuO NP (250 nm), ZnO NP (350 nm), Fe_2O_3 NP (290 nm), TiO_2 NP (290 nm). The measurement error was determined to be ±20%. The particle size was analyzed in separation experiments.

Zeta potentials of AgNP and AuNP were measured with the electrical EAF-FFF in Milli-Q water with potassium nitrate (1 mM) as eluent at various applied currents: neutral, -0.7 mA, -1.5 mA, -3 mA.

Samples were measured with and without separation, according to the following methods:

Table S 1. AF-FFF method for measuring AuNP and AgNP.

Step	Parameter*		With separation AuNP	With separation AgNP	Without separation
	Injection volume [µl]		20	20	20
	Detector flow [mL/min]		0.5	0.5	0.5
Focusing	Injection flow [mL/min]		0.2	0.2	0.2
	Injection time [min]		5	6	1
	Crossflow		0.7	0.7	0
	Transition time		0.5	0.5	0.5
Elution	Step 1	Elution time [min]	2	3	10
		From [mL/min]	0.7	0.7	0
		To [mL/min]	0.7	0.7	0
		Type	Const.	Const.	Const.
	Step 2	Elution time [min]	20	35	
		From [mL/min]	0.7	0.7	None
		To [mL/min]	0	0	
		Type	0.05 power	0.2 power	
Rinsing					5

*AuNP were measured in Milli-Q water, AgNP were measured in Milli-Q water pH 9.

Table S 2. AF-FFF method for ZnO NP, CuO NP, TiO_2 NP, and Fe_2O_3 NP.

Step	Parameter*		ZnO	CuO	TiO_2	Fe_2O_3
	Injection volume [µl]		20	20	20	20
	Detector flow [mL/min]		0.5	0.5	0.5	0.5
Focusing	Injection flow [mL/min]		0.2	0.2	0.2	0.2
	Injection time [min]		8	10	5	7
	Crossflow		0.6	0.7	0.6	0.6
	Transition time		0.5	0.5	0.5	0.5
Elution	Step 1	Elution time [min]	4	2	2	3
		From [mL/min]	0.6	0.7	0.6	0.6
		To [mL/min]	0.6	0.7	0.6	0.6
		Type	Const.	Const.	Const.	Const.
	Step 2	Elution time [min]	30	40	30	30
		From [mL/min]	0.6	0.7	0.6	0.6
		To [mL/min]	0	0	0	0
		Type	0.2 Power	0.3 Power	0.2 Power	0.2 Power
Rinsing	Time [min]		5	5	5	5

*Metal oxide NP were measured after the addition of PVP-360 to the samples and in Milli-Q water with 0.8 wt% Novachem.

Transmission electron microscope (TEM)

For TEM measurements, 2 µL of nanoparticle dispersion was dropped on top of the carbon-coated copper grid (Carbon support film, 16 200 mesh, copper). Measurement was executed on Leo 922 from Zeiss at an acceleration voltage of 200 kV, with a LaB6 crystal as a cathode. At least 70 nanoparticles were measured with ImageJ software for mean particle diameter.

Scanning electron microscope (SEM)

Samples were prepared on a coal film. Membranes were sputtered with 1.3 nm platinum by the Cressington platinum-sputter coater 208HR or coated with a coal film by the Leica EM ACE 600. Leo 1530 from Zeiss was used for measurements at an acceleration voltage of 3 kV and a pressure of 2.0 x 10-5 bar for pictures with inlense and secondary electron (Everhart Thornley) detector. The backscattering detector from Centaurus (10 mm working distance) was used at 10 kV acceleration voltage and the Ultradry-EDX-detector from Thermo Fisher Scientific NS7 (8 mm working distance) at an acceleration voltage of 20 kV under the usual pressure.

Dynamic light scattering (DLS)

A system from ALV-5000EPP Laservertriebsgesellschaft mbH, with a photon-counting module from Perkin Elmer (SPCM-CD 3017) was used. DLS measurements were done at a wavelength of 632 nm, with a detector angle of 90°, and a temperature of 294 K. Samples were all prepared in water with a viscosity of 0.9711 cp. The data were analyzed with WINDOWS-95/98/NT-4.0 control and data reduction software.

Inductively coupled plasma-optical emission spectroscopy (ICP-OES)

Measurements were performed on an Avio 200 (Perkin Elmer) in radial viewed plasma with purged polychromator configurations. The measurement was calibrated with four multi-ion standard solutions at concentrations of 0.1, 0.5, 1, and 10 mg l-1. The sample flow rate was set to 1.2 mL/min. The detected wavelengths for each metal ion were set to: Cu (327.393 nm/ 324.752 nm), Zn (206.200 nm/ 213.857 nm), Fe (238.204 nm/ 239.562 nm), Ag (328.068 nm/ 338.289 nm), and Au (267.595 nm/ 242.795 nm). AuNP samples were prepared by diluting the dispersions with aqua regia (HNO3:HCl 1:3) and Milli-Q water. AgNP, CuO NP, ZnO NP, and Fe_2O_3 NP were dissolved in nitric acid with an acid concentration of 5 vol%. Standard deviations of the ICP-OES measurements were ±10%.

Zeta sizer

Nanoparticle samples were prepared in water with a concentration of 0.009-0.05 mg/mL and were measured by a zeta sizer of Malvern. The Malvern software automatically set an optimum measurement position and voltage. The measuring temperature was 20 °C.

Synthesis

Gold Nanoparticles

Gold nanoparticles were synthesized according to the procedure of Neus G. Bastus.[2] The aqueous solution of $HAuCl_4$ dihydrate (39.36 mg, 2.5 x 10-4 M) was heated to the boiling point, followed by the dropwise addition of trisodium citrate (105.12 mg, 39.17 mM). In the next 5 min, the solution color changed from yellow to white, grey, faint blue, and finally purple/red, indicating the AuNP's formation. After another 30 min of reaction time, the solution was cooled down to room temperature and was stored at 4 °C. The nanoparticle dispersion is stable for more than half a year. These NP were used for ligand exchange reactions.

Gold nanoparticle synthesize via growth method [3]

Gold nanoparticle seeds were synthesized by adding tetrachloroaurate (25 mM, 0.5 mL) to a sodium citrate solution (2.2 mM, 75 mL) at 95 °C. Now the first growth step was started by injecting two times tetrachloroaurate (25 mM, 0.5 mL) with a dwell time of 25 min. Then 27.5 mL were removed, the reaction vessel was filled with 25 mL of Milli-Q water and 1 mL of sodium citrate solution (2.2 mM) and tempered at 95 °C. The growth steps were repeated six times. The solution color of each growth step changes from red to dark-red to red-orange. The nanoparticle fractions 1-4 were stable.

Gold nanoparticle ligand exchange to PVP

Gold nanoparticles, which had been synthesized in section "gold nanoparticle synthesis," were used for ligand exchange reactions according to Rostek et al. [4] The AuNP dispersion (20 mL) was mixed with PVP-360 (1.32 mg) and stirred overnight at room temperature. The red dispersion was then centrifuged a minimum of three times (10000 rpm) and washed with water.

Gold nanoparticle ligand exchange to MUA

AuNP from the section "gold nanoparticle synthesis" was used for ligand exchange reactions according to Smith et al. [5] AuNP (920 µL) were mixed with a solution of 11-mercapto-undecanoic acid (3.26 mg) and sodium hydroxide (12 mg), and stirred at room temperature overnight. The red dispersion was centrifuged three times and washed with Milli-Q water to receive the MUA@AuNP particles.

Silver nanoparticles [6]

Sodium borohydride (16.7 mg, 0.44 mmol) was filled into a beaker and cooled down to 0°C before water (220 mL) was added. Silver nitrate (7.22 mg, 42.5 µmol) was dissolved in water (5 mL) and cooled down to 0 °C, too, before it was dropped slowly into the borohydride solution under vigorous stirring. Then stirring was stopped for 30 min. Afterward, PVP 360 (20 mg, 5 mL) was added, and the whole dispersion was filled up to 440 mL. The silver nanoparticle dispersion is used without further work-up. It is stored at 5 °C.

Copper oxide nanoparticles

Copper oxide nanoparticles were synthesized according to Maqusood Ahamed et al. [7] Copper acetate (10.5 g, 57.8 mmol) was dissolved in Milli-Q water (300 mL) and glacial acetic acid (1 mL). The blue solution was heated up to 100 °C, and sodium hydroxide (15 mL, 6 M) solution was added under the formation of a black dispersion. After two more hours of stirring, the dispersion was cooled down to room temperature, followed by centrifugation and washing with water and acetone. The copper oxide nanoparticles are stored under room temperature at a 23.1 mg/mL concentration.

Zinc oxide nanoparticles

Zinc oxide nanoparticles were synthesized according to Meseret Amde et al. [8] Zinc acetate dihydrate (1 g, 4.57 mmol) was dissolved in methanol (40 mL) at 60 °C, and Milli-Q water was slowly dropped to the solution (3.5 mL) as well as sodium hydroxide solution (0.36 g, 30 mL methanol). After 30 min of stirring, the solution was cooled down to room temperature and was centrifuged and washed with water and acetone. The zinc oxide nanoparticles are stored under room temperature with a 13 mg/mL concentration in Milli-Q water.

Iron oxide nanoparticles

Iron oxide nanoparticles were synthesized according to I.T. Lucas et al. [9] Iron (II) chloride tetrahydrate (0.325 g, 1.64 mmol) and iron(III) chloride (0.532 g, 3.28 mmol) were dissolved in Milli-Q water (32 mL), and argon was bubbled through the solution for 15 min. Under vigorous stirring, ammonia (4.5 mL, 25%) was dropped slowly to the orange solution under the formation of a black dispersion. After 1 h of stirring, the particles were sedimented, the supernatant was removed, and the nanoparticles were washed twice with water. The nanoparticles were re-dispersed in Milli-Q water with pH 3 (HNO_3) and stirred under air for two days, forming a brown, magnetic dispersion. The nanoparticles were stored under room temperature with a concentration of 13.7 mg/mL in Milli-Q water at pH 3.

Titanium dioxide nanoparticles

Titanium dioxide nanoparticles were synthesized according to S. Mashid et al. [10] Titanium isopropoxide (5 mL, 16.9 mmol) was mixed with isopropanol (20 mL) and was dropped slowly to Milli-Q water (300 mL) at 75 °C. The resulting dispersion was stirred for 18 h and a blue opaque dispersion formed, which was cooled down to room temperature. The dispersion was used as produced and was stored at room temperature.

Particle Filtration Test

The membranes were cut into pieces with a diameter of 14 mm and were deposited on top of a sheet of PET mesh with a pore size of 50 μm. A reusable filtering apparatus from Satorius AG was utilized limiting the used membrane area for filtration to 0.95 cm2. A syringe pump (Landgraf Laborsysteme, model no. LA 30) adjusted the solution flow rate, and the filtrate is collected in vials with a volume of 1.5 mL. Main filtration tests were carried out with 1 mL/min flow rate, a double layer of nonwoven, and a total collection time of 6 min. Each batch was then further analyzed by UV/Vis, AF-FFF, and ICP-OES. For TiO_2 NP ICP-OES measurements were skipped. The filtration efficiency was calculated from the three different measurement methods. For repeated filtration experiments, data points with high deviation were excluded.

Membrane combination

The AA containing copolymer was simultaneously electrospun with the Nplus containing polymer on a rotating disc collector. The combined membrane layers were produced by electrospinning the Nplus copolymer on a rotating disc collector, followed by electrospinning the AA copolymer. Both copolymer solutions contain 0.25 wt% in DMF. The filtrates were analyzed with UV/Vis and AF-FFF. ICP-OES measurements were not possible for the NP mixture due to the different dissolution properties.

Membrane capacity

To determine the membrane capacity for the different NP, a specific volume was filtered twice with a flow rate of 1 mL/min through the filtration apparatus. The filtered volume is for all NP 20 mL, except for AgNP, where only 15 mL are used.

Membrane regeneration

The membranes were first used for filtration of 4.5 mL nanoparticle dispersion followed by rinsing with acidic solutions (3 mL) and 5 mL of Milli-Q water. For the copper oxide and zinc oxide nanoparticles, nitric acid (5 vol%) was used for regeneration, rinsing continuously for 3 min. The iron oxide nanoparticles were recycled by using phosphoric acid (10 vol%) with dwell times of 2 h before 1 mL of phosphoric acid is released out of the filtering apparatus. For silver nanoparticles, nitric acid (10 vol%) is used as well. However, a dwell time of 3 h between releasing each time 1 mL is required.

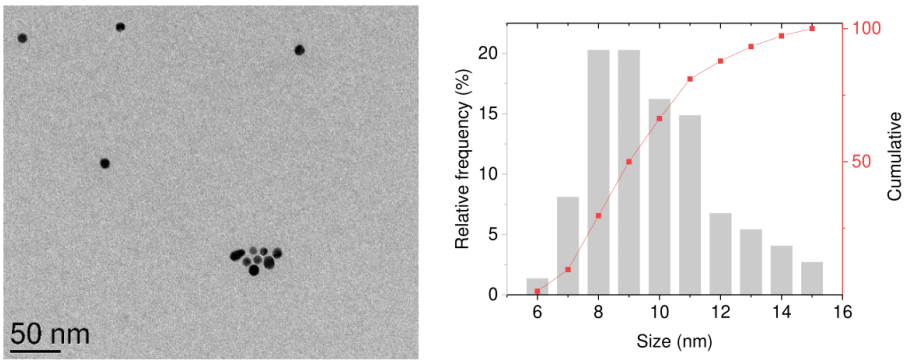

Figure S 1. Particle size distribution of AgNP measured with TEM with an average diameter of 10.4 ±2.2 nm.

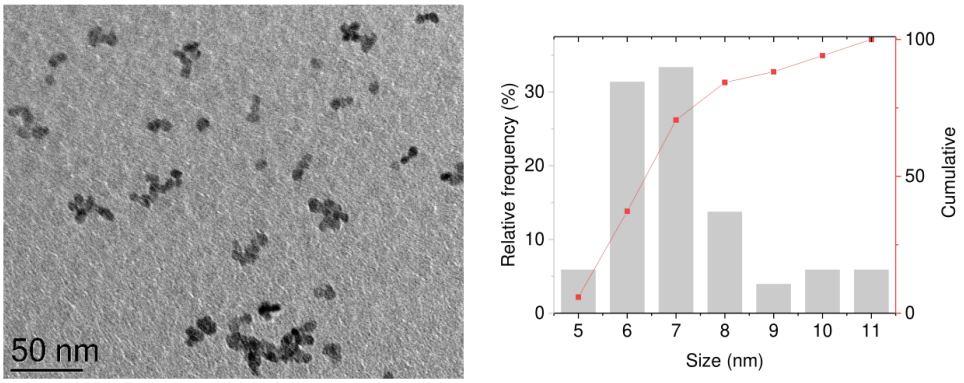

Figure S 2. Particle size distribution of CuO NP measured with TEM with an average particle diameter of 7.7 ±1.4 nm.

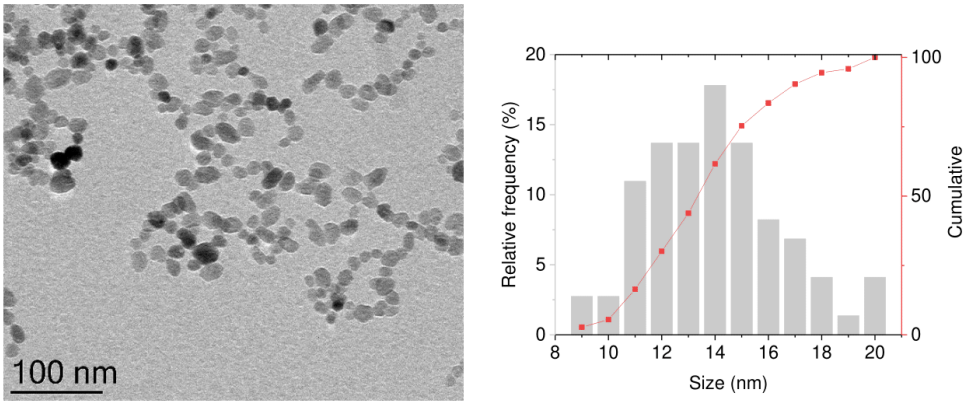

Figure S 3. Particle size distribution of ZnO NP measured with TEM with an average particle diameter of 14.6 ±2.5 nm.

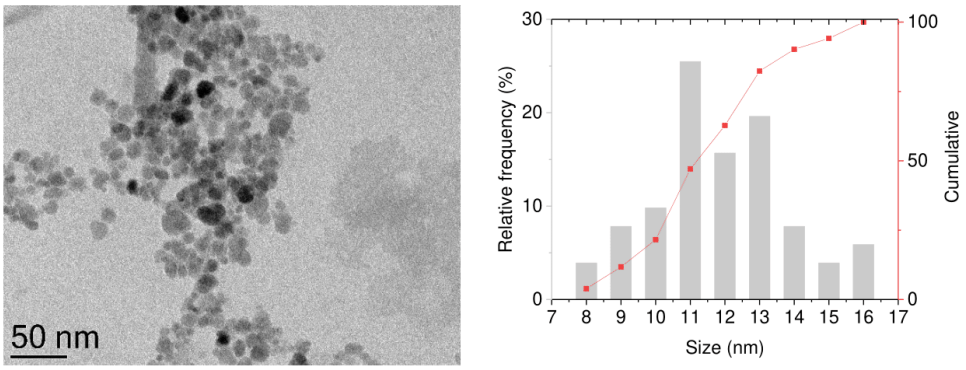

Figure S 4. Particle size distribution of Fe_2O_3 NP measured with TEM with an average particle diameter of 12.5 ±1.9 nm.

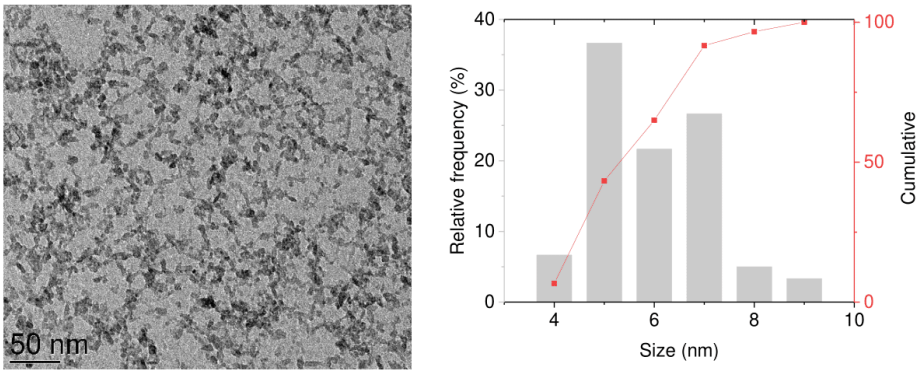

Figure S 5. Particle size distribution of TiO_2 NP measured with TEM with an average particle diameter of 6.5 ±1.2 nm.

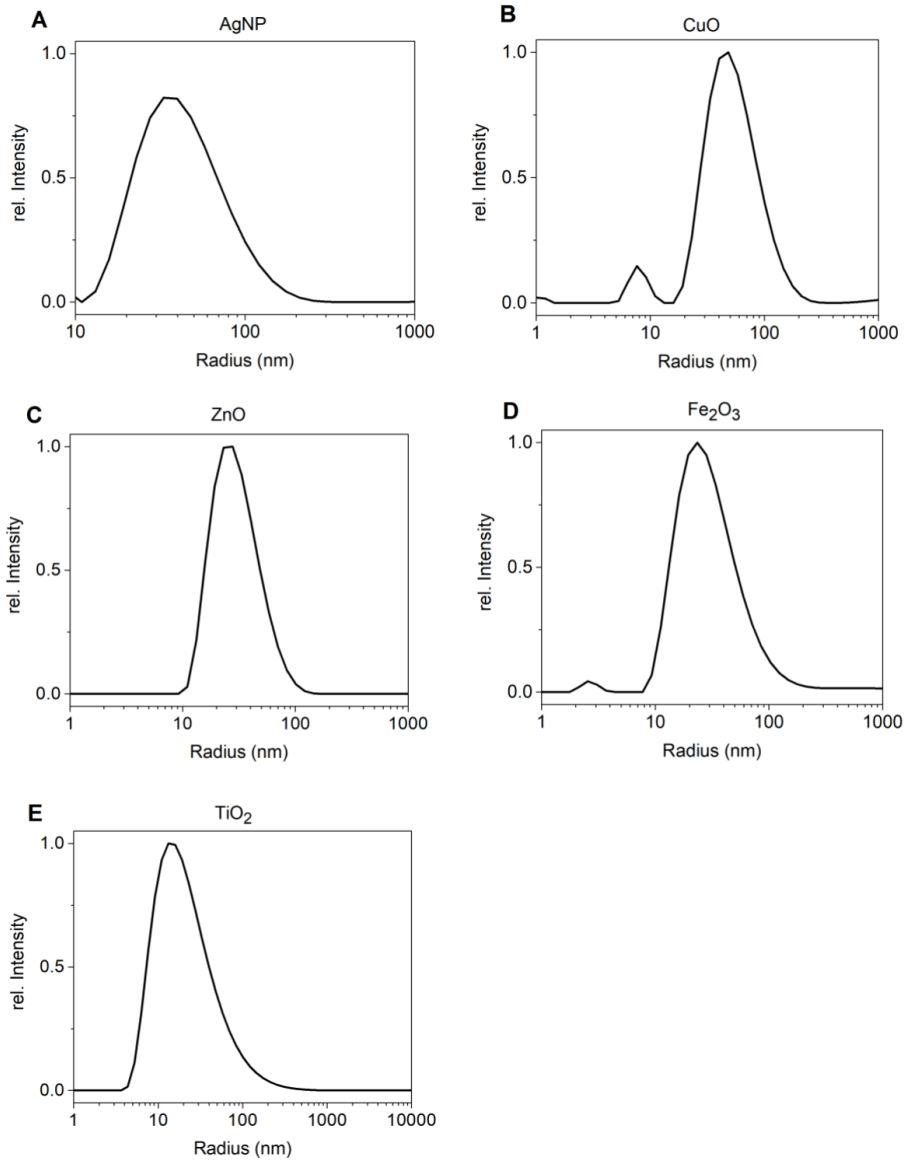

Figure S 6. DLS measurements for A) AgNP with a radius of 33 nm, B) CuO NP with a radius of 47 nm, C) ZnO NP with a radius of 27 nm, D) Fe_2O_3 NP with a radius of 25 nm, and D) TiO_2 NP with a radius of 16 nm.

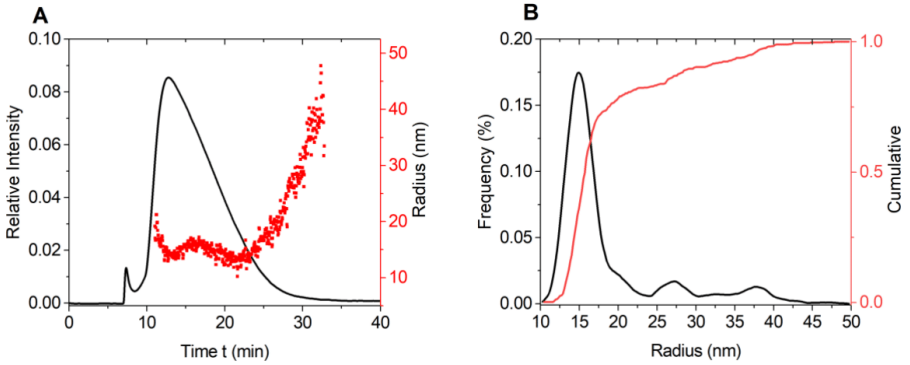

Figure S 7. A) AF-FFF measurement of AgNP in Milli-Q water pH 8 with B) an average radius of 16 nm.

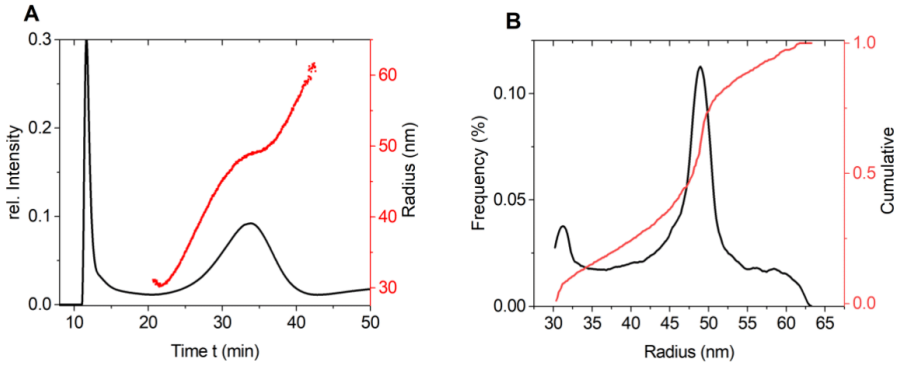

Figure S 8. A) AF-FFF measurement of CuO NP in 0.8% novachem and PVP-360 with B) an average radius of 50 nm.

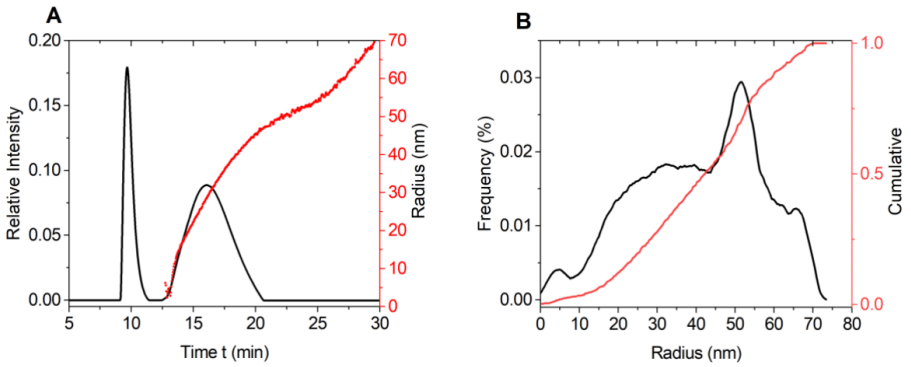

Figure S 9. A) AF-FFF measurement of ZnO NP in 0.8% novachem and PVP-360 with B) an average radius of 45 nm.

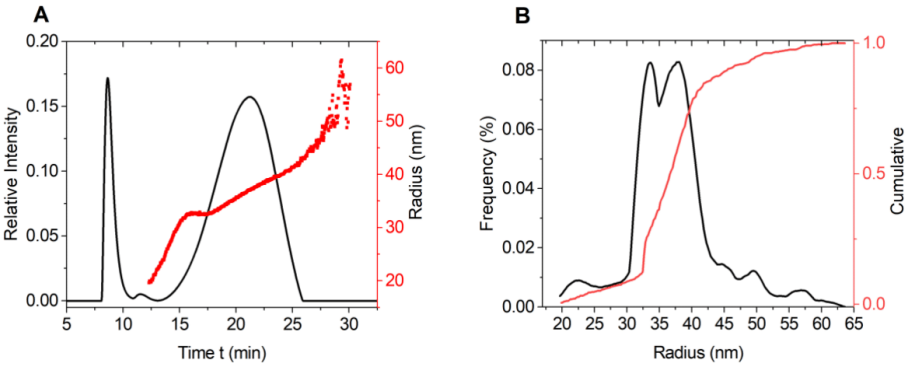

Figure S 10. A) AF-FFF measurement of Fe_2O_3 NP in 0.8% novachem and PVP-360 with B) a particle radius of 35 nm.

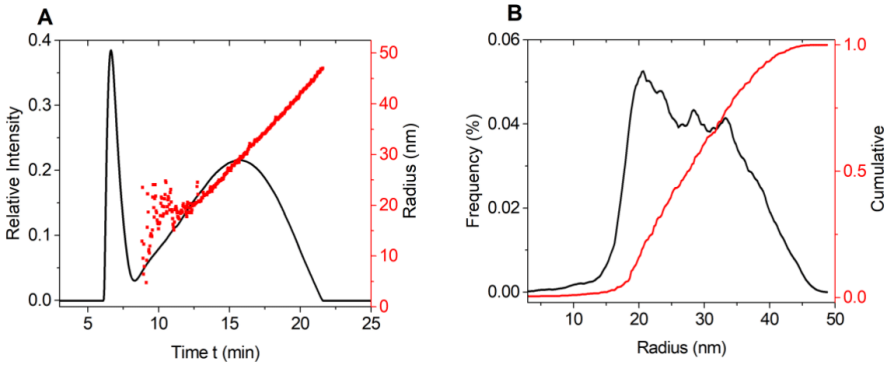

Figure S 11. A) AF-FFF measurement of TiO_2 NP in 0.8% novachem and PVP-360 with B) an average radius of 27 nm.

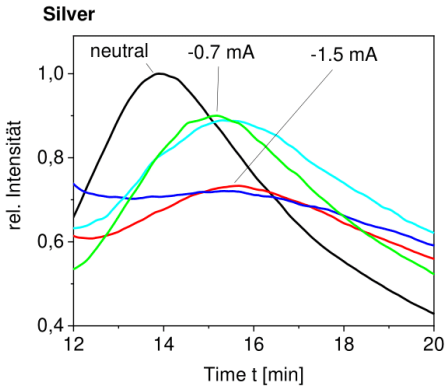

Figure S 12. Zeta potential measurement with EAF-FFF for AgNP.

Table S 3. Hydrodynamic size and zeta potential for AuNP with the ligands citrate, MUA, and PVP.

AuNP ligand	*Hydrodyn. Size [nm] (DLS)*	*Zeta potential [mV]**
Citrate	9 ±4 nm	-35 ±2
MUA	18 ±6 nm	-22 ±2
PVP	22 ±9 nm	-15 ±1

*Zeta potential is measured for the NP dispersion with the zeta sizer.

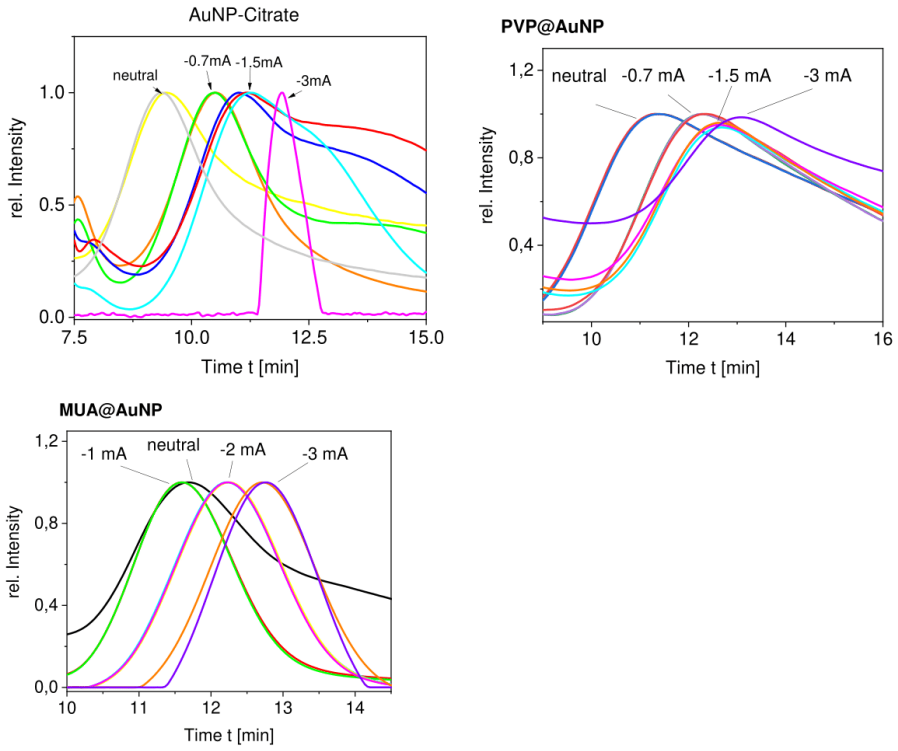

Figure S 13. Zeta potential measurement with EAF-FFF for AuNP with the ligands: A) citrate, B) PVP, and C) MUA.

Table S 4. AuNP penetration depth depending on the particle size.

AuNP	Particle size [nm] (TEM)	Particle size [nm] (DLS)	Penetration depth [µm]*
Growth 1	26 ±2	28 ±5	13 ±0.5
Growth 3	38 ±4	44 ±9	12 ±0.7
Growth 4	50 ±6	56 ±14	6.5 ±0.8
Growth 5	108 ±20	104 ±39	6.8 ±0.9
Growth 6	156 ±41	122 ±48	3.7 ±0.6

*Penetration depth was calculated from SEM images.

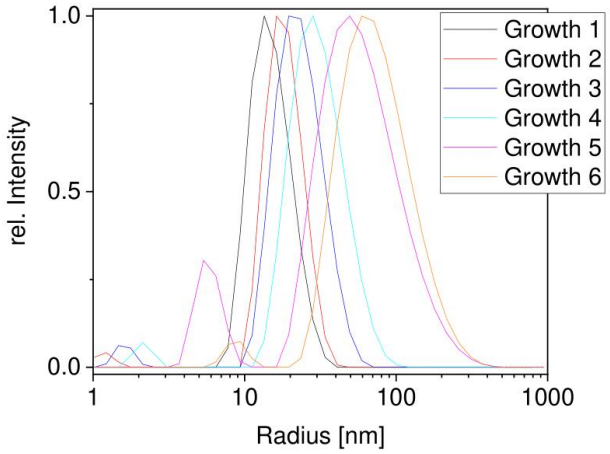

Figure S 14. DLS measurement of AuNP in different growth stages.

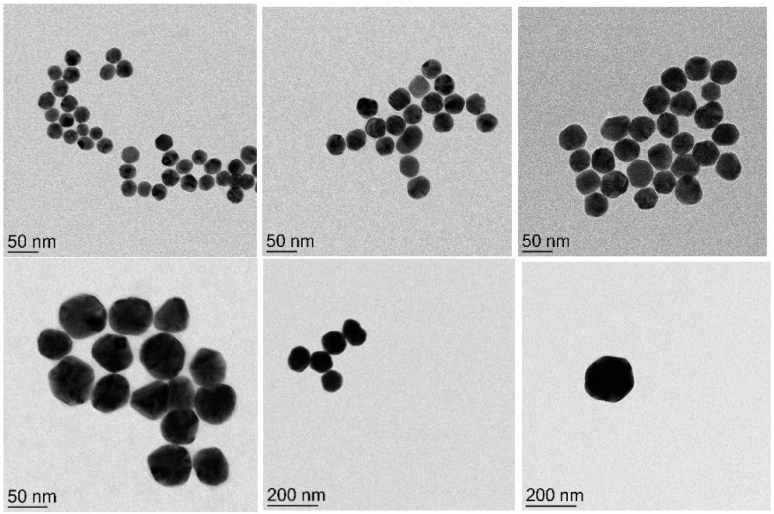

Figure S 15. TEM image of AuNP from growth 1-6.

Table S 5. Zeta potential of AuNP synthesized by particle growth mechanism.

Growth	Zeta potential [mV] *
1	-32
3	-38
4	-33
5	-35
6	-31

*Zeta potentials were measured by the zeta sizer.

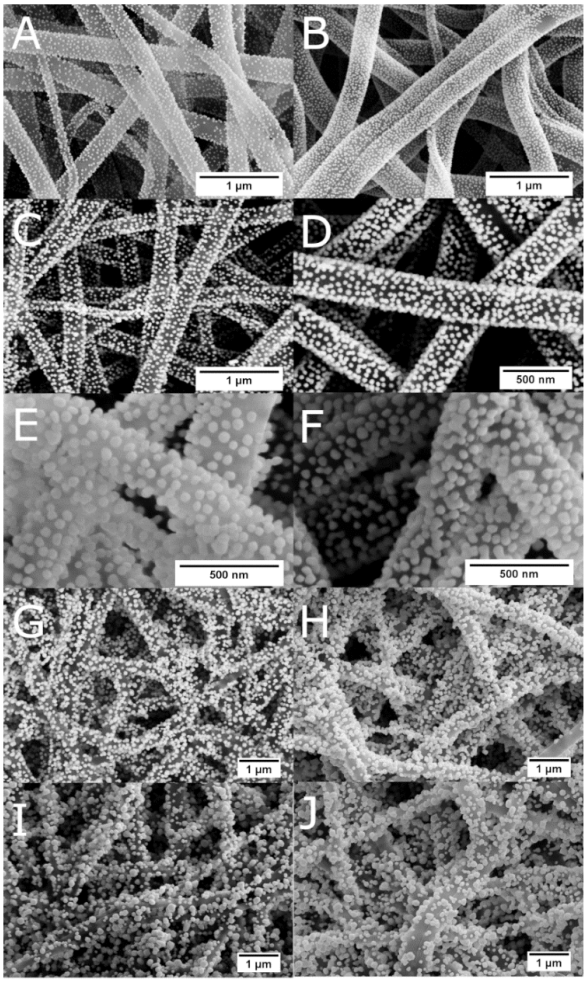

Figure S 16. SEM images after AuNP filtration with Pyr membrane (A, C, E, G, I) or Nplus membrane (B, D, F, H, J) and different AuNP sizes. Growth 1 (A, B); Growth 3 (C, D); Growth 4 (E, F); Growth 5 (G, H); Growth 6 (I, J).

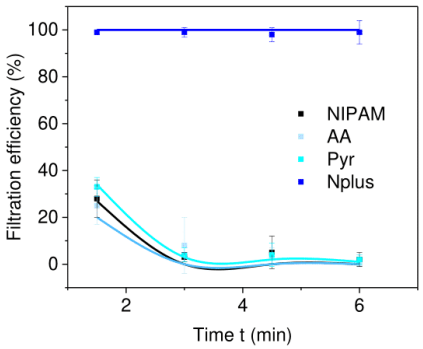

Figure S 17. Time-dependent filtration efficiency of AgNP with different membranes. Filtration tests were repeated with new membranes. The standard deviation was calculated from both tests and the analysis methods.

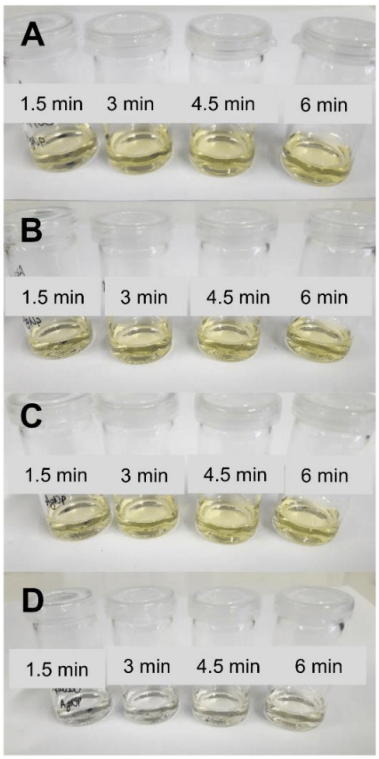

Figure S 18. Picture of filtrate of AgNP dispersions with A) NIPAM, B) AA, C) Pyr, and D) Nplus membrane.

Figure S 19. Pictures of membranes after AgNP filtration test with the functional groups: NIPAM, AA, Pyr, and Nplus.

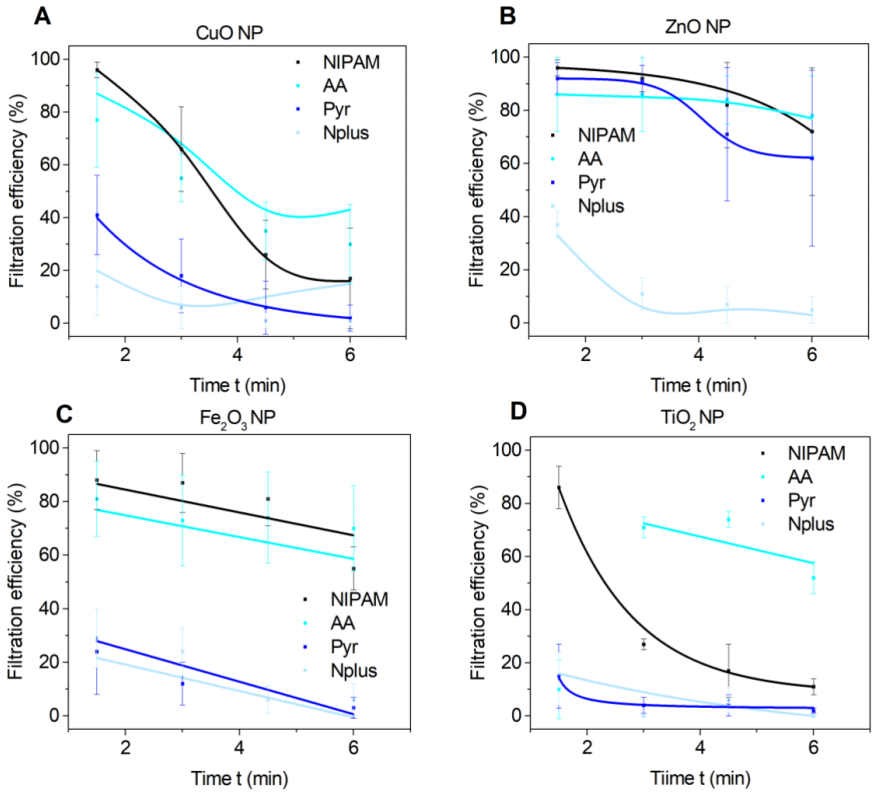

Figure S 20. Time-dependent filtration efficiency for A) CuO NP, B) ZnO NP, C) Fe_2O_3 NP, and D) TiO_2 NP. Filtration tests were repeated with new membranes. For CuO NP and ZnO NP a new batch of NP was used. Standard deviation was calculated from both tests and the different analysis methods.

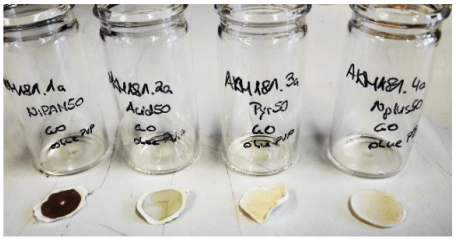

Figure S 21. Pictures of membranes after CuO NP filtration tests with the functional groups: NIPAM, AA, Pyr, and Nplus.

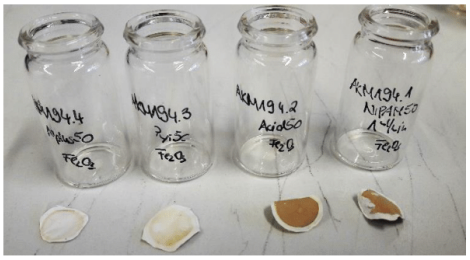

Figure S 22. Pictures of membranes after Fe_2O_3 NP filtration tests with the functional groups: Nplus, Pyr, AA, and NIPAM.

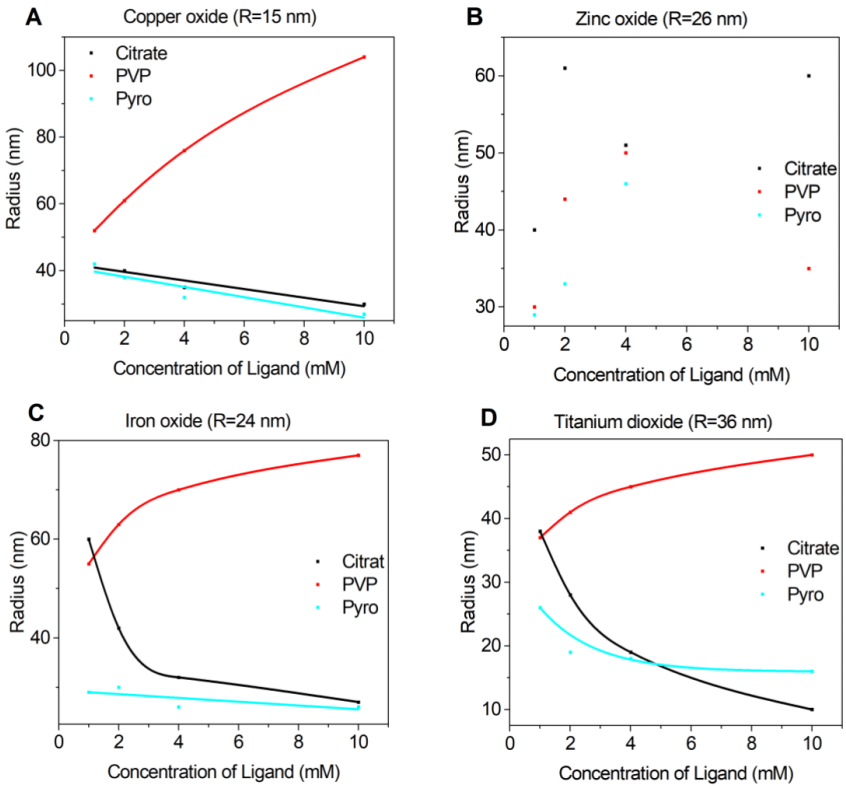

Figure S 23. NP radius in dependence on the ligand concentration for A) CuO NP, B) ZnO NP, C) Fe_2O_3 NP, and D) TiO_2 NP.

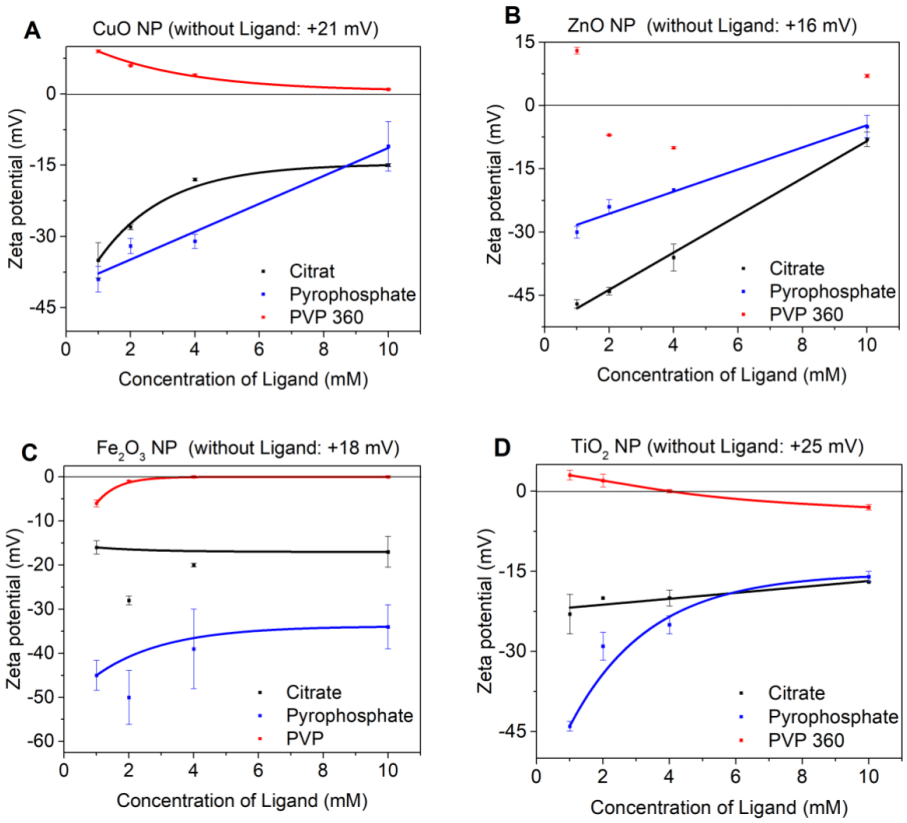

Figure S 24. Zeta potential in dependence on the ligand concentration for A) CuO NP, B) ZnO NP, C) Fe_2O_3 NP, and D) TiO_2 NP.

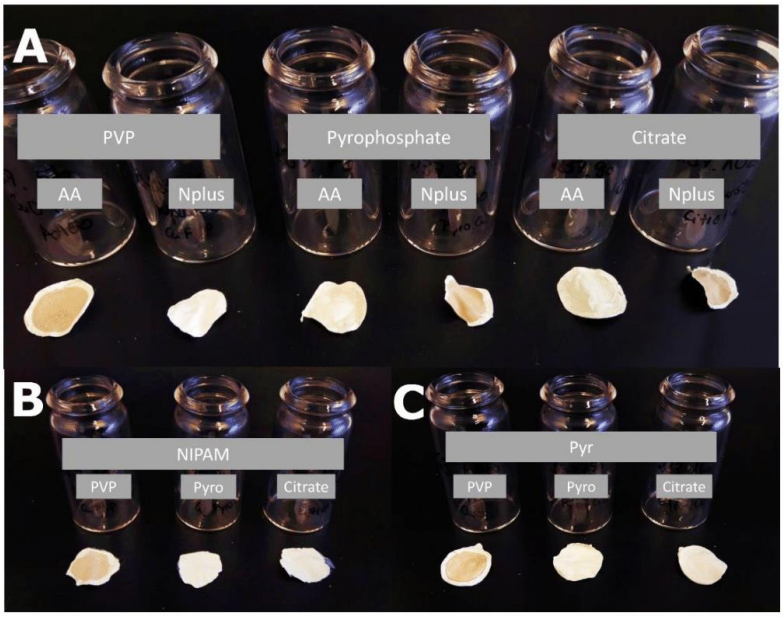

Figure S 25. Membranes after filtration of CuO NP wih A) different ligands and AA and Nplus membranes, B) different ligands and NIPAM membrane, and C) different ligands and Pyr membrane.

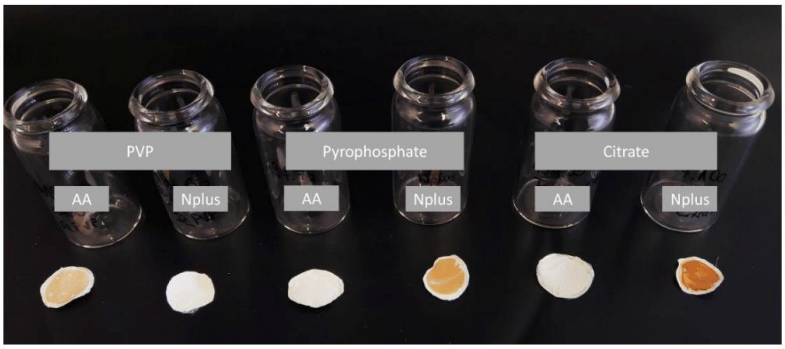

Figure S 26. Pictures of membranes after filtration of Fe_2O_3 NP with different ligands and the AA and Nplus membranes.

Table S 6. Average capacity [mg NP/mg membrane] of combined membranes for different NP.

Nanoparticle	Capacity [mg NP/mg membrane]	
	Parallel	layers
AuNP	0.108 ±0.034	0.137 ±0.067
AgNP	Not tested	0.058 ±0.002
ZnO NP		0.063 ±0.063
ZnO NP with 1mM pyrophosphate		0.027 ±0.006
Fe_2O_3 NP		0.045 ±0.021
Fe_2O_3 NP with 1mM pyrophosphat		0.069 ±0.005
TiO_2 NP with 1mM pyrophosphate		0.065 ±0.003
CuO without ligand	0.056 ±0.038	0.063 ±0.018
CuO with 1mM citrate	0.040 ±0.016	0.066 ±0.039

*Average values were calculated from UV/Vis, AF-FFF, and ICP-OES. The deviation was determined from the three measurement methods.

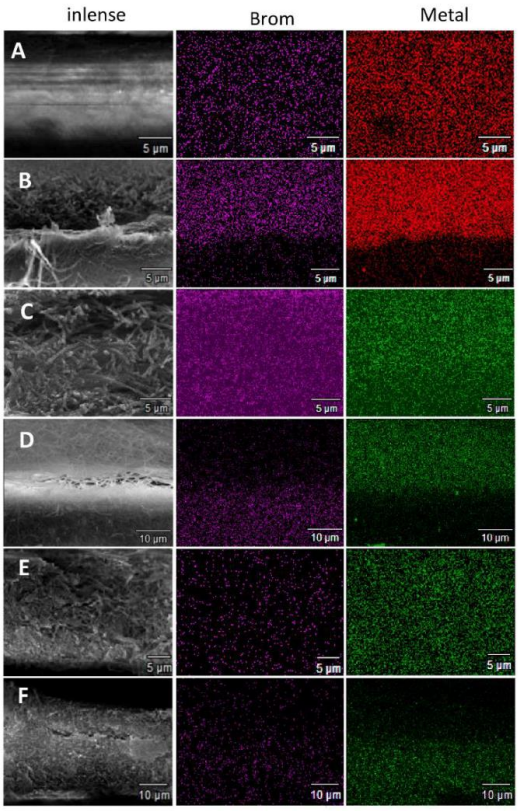

Figure S 27. SEM image with EDX detector of AuNP filtered with A) parallel electrospun combi membrane, B) layer combi membrane, and images of CuO NP with C) parallel electrospun combi membrane, D) layer combi membrane, and images of CuO NP with citrate-ligand with E) parallel electrospun combi membrane, or F) layer combi membrane.

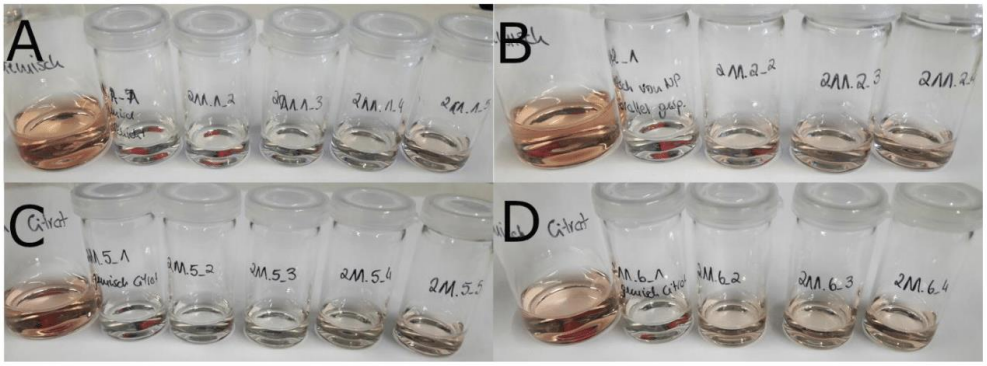

Figure S 28. Pictures of NP mixture after filtration with combi membranes A) layer combi membrane, B) parallel electrospun combi membrane, C) layer membrane with citrate as ligand, and D) parallel electrospun membrane with citrate as ligand.

References

(1) Müller, A.-K.; Xu, Z.-K.; Greiner, A. Preparation and Performance Assessment of Low-Pressure Affinity Membranes Based on Functionalized, Electrospun Polyacrylates for Gold Nanoparticle Filtration. *ACS Appl. Mater. Interfaces* **2021**, *13*, 15659–15667.

(2) Piella, J.; Bastús, N. G.; Puntes, V. Size-Controlled Synthesis of Sub-10-nanometer Citrate-Stabilized Gold Nanoparticles and Related Optical Properties. *Chem. Mater.* **2016**, *28*, 1066–1075.

(3) Bastús, N. G.; Comenge, J.; Puntes, V. Kinetically Controlled Seeded Growth Synthesis of Citrate-Stabilized Gold Nanoparticles of up to 200 nm: Size Focusing versus Ostwald Ripening. *Langmuir* **2011**, *27*, 11098–11105.

(4) Rostek, A.; Mahl, D.; Epple, M. Chemical Composition of Surface-functionalized Gold Nanoparticles. *J. Nanopart. Res.* **2011**, *13*, 4809–4814.

(5) Smith, A. M.; Marbella, L. E.; Millstone, J. E. Quantitative Analysis of Thiolated Ligand Exchange on Gold Nanoparticles Monitored by 1H NMR Spectroscopy. *Anal. Chem.* **2015**, *87*, 2771–2778.

(6) Mirzaei, A.; Janghorban, K.; Neri, G. Characterization and Optical Studies of PVP-Capped Silver Nanoparticles. *J. Nanostruct. Chem.* **2017**, *7*, 37–46.

(7) Ahamed, M.; Alhadlaq, H. A.; Al-Dhabi, N. A. Synthesis, Characterization, and Antimicrobial Activity of Copper Oxide Nanoparticles. *J. Nanomater.* **2014**, *2015*, 1–4.

(8) Amde, M.; Tan, Z.-Q.; Liu, J. Separation and Size Characterization of Zinc Oxide Nanoparticles in Environmental Waters Using Asymmetrical Flow Field-Flow Fractionation. *Talanta* **2019**, *200*, 357–365.

(9) Lucas, I. T.; Durand-Vidal, S.; Turq, P. Surface Charge Density of Maghemite Nanoparticles: Role of Electrostatics in the Proton Exchange. *J. Phys. Chem.* **2007**, *111*, 18568–18576.

(10) Mahshid, S.; Askari, M.; Ghamsari, M. S. Synthesis of TiO2 Nanoparticles by Hydrolysis and Peptization of Titanium Isopropoxide Solution. *J. Mater. Process. Technol.* **2007**, *189*, 296–300.

3.3 Publication (3)

Ecotoxicology and Environmental Safety 242 (2022) 113877

Contents lists available at ScienceDirect

Ecotoxicology and Environmental Safety

journal homepage: www.elsevier.com/locate/ecoenv

Disentangling biological effects of primary nanoplastics from dispersion paints' additional compounds

Ann-Kathrin Müller [a], Julian Brehm [b], Matthias Völkl [c], Valérie Jérôme [c], Christian Laforsch [b,*], Ruth Freitag [c,*], Andreas Greiner [a,*]

[a] Macromolecular Chemistry and Bavarian Polymer Institute, University of Bayreuth, D-95440 Bayreuth, Germany
[b] Department of Animal Ecology I and BayCEER, University of Bayreuth, D-95440 Bayreuth, Germany
[c] Department of Process Biotechnology, Faculty of Engineering Sciences, University of Bayreuth, D-95440 Bayreuth, Germany

ARTICLE INFO

Edited by Dr. Caterina Faggio

Keywords:
Paints
Nanoparticles
Dissolved polymers
Nanoplastics
Daphnia magna
Murine cells

ABSTRACT

Microplastic particles (MP) and nanoplastic particles (NP) as persistent anthropogenic pollutants may impact environmental and human health. A relevant potential source of primary MP and NP is water-based dispersion paint which are commonly used in any household. Given the worldwide high application volume of dispersion paint and their diverse material composition MP and NP may enter the environment with unforeseeable consequences. In order to understand the relevance of these MP and NP from paint dispersion we investigated the components of two representative wall paints and analyzed their composition in detail. The different paint components were then investigated for their impact on the model organism *Daphnia magna* and on a murine cell line. Plastic NP, dissolved polymers, titanium dioxide NPs, and calcium carbonate MPs demonstrated adverse effects in both biological test systems, indicating detrimental consequences of several typical components of wall paints upon release into the environment. The outcome of this study may form the basis for the evaluation of impact on other organisms, environmental transport and impact, other related technical materials and for the development of strategies for the prevention of potential detrimental effects on organisms.

1. Introduction

The presence of MP in the environment has raised concerns in the past decades (Law and Thompson, 2014). The high plastic utilization worldwide accompanied by low collection and recycling rates lead to its uncontrolled disposal into the environment, where plastics remain and accumulate as a persistent anthropogenic pollutant (Ribeiro et al., 2019). Most plastics are resistant to biodegradation, but under UV-irradiation (Meides et al., 2021), in hydrolytic surrounding (Arhant et al., 2019), and when subjected to mechanical abrasion (Chubarenko et al., 2020), these plastics become brittle and disintegrate into smaller pieces until they become MP (by definition: size range of 1 μm up to 5 mm (Frias and Nash, 2019)). Moreover, this process continues to the formation of NP, which are defined as particles with sizes below 1000 nm (Gigault et al., 2018) and could display properties that differ from those of the original material and MP (Mitrano et al., 2021). In addition, MP and NP can enter the environment via abrasion of various synthetic products (Yang et al., 2021) and via the release of so-called primary MP and NP (van Wezel et al., 2016). Primary NP are manufactured for certain functions, such as exfoliant in personal care products (Prata, 2018) or as components in water-based dispersion paints. While the use of primary NP in cosmetics is decreasing, water-based dispersion paints are used in volumes of approximately 17 million tons per year for architectural coatings (Anon, 2020). Secondary MP stemming from abrasion of paint have been shown to constitute a significant fraction of the MP polluting the oceans (van Wezel et al., 2016). They can presumably arise from the abrasion of ship hulls, road markings, and external surfaces of buildings (Gaylarde et al., 2021). Water-based dispersion paints contain for practical reasons a complex mixture of inorganic and polymer nano- or micro-sized particles, or dissolved polymers. The practical reasons could be appropriate paint viscosity, colloidal stability, and handling (e.g. "no drip") (Dubbert et al., 2014). For instance, titanium dioxide (TiO_2) nanoparticles are incorporated in many white paints and have been shown to be released from painted facades at concentrations of 168 ± 121 μg/m^2 during seven weeks in the winter time (Azimzada et al., 2020). Once released, their high surface to

* Corresponding authors.
E-mail addresses: christian.laforsch@uni-bayreuth.de (C. Laforsch), ruth.freitag@uni-bayreuth.de (R. Freitag), greiner@uni-bayreuth.de (A. Greiner).

https://doi.org/10.1016/j.ecoenv.2022.113877
Received 27 April 2022; Received in revised form 6 July 2022; Accepted 9 July 2022
Available online 16 July 2022

volume ratio and adhering natural organic matter determine their properties, fate, and biological impact (Wu et al., 2021).

For TiO_2 nanoparticles adverse effects have been demonstrated with a variety of model organisms. For instance, the crustacean waterflea *D. magna* is affected when taking up TiO_2 nanoparticles (Kim et al., 2010). These effects could presumably be amplified via synergistic effects with other toxic compounds, for example the facilitated, simultaneous uptake with cadmium and zinc ions (Tan and Wang, 2014), or benzophenone and paraben (La Soler de Vega et al., 2019).

The potential impact of NP, has been investigated in recent years as well. The main uptake route of NP for various organisms is via ingestion or adsorption on their surfaces (Zhang et al., 2020), resulting in the threat of bioaccumulation and biomagnification in food webs (Wang et al., 2019). NP induce the activation of a cellular response in different biological systems, from mammalian cells, bacteria (Fringer et al., 2020), plants (Sun et al., 2020), animals (Gu et al., 2020), up to human beings (Rubio et al., 2020). Further adverse effects of NP in vivo include: inflammation, production of reactive oxygen species, or cytotoxicity (Hu and Palić, 2020). Recent publications demonstrated that survival, reproduction, and embryo development of *D. magna* is significantly affected by exposure to polystyrene NP (Cui et al., 2017). Moreover, toxic concentration determined for *D. magna* in acute toxicity tests with positively or negatively charged polystyrene nanoparticles (53 nm) can easily be two orders of magnitude lower in life-time exposure tests (Kelpsiene et al., 2020).

Adverse effects of compounds included in dispersion paints may also result from dissolved polymers. Currently, dissolved polymers are excluded from evaluation within REACH (Registration, Evaluation, Authorization of Chemicals), since they are considered as non-toxic due to their chain length (Duis et al., 2021). Environmental concentrations, e.g. 0.57 mg/L measured for polyacrylic acids in effluents, typically do not reach concentrations observed in acute toxicity tests with *D. magna* (lowest reported value EC_{50} = 40 mg/L). However, in chronic exposure tests relevant concentrations are often significantly lower (e.g. EC_{50} = 12 mg/L) (DeLeo et al., 2020).

In this study, we focus on the analysis of paint composition and biological properties considering paint as a potential source for the release of polymers and particles into the environment. Paints contain different materials, such as nanoparticles of inorganic or polymeric origin, metal oxide microparticles and dissolved polymers, with potentially high impact on biological systems, which have so far been overlooked. Most studies investigating the toxicity of these new material classes focus on single, lab prepared materials which might not represent the effects of a product produced as a material mixture and used worldwide. We studied the response to the paint fractions at the cellular level using murine fibroblasts (L929 cells) as well as in an organism (*D. magna*), commonly used as an indicator to assess environmental toxicity. Both organisms were exposed to different concentrations of the paint fractions and the *D. magna* immobility as well as the cells' metabolic activity were defined as essential indicators to determine the paint fractions impact.

2. Experimental section

2.1. Materials

Various paints are available for different purposes, for example indoor/ outdoor paint, paint for wood/metal/plastic with surfaces being rough/smooth, or wall/ceiling paint. We decided to focus on standard wall and ceiling paints since these are already known for their propensity to release nanoparticles into the environment (Azimzada et al., 2020). The wall paint will be termed as paint 1 and the ceiling paint as paint 2.

Sodium hydroxide (Merck, > 98 %) was used without further purification. Nitric acid (65 %) (B. Kraft, analysis) was used as received. Postnova GmbH supplied the special tenside novachem for asymmetric flow-field flow fractionation (AF-FFF) measurements.

If not otherwise indicated, cell culture materials were obtained from Greiner Bio-One GmbH (Frickenhausen, Germany) and Thermo Fisher Scientific (Schwerte, Germany). L-glutamine, penicillin, streptomycin, 1 x trypsin/EDTA, Dulbecco's Phosphate-Buffered Saline without Ca^{2+} and Mg^{2+} (DPBS), Dulbecco's Modified Eagle's Medium (DMEM) was obtained from Lonza (Lonza Group Ltd, Basel, Switzerland). Minimum Essential Medium (MEM) without phenol red was from Thermo Fisher Scientific (Schwerte, Germany). Foetal calf serum (FCS), and 3-(4,5-dimethyl-2-thiazolyl)− 2,5-Diphenyl-2 H-tetrazolium bromide (MTT) were obtained from Sigma Aldrich (Taufkirchen, Germany).

2.2. Measurements and procedures

2.2.1. Physical characteristics

2.2.1.1. Dynamic light scattering (DLS). A system from ALV-5000EPP Laservertriebsgesellschaft mbH, with a photon-counting module from Perkin Elmer (SPCM-CD 3017) was used. DLS measurements were done at a wavelength of 632 nm, with a detector angle of 90°, and a temperature of 294 K. Samples were all prepared in Milli-Q water with a viscosity of 0.9711 cp. The data were analyzed with WINDOWS-95/98/NT-4.0 control and data reduction software.

2.2.1.2. Zeta sizer measurement. Paint samples were prepared in Milli-Q water with a concentration of 0.057–0.068 mg/mL or 0.22–0.9 mg/mL for paint supernatant and were measured by a zeta sizer of Malvern. The Malvern software automatically set an optimum measurement position and voltage. The measuring temperature was 20 °C. The zeta potential of the paint dispersions in dilution was measured dependent on the pH-value, which was adjusted by utilizing nitric acid or sodium hydroxide solutions. Zeta potentials were measured for diluted paint dispersions at different salt concentrations, which were adjusted with sodium chlorid in Milli-Q water (pH 5).

2.2.1.3. Scanning electron microscopy (SEM). Samples were prepared on a coal film. Membranes were sputtered with 1.3 nm platinum by the Cressington platinum-sputter coater 208HR or coated with a coal film by the Leica EM ACE 600. Leo 1530 from Zeiss was used for measurements at an acceleration voltage of 3 kV and a pressure of 2.0×10^{-5} bar for pictures with inlense and secondary electron (Everhart Thornley) detector. The backscattering detector from Centaurus (10 mm working distance) was used at 10 kV acceleration voltage and the Ultradry-EDX-detector from Thermo Fisher Scientific NS7 (8 mm working distance) at an acceleration voltage of 20 kV under the usual pressure.

2.2.1.4. Asymmetric flow-field flow fractionation (AF-FFF). AF-FFF was performed on an AF2000 system from Postnova Analytics (Landsberg am Lech, Germany). The channel (295 ×30 mm) was equipped with a NovaRC 10 kDa membrane and with a 350 μm spacer. Novachem (0.2 wt %) in Milli-Q water (pH 5) was used as eluent. Analysis was done with a UV detector and multiple angle light scattering (MALS) detector (532 nm). Postnova AF2000 Control software was applied for size evaluation.

The UV detector signal for measurements without separation was used for concentration determination, and the recovery rate was calculated for measurements with separation. The wavelength was set to 250 nm for detection. The measurement error was determined to be ± 17 %. The particle size was analyzed in separation experiments. (Table 1).

Sample were measured with and without separation, according to the following methods:

2.2.1.5. Thermogravimetric analysis (TGA). TGA measurements were done with the model TG 209 F1 Libra from Netsch. Samples were prepared with 10 mg sample weight in aluminium oxide crucibles. The

Table 1
AF-FFF method for measuring paint 1 supernatant (P 1) and paint 2 supernatant (P 2).

Step	Parameter[a]		With separation		Without separation
Substance			P 1	P 2	both
	Injection volume [µL]		20	20	20
	Detector flow [mL/min]		0.5	0.5	0.5
Focusing	Injection flow [mL/min]		0.2	0.2	0.2
	Injection time [min]		5	3	1
	Crossflow		0.7	0.6	0.1
	Transition time		0.5	0.5	0.5
Elution	Step 1	Elution time [min]	1	1	10
		From [mL/min]	0.7	0.6	0.1
		To [mL/min]	0.7	0.6	0.1
		Type	Const.	Const.	Const.
	Step 2	Elution time [min]	80	20	None
		From [mL/min]	0.7	0.6	
		To [mL/min]	0	0	
		Type	0.7 power	0.2 power	
Rinsing			1	5	5

[a] Paint 1 samples were measured in Milli-Q water with 0.2 wt % Novachem.

samples were heated up to 800 °C with a rate of 10 K/min under nitrogen atmosphere. Measurement resolution is 0.1 µg.

2.2.1.6. Rheometeric measurements. For rheology measurements the paint dispersions were used as bought. Rheology measurements were done with a rheometer from Anton Paar (model no. MCR302, 2017) and were performed with a cone plate (D=25 mm, 60 mm). Measurement temperature is controlled by a Peltier plate (P-PTD200) and was set to 25 °C. Paint dispersions were measured in a rotational mode with normal forces in between 0.01 and 50 N. Shear rate was increased from 0.1 up to 100 s^{-1} and 16 data points were measured for shear stress at different time intervals. Viscosity was automatically calculated and a regression fit was done according to Carreau-Yasuda.

2.2.1.7. Centrifugation. For sample centrifugation a Heraeus Megafuge 16 R (Serial No. 41535480) from Thermo Scientific was used. Samples were centrifuged in 40 mL tubes at a rotation speed of maximum 10000 rounds/min.

2.2.2. Chemical characteristics

2.2.2.1. Raman microscopy. Dry samples were prepared on a glass slide. Raman spectra were recorded with a combined Raman-Imaging/Scanning Force Microscope System (Model Alpha 300 RA+) from WITEC. Two laser sources can be used: UHTS 300 spectrometer, back-illuminated Andor Newton 970 EMCCD camera (532 nm wavelength) or UHTS 400 spectrometer, back-illuminated deep depletion Andor iDUS CCD camera (785 nm wavelength) with a maximum power of 50 mW. Spectra range was set to 0–3600 cm^{-1} with collecting data points in an interval of 3 cm^{-1}. Spectra were analyzed with the software WITEC Project five 5.1 and were corrected from cosmic noise.

2.2.2.2. Paint separation procedure. Paint 1 was dispersed in Milli-Q water (2 g/400 mL) and stored for four weeks. The supernatant was centrifuged at 10000 x *g* for 20 min. The sediment was removed. This procedure was repeated three times. The solid from the 200 mL batch was redispersed in Milli-Q water und centrifuged at 2000 x *g* for 10 min. The sediment was washed with water and centrifuged again. The washing step was repeated three times. Both fractions were stored in aqueous media.

Paint 2 was dispersed in Milli-Q water (8 g/40 mL) and was centrifuged at 2000 x *g*. The supernatant was removed and the sediment was washed with Milli-Q water and centrifuged again two times. The supernatant from the first centrifugation step was again centrifuged at 10000 x *g* for 30 min. The sediment was discarded. This procedure was repeated three times to receive the purified paint 2 supernatant.

All four samples were used for biology tests.

2.2.3. Biological effects

2.2.3.1. D. magna cultivation. The used *D. magna* clone BL2.2 originates from a small pond (Oud Meren) in Leuven, Belgium is in culture since 1997 and has been used in several studies with microplastic in our laboratory. Animals were cultured in M4 medium at 20 ± 0.5 °C and a 16 h: 8 h light:dark regime and fed ad libitum with the green algae *Acutodesmus obliquus*. As recommended in the OECD guideline 202, tests with a reference substance are performed at least twice a year (last test: NaCl (EC_{50} (48 h) = 4.925 µg/mL; comparable to clones used in other studies.

2.2.3.2. Experimental procedure – D. magna. 24 h before the experiment, neonates were separated from the mother cultures, then 24 h later, all newborn neonates were collected with glass pipettes. Those age-synchronized (born within 24 h) animals were randomly placed in groups of five, each in 10 mL M4 in one well of a six-well plate. A total of 420 animals were exposed to five concentrations of the four substances with four replicates each: 31.25 mg/L, 62.5 mg/L, 125 mg/L, 250 mg/L, 500 mg/L, plus the controls (0 mg/L). Stock solutions (500 mg/L) of the respective substances in M4 media were prepared beforehand, shaken for 48 h, and then diluted in M4 via dilution series to achieve the respective concentrations. According to the OECD Guideline 202, no food was added, and no medium exchange was done during the exposure. The test was prolonged to 96 h following the recommendation of Baumann et al. (2014). After 24, 48, and 96 h, animals were visually checked for immobilization.

2.2.3.3. Image acquisition. After 96 h of exposure, images of the exposed organisms were taken using a digital microscope (Leica Microsystems, Model: DVM6 M, Heerbrugg, Switzerland). The animals were individually placed on a concavity microscope slide, and the excess water was removed with a Pasteur glass pipette before the image was acquired. After calibration using a stage micrometer (Pyser Optics Limited, Edenbridge, Kent), all images were acquired using LASX (Leica Application Suite X).

2.2.3.4. Statistical analysis – D. magna. Data analysis was conducted in R (R Core Team, 2018), half-maximal effective concentrations (EC_{50}) were calculated utilizing the package morse ("Modelling tools for Reproduction and Survival data in Ecotoxicology") which utilizes one type of Toxicokinetic/Toxicodynamic (TKTD) models, namely General Unified Treshold models of Survival (GUTS). Model evaluation was performed using the function "ppc" (posterior predictive check plot) implemented in the package morse.

2.2.3.5. Cell cultivation. L929 cell line (murine fibroblasts, CCL-1) was obtained from the American Type Culture Collection (ATCC, Manassas, USA). Cells were cultivated in complete growth medium containing DMEM, supplemented with 2 mM glutamine, 10 % (v/v) FCS and 100 U/mL penicillin/streptomycin in a standard cell culture incubator (5 % CO_2/95 % humidity) at 37 °C. Cells were passaged three times a week with a starting concentration of about 100000 cells/mL. For detaching the cells, 1 x Trypsin/EDTA was used.

2.2.3.6. MTT assay procedure. A MTT assay was used to measure the metabolic activity of the cells. This assay is based on the ability of the

cells to convert tetrazolium salt (4,5-dimethyl-2-thiazolyl)− 2,5-diphenyl-2 H-tetrazolium bromide) to formazan crystals which is directly dependent to their metabolic activity and in consequence to their viability. The experiment was performed according to the ISO 10993–5. Briefly, 10000 cells/well were seeded in 96-well-plates (100 μL medium per well). After 24 h incubation time, the supernatant was aspirated and a freshly prepared test solution (100 μL per well) was added. The test solution was prepared by a dilution series from the stock solution of paint 1 (supernatant and solid) and paint 2 (supernatant and solid) diluted with complete growth medium. Highest tested concentration was respective to 10 v/v % of paint solutions. After another 24 h of incubation, the supernatant was aspirated and 50 μL of MTT (1 mg/mL) reagent dissolved in MEM without phenol red were added. This solution was discarded after 2 h of incubation and 100 μL of isopropanol were added to each well to dissolved the formed formazan crystals. The plate was shaken for 5 min at 600 rpm for homogenization. Absorbance was measured at 570 nm (reference wavelength 650 nm) with a TECAN GENios Pro plate reader (Tecan Austria GmbH, Gröding) and metabolic activity was calculated according to Eq. 1. Cells incubated solely in growth medium were used as negative control (metabolic activity: 100 %), growth medium containing 0.3 v/v % Triton X-100 was used as positive control.

$$metabolic \quad activity \quad [\%] = \frac{Abs570_{sample}}{Abs570_{blank}} x \quad 100 \tag{1}$$

where: $Abs_{570\text{-sample}}$ is the mean value of the measured absorption of the test sample; $Abs_{570\text{-blank}}$ is the mean value of the measured absorption of the negative control.

3. Results

3.1. Paint composition

We aimed to choose two wall paints, being as representative as possible for commercial paints for household applications. Thus, we chose two paints which differ in terms of their application. The paint 1 is sold for painting walls and the paint 2 is sold for painting ceilings promoted for low tendency of dripping. In general, paints with low tendency of dripping must contain a rheological modifier and can be expected to be chemically different and potentially possess different toxicity. Furthermore, we also wanted to select two paints containing those materials being most often comprised in paints, such as silicon dioxide, titanium dioxide, calcium carbonate and/or polyacrylates. By selecting paints, which represent the composition of the majority of paints, we secured the greatest significance of investigating their potential toxicity on biological systems.

In order to gain a comprehensive understanding of the mechanisms of interaction between paints and biological systems, we have examined the compositions of paint 1 and 2. The solid content was examined by freeze-drying and the organic content by thermogravimetric analysis (TGA). The solid content of paint 1 is 49 wt % comprising an organic portion of 21 wt % (Fig. S1A). The paint 2 contains 57 wt % solid materials with a portion of 7 wt % organic materials (Fig. S1B). Scanning electron microscopy (SEM)- energy dispersive x-ray analysis (EDX) further revealed, that the paints are a composition of different materials (Fig. S2- S3).

Since more than one component is included in the paint dispersions, the dispersions were separated by centrifugation producing two fractions for each paint (Fig. 1). The paint fractions were termed as supernatant and solid and were received all as turbid dispersions. According to SEM-EDX measurements, the paint 1 supernatant consists of carbon and oxygen atoms (Table S1), which can be attributed to polyacrylate with hydroxyl functionalities due to peaks of esters at 1728 cm^{-1} and hydroxyl groups at 3311 cm^{-1} in the corresponding IR-spectra (Fig. 2A). Particle sizes observed in the supernatant of paint 1 are in the size range of roughly 242 ± 59 nm (Fig. 1A). The paint 1 solid is a mixture of TiO_2 and silicon dioxide (6.8 ± 1.1 μm) according to the SEM-EDX and Raman measurements (Table S1, Fig. 2C). TiO_2 appears in the nanoparticle size range up to 100 nm (Fig. 1B). SEM-EDX measurements of the paint 2 supernatant identified carbon, oxygen, and sodium as main components (Table S1). Peaks from IR spectra further proved ester (1732 cm^{-1}) and alcohol (3438 cm^{-1}) functionalities (Fig. 2B). Sodium might indicate deprotonated acid functionalities. The copolymer does not occur in particulate shape, and thus, is described as dissolved polymer (Fig. 1C). The paint 2 solid consists of calcium carbonate ($CaCO_3$) as particulate matter from 150 nm up to 10 μm (Fig. 1D) which

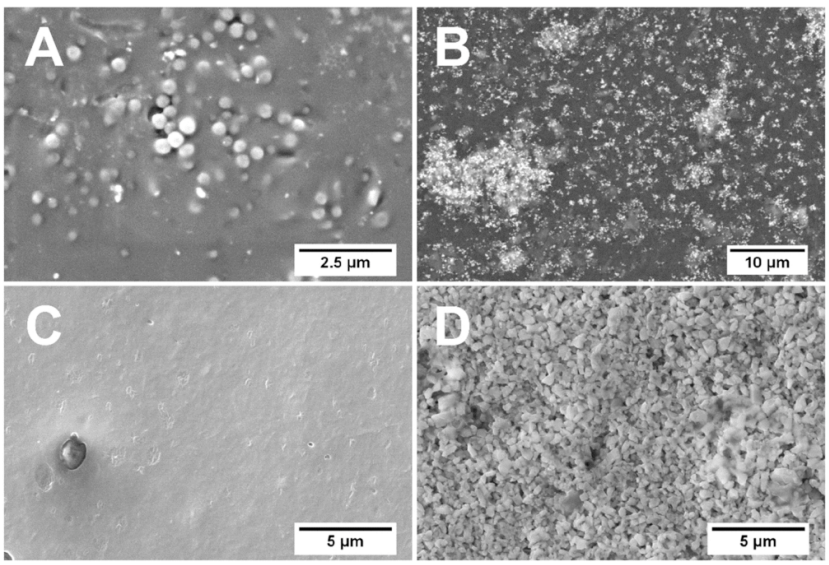

Fig. 1. SEM images of paint fractions at the position of EDX measurement. Samples were prepared by centrifugation procedure. Figures show SEM images of A) paint 1 supernatant, B) paint 1 solid, C) paint 2 supernatant, and D) paint 2 solid.

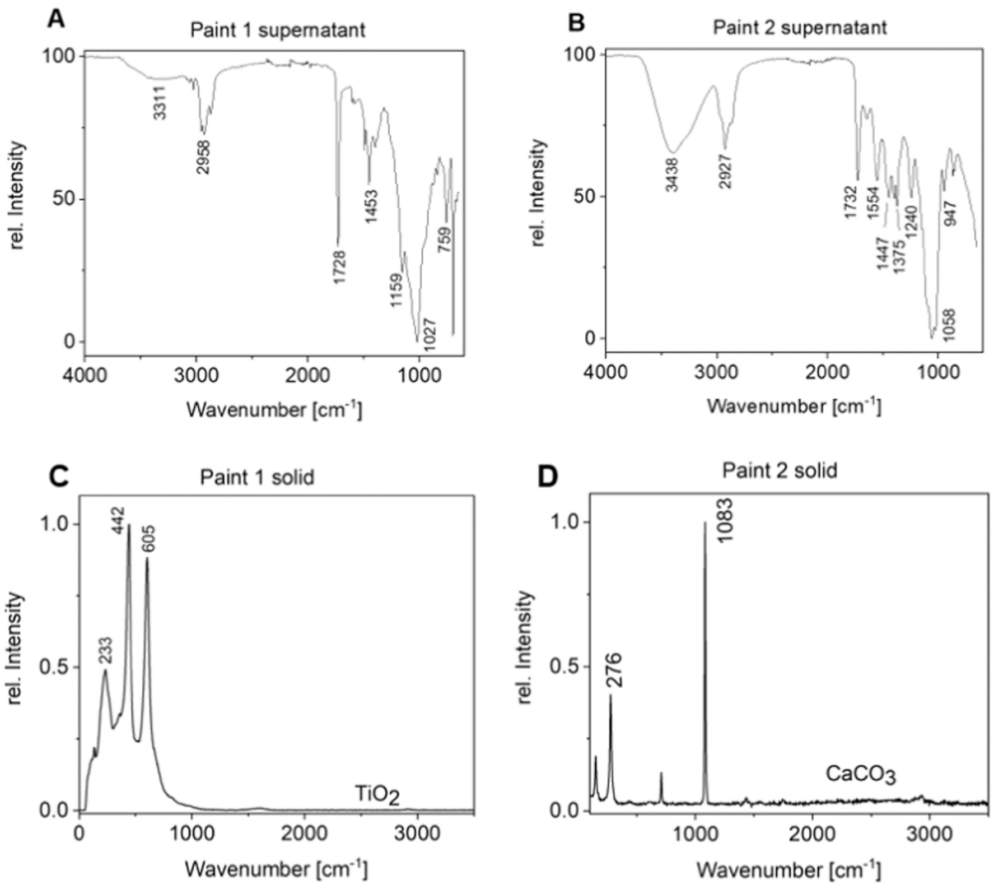

Fig. 2. IR spectra of paint 1 supernatant (A) and paint 2 supernatant (B), as well as Raman spectra of paint 1 solid (C) and paint 2 solid (D). All fractions measured were received by centrifugation.

was proven by SEM-EDX and Raman measurements (Table S1, Fig. 2D).

3.2. Particle properties and stability

The zeta potential is causative for the colloidal stability and interaction with biological systems. Particles with zeta potentials exceeding ± 10 mV are generally assumed to be stabilized by charge repulsion effects. The zeta potential depends on the pH value and the salt concentration of the surrounding matrix. In this experiment the impact of environmental relevant pH values (3–9) and salt concentrations (salt conc.: ≥20 mM tap water up to 600 mM for ocean water) on the paint colloidal stability were studied. Here, the dispersion paint was used as received in dilution with water and was not fractionated by centrifugation.

Particles from paint 1 show a negative zeta potential for all investigated pH values. At a pH of 3 the zeta potential is − 5 mV resulting in colloidal instability (Fig. 3A). Instability is also reached with increasing salt concentration, which is here represented by sodium chloride (NaCl) (Fig. 3B).

Besides, chemically triggered aggregation, deposition could also occur over time due to microparticle sedimentation. The microparticle sedimentation is proven by a reduction in the average hydrodynamic radius of the suspended particles in the paint dispersions. For example, the mean particle size decreased from 400 nm to 200 nm within five days because microparticles sedimented independently of the dispersion's pH value (Fig. 3C). In consequence, the resulting supernatant shows a strong decline in particle size and also particle size distribution (Fig. 3D). Only nanoplastic particles (average radius 98 nm according to DLS measurement) were stable enough to persist in the supernatant. These possess a zeta potential close to zero at a pH of 4 (Fig. 3A). The nanoplastic hydrodynamic radius of 97 nm was further corroborated by asymmetric flow-field flow fractionation (AF-FFF) measurements (Fig. S4A, B).

Comparable properties were observed for paint 2. The particles in this paint are stabilized by negative surface charges (Fig. S5A). The zeta potentials for paint 2 reached values of roughly − 30 mV at pH 6 in comparison to − 37 mV at pH 6 for paint 1. Paint 2 maintained its colloidal stability due to charge repulsion even at high salt concentrations (Fig. S5B), but also sedimented over time (Fig. S5C). Paint separation by sedimentation resulted in mean particle size of 680 nm for paint 2 and 200 nm for its supernatant measured by DLS (Fig. S5D, 320 nm for supernatant measured by AF-FFF (Fig. S4C, D)). The dissolved copolymer in the supernatant possesses a negative zeta potential of roughly − 50 mV at pH 6 and, thus, is also stabilized by charge repulsion (Fig. S5A).

Although both paint dispersions demonstrated in total a negative zeta potential, significant differences in their composition and function are apparent. Paint 1 contains mainly sterically stabilized nanoplastic particles, while paint 2 includes a negatively charged copolymer. Thereby, paint 2 exhibits a higher viscosity preventing drop formation

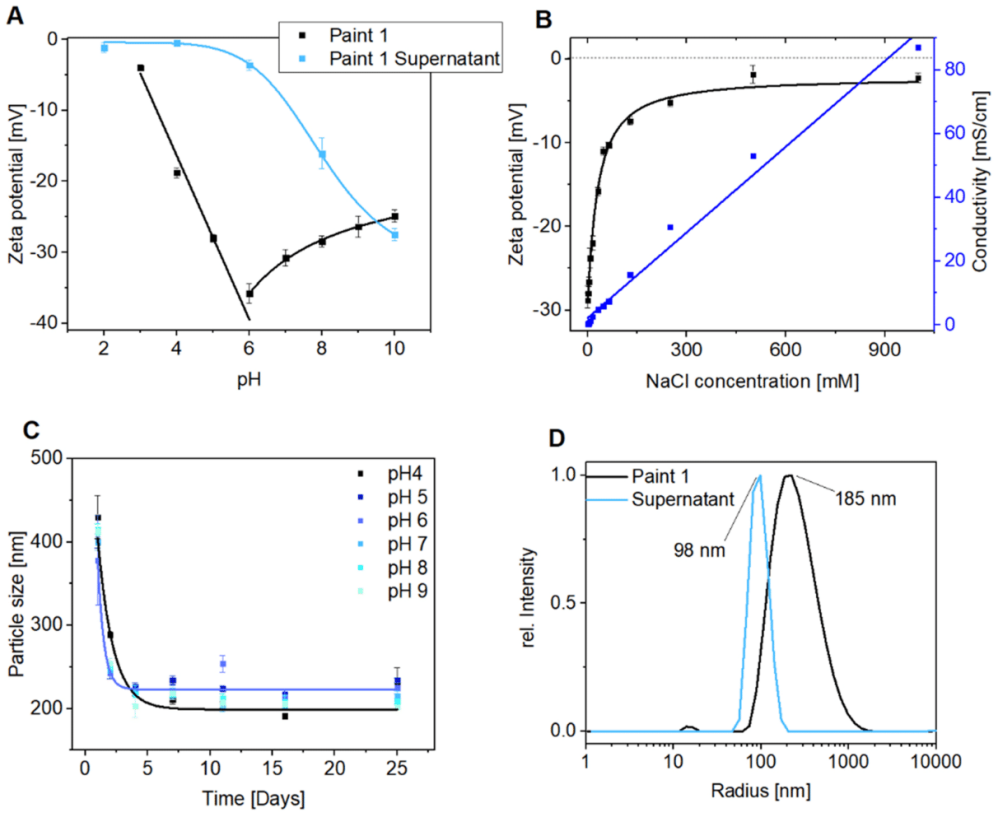

Fig. 3. Properties of paint 1. Different properties of paint 1 were investigated to estimate particle behavior, such as A) zeta potential dependent on pH with a dispersion concentration of 0.12 mg/mL in Milli-Q water, B) zeta potential and dispersion conductivity dependent on NaCl concentration with a dispersion concentration of 0.12 mg/mL in Milli-Q water, C) particle size dependent on time at different pH values measured by DLS, and D) DLS measurement for paint 1 and paint 1 supernatant resulting from a paint dispersion of 0.5 mg/mL in Milli-Q water by sedimentation. Data points represent mean value ± SD for three replicates.

by thixothrophic effects (Fig. S6).

In order to learn about the potential hazards of aqueous particle dispersions, stemming from paints, we studied two model organisms: *D. magna* and murine cells. All tests on biological systems were conducted with the paint fractions produced by centrifugation as described above.

3.3. *D. magna* experiments

In order to understand the potential impact of paint components on organisms, we investigated the impact on *D. magna*. according to the OECD guidelines for testing of chemicals (OECD Test No. 202). Here, acute toxicity is expressed as the median effective concentration (EC_{50}) which immobilizes 50 % of *D. magna* in a test batch within a continuous period of exposure (usually 48 h) (Test No. 202, 2004). We exposed *D. magna* to the supernatant and solid of both paints in Elendt M4 media (pH 8.2 ± 0.2) (Fig. 4). Calculated EC_{50} for immobilization after 24 and 48 h ranged outside the tested concentrations of up to 500 μg/mL. Nevertheless, as nanomaterials tend to show effects only after a longer exposure period, EC_{50} values were also calculated after 96 h of exposure.

The presence of supernatant of both paints in the entire gut of the daphnids indicates a higher bioavailability of the components in the supernatants than for the components in the solids, which were only found in the hindgut (Fig. 4C, D). Observed toxicity of paint 1 supernatant may be linked to the present polyacrylate nanoparticles. However, only little is known about the toxicity of polyacrylates on organisms. As polyacrylates do not contain acrylamide monomers, they are generally assumed to be non-toxic by manufacturers (Gilda Dell' Ambrogio and Wong, 2019). However, our results are in concordance with Hayes et al. who showed toxic effects for dissolved polyacrylate (LC_{50} of 175 μg/mL after 48 h) (Hayes et al., 1993). Both findings indicate that polyacrylates might be detrimental to organisms. The supernatant of paint 2, which consists of dissolved copolymer also accumulated in the entire daphnid gut (Fig. 4E) and showed the lowest EC_{50} (78.2 μg/mL) of all tested fractions. As for the polyacrylates, toxicity data for dissolved polymers is scarce. Therefore, our data provides one of the first indications of possible toxicity of dissolved polymers to aquatic organism. Due to comparable EC_{50} values (Eltemsah and Bøhn, 2019) and the accumulation in the gut, we hypothesize that the mechanisms of toxicity are similar to those of solid MP, where a combination of gut blockage (An et al., 2021) and physico-chemical properties (Schwarzer et al., 2021) might be the cause for observed effects.

The solid of paint 1 consisted of SiO_2 micro- and TiO_2 nanoparticles and revealed only slight toxicity with an EC_{50} of 481.7 μg/mL. For TiO_2 nanoparticles, Strigul et al. could not determine the LD_{50} after 48 h with concentrations up to 250 μg/mL, similar to our findings, but did not prolong the exposure time (Strigul et al., 2009). In addition, we observed the components of paint 1 solid to be adsorbed onto the carapace of *D. magna* (Fig. 4F). A variety of effects might result from this direct contact. For example, Wang et al. found an increased molting activity after TiO_2 and SiO_2 nanoparticles exposure and hypothesized that daphnids initiated molting and increased their energy metabolism to

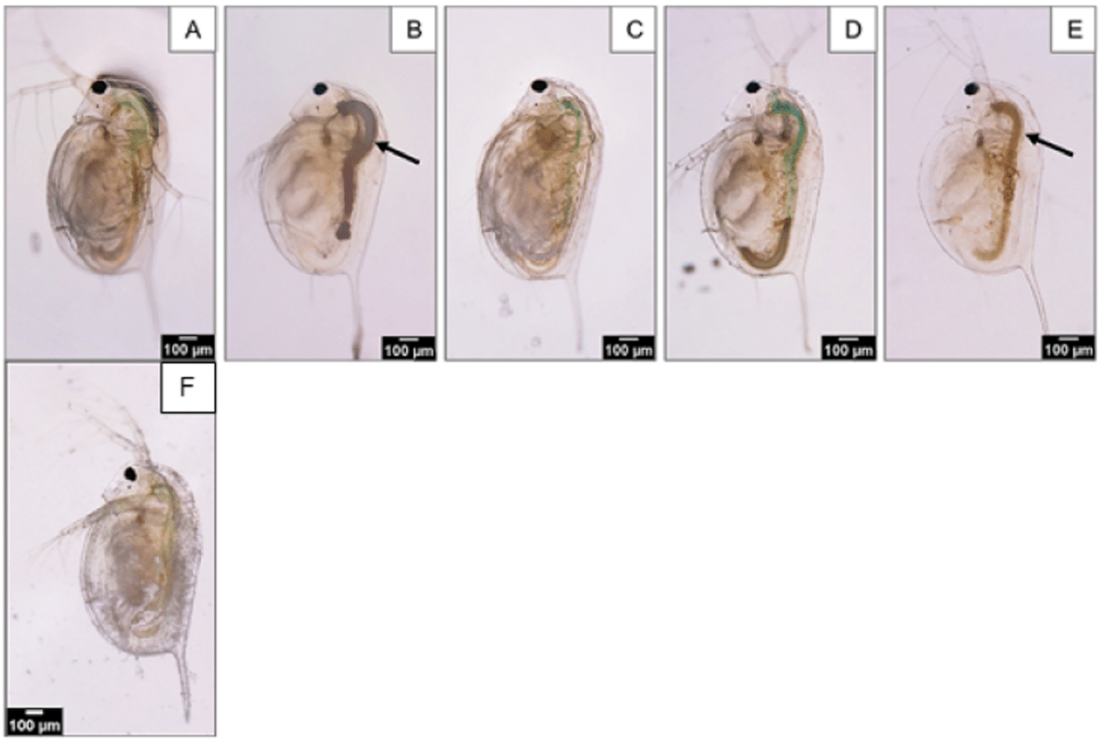

Fig. 4. Images taken of *D. magna* after 96 h of exposure without feed. Experiments were performed using neonates exposed to paint fractions without addition of food, according to OECD Guideline 202.(Test No. 202, 2004) Images show *D. magna* in the control treatment (A) and exposed to 125 µg/mL of paint 1 supernatant (B), paint 1 solid (C), paint 2 solid (D), and paint 2 supernatant (E). Paint 1 solid components adhered to the carapace of *D. magna*, after 96 h of exposure at a concentration of 250 µg/mL (F). Black arrows point to a filled gut with according particles.

remove the burden of attached particles (Wang et al., 2021). The increased energy consumption could then lead to detrimental effects in the long term. For the paint 2 solid, an EC_{50} of 162.5 µg/mL was found, even though the $CaCO_3$ microparticles as the main component exhibited the tendency to sediment over time. It is likely, that the observed toxic effect may be linked to an increased calcium ion concentration in the media resulting from partial dissolution, which has already been shown before (Bogart et al., 2016).

3.4. Cell experiments

Besides, observing potential impacts on the organismic level, we also

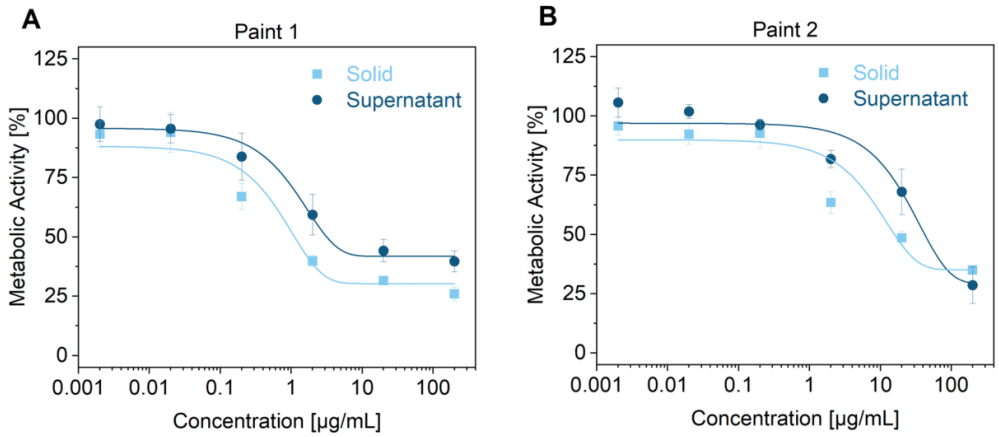

Fig. 5. Metabolic activity of L929 cell line exposed to paint fractions. Metabolic activity is determined in an MTT-test after 24 h exposure to paint 1 supernatant and solid (A), and paint 2 supernatant and solid (B). Experiments were done according to ISO 10993-5. Data points represent mean ± SD, n = 3 biological replicates; the line represents a non-linear sigmoidal fitting of the data points.

wanted to contrast the impairment at the cellular level, which was investigated by MTT assay in L929 cells (murine fibroblast). Such an assay measures the metabolic activity of cells and hence gives an indication about their vitality. For all fractions of both paints a dose-dependent reduction in cell activity was found. Significant effects were reached at paint concentrations ≥ 0.2 µg/mL for paint 1 supernatant ($LD_{50} = 3.1$ µg/mL) and paint 1 solid ($LD_{50} = 1.1$ µg/mL) (Fig. 5A) and ≥ 2 µg/mL for paint 2 solid ($LD_{50} = 15.5$ µg/mL) and ≥ 2 µg/mL for paint 2 supernatant ($LD_{50} = 42.2$ µg/mL) (Fig. 5B).

In our study, the effect of paint 1 solid and supernatant on the cell vitality are similar even though nanoplastics and TiO_2 nanoparticles, which are the major components in these fractions, are made of different materials with different sizes and properties. Thus, no correlation between particle characteristics and environmental impact can be drawn. The paint 2 components demonstrated much higher LD_{50} values, and thus, must have less interfered with the cells. We ascribe these results to the distinctly negative zeta potential of the dissolved polyacrylate, and the microsize and material of the $CaCO_3$ particles.

For tests with a different kind or organisms cells were exposed to paint fractions received from centrifugation instead of pure compounds, which needs to be considered when comparing our results with literature. So far, no distinct correlation between polymer nanoparticle size and uptake was proven (Varela et al., 2012) but a major impact on the uptake of polymeric nanoparticles possess the particles' zeta potential and the cell type (He et al., 2010). For the here tested L929 cells we detected an LD_{50} of 1.1 µg/mL for paint 1 supernatant primarily consisting of polyacrylate nanoparticles. Palaniappan et al. observed for L929 cells increased oxidative stress under exposure to polystyrene and polyethylene microplastics, which demonstrated at even the lowest test concentration of 1 µg/mL a significant impact on the metabolic activity (Palaniappan et al., 2021). Also negatively charged 60 nm amino-modified polystyrene nanoparticles led to a significant decrease in macrophage cell viability at concentrations above 10 µg/mL (Xia et al., 2008). Similarly to the paint 1 supernatant composed of polyacrylate nanoparticles, also the paint 1 solid, mainly consisting of TiO_2 nanoparticles besides some SiO_2 microparticles, caused reduced metabolic activity with an LD_{50} value of 1.1 µg/mL. An impairment in the same magnitude has already been reported for TiO_2 particles in the anatase form at diameters below 20 nm, which was found to decrease the viability in mouse fibroblast (L929 cells) in a dose-dependent manner and have significant effects starting at a concentration of 6 µg/mL (Jin et al., 2008). These negative effects of TiO_2 nanoparticles might result from an impact on the carbohydrate metabolism, which had previously been shown proven for L929 cells for TiO_2 nanoparticles (5 nm size, anatase form) at concentrations above 50 µg/mL (Jin et al., 2013). In contrast to the impact of the before mentioned fractions, the paint 2 solid showed moderate influence and the paint 2 supernatant demonstrated no significant effect on the cells' metabolic activity. The main component of the paint 2 solid is $CaCO_3$, which is known to possess very low cytotoxicity even in form of nanoparticles and which in consequence is often used as component in drug-delivery systems (Melgar Aguilar et al., 2021). Also the dissolved polyacrylate, being the main component of the paint 2 supernatant, did not affect the metabolic activity of the cells at low concentrations, which might be explained by the strongly negative zeta potential of the dissolved polymer. For example, Shao et al. reported a correlation between a strongly negative zeta potential of nanoplastics and a lower cytotoxicity for L929 cells (Shao et al., 2015). Finally, the L929 cell vitality in our study was more strongly affected by nanosized components with moderate zeta potentials.

4. Conclusion

In conclusion, of the eco-toxicity tests, *D. magna* was strongly affected by exposure to dissolved polymers, but we could also observe decreased cell vitality induced by NP, $CaCO_3$ MP, and TiO_2 nanoparticles. The metal oxide and plastic nanoparticles both substantially reduced the metabolic activity of L929 cells, whereas $CaCO_3$ microparticles and dissolved polymers had little impact in that case. Our findings demonstrate that daily-life products, such as dispersion paints can induce varying degrees of responses in organisms and cells, which might depend on different interaction mechanisms. Furthermore, the here reported response of *D. magna* and L929 cells on paint components, such as NP and TiO_2 nanoparticles further emphasized major concerns about considerable impairment on environmental and human health by inorganic and NP and expands current discussion to the field of water-soluble polymeric additives. Combined adverse effects of NP and inorganic nanoparticles cannot be excluded and might increase effects on organisms. Surely, the impact on other organisms needs to be investigated and compared with our findings in order to achieve a more comprehensive overview of potential detrimental impact of aqueous dispersion paints. Nevertheless, it is obvious from our studies that aqueous dispersion paint should not be disposed in carelessly. Otherwise, alternatively, strategies for the sequestration of paint components from waste-water are required.

Author's contribution

A.G., R.F., and C.L. conceived and supervised the project. A-K.M. managed project administration. A-K.M. analyzed and prepared the paint, J.B. executed viability test with *Daphnia magna*, and M.V. conducted the MTT assays. A-K.M. wrote together with A.G. and contributions of J.B., M.V. the manuscript. All authors, including V.J., R.F., and C.L., reviewed and edited the manuscript.

Declaration of Competing Interest

The authors declare that they have no known competing financial interests or personal relationships that could have appeared to influence the work reported in this paper.

Acknowledgements

We acknowledge financial support from the German Research Foundation, CRC 1357- "Mikroplastik" 391977956. We thankfully acknowledge the use of the research facilities of the University of Bayreuth, the Bavarian Polymer Institute, and for the use and help for SEM measurements in the Keylab Electron and Optical Microscopy. Further thanks go to Lothar Benker for measurement of Raman spectra, to Prof. G. Papastavrou for providing devices for zeta potential measurements and to Simona Mondellini for support of the *D. magna* experiments.

Appendix A. Supporting information

Supplementary data associated with this article can be found in the online version at doi:10.1016/j.ecoenv.2022.113877.

References

An, D., Na, J., Song, J., Jung, J., 2021. Size-dependent chronic toxicity of fragmented polyethylene microplastics to Daphnia magna. Chemosphere 271, 129591. https://doi.org/10.1016/j.chemosphere.2021.129591.

AnonZarras, P., Soucek, M., Tiwari, A. (Eds.), 2020. Handbook of waterborne coatings, 356 pp.

Arhant, M., Le Gall, M., Davies, P., 2019. Impact of hydrolytic degradation on mechanical properties of PET - Towards an understanding of microplastics formation. Polym. Degrad. Stab. 161, 175–182. https://doi.org/10.1016/j.polymdegradstab.2019.01.021.

Azimzada, A., Farner, J.M., Hadioui, M., Liu-Kang, C., Jreije, I., Tufenkji, N., Wilkinson, K.J., 2020. Release of TiO2 nanoparticles from painted surfaces in cold climates: characterization using a high sensitivity single-particle ICP-MS. Environ. Sci. Nano 7, 139–148. https://doi.org/10.1039/c9en00951e.

Baumann, J., Sakka, Y., Filser, J., 2014. Adaptation of the daphnia sp. acute toxicity test: miniaturization and prolongation for the testing of nanomaterials. Environ. Sci. Pollut. Res. Int. 21, 2201–2213. https://doi.org/10.1007/s11356-013-2094-y.

Bogart, S.J., Woodman, S., Steinkey, D., Meays, C., Pyle, G.G., 2016. Rapid changes in water hardness and alkalinity: calcite formation is lethal to Daphnia magna. Sci. Total Environ. 559, 182–191. https://doi.org/10.1016/j.scitotenv.2016.03.137.

Chubarenko, I., Efimova, I., Isachenko, I., 2020. On mechanical fragmentation of single-use plastics in the sea swash zone with different types of bottom sediments: Insights from laboratory experiments. Mar. Pollut. Bull. 150, 110726 https://doi.org/10.1016/j.marpolbul.2019.110726.

Cui, R., Kim, S.W., An, Y.-J., 2017. Polystyrene nanoplastics inhibit reproduction and induce abnormal embryonic development in the freshwater crustacean Daphnia galeata. Sci. Rep. 7, 12095. https://doi.org/10.1038/s41598-017-12299-2.

DeLeo, P.C., Summers, H., Stanton, K., Lam, M.W., 2020. Environmental risk assessment of polycarboxylate polymers used in cleaning products in the united states. Desalination 258, 127242. https://doi.org/10.1016/j.chemosphere.2020.127242.

Dubbert, W., Schwirn, K., Völker, D., Apel, P., 2014. Use of nanomaterials in coatings. ⟨https://www.umweltbundesamt.de/sites/default/files/medien/378/publikationen/use_of_nanomaterials_in_coatings_0.pdf⟩. Accessed 27.08.21.

Duis, K., Junker, T., Coors, A., 2021. Environmental fate and effects of water-soluble synthetic organic polymers used in cosmetic products. Environ. Sci. Eur. 33, 151. https://doi.org/10.1186/s12302-021-00466-2.

Eltemsah, Y.S., Bøhn, T., 2019. Acute and chronic effects of polystyrene microplastics on juvenile and adult Daphnia magna. Environ. Pollut. 254, 112919 https://doi.org/10.1016/j.envpol.2019.07.087.

Frias, J.P.G.L., Nash, R., 2019. Microplastics: finding a consensus on the definition. Mar. Pollut. Bull. 138, 145–147. https://doi.org/10.1016/j.marpolbul.2018.11.022.

Fringer, V.S., Fawcett, L.P., Maurer-Jones, M.A., 2020. Impact of nanoplastics on the viability and riboflavin secretion in the model bacteria shewanella oneidensis. Front. Environ. Sci. 8, 1–11. https://doi.org/10.3389/fenvs.2020.00097.

Gaylarde, C.C., Neto, J.A.B., da Fonseca, E.M., 2021. Paint fragments as polluting microplastics: a brief review. Mar. Pollut. Bull. 162, 111847 https://doi.org/10.1016/j.marpolbul.2020.111847.

Gigault, J., Halle, A.T., Baudrimont, M., Pascal, P.-Y., Gauffre, F., Phi, T.-L., El Hadri, H., Grassl, B., Reynaud, S., 2018. Current opinion: what is a nanoplastic? Environ. Pollut. 235, 1030–1034. https://doi.org/10.1016/j.envpol.2018.01.024.

Gilda Dell' Ambrogio, J., Wong, B., 2019. Ecotoxicological effects of polyacrylate, acrylic acid, polyacrylamide and acrylamide on soil and water organisms. ⟨https://www.oekotoxzentrum.ch/media/194999/2019_dellambrogio_polyacryl.pdf⟩. Accessed 11.01.22.

Gu, H., Wang, S., Wang, Y., 2020. Nanoplastics impair the intestinal health of the juvenile large yellow croaker Larimichthys crocea. J. Hazard. Mater. 397, 122773 https://doi.org/10.1016/j.jhazmat.2020.122773.

Hayes, K.R., Douglas, W.S., Terrell, Y., Fischer, J., Lyons, L.A., Briggs, L.J., 1993. Predictive ability of the Daphnia magna IQ toxicity test for ten diverse water treatment additives. Bull. Environ. Contam. Toxicol. 51, 909–913. https://doi.org/10.1007/BF00198289.

He, C., Hu, Y., Yin, L., Tang, C., Yin, C., 2010. Effects of particle size and surface charge on cellular uptake and biodistribution of polymeric nanoparticles. Biomaterials 31, 3657–3666. https://doi.org/10.1016/j.biomaterials.2010.01.065.

Hu, M., Palić, D., 2020. Micro- and nano-plastics activation of oxidative and inflammatory adverse outcome pathways. Redox Biol. 37, 101620 https://doi.org/10.1016/j.redox.2020.101620.

Jin, C., Liu, Y., Sun, L., Chen, T., Zhang, Y., Zhao, A., Wang, X., Cristau, M., Wang, K., Jia, W., 2013. Metabolic profiling reveals disorder of carbohydrate metabolism in mouse fibroblast cells induced by titanium dioxide nanoparticles. J. Appl. Toxicol. 33, 1442–1450. https://doi.org/10.1002/jat.2808.

Jin, C.-Y., Zhu, B.-S., Wang, X.-F., Lu, Q.-H., 2008. Cytotoxicity of titanium dioxide nanoparticles in mouse fibroblast cells. Chem. Res. Toxicol. 21, 1871–1877. https://doi.org/10.1021/tx800179f.

Kelpsiene, E., Torstensson, O., Ekvall, M.T., Hansson, L.-A., Cedervall, T., 2020. Long-term exposure to nanoplastics reduces life-time in Daphnia magna. Sci. Rep. 10, 5979. https://doi.org/10.1038/s41598-020-63028-1.

Kim, K.T., Klaine, S.J., Cho, J., Kim, S.-H., Kim, S.D., 2010. Oxidative stress responses of Daphnia magna exposed to TiO(2) nanoparticles according to size fraction. Sci. Total Environ. 408, 2268–2272. https://doi.org/10.1016/j.scitotenv.2010.01.041.

La Soler de Vega, A.C., Molins-Delgado, D., Barceló, D., Díaz-Cruz, M.S., 2019. Nanosized titanium dioxide UV filter increases mixture toxicity when combined with parabens. Ecotoxicol. Environ. Saf. 184, 109565 https://doi.org/10.1016/j.ecoenv.2019.109565.

Law, K.L., Thompson, R.C., 2014. Oceans. Microplastics in the seas. Science 345, 144–145. https://doi.org/10.1126/science.1254065.

Meides, N., Menzel, T., Poetzschner, B., Löder, M.G.J., Mansfeld, U., Strohriegl, P., Altstaedt, V., Senker, J., 2021. Reconstructing the environmental degradation of polystyrene by accelerated weathering. Environ. Sci. Technol. 55, 7930–7938. https://doi.org/10.1021/acs.est.0c07718.

Melgar Aguilar, A.E., Fagundes, A.P., Macuvele, D.L.P., Cesca, K., Porto, L., Padoin, N., Soares, C., Gracher Riella, H., 2021. Green synthesis of nano hydroxyapatite: morphology variation and its effect on cytotoxicity against fibroblast. Mater. Lett. 284, 129013 https://doi.org/10.1016/j.matlet.2020.129013.

Mitrano, D.M., Wick, P., Nowack, B., 2021. Placing nanoplastics in the context of global plastic pollution. Nat. Nanotechnol. 16, 491–500. https://doi.org/10.1038/s41565-021-00888-2.

Palaniappan, S., Sadacharan, C.M., Rostama, B., 2021. Polystyrene and polyethylene microplastics decrease cell viability and dysregulate inflammatory and oxidative stress markers of MDCK and L929 cells in vitro. Expo. Health 1–11. https://doi.org/10.1007/s12403-021-00419-3.

Prata, J.C., 2018. Microplastics in wastewater: State of the knowledge on sources, fate and solutions. Mar. Pollut. Bull. 129, 262–265. https://doi.org/10.1016/j.marpolbul.2018.02.046.

Ribeiro, F., O'Brien, J.W., Thomas, K.V., 2019. Accumulation and fate of nano- and micro-plastics and associated contaminants in organisms. TrAC Trends Anal. Chem. 111, 139–147. https://doi.org/10.1016/j.trac.2018.12.010.

Rubio, L., Marcos, R., Hernández, A., 2020. Potential adverse health effects of ingested micro- and nanoplastics on humans. Lessons learned from in vivo and in vitro mammalian models. J. Toxicol. Environ. Health 23, 51–68. https://doi.org/10.1080/10937404.2019.1700598.

Schwarzer, M., Brehm, J., Vollmer, M., Jasinski, J., Xu, C., Zainuddin, S., Fröhlich, T., Schott, M., Greiner, A., Scheibel, T., Laforsch, C., 2021. Shape, size, and polymer dependent effects of microplastics on Daphnia magna. J. Hazard. Mater. 426, 128136 https://doi.org/10.1016/j.jhazmat.2021.128136.

Shao, X.-R., Wei, X.-Q., Song, X., Hao, L.-Y., Cai, X.-X., Zhang, Z.-R., Peng, Q., Lin, Y.-F., 2015. Independent effect of polymeric nanoparticle zeta potential/surface charge, on their cytotoxicity and affinity to cells. Cell Prolif. 48, 465–474. https://doi.org/10.1111/cpr.12192.

Strigul, N., Vaccari, L., Galdun, C., Wazne, M., Liu, X., Christodoulatos, C., Jasinkiewicz, K., 2009. Acute toxicity of boron, titanium dioxide, and aluminum nanoparticles to Daphnia magna and vibrio fischeri. Desalination 248, 771–782. https://doi.org/10.1016/j.desal.2009.01.013.

Sun, X.-D., Yuan, X.-Z., Xing, B., 2020. Differentially charged nanoplastics demonstrate distinct accumulation in Arabidopsis thaliana. Nat. Nanotechnol. 15, 755–760. https://doi.org/10.1038/s41565-020-0707-4.

Tan, C., Wang, W.-X., 2014. Modification of metal bioaccumulation and toxicity in Daphnia magna by titanium dioxide nanoparticles. Environ. Pollut. 186, 36–42. https://doi.org/10.1016/j.envpol.2013.11.015.

Test No. 202: Daphnia sp. acute immobilisation test. OECD. 2004.

Varela, J.A., Bexiga, M.G., Åberg, C., Simpson, J.C., Dawson, K.A., 2012. Quantifying size-dependent interactions between fluorescently labeled polystyrene nanoparticles and mammalian cells. J. Nanobiotechnol. 10, 39. https://doi.org/10.1186/1477-3155-10-39.

Wang, W., Gao, H., Na, G., 2019. The ecotoxicological effects of microplastics on aquatic food web, from primary producer to human: a review. Ecotox. Environ. Safe 173, 110–117. https://doi.org/10.1016/j.ecoenv.2019.01.113.

Wang, W., Yang, Y., Yang, L., Luan, T., Lin, L., 2021. Effects of undissociated SiO2 and TiO2 nano-particles on molting of Daphnia pulex: comparing with dissociated ZnO nano particles. Ecotoxicol. Environ. Saf. 222, 112491 https://doi.org/10.1016/j.ecoenv.2021.112491.

van Wezel, A., Caris, I., Kools, S.A.E., 2016. Release of primary microplastics from consumer products to wastewater in the netherlands. Environ. Toxicol. Chem. 35, 1627–1631. https://doi.org/10.1002/etc.3316.

Wu, J., Jiang, R., Liu, Q., Ouyang, G., 2021. Impact of different modes of adsorption of natural organic matter on the environmental fate of nanoplastics. Chemosphere 263, 127967. https://doi.org/10.1016/j.chemosphere.2020.127967.

Xia, T., Kovochich, M., Liong, M., Zink, J.I., Nel, A.E., 2008. Cationic polystyrene nanosphere toxicity depends on cell-specific endocytic and mitochondrial injury pathways. ACS Nano 2, 85–96. https://doi.org/10.1021/nn700256c.

Yang, T., Luo, J., Nowack, B., 2021. Characterization of nanoplastics, fibrils, and microplastics released during washing and abrasion of polyester textiles. Environ. Sci. Technol. 55, 15873–15881. https://doi.org/10.1021/acs.est.1c04826.

Zhang, R., Silic, M.R., Sepúlveda, M.S., 2020. Exposure route affects the distribution and toxicity of polystyrene nanoplastics in zebrafish. Sci. Total Environ. 724, 138065 https://doi.org/10.1016/j.scitotenv.2020.138065.

Supplementary Materials for

Disentangling biological effects of primary nanoplastics from dispersion paints' additional compounds

Authors: Ann-Kathrin Müller[1], Julian Brehm[2], Matthias Völkl[3], Valérie Jérôme[3], Christian Laforsch[2]*, Ruth Freitag[3]*, Andreas Greiner[1]*

Affiliations:

[1]Macromolecular Chemistry and Bavarian Polymer Institute, University of Bayreuth, D-95440 Bayreuth, Germany.

[2] Department of Animal Ecology I and BayCEER, University of Bayreuth, D-95440 Bayreuth, Germany.

[3]Department of Process Biotechnology, Faculty of Engineering Sciences, University of Bayreuth, D-95440 Bayreuth, Germany.

Correspondence to: greiner@uni-bayreuth.de, christian.laforsch@uni-bayreuth.de, ruth.freitag@uni-bayreuth.de

This PDF file includes:

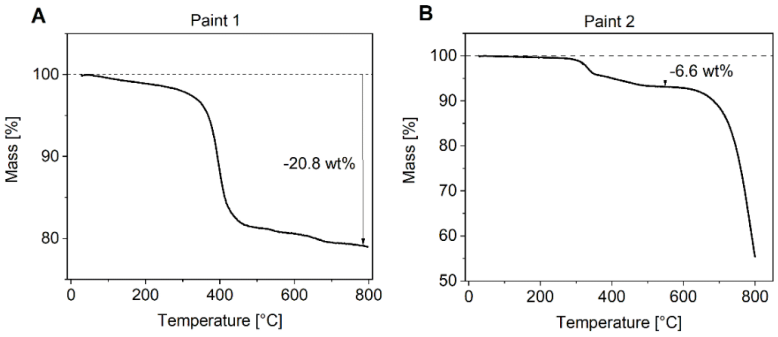

Figure S 1. Thermogravimetric analysis of freeze-dried A) paint 1 and B) paint 2.

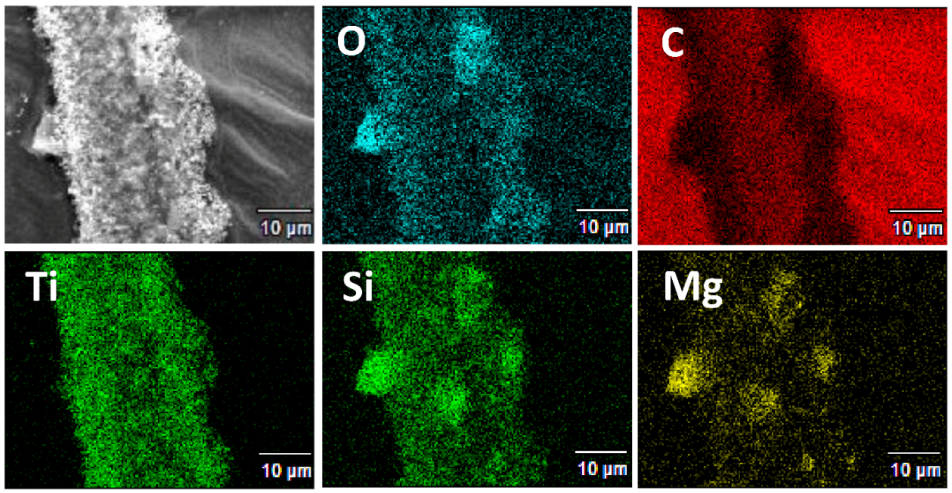

Figure S 2. Pictures of SEM-EDX measurement of paint 1. Particle composition is demonstrated by colored areas, marking the appearance of oxygen (O), carbon (C), titanium (Ti), silicon (Si), or magnesium (Mg) atoms.

Figure S3 demonstrates that paint 1 consists of different components, which vary in terms of size and material type. Titanium dioxide nanoparticles and silicium dioxide microparticles are main components of paint 1.

2

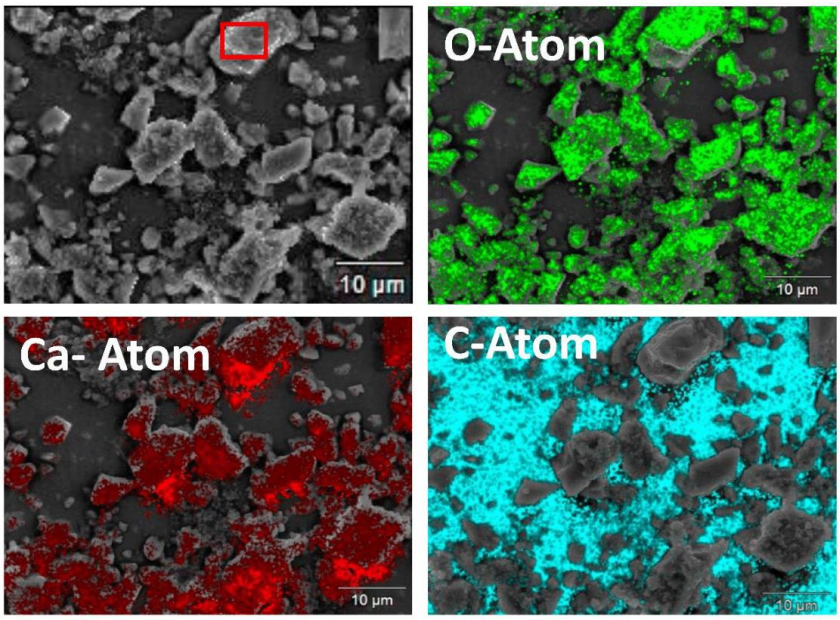

Figure S 3. Pictures of SEM-EDX measurements of paint 2. Particle composition is demonstrated by colored areas marking the appearance of the oxygen (O), calcium (Ca), or carbon (C) atom.

Figure S4 demonstrates that calcium carbonate is the main material of paint 2, which occurs in different sizes and shapes.

Table 1. Material composition derived from SEM-EDX measurement for paint 1 supernatant, paint 1 solid, paint 2 supernatant, and paint 2 solid.

Atom	Atom [%]			
	Paint 1		Paint 2	
	Supernatant	Solid	Supernatant	Solid
C	72	6	45	11
O	24	60	42	63
Na	0	0	8	0
Ca	0	0	0	24
Ti	0	17	0	0
Si	0	7	0	0

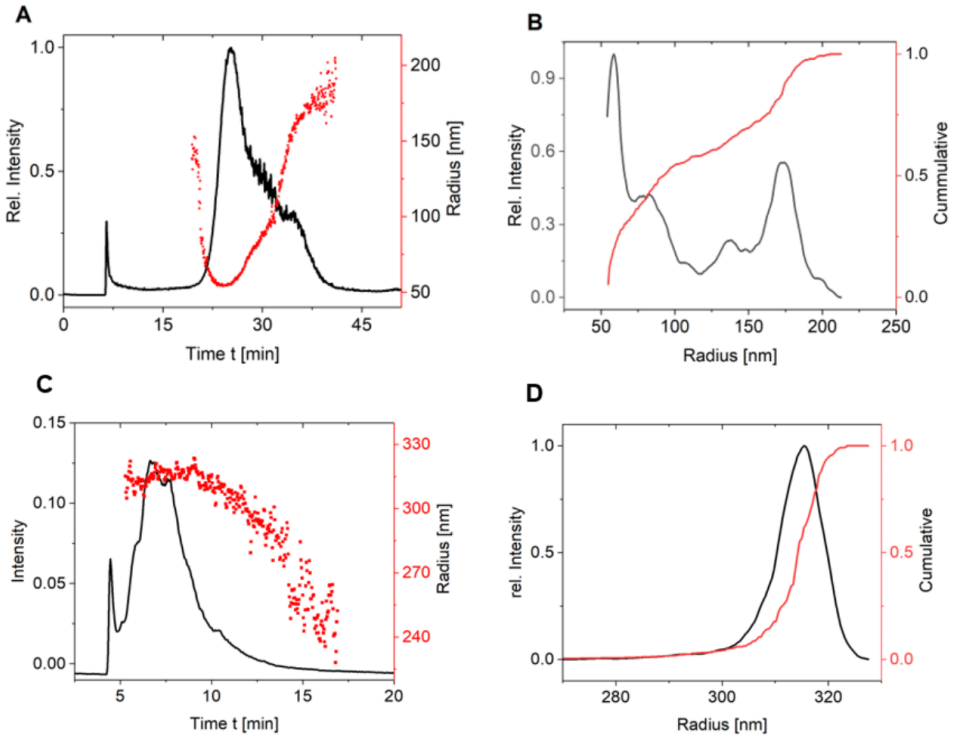

Figure S 4. AF-FFF measurement of paint 1 supernatant and paint 2 supernatant. Figures show A) flow-diagram and B) particle size distribution for paint 1 supernatant and C) flow-diagram and D) particle size distribution for paint 2 supernatant.

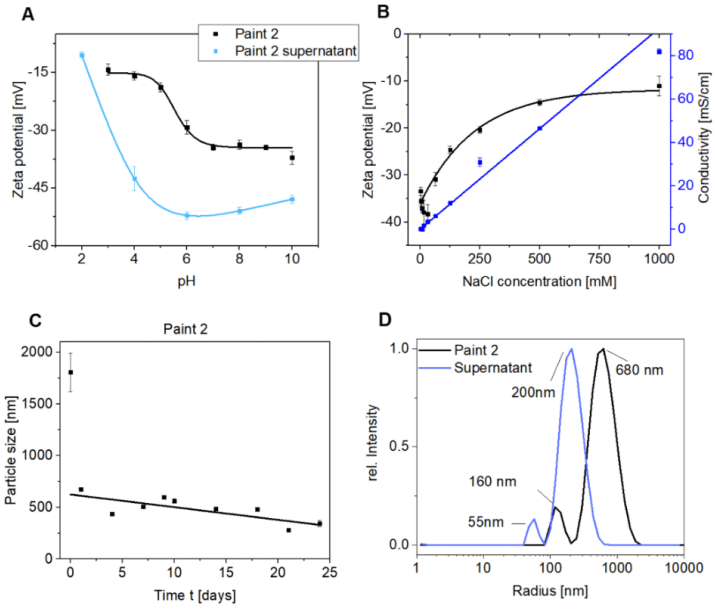

Figure S 5. Properties of paint 2. Different properties of paint 1 were investigated to estimate particle behavior and fate, such as A) zeta potential dependent on pH, B) zeta potential dependent on NaCl concentration, and C) DLS measurement for paint 2 and paint 2 supernatant.

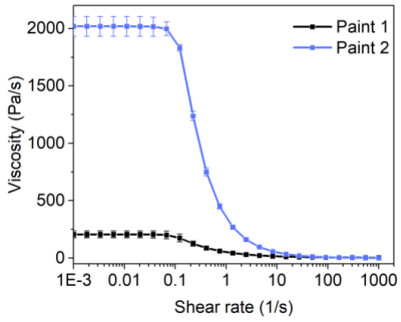

Figure S 6. Rheology measurement for paint 1 and paint 2.

3.4 Publication (4)

RESEARCH ARTICLE

Macromolecular Materials and Engineering
www.mame-journal.de

Filtration of Paint-Contaminated Water by Electrospun Membranes

*Ann-Kathrin Müller, Zhi-Kang Xu, and Andreas Greiner**

Micro- and nanosized plastics as persistent anthropogenic pollutants have attracted more and more attention in recent years. A source of nanoparticles is, for example, water-borne dispersion paint, which consists of a variety of different materials with potential adverse effects on living systems. Therefore, a rising challenge becomes apparent to investigate remediation strategies for environmental media. This problem is addressed by utilizing electrospun membranes for filtration applications because of their outstanding properties, such as their high surface-to-volume ratio and ease of functionalization. The electrospun membranes are able to successfully filter different paint components, such as titanium dioxide and polyacrylate nanoparticles, as well as dispersed polymers and calcium carbonate microparticles. Besides the known size-exclusion mechanism, the membranes featured extraordinary properties, such as effective separation of components smaller than the pore size of the electrospun membranes. This property occurs due to the fiber surface functionalization and enables not only filtration of nanosized or dissolved mater at high filtration efficiencies up to 100% but also at a very low operating pressure. This combination of filter material properties cannot be achieved by conventional nanofiltration membranes and thus, demonstrates the high potential of electrospun membranes for the application in filtration for future environmental pollutants.

1. Introduction

In recent decades, the establishment of nanomaterials led to the rapid development of the economic sector and the implementation of nanomaterials in diverse products.[1] Nanoparticles (NPs) as part of nanomaterials feature particle sizes below 1000 nm[2] and can be made of metal or polymer materials. Both metal NPs and nanoplastics are currently attracting attention due to their unique properties and their still unknown impacts on the environment and human health. The potential impacts of metal NPs and nanoplastics have been deeply investigated in recent years since the human body is exposed to metal NPs and nanoplastics via diet, arising the thread of bioaccumulation in food webs.[3] Metal NPs and nanoplastics can induce the activation of a cell-response in different biological systems[4–7] up to human beings.[8–10] Adverse effects in vivo include: inflammation, production of reactive oxygen species, or cytotoxicity.[11, 12]

Paints from buildings and road markings are a source of metal and metal oxide NPs[13] and plastic particles.[14,15] It is estimated that roughly 10–30% of titanium dioxide NPs production was used for paints and/or related products.[16] Since external surfaces of buildings and road markings are exposed to weathering, paint erosion occurs.[17,18] Weathering elements cause paint matrix degradation which is dependent on the painted materials, the nature of contact,[19] the season,[20] weathering duration, water pH, rainfall duration and intensity.[21] When the paint matrix is degraded, former embedded titanium dioxide NPs are released into the environment by effects of rain, condensed water, wind, and mechanical vibrations.[22] In 2008, it was evidenced for the first time that titanium dioxide NPs were found in the environment as a consequence of leaching from paint.[23] Quantities of titanium dioxide NPs released from facades might be in the range of 168 ± 121 µg m^{-2} during seven weeks in the winter.[20]

The paint matrix often consists of polymer particles but also secondary plastic particles result from paint degradation, which have been shown to be a significant fraction of microplastic polluting the oceans.[14,24] They might arise from the abrasion of ship hulls, road markings, and external surfaces of buildings.[25] Novel "green" chemical technologies had been developed to reduce paint fouling by implementing antimicrobial functions.

A.-K. Müller, A. Greiner
Macromolecular Chemistry and Bavarian Polymer Institute
University of Bayreuth
Universitätsstraße 30, 95440 Bayreuth, Germany
E-mail: greiner@uni-bayreuth.de
Z.-K. Xu
MOE Key Laboratory of Macromolecular Synthesis and Functionalization and Key Laboratory of Adsorption and Separation Materials & Technologies of Zhejiang Province
Department of Polymer Science and Engineering
Zhejiang University
Hangzhou 310027, China

The ORCID identification number(s) for the author(s) of this article can be found under https://doi.org/10.1002/mame.202200238

DOI: 10.1002/mame.202200238

ADVANCED SCIENCE NEWS
www.advancedsciencenews.com

Macromolecular Materials and Engineering
www.mame-journal.de

These are based on amphiphilic block copolymers exhibiting tailored surface reactivity, functionality, and reconstruction for antifouling applications.[26] An inherent drawback is the non-biodegradability deteriorating plastic problems in the environment.

Metal NPs and nanoplastics released from paints are supposed to end up in municipal wastewater treatment plants, where they had been proven in 2011 for the first time.[27] Municipal wastewater treatment plants are often based on degradation by activated sludge, which arose concerns in recent years, since many NPs are known for their toxic effects on microbes.[28] Nevertheless, different publications demonstrate that metal oxide NPs and microplastics can be removed from aqueous media with a retention of more than 82%.[27,29] Often the sludge is applied as fertilizer to soils, resulting in the discharge of NPs in the environment.[30] Wastewaters from paint industry are currently treated by a combination of different processes, such as coagulation/flocculation/membrane filtration, since these are considered as a non-expensive and efficient methods.[31] Ultrafiltration was utilized to remove the smallest particles. However, efficiency was often insufficient and very high pressures were needed.[32] Recently, the focus on highly efficient purification methods was directed to membrane techniques.[33] For example, Wang et al. demonstrated the efficient removal of polystyrene NPs from water by electrospun membranes as model system.[34] Additionally, Batool et al. described the batch adsorption of different nanoplastics by electrospun cellulose fibers coated with polyethylene imine.[35] However, model NPs might not represent the particle characteristics from commercial sources and might feature a different behavior in water treatments.

In this study, we focus on membrane filtration of paint-contaminated wastewater. Since paints are known to be a NP source polluting the environment with potential adverse effects on biota, an urgent need for purification methods becomes apparent. We address this prospective problem by utilizing electrospun membranes for filtration application. So far publications focused on the filtration of one, in lab synthesized particle or material, with specific material properties. However, this might not represent the conditions, observed in real systems. Here, often mixtures of various materials occur, which might interact with each other and thus, change their original particle properties, for example, surface charge, swelling state of polymer, particle stability, surface functional groups. We chose two different wall paints as real-life examples to get a more realistic insight into the behavior of commercial material mixtures in filtration applications. This work contributes to the understanding of filtration mechanisms of new occurring pollutant mixtures, such as metal and plastic NPs from paints.

2. Results and Discussion

2.1. Paint Composition and Potential Environmental Hazard

Two commercial walls, respectively, ceiling water-borne dispersion paints were selected as real sources of metal NPs and nanoplastics. The wall paint will be termed paint 1, in contrast to the ceiling paint, which is named as paint 2. In our previous paper, both paint mixtures have been separated into two fractions for each paint. The fractions were termed as supernatant and sludge and consist of one, pure compound. The size, shape, and composition of the components were analyzed: paint 1 supernatant (≈200 nm polyacrylate NPs), paint 1 sludge (50–150 nm titanium dioxide NPs), paint 2 supernatant (≈800 nm dispersed copolymer), paint 2 sludge (up to 10 µm calcium carbonate microparticles). Additionally, the toxicity of the compounds was tested on biological systems, such as Daphnia magna and cell cultures, demonstrating concentration dependent adverse effects on their vitality. Thus, purification of paint-contaminated surface waters is becoming an important issue.

2.2. Membrane Filtration

Electrospun membranes are a versatile module for wastewater purification and can easily be fine-tuned for specialized filtration applications, such as affinity separation.[36] Since the paint dispersions possess a negative zeta potential, they can be attracted by a positively charged affinity membrane. The positive charges on the membrane surfaces are provided by a copolymer containing 50 mol% quaternary amine groups as possible adsorption sites for particles. The copolymer was synthesized by free-radical copolymerization and was electrospun and cross-linked under UV light to obtain a membrane with high mechanical stability. The polymer synthesis, electrospinning procedure, and membrane properties have already been reported in our previous publication.[37]

The electrospun affinity membrane was tested for filtration of the two paints. The pore size of the membrane was in the range of 1.2–1.7 µm with a fiber diameter of 300–400 nm. The filtration experiments were conducted for the paint dispersion and the paint supernatant at a flow rate of 1 mL min^{-1} and different paint concentrations, such as 0.12–0.5 mg mL^{-1}. The filtration efficiency was measured in 1.5 mL intervals with UV–vis and AF-FFF. Measurement parameters for AF-FFF measurements are described in Tables S1 and S2 (Supporting Information).

2.2.1. Filtration of Paint 1

The filtration efficiency for paint dispersions reached up to 100% for all used concentrations (**Figure 1**A), in contrast to the filtration efficiency of the paint supernatant. Here, the efficiency decreased over time (Figure 1B). These phenomena could also be observed from the filtrates (Figure S1, Supporting Information).

The pressure drop was recorded during the filtration experiments revealing an exponential increase after a certain filtration time (**Figure 2**). The elapsed time until the pressure increased was dependent on the paint concentration. However, no increase in pressure was detected during the filtration of paint 1 supernatant. The former observations can be explained by the different filtration mechanisms.

The filtration mechanism for paint 1 dispersion is size-exclusion. In the size-exclusion filtration, microparticles were separated on the top of the membrane resulting in a complete pore blockage. Therefore, the paint dispersion could not pass the membrane, which led to an increasing pressure drop. A conventional method to restore the membrane performance is the back-flushing method, where a washing fluid is pressed through the membrane in the opposite flow direction.

ADVANCED SCIENCE NEWS
www.advancedsciencenews.com

Macromolecular Materials and Engineering
www.mame-journal.de

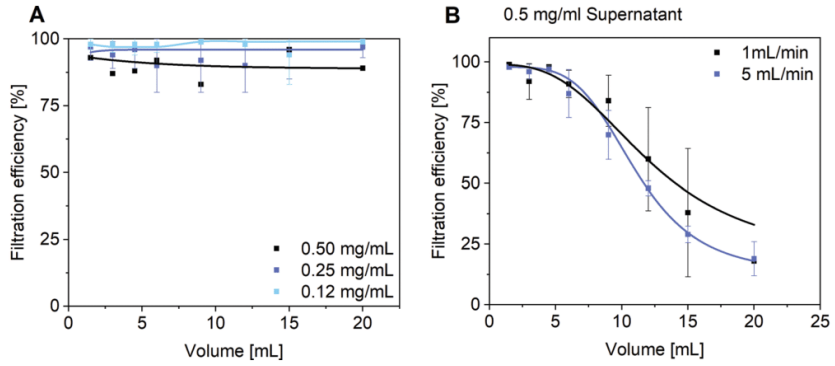

Figure 1. Filtration efficiency of paint 1 A) dependent on paint concentration and B) for paint supernatant dependent on the flow-rate. Filtration was done in triplicate with the diluted paint 1 (A) and the paint 1 supernatant received from centrifugation of paint 1 (B).

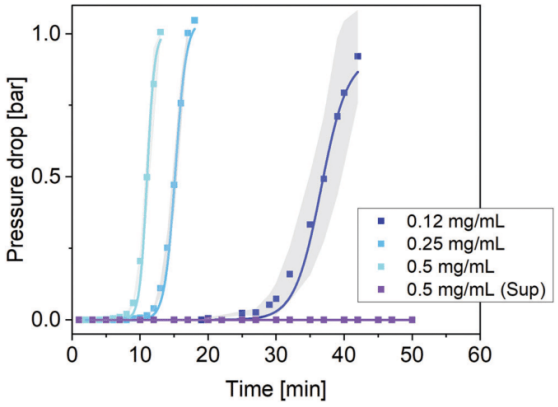

Figure 2. Pressure drop on the membrane at different paint concentrations for paint 1. Measurements were done in triplicate, the gray background marks the area of standard deviation.

The SEM images demonstrate the location of the three particle types of paint 1 on the fiber surface at low paint concentrations (**Figure 3**A). With ongoing filtration time, the amount of microparticles on the membrane surface was increased (Figure 3B) but nanosized, negatively charged titanium dioxide particles passed into the membrane bulk, where they were adsorbed on the fiber surfaces (Figure 3C).

In the second experiment, the paint 1 was separated by centrifugation (refer to Supporting Information for more details) and the supernatant was used for filtration experiments. The paint 1 supernatant did not contain nano or micro metal particles (**Figure 4**A) but only consisted of nanoplastic particles, which was proven by the SEM-BSD images. With the abundance of microparticles, no pore blockage, respectively, exponentially increasing pressure drop occurred. The nanoplastic particles passed through the membrane bulk, where they were adsorbed on the fibers (Figure 4B,C).

The second filtration mechanism, occurring at paint 1 supernatant filtration, is the affinity separation. The paint 1 supernatant consists of polyacrylate nanoparticles, which possess a negative zeta potential measured in tap water caused by their surface functional groups. These negatively charged nanoplastics can then be adsorbed by the positively charged quaternary ammonium groups on the membrane surface due to electrostatic attraction. Since electrostatic forces are stronger than most other physical interactions, all nanoparticles, which come into contact with a free adsorption site on the membrane surface, while passing through the membrane, are strongly bond to the quaternary ammonium groups located on the membrane surface. Thus, high filtration efficiencies can be reached and the strongly bond nanoplastics are prevented from leaching out of the membrane with ongoing filtration time. However, with ongoing filtration time more and more adsorption sites are blocked and thus, also more and more nanoplastic particles can pass through the membrane without the required contact to a free adsorption site. This results in a decreasing filtration efficiency of the electrospun membrane and once all adsorption sites are blocked with nanoplastic particles, the maximum capacity of the membrane is reached and from that time on no following particles can be filtered.

This affinity mechanism demonstrates extraordinary properties, such as filtering particles smaller than the pore size at high filtration efficiencies with no pressure on the membrane. Thus, the affinity mechanism of these electrospun membranes, featuring high surface areas compared to conventional membranes, opens up unique possibilities in terms of nanoparticle filtration.

2.2.2. Filtration of Paint 2

Filtration experiments were also conducted for paint 2 and its supernatant. The filtration efficiency increased with rising paint concentration up to 100% during measurement time (**Figure 5**A). A high filtration efficiency becomes evident from the picture of filtrates, too (Figure S2, Supporting Information). However, the paint 2 supernatant demonstrated a low filtration efficiency of ≈50%, which was improved up to 80% by utilizing a higher membrane weight (Figure 5B). This improvement can be explained by the fact that a higher membrane weight correlates to more available adsorption sites for contaminant filtration. A similar effect

ADVANCED SCIENCE NEWS
www.advancedsciencenews.com

Macromolecular Materials and Engineering
www.mame-journal.de

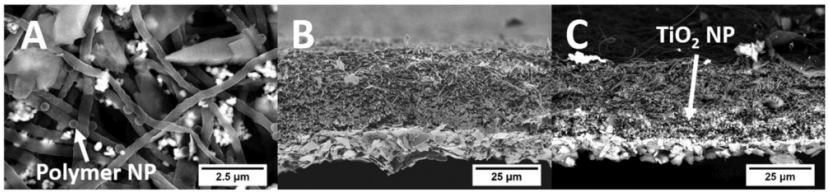

Figure 3. SEM images after filtration of paint 1. A) Top view with BSD detector, B) cross-section with SE2 detector, and C) cross-section with BSD detector.

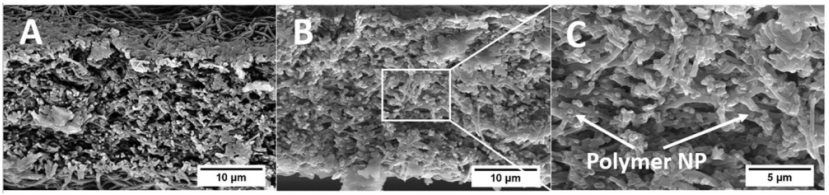

Figure 4. SEM cross-section images after filtration of paint 1 supernatant. A) Membrane with BSD detector, B) membrane with SE2 detector, and C) zoom-in of image (B).

can be achieved by reducing the used dispersion concentration of 10 mg mL^{-1} because a higher dispersion volume can then be filtered before capacity is reached. The capacity, which is defined as the ratio of adsorbed contaminant weight to the membrane weight, did not stabilized on a constant level but experiences a decline with increasing membrane weight.

The selection of the dispersion concentration was limited by the resolution of the measurement techniques, such as UV–vis. Thus, a higher concentration of paint 2 supernatant compared to paint 2 was utilized for filtration experiments. A higher or lower polymer concentration might not only change the ratio of membrane surface area to polymer concentration but also the polymer chain entanglement.

During the filtration process the increase in pressure was detected. The pressure drop increased not only for paint 2 but also for paint 2 supernatant. Filtration of paint 2 led to a pressure drop increase after a certain time (**Figure 6**A), in contrast to paint 2 supernatant, which provoked at nearly ten times higher test concentrations a rising pressure drop from the beginning onwards (Figure 6B). The continuously increasing pressure drop differentiates the filtration mechanism of paint 2 supernatant from others.

The filtration mechanism for paint 2 can be described as a size-exclusion type because microparticles block the membrane surface (**Figure 7**A). Since paint 2 supernatant did not contain particles but consisted of a dispersed copolymer, it can be supposed that it glued fibers and pores and thereby, blocked the membrane volume leading to the constantly rising pressure.

The dispersed copolymer contains acetate functional groups, which results in a strongly negative zeta potential at all pH values. Thus, we observe here again an electrostatic interaction between the dispersed polymer and the quaternary ammonium groups on the membrane surface. This enables successful filtration of the dispersed polymer but due to the high charge and high concentration affecting polymer chain entanglement of the dispersed polymer and the highly charged membrane surface, it might

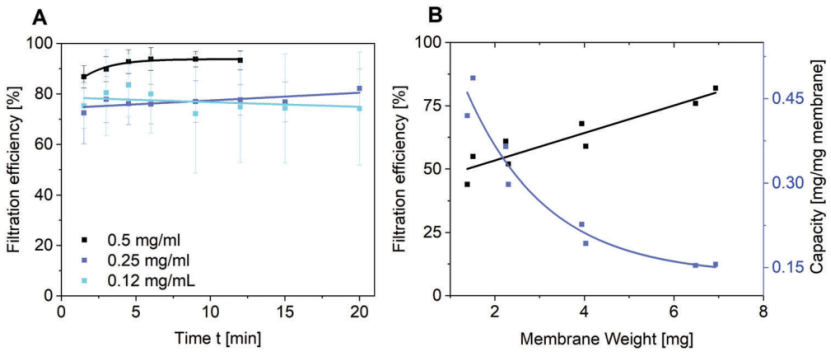

Figure 5. Filtration efficiency over time for A) paint 2 and B) paint 2 supernatant. Standard membrane weight is ≈2.2 mg.

ADVANCED SCIENCE NEWS
www.advancedsciencenews.com

Macromolecular Materials and Engineering
www.mame-journal.de

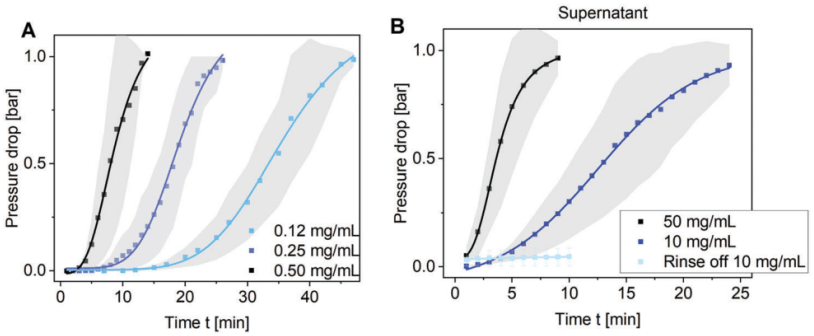

Figure 6. Pressure drop on the membrane at different paint concentrations for A) paint 2 and B) for paint 2 supernatant. Measurements were done in triplicate, the grey background marks the area of standard deviation.

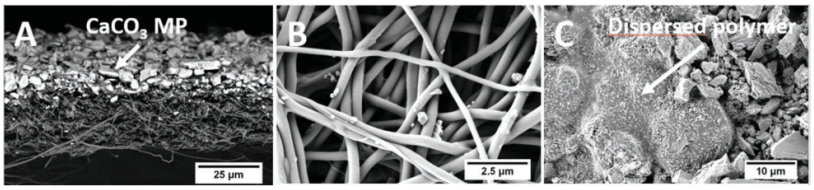

Figure 7. SEM images after filtration of paint 2. A) Membrane in cross-section with BSD detector, B) membrane top view with SE2 detector, and C) top view of membrane after filtration.

also cause a collective coagulation of more than just one layer of the polyelectrolyte on the membrane surface. And each polyelectrolyte can be expected to be in a voluminous, swollen state in aqueous media. The combination of these factors might also explain the expected pore blocking leading to the constantly increasing pressure on the membrane.

Although a pore blockage is expected, the dispersed polymer can hardly be seen on the dry membrane surface in SEM images (**Figure 8**A) only in some distinct areas fiber gluing can be observed (Figure 8B). However, its appearance can be recognized all over the filter area by a higher charge density in the SEM images (Figure 8C). The hypothesis of the even distribution of dispersed polymer in the membrane volume can be further evidenced by pictures of the membranes taken under UV irradiation (312 nm). These pictures show a higher reflection intensity in the inner membrane area, which was used for filtration (Figure S3D, Supporting Information).

The pore gluing by the dispersed polymer, which is assumed to be the driver for the increasing pressure drop can hardly be recognized on the membrane in the SEM images. An explanation can be the reversibility of the fiber gluing. Drying of the membranes after filtration might have led to ionomer type formation and, thus, opened the pores again. Therefore, SEM images demonstrate only fiber coating but no film formation. Further evidence was gained from a rinsing procedure. In this procedure, dried membranes from pressure drop tests were utilized, which have experienced a pressure drop of 1 bar at the end of the filtration experiment. These membranes were—after drying—again placed in the filtration apparatus and Milli-Q water can pass the filter at a pressure drop of roughly 0 bar (Figure 6B). Besides, no polymer was detected in the filtrate. Thus, pores were only temporarily blocked during paint 2 supernatant filtration experiment.

The trade-off between a rising pressure on the membrane and the even distribution of contaminant in the membrane volume points out that the filtration of paint 2 supernatant can be described best by a combination of both mechanisms. The filtration of paint 2 supernatant fits the criteria of an affinity separation because negatively charged copolymers were attracted to the positively charged fibers and were not only filtered on the membrane surface but by depth filtration throughout the whole membrane volume. Additionally, the dispersed polymer might have glued the membranes pores, resulting in typical symptoms of size-exclusion filtration, such as rising pressure drop. However, it is expected, that a rising pressure on the membrane can be avoided and the filtration efficiency be increased by filtering lower concentrated polymer dispersions, which are supposed to feature less polymer chain entanglement.

The adsorption of contaminants, such as organic nanoparticles or dispersed polymers, on the membrane can also be understood as membrane fouling, which hinders membrane use for longer time periods. Either remediation strategies might be established or membranes can in future be designed as photocatalytic membranes.[38]

3. Conclusion

We have demonstrated the importance of noticing paints as a source for particle release with potential hazards to the environment. The release of paints into the environment, for example, by mechanical abrasion or in wastewater will result in a potential hazard for the environment and biota. Therefore, we propose a

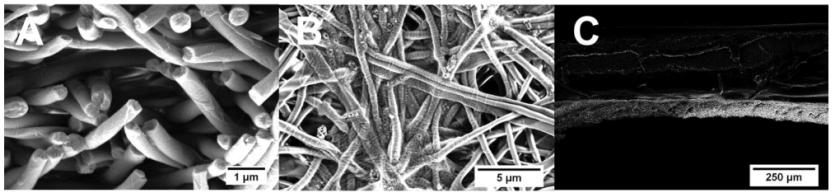

Figure 8. SEM images with SE2 detector after filtration of paint 2 supernatant A) in cross-section, B) top view, and C) zoom-out of figure (A).

feasible method to deal with this essential issue for water purification by membrane filtration process. Electrospun membranes successfully filtered particulate matter and dissolved materials with efficiencies up to 100%. The microparticles were filtered by size-exclusion mechanism in contrast to the titanium dioxide NPs, polyacrylate NPs, and the dispersed copolymers. Those contain charges on their surface, which enable electrostatic interaction with the membrane surface. Due to the electrostatic mechanism they can be filtered even though their size is smaller than the membrane pores and thus, no pore blocking occurs. Since they do not block membrane pores, they do not contribute to the pressure on the membrane at low concentrations, which are anyway more realistic to occur in the environment. This publication demonstrates the application of electrospun membranes for filtration of daily-life systems, which are composed of a mixture of different materials and evidenced the successful transfer of filtration principles from model NPs to daily-life systems.

Supporting Information

Supporting Information is available from the Wiley Online Library or from the author.

Acknowledgements

The authors gratefully acknowledge financial support from Bavarian State Ministry of the Environment and Consumer Protection (funding code TNT01NaT-72524) and the German Research Foundation, CRC 1357-"Mikroplastik" 391977956. Further thanks go to the KeyLab Electron and Optical Microscopy of the Bavarian Polymer Institute (BPI) for providing support and equipment for SEM measurements.

Open Access funding enabled and organized by Projekt DEAL.

Conflict of Interest

The authors declare no conflict of interest.

Data Availability Statement

The data that support the findings of this study are available in the supplementary material of this article.

Keywords

affinity membranes, dispersed polymers, electrospun membranes, filtration, nanomaterials, paints

Received: April 6, 2022
Revised: June 28, 2022
Published online:

[1] A. B. Sengul, E. Asmatulu, *Environ. Chem. Lett.* **2020**, *18*, 1659.
[2] J. Gigault, A. T. Halle, M. Baudrimont, P.-Y. Pascal, F. Gauffre, T.-L. Phi, H. El Hadri, B. Grassl, S. Reynaud, *Environ. Pollut.* **2018**, *235*, 1030.
[3] W. Wang, H. Gao, S. Jin, R. Li, G. Na, *Ecotoxicol. Environ. Saf.* **2019**, *173*, 110.
[4] X.-D. Sun, X.-Z. Yuan, Y. Jia, L.-J. Feng, F.-P. Zhu, S.-S. Dong, J. Liu, X. Kong, H. Tian, J.-L. Duan, Z. Ding, S.-G. Wang, B. Xing, *Nat. Nanotechnol.* **2020**, *15*, 755.
[5] V. S. Fringer, L. P. Fawcett, D. M. Mitrano, M. A. Maurer-Jones, *Front. Environ. Sci.* **2020**, *8*, https://doi.org/10.3389/fenvs.2020.00097
[6] H. Gu, S. Wang, X. Wang, X. Yu, M. Hu, W. Huang, Y. Wang, *J. Hazard. Mater.* **2020**, *397*, 122773.
[7] J. Hou, L. Wang, C. Wang, S. Zhang, H. Liu, S. Li, X. Wang, *J. Environ. Sci.* **2019**, *75*, 40.
[8] D. Magrì, P. Sánchez-Moreno, G. Caputo, F. Gatto, M. Veronesi, G. Bardi, T. Catelani, D. Guarnieri, A. Athanassiou, P. P. Pompa, D. Fragouli, *ACS Nano* **2018**, *12*, 7690.
[9] L. Rubio, R. Marcos, A. Hernández, *J. Toxicol. Environ. Health* **2020**, *23*, 51.
[10] K. Sawicki, M. Czajka, M. Matysiak-Kucharek, B. Fal, B. Drop, S. Męczyńska-Wielgosz, K. Sikorska, M. Kruszewski, L. Kapka-Skrzypczak, *Nanotechnol. Rev.* **2019**, *8*, 175.
[11] M. Hu, D. Palić, *Redox Biol.* **2020**, *37*, 101620.
[12] Z. Yu, Q.i Li, J. Wang, Y. Yu, Y. Wang, Q. Zhou, P. Li, *Nanoscale Res. Lett.* **2020**, *15*, 115.
[13] J. Wang, M.d M. Nabi, S. K. Mohanty, A. N. Afrooz, E. Cantando, N. Aich, M. Baalousha, *Chemosphere* **2020**, *248*, 126070.
[14] S. Galafassi, L. Nizzetto, P. Volta, *Sci. Total Environ.* **2019**, *693*, 133499.
[15] A. Turner, *Water Res.: X* **2021**, *12*, 100110.
[16] D. M. Mitrano, S. Motellier, S. Clavaguera, B. Nowack, *Environ. Int.* **2015**, *77*, 132.
[17] A. Cogulet, P. Blanchet, V. Landry, *Coatings* **2019**, *9*, 121.
[18] M. J. Llana, M. S. Tolentino, N. C. C. Valeza, J. P. Reyes, B. A. Basilia, *IOP Conf. Ser.: Mater. Sci. Eng.* **2021**, *1117*, 012029.
[19] A. Azimzada, J. M. Farner, I. Jreije, M. Hadioui, C. Liu-Kang, N. Tufenkji, P. Shaw, K. J. Wilkinson, *Front. Environ. Sci.* **2020**, *8*, 2186.
[20] A. Azimzada, J. M. Farner, M. Hadioui, C. Liu-Kang, I. Jreije, N. Tufenkji, K. J. Wilkinson, *Environ. Sci.: Nano* **2020**, *7*, 139.
[21] X. Zhang, M. Wang, S. Guo, Z. Zhang, H. Li, *J. Nanopart. Res.* **2017**, *19*, 374.
[22] L. Sung, D. Stanley, J. M. Gorham, S. Rabb, X. Gu, L. L. Yu, T. Nguyen, *J. Coat. Technol. Res.* **2015**, *12*, 121.
[23] R. Kaegi, A. Ulrich, B. Sinnet, R. Vonbank, A. Wichser, S. Zuleeg, H. Simmler, S. Brunner, H. Vonmont, M. Burkhardt, M. Boller, *Environ. Pollut.* **2008**, *156*, 233.
[24] A. Van Wezel, I. Caris, S. A. E. Kools, *Environ. Toxicol. Chem.* **2016**, *35*, 1627.
[25] C. C. Gaylarde, J. A. B. Neto, E. M. Da Fonseca, *Mar. Pollut. Bull.* **2021**, *162*, 111847.

[26] G. Galli, E. Martinelli, *Macromol. Rapid Commun.* **2017**, *38*, 1600704.
[27] P. Westerhoff, G. Song, K. Hristovski, M. A. Kiser, *J. Environ. Monit.* **2011**, *13*, 1195.
[28] X. Wang, T. Han, Y. Sun, H. Geng, B. Li, H. Dai, *Environ. Pollut.* **2021**, *285*, 117408.
[29] P. U. Iyare, S. K. Ouki, T. Bond, *Environ. Sci.: Water Res. Technol.* **2020**, *6*, 2664.
[30] A. A. Horton, A. Walton, D. J. Spurgeon, E. Lahive, C. Svendsen, *Sci. Total Environ.* **2017**, *586*, 127.
[31] D. P. Zagklis, P. G. Koutsoukos, C. A. Paraskeva, *Ind. Eng. Chem. Res.* **2012**, *51*, 15456.
[32] S. Nair K, B. Manu, A. Azhoni, *J. Environ. Manage.* **2021**, *296*, 113105.
[33] M. Malankowska, C. Echaide-Gorriz, J. Coronas, *Environ. Sci.: Water Res. Technol.* **2021**, *7*, 243.
[34] R. Wang, L. Zhang, B. Chen, X. Zhu, *J. Membr. Sci.* **2020**, *614*, 118470.
[35] A. Batool, S. Valiyaveettil, *J. Hazard. Mater.* **2021**, *413*, 125301.
[36] Z. Uddin, F. Ahmad, T. Ullan, Y. Nawab, S. Ahmad, F. Azam, A. Rasheed, M. S. Zafar, *Int. J. Environ. Sci. Technol.* **2021**, *356*, 15.
[37] A.-K. Müller, Z.-K. Xu, A. Greiner, *ACS Appl. Mater. Interfaces* **2021**, *13*, 15659.
[38] A. M. Nasir, N. Awang, J. Jaafar, A. F. Ismail, M. H. D. Othman, M. A. Rahman, F. Aziz, M. A. Mat Yajid, *J. Water Process Eng.* **2021**, *40*, 101878.

Macromolecular Materials and Engineering

Supporting Information

for *Macromol. Mater. Eng.*, DOI 10.1002/mame.202200238

Filtration of Paint-Contaminated Water by Electrospun Membranes

*Ann-Kathrin Müller, Zhi-Kang Xu and Andreas Greiner**

WILEY-VCH

Supporting Information

Filtration of Paint-contaminated Water by Electrospun Membranes

*Ann-Kathrin Müller, Zhi-Kang Xu, Andreas Greiner**

Experimental Section

Materials

PET mesh (50 µm) was bought from Franz Eckert GmbH. Postnova GmbH supplied the special tenside novachem for AF-FFF measurements.

Measurements

Ultraviolet/visible light (UV/Vis)

V-630 spectrometer from Jasco with spectra manager CFR software was used for recording UV/Vis spectra. The measured wavelength region was set to 190-800 nm, and data points were collected in a distance of 2 nm. Aqueous samples were prepared with concentrations between 0.1 up to 2.8 mg/g dispersion. The measurements were executed in a quartz cuvette (1 cm x 1cm). The standard measurement error was determined to be ±11 %.

Asymmetric flow-field flow fractionation (AF-FFF)

AF-FFF was performed on an AF2000 system from Postnova Analytics (Landsberg am Lech, Germany). The channel (295x30 mm) was equipped with a NovaRC 10 kDa membrane and with a 350 µm spacer. Analysis was done with a UV detector and multiple angle light scattering (MALS) detector (532 nm). Postnova AF2000 Control software was applied for size evaluation.

The UV detector signal for measurements without separation was used for concentration determination, and the recovery rate was calculated for measurements with separation. The wavelength was set to 250 nm for detection. The measurement error was determined to be ±17 %. The particle size was analyzed in separation experiments.

Samples were measured with and without separation, according to the following methods:

Table S 1. AF-FFF method for measuring paint 1 supernatant.

Step	Parameter*		With separation	Without separation
	Injection volume [µl]		20	20
	Detector flow [mL/min]		0.5	0.5
Focusing	Injection flow [mL/min]		0.2	0.2
	Injection time [min]		5	1
	Crossflow		0.7	0.1
	Transition time		0.5	0.5
Elution	Step 1	Elution time [min]	1	10
		From [mL/min]	0.7	0.1
		To [mL/min]	0.7	0.1
		Type	Const.	Const.
	Step 2	Elution time [min]	80	None
		From [mL/min]	0.7	
		To [mL/min]	0	
		Type	0.7 power	
Rinsing			1	5

*Paint 1 samples were measured in Milli-Q water with 0.2 wt% Novachem.

Table S 2. AF-FFF method for paint 2 supernatant.

Step	Parameter*		With separation	Without separation
	Injection volume [µl]		20	20
	Detector flow [mL/min]		0.5	0.5
Focusing	Injection flow [mL/min]		0.2	0.2
	Injection time [min]		3	1
	Crossflow		0.6	0.1
	Transition time		0.5	0.5
Elution	Step 1	Elution time [min]	1	8
		From [mL/min]	0.6	0.1
		To [mL/min]	0.6	0.1
		Type	Const.	Const.
	Step 2	Elution time [min]	20	none
		From [mL/min]	0.6	

	To [mL/min]	0	
	Type	0.2 Power	
Rinsing	Time [min]	5	5

*Paint 2 samples were measured in Milli-Q water with 0.2 wt% Novachem.

Scanning electron microscope (SEM)

Samples were prepared on a coal film. Membranes were sputtered with 1.3 nm platinum by the Cressington platinum-sputter coater 208HR or coated with a coal film by the Leica EM ACE 600. Leo 1530 from Zeiss was used for measurements at an acceleration voltage of 3 kV and a pressure of 2.0 x 10-5 bar for pictures with inlense and secondary electron (Everhart Thornley) detector. The backscattering detector (BSD) from Centaurus (10 mm working distance) was used at 10 kV acceleration voltage and the Ultradry-EDX-detector from Thermo Fisher Scientific NS7 (8 mm working distance) at an acceleration voltage of 20 kV under the usual pressure. The BSD shows higher brightness on the pictures for metal components than for organic material and thus, was used for characterizing the type (metal / organic) of observed nanoparticles on the membrane surface. The SE2 detector has a higher resolution than BSD and the topography of the scanned materials can be recognized, which enables good picture quality for fibrous material.

Dynamic light scattering (DLS)

A system from ALV-5000EPP Laservertriebsgesellschaft mbH, with a photon-counting module from Perkin Elmer (SPCM-CD 3017) was used. DLS measurements were done at a wavelength of 632 nm, with a detector angle of 90°, and a temperature of 294 K. Samples were all prepared in water with a viscosity of 0.9711 cp. The data were analyzed with WINDOWS-95/98/NT-4.0 control and data reduction software.

Zeta sizer

Paint samples were prepared in water with a concentration of 0.057-0.068 mg/mL or 0.22-0.9 mg/mL for paint supernatant and were measured by a zeta sizer of Malvern. The Malvern software automatically set an optimum measurement position and voltage. The measuring temperature was 20 °C.

Raman microscope

Raman spectra were recorded with a combined Raman-Imaging/Scanning Force Microscope System (Model Alpha 300 RA+) from WITEC. Two laser sources can be used: UHTS 300 spectrometer, back-illuminated Andor Newton 970 EMCCD camera (532 nm wavelength) or

UHTS 400 spectrometer, back-illuminated deep depletion Andor iDUS CCD camera (785 nm wavelength) with a maximum power of 50 mW. Spectra range was set to 0-3600 cm^{-1} with collecting data points in an interval of 3 cm^{-1}. Spectra were analyzed with the software WITEC Project five 5.1 and were corrected from cosmic noise.

UV-Lamp

Pictures of membranes after paint filtration were taken under UV irradiation at a wavelength of 213 nm. The lamp used is made by LTF-Labortechnik GmbH & CO.KG and has a serial number of MO3 4709. Lamp specifications are: voltage of 230 V at 50 Hz with a power of 6 W.

Centrifuge

For sample centrifugation a Heraeus Megafuge 16R (Serial No. 41535480) from Thermo Scientific was used. Samples were centrifuged in 40 mL tubes at a rotation speed of maximum 10000 rounds/min.

Paint separation procedure

The solid part of the paint 1 consist of 21 wt% and paint 2 consists of 7 wt% organic materials.

Paint 1 was dispersed in water (2 g/400 mL) and stored for four weeks. The supernatant was centrifuged at 10000 U for 20 min. The sediment was removed. This procedure was repeated three times. The sludge from the 200 mL batch was redispersed in water und centrifuged at 2000 U for 10 min. The sediment was washed with water and centrifuged again. The washing step was repeated three times. Both fractions were stored in aqueous media.

Paint 2 was dispersed in water (8 g/40 mL) and was centrifuged at 2000 U. The supernatant was removed and the sediment was washed with water and centrifuged again two times. The supernatant from the first centrifugation step was again centrifuged at 10000 U for 30 min. The sediment was discarded. This procedure was repeated three times to receive the purified paint 2 supernatant.

All four samples were used for biology tests. Paint 1 and paint 2 supernatant were used for filtration tests at different dilution concentrations. The paints were furthermore tested on their zeta potential, which was for both paints between -2 to -50 mV in the pH range of 2 to 10.

Filtration tests

Filtration tests were done with membranes containing 50 mol% of the Nplus-, 10 mol% of MABP, and 40 mol% MMA. The polymers were synthesized by free-radical copolymerization at 80°C in DMSO, which were precipitated and dried. The resulting

polymers were electrospun from DMF onto a rotating disc collector. The electrospinning was conducted at 23°C with flow rate of 0.32 mL/min and an acceleration voltage of 17/-1 kV. The membranes were subsequently treated with UV-light for 3 h to execute the cross-linking. The evolving cross-linking was tract with IR-spectroscopy. The cross-linking enables low swelling and good mechanical stability of the electrospun membranes, which is both needed for good filtration performance. The membranes received are hydrophilic due to the Nplus functional groups and can easily be wetted by water. Water drops placed on top of the membrane are soaked into the membranes within seconds. Due to the hydrophilicity of the membrane material no pressure on the membrane occurs at flow rates, such as 1 mL/min. The polymer synthesis and membrane preparation were done according to the procedure in the previous paper.[37]

Particle filtration test

The membranes were cut into pieces with a diameter of 14 mm and were deposited on top of a sheet of PET mesh with a pore size of 50 µm. A reusable filtering apparatus from Satorius AG was utilized limiting the used membrane area for filtration to 0.95 cm2. A syringe pump (Landgraf Laborsysteme, model no. LA 30) adjusted the solution flow rate, and the filtrate is collected in vials with a volume of 1.5 mL. Main filtration tests were carried out with 1 mL/min flow rate, and a total collection time of 6 min up to 20 min. Each batch was then further analyzed by UV/Vis and AF-FFF. The filtration efficiency was calculated from the two different measurement methods. For repeated filtration experiments, data points with high deviation were excluded.

Paint 2 superantant was used for filtration tests. The supernatant was prepared from a 50 mg/mL solution by centrifugation triple times at 10.000 U^{-1}. The resulting supernatant contains 0.11 wt%. Thus, the concentration for filtration tests was 10 mg/mL.

Paint 1 supernatant was prepared by sedimentation of a 0.5 mg/mL dispersion over 4 weeks. The resulting supernatant contains 0.179 wt% (0.179 mg/mL).

Pressure drop measurements

Pressure drop measurements were done with a battery powered digital manometer (digi-04). The digital pressure gauge has an accuracy of 0.4 % in the measuring range of 0-2.5 bar. The pressure gauge was installed between a syringe pump (Landgraf Laborsysteme, model no. LA 30) and the filtration apparatus.

Membrane capacity

Paint 2 supernatant (6 mL) was filtered once through membranes with different weights. Membrane capacity for paint 2 supernatant was calculated from the filtered dispersion volume ($V_{filtered}$), the start concentration of the paint dispersion ($C_{paint\ dispersion}$), the filtration efficiency ($E_{efficiency}$), and the membrane mass ($M_{membrane\ mass}$).

$$Capacity = \frac{\left(V_{filtered} \cdot C_{paint\ dispersion} \cdot E_{efficiency}\right)}{M_{membrane\ mass}}$$

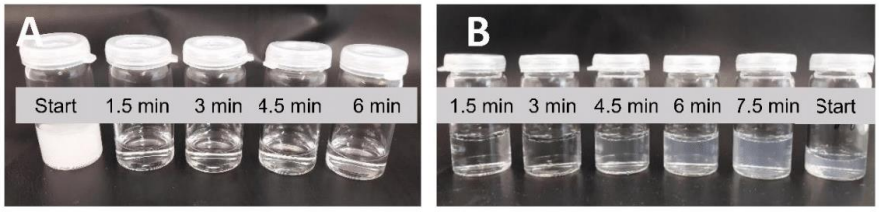

Figure S 1. Pictures of filtrate A) from paint 1 and B) from paint 1 supernatant.

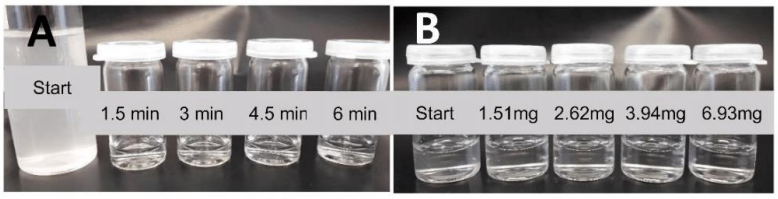

Figure S 2. Picture of filtrate after filtration of A) paint 2 and B) paint 2 supernatant with different membrane weights.

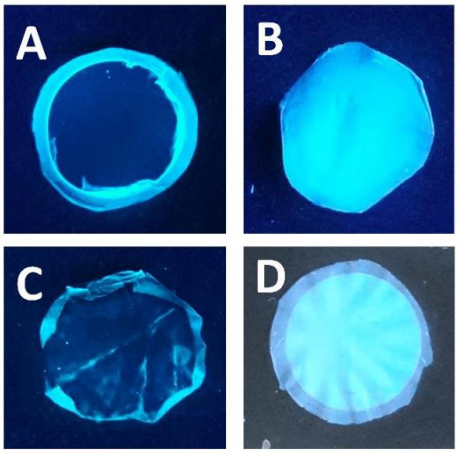

Figure S 3. Pictures of Nplus membranes under UV irradiation (213 nm) after filtering A) paint 1, B) paint 1 supernatant, C) paint 2, and D) paint 2 supernatant

References Supporting Information

[1] A.-K. Müller, Z.-K. Xu, A. Greiner, Preparation and performance assessment of low-pressure affinity membranes based on functionalized, electrospun polyacrylates for gold nanoparticle filtration, ACS Appl. Mater. Interfaces 13 (2021) 15659–15667.

4. Supplementary

Abbreviations

AA	Acrylic acid
AF-FFF	Asymmetric flow field flow fractionation
DLVO	DERJAGUIN-LANDAU-VERWEY-OVERBEEK
EAF-FFF	Electrical asymmetric flow field flow fractionation
EDX	Energy dispersive X-ray spectroscopy
EPS	Extracellular polymeric substance
ICP-OES	Inductively coupled plasma optical emission spectrometry
IR	Infrared
NIPAM	N-Isopropyl acrylamide
NMR	Nuclear magnetic resonance
NOM	Natural organic matter
Nplus	Dimethyldecyl ammoniumethyl methacrylbromide
PAN	Polyacrylonitrile
PEI	Polyethylene imine
PMMA	Polymethyl methacrylate
PVA	Polyvinyl alcohol
PVAc	Polyvinyl acetate
PVP	Polyvinyl pyrrolidone
Pyr	4-Vinyl pyridine
ROS	Reactive oxygen species

SEC	Size exclusion chromatography
SEM	Scanning electron microscopy
T*EM*	Transmission electron microscope
UV/Vis	Ultraviolet/ visible

5. References

[1] L. A. Kolahalam, I. V. Kasi Viswanath, B. S. Diwakar, B. Govindh, V. Reddy, Y.L.N. Murthy, *Mater. Today Proc.* **2019**, *18*, S. 2182–2190.

[2] V. Prakash Sharma, U. Sharma, M. Chattopadhyay, V. N. Shukla, *Mater. Today Proc.* **2018**, *5*, S. 6376–6380.

[3] N. H. Hong (Hrsg.) *Micro and nano technologies series*, Elsevier, Amsterdam, Netherlands, **2019**.

[4] S. Anu Mary Ealia, M. P. Saravanakumar, *IOP Conf. Ser.: Mater. Sci. Eng.* **2017**, *263*, S. 32019.

[5] P. Iqbal, J. A. Precce, P. M. Mendes, *Supramol. Chem.* **2012**.

[6] P. G. Jamkhande, N. W. Ghule, A. H. Bamer, M. G. Kalaskar, *J. Drug Deliv. Sci. Technol.* **2019**, *53*, S. 101174.

[7] A. V. Nikam, B. L. V. Prasad, A. A. Kulkarni, *Cryst. Eng. Comm.* **2018**, *20*, S. 5091–5107.

[8] A. Escudero, C. Carrillo-Carrión, E. Romero-Ben, A. Franco, C. Rosales-Barrios, M. C. Castillejos, N. Khiar, *Inorganics* **2021**, *9*, S. 58.

[9] X. Gu, Z. Xu, L. Gu, H. Xu, F. Han, B. Chen, X. Pan, *Environ. Chem. Lett.* **2021**, *19*, S. 167–187.

[10] N. G. Bastús, F. Merkoçi, J. Piella, V. Puntes, *Chem. Mater.* **2014**, *26*, S. 2836–2846.

[11] C. Daruich De Souza, B. Ribeiro Nogueira, M. E. C.M. Rostelato, *J. Alloys Compd.* **2019**, *798*, S. 714–740.

[12] J. Polte, *Cryst. Eng. Comm.* **2015**, *17*, S. 6809–6830.

[13] A. V. Samrot, C. S. Sahithya, J. Selvarani A, S. K. Purayil, P. Ponnaiah, *Curr. Res. Green Sustain. Chem.* **2021**, *4*, S. 100042.

[14] J. Baumgartner, A. Dey, P. H. H. Bomans, C. Le Coadou, P. Fratzl, N. A. J. M. Sommerdijk, D. Faivre, *Nat. Mater.* **2013**, *12*, S. 310–314.

[15] D. Yang, *Titanium Dioxide - Material for a Sustainable Environment*, InTech, **2018**.

[16] L. P. Singh, S. K. Bhattacharyya, R. Kumar, G. Mishra, U. Sharma, G. Singh, S. Ahalawat, *Adv. Colloid Interface Sci.* **2014**, *214*, S. 17–37.

[17] M. Parashar, V. K. Shukla, R. Singh, *J. Mater. Sci. Mater. Electron.* **2020**, *31*, S. 3729–3749.

[18] S. Esposito, *Materials* **2019**, *12*.

[19] A. A. Hashim, *The Delivery of Nanoparticles*. *Chapter 4*, InTech, s.l., **2012**.

[20] W. Xi, H. T. Phan, A. J. Haes, *Anal. Bioanal. Chem.* **2018**, *410*, S. 6113–6123.

[21] H. T. Phan, A. J. Haes, *J. Phys. Chem. Nanomater. Interfaces* **2019**, *123*, S. 16495–16507.

[22] E. M. Hotze, T. Phenrat, G. V. Lowry, *J. Environ. Qual.* **2010**, *39*, S. 1909–1924.

[23] K. Hosokawa, K. Nogi, M. Naitō, T. Yokoyama (Hrsg.) *Nanoparticle Technology Handbook*, Elsevier, Amsterdam, Netherlands, **2018**.

[24] T. L. Doane, C.-H. Chuang, R. J. Hill, C. Burda, *Acc. Chem. Res.* **2012**, *45*, S. 317–326.

[25] S. Bhattacharjee, *J. Control. Release* **2016**, *235*, S. 337–351.

[26] S. V. Babu (Hrsg.) *Woodhead publishing series in electronic and optical materials, number 86*, Woodhead Publishing, Waltham, MA, **2016**.

[27] K. J. Si, Y. Chen, Q. Shi, W. Cheng, *Adv. Sci.* **2018**, *5*, S. 1700179.

[28] R. López-Esparza, M. A. Balderas Altamirano, E. Pérez, A. Gama Goicochea, *Adv. Condens. Matter Phys.* **2015**, *2015*, S. 1–8.

[29] H. Ohshima (Hrsg.) *Electrical Phenomena at Interfaces and Biointerfaces*. *Fundamentals and Applications in Nano-, Bio-, and Environmental Sciences*, Wiley, Hoboken, N.J, **2012**.

[30] M. Madkour, A. Bumajdad, F. Al-Sagheer, *Adv. Colloid Interface Sci.* **2019**, *270*, S. 38–53.

[31] S. Elbasuney, *Appl. Surf. Sci.* **2017**, *409*, S. 438–447.

[32] J. Yan, M. R. Bockstaller, K. Matyjaszewski, *Progr. Polym. Sci.* **2020**, *100*, S. 101180.

[33] E. M. Benetti, M. Divandari, S. N. Ramakrishna, G. Morgese, W. Yan, L. Trachsel, *Chemistry* **2017**, *23*, S. 12433–12442.

[34] H. Heinz, C. Pramanik, O. Heinz, Y. Ding, R. K. Mishra, D. Marchon, R. J. Flatt, I. Estrela-Lopis, J. Llop, S. Moya et al., *Surf. Sci. Rep.* **2017**, *72*, S. 1–58.

[35] R. A. Bohara, N. D. Thorat, S. H. Pawar, *RSC Adv.* **2016**, *6*, S. 43989–44012.

[36] A. Heuer-Jungemann, N. Feliu, I. Bakaimi, M. Hamaly, A. Alkilany, I. Chakraborty, A. Masood, M. F. Casula, A. Kostopoulou, E. Oh et al., *Chem. Rev.* **2019**, *119*, S. 4819–4880.

[37] M. S. Rodrigues, J. Borges, C. Lopes, R. M. S. Pereira, M. I. Vasilevskiy, F. Vaz, *Appl. Sci.* **2021**, *11*, S. 5388.

[38] A. Akbarzadeh, M. Samiei, S. Davaran, *Nanoscale Res. Lett.* **2012**, *7*, S. 144.

[39] B. Roldan Cuenya, F. Behafarid, *Surf. Sci. Rep.* **2015**, *70*, S. 135–187.

[40] L. Xu, H.-W. Liang, Y. Yang, S.-H. Yu, *Chem. Rev.* **2018**, *118*, S. 3209–3250.

[41] H. Mistry, R. Reske, P. Strasser, B. Roldan Cuenya, *Catal. Today* **2017**, *288*, S. 30–36.

[42] F. Viñes, J. R. B. Gomes, F. Illas, *Chem. Soc. Rev.* **2014**, *43*, S. 4922–4939.

[43] C. Dong, C. Lian, S. Hu, Z. Deng, J. Gong, M. Li, H. Liu, M. Xing, J. Zhang, *Nat. Commun.* **2018**, *9*, S. 1252.

[44] B. Zhu, J. Meng, W. Yuan, X. Zhang, H. Yang, Y. Wang, Y. Gao, *Angew. Chem.* **2020**, *59*, S. 2171–2180.

[45] J. Tournebize, A. Boudier, A. Sapin-Minet, P. Maincent, P. Leroy, R. Schneider, *ACS Appl. Mater. Interfaces* **2012**, *4*, S. 5790–5799.

[46] L. DeRita, J. Resasco, S. Dai, A. Boubnov, H. V. Thang, A. S. Hoffman, I. Ro, G. W. Graham, S. R. Bare, G. Pacchioni et al., *Nat. Mater.* **2019**, *18*, S. 746–751.

[47] V. Amendola, R. Pilot, M. Frasconi, O. M. Maragò, M. A. Iatì, *J. Phys. Condens. Matter* **2017**, *29*, S. 203002.

[48] O. Kvítek, J. Siegel, V. Hnatowicz, V. Švorčík, *J. Nanomater.* **2013**, *2013*, S. 1–15.

[49] G. Barbillon, *Nanoplasmonics - Fundamentals and Applications*, InTech, **2017**.

[50] Garcia M.A., *J. Appl. Phy.* **2012**, *44*.

[51] L. Wang, M. Hasanzadeh Kafshgari, M. Meunier, *Adv. Funct. Mater.* **2020**, *30*, S. 2005400.

[52] H. Liang, H. Wei, D. Pan, H. Xu, *Nanotechnol. Rev.* **2015**, *4*.

[53] L. A. Austin, B. Kang, M. A. El-Sayed, *Nano Today* **2015**, *10*, S. 542–558.

[54] G. Mie, *Ann. Phys.* **1908**, *330*, S. 377–445.

[55] V. A. Ogarev, V. M. Rudoi, O. V. Dement'eva, *Inorg. Mater. Appl. Res.* **2018**, *9*, S. 134–140.

[56] J. A. Scholl, A. L. Koh, J. A. Dionne, *Nature* **2012**, *483*, S. 421–427.

[57] C.-G. Stefanita, *Magnetism. Basics and Applications*, Springer, Berlin, **2012**.

[58] U. Jeong, X. Teng, Y. Wang, H. Yang, Y. Xia, *Adv. Mater.* **2007**, *19*, S. 33–60.

[59] B. Issa, I. M. Obaidat, B. A. Albiss, Y. Haik, *Int. J. Mol. Sci.* **2013**, *14*, S. 21266–21305.

[60] A. G. Kolhatkar, A. C. Jamison, D. Litvinov, R. C. Willson, T. R. Lee, *Int. J. Mol. Sci.* **2013**, *14*, S. 15977–16009.

[61] D. L. Huber, *Small* **2005**, *1*, S. 482–501.

[62] A. B. Sengul, E. Asmatulu, *Environ. Chem. Lett.* **2020**, *18*, S. 1659–1683.

[63] F. Piccinno, F. Gottschalk, S. Seeger, B. Nowack, *J. Nanopart. Res.* **2012**, *14*, S. 300.

[64] McWilliams, "The Maturing Nanotechnology Market: Products and Applications", zu finden unter https://www.prnewswire.com/news-releases/the-maturing-nanotechnology-market-products-and-applications-300369337.html, **2016**.

[65] M. Bundschuh, J. Filser, S. Lüderwald, M. S. McKee, G. Metreveli, G. E. Schaumann, R. Schulz, S. Wagner, *Environ. Sci. Eur.* **2018**, *30*, S. 6.

[66] J. Labille, R. Catalano, D. Slomberg, S. Motellier, A. Pinsino, P. Hennebert, C. Santaella, V. Bartolomei, *Front. Environ. Sci.* **2020**, *8*, S. 416.

[67] A. Rodríguez-Romero, G. Ruiz-Gutiérrez, J. R. Viguri, A. Tovar-Sánchez, *Environ. Sci. Technol.* **2019**, *53*, S. 10177–10187.

[68] R. Włodarczyk, A. Kwarciak-Kozłowska, *Sustainability* **2021**, *13*, S. 5805.

[69] A. Azimzada, J. M. Farner, M. Hadioui, C. Liu-Kang, I. Jreije, N. Tufenkji, K. J. Wilkinson, *Environ. Sci. Nano* **2020**, *7*, S. 139–148.

[70] S. Bhattacharjee, R. Joshi, M. Yasir, A. Adhikari, A. A. Chughtai, D. Heslop, R. Bull, M. Willcox, C. R. Macintyre, *ACS Appl. Bio Mater.* **2021**, *4*, S. 6175–6185.

[71] D. Licina, G. C. Morrison, G. Bekö, C. J. Weschler, W. W. Nazaroff, *Environ. Sci. Technol.* **2019**, *53*, S. 5559–5575.

[72] N. V. S. Vallabani, S. Singh, *3 Biotech* **2018**, *8*, S. 279.

[73] Y. Zhu, X. Liu, Y. Hu, R. Wang, M. Chen, J. Wu, Y. Wang, S. Kang, Y. Sun, M. Zhu, *Environ. Res.* **2019**, *174*, S. 54–60.

[74] M. Li, P. Zhang, M. Adeel, Z. Guo, A. J. Chetwynd, C. Ma, T. Bai, Y. Hao, Y. Rui, *Environ. Pollut.* **2021**, *269*, S. 116134.

[75] M. Kumar, H. Singh Dosanjh, Sonika, J. Singh, K. Monir, H. Singh, *Environ. Sci. Water Res. Technol.* **2020**, *6*, S. 491–514.

[76] M. Amde, J.-F. Liu, Z.-Q. Tan, D. Bekana, *Environ. Pollut.* **2017**, *230*, S. 250–267.

[77] D. M. Mitrano, S. Motellier, S. Clavaguera, B. Nowack, *Environ. Int.* **2015**, *77*, S. 132–147.

[78] A. Cogulet, P. Blanchet, V. Landry, *Coatings* **2019**, *9*, S. 121.

[79] M. J. Llana, M. S. Tolentino, N. C. C. Valeza, J. P. Reyes, B. A. Basilia, *IOP Conf. Ser.: Mater. Sci. Eng.* **2021**, *1117*, S. 12029.

[80] L. Sung, D. Stanley, J. M. Gorham, S. Rabb, X. Gu, L. L. Yu, T. Nguyen, *J. Coat. Technol. Res.* **2015**, *12*, S. 121–135.

[81] X. Zhang, M. Wang, S. Guo, Z. Zhang, H. Li, *J. Nanopart. Res.* **2017**, *19*, S. 374.

[82] J. Wang, M. M. Nabi, S. K. Mohanty, A. N. Afrooz, E. Cantando, N. Aich, M. Baalousha, *Chemosphere* **2020**, *248*, S. 126070.

[83] N. B. Turan, H. S. Erkan, G. O. Engin, M. S. Bilgili, *Process Saf. Environ. Prot.* **2019**, *130*, S. 238–249.

[84] Q. Abbas, B. Yousaf, Amina, M. U. Ali, M. A. M. Munir, A. El-Naggar, J. Rinklebe, M. Naushad, *Environ. Int.* **2020**, *138*, S. 105646.

[85] S. Roy, Z. Liu, X. Sun, M. Gharib, H. Yan, Y. Huang, S. Megahed, M. Schnabel, D. Zhu, N. Feliu et al., *Bioconjug. Chem.* **2019**, *30*, S. 2751–2762.

[86] P. Fatehbasharzad, P. Fatehbasharzad, M. Sillanpää, Z. Shamsi, *Part. Part. Syst. Charact.* **2021**, *2008*, S. 2100112.

[87] M. Garcés, L. Cáceres, D. Chiappetta, N. Magnani, P. Evelson, *New J. Chem.* **2021**, *45*, S. 14328–14344.

[88] J. C. Bonner, J. M. Brown, *Interaction of Nanomaterials with the Immune System*. *Chapter 7*, 1. Aufl., **2020**.

[89] Z. Yu, Q. Li, J. Wang, Y. Yu, Y. Wang, Q. Zhou, P. Li, *Nanoscale Res. Lett.* **2020**, *15*, S. 115.

[90] R. Lehner, C. Weder, A. Petri-Fink, B. Rothen-Rutishauser, *Environ. Sci. Technol.* **2019**, *53*, S. 1748–1765.

[91] K. L. Law, R. C. Thompson, *Science* **2014**, *345*, S. 144–145.

[92] "An Analysis of European Plastic Production. Demand and Waste Data", zu finden unter https://www.plasticseurope.org/application/files/5715/1717/4180/Plastics_the_facts_2017_FINAL_for_website_one_page.pdf, **2018**.

[93] T. M. Letcher, *Plastic Waste and Recycling*. *Environmental Impact, Societal Issues, Prevention, and Solutions*, **2020**.

[94] A. Chamas, H. Moon, J. Zheng, Y. Qiu, T. Tabassum, J. H. Jang, M. Abu-Omar, S. L. Scott, S. Suh, *ACS Sustain. Chem. Eng.* **2020**, *8*, S. 3494–3511.

[95] K. Zhu, H. Jia, Y. Sun, Y. Dai, C. Zhang, X. Guo, T. Wang, L. Zhu, *Water Res.* **2020**, *173*, S. 115564.

[96] I. Chubarenko, I. Efimova, M. Bagaeva, A. Bagaev, I. Isachenko, *Mar. Pollut. Bull.* **2020**, *150*, S. 110726.

[97] A. L. Andrady, *Mar. Pollut. Bull.* **2011**, *62*, S. 1596–1605.

[98] J. G.B. Derraik, *Mar. Pollut. Bull.* **2002**, *44*, S. 842–852.

[99] L. M. Hernandez, N. Yousefi, N. Tufenkji, *Environ. Sci. Technol. Lett.* **2017**, *4*, S. 280–285.

[100] S. Galafassi, L. Nizzetto, P. Volta, *Sci. Total Environ.* **2019**, *693*, S. 133499.

[101] S. L. Wong, B. B. Nyakuma, K. Y. Wong, C. T. Lee, T. H. Lee, C. H. Lee, *Mar. Pollut. Bull.* **2020**, *158*, S. 111432.

[102] W. Wang, H. Gao, S. Jin, R. Li, G. Na, *Ecotoxicol. Environ. Saf.* **2019**, *173*, S. 110–117.

[103] Q. Liu, Z. Chen, Y. Chen, F. Yang, W. Yao, Y. Xie, *J. Agric. Food Chem.* **2021**, *69*, S. 10450–10468.

[104] J. C. Prata, J. P. da Costa, I. Lopes, A. C. Duarte, T. Rocha-Santos, *Sci. Total Environ.* **2020**, *702*, S. 134455.

[105] D. Li, J. Ji, Y. Yuan, D. Wang, *Chemosphere* **2020**, *245*, S. 125625.

[106] N. Singh, N. Khandelwal, E. Tiwari, N. Naskar, S. Lahiri, J. Lützenkirchen, G. K. Darbha, *Water Res.* **2021**, *189*, S. 116622.

[107] E. Kabir, V. Kumar, K.-H. Kim, A. C. K. Yip, J. R. Sohn, *J. Environ. Manage.* **2018**, *225*, S. 261–271.

[108] A. Batool, S. Valiyaveettil, *J. Hazard. Mater.* **2021**, *413*, S. 125301.

[109] Y. Zhang, Y. Li, F. Su, L. Peng, D. Liu, *Sci. Total Environ.* **2021**, *802*, S. 149658.

[110] C. M. Park, K. H. Chu, N. Her, M. Jang, M. Baalousha, J. Heo, Y. Yoon, *Sep. Purif. Rev.* **2016**, *46*, S. 255–272.

[111] Y. Zhang, A. Diehl, A. Lewandowski, K. Gopalakrishnan, T. Baker, *Sci. Total Environ.* **2020**, *720*, S. 137383.

[112] M. Enfrin, L. F. Dumée, J. Lee, *Water Res.* **2019**, *161*, S. 621–638.

[113] T. Poerio, E. Piacentini, R. Mazzei, *Molecules* **2019**, *24*.

[114] P. U. Iyare, S. K. Ouki, T. Bond, *Environ. Sci.: Water Res. Technol.* **2020**, *6*, S. 2664–2675.

[115] T. Lange, P. Schneider, S. Schymura, K. Franke, *Water* **2020**, *12*, S. 2509.

[116] S. T. M., A. B. Arshad, P. T. Lin, J. Widakdo, M. H. K., H. F. M. Austria, C.-C. Hu, J.-Y. Lai, W.-S. Hung, *RSC Adv.* **2021**, *11*, S. 9638–9663.

[117] Z. Uddin, F. Ahmad, T. Ullan, Y. Nawab, S. Ahmad, F. Azam, A. Rasheed, M. S. Zafar, *Int. J. Environ. Sci. Technol.* **2021**, *356*, S. 15.

[118] H. M. Ibrahim, A. Klingner, *Polym. Test.* **2020**, *90*, S. 106647.

[119] C. V. Boys, *Proc. Phys. Soc. London* **1887**, *9*, S. 8–19.

[120] J. F. Cooley, US Patent 692631.

[121] W. J. Morton, US Patent 705691A, **1902**.

[122] K. Ghosal, C. Agatemor, N. Tucker, E. Kny, S. Thomas in *Soft Matter Series* (Hrsg.: E. Kny, K. Ghosal, S. Thomas), Royal Society of Chemistry, Cambridge, **2018**, S. 1–23.

[123] G. Taylor, *Proc. R. Soc. Lond. A* **1964**, *280*, S. 383–397.

[124] G. Taylor, *Proc. R. Soc. Lond. A* **1966**, *291*, S. 145–158.

[125] G. Taylor, *Proc. R. Soc. Lond. A* **1969**, *313*, S. 453–475.

[126] N. T. M. Balakrishnan, R. Prasanth, *Electrospinning for Advanced Energy Storage Applications*, 1. Aufl., **2021**.

[127] G. Z. Kyzas, A. C. Mitropoulos (Hrsg.) *Novel Nanomaterials*. *Synthesis and Applications*, IntechOpen, London, **2018**.

[128] J. Xue, T. Wu, Y. Dai, Y. Xia, *Chem. Rev.* **2019**, *119*, S. 5298–5415.

[129] S. Jiang, Y. Chen, G. Duan, C. Mei, A. Greiner, S. Agarwal, *Polym. Chem.* **2018**, *9*, S. 2685–2720.

[130] H. El-Sayed, C. Vineis, A. Varesano, S. Mowafi, R. Andrea Carletto, C. Tonetti, M. Abou Taleb, *Nanotechnol. Rev.* **2019**, *8*, S. 236–245.

[131] D.-G. Yu, M. Wang, X. Li, X. Liu, L.-M. Zhu, S. W. Annie Bligh, *Nanomed. Nanobiotechnol.* **2020**, *12*, e1601.

[132] B. Ding, J. Yu, X. Wang, *Electrospinning*. *Nanofabrication and Applications*, William Andrew, San Diego, **2018**.

[133] R. K. Mishra, P. Mishra, K. Verma, A. Mondal, R. G. Chaudhary, M. M. Abolhasani, S. Loganathan, *Environ. Chem. Lett.* **2019**, *17*, S. 767–800.

[134] A. Abdelrasoul, *Advances in Membrane Technologies*, IntechOpen, **2020**.

[135] Inamuddin, R. Boddula, M. I. Ahamed, A. M. Asiri, *Electrospun Materials and Their Allied Applications*, Wiley, **2020**.

[136] Y. Wang, C. Wang, *Polymer* **2021**, *222*, S. 123672.

[137] Inamuddin, A. M. Ai, A. Mohammad (Hrsg.) *Woodhead Publishing series in biomaterials*, Woodhead Publishing, Cambridge, MA, **2018**.

[138] S. Tabe, *J. Mem. Sci.* **2017**, *3*, S. 228–239.

[139] M. Alazab, G. R. Mitchell, F. J. Davis, S. D. Mohan, *Procedia Manuf.* **2017**, *12*, S. 66–78.

[140] X. Yang, J. Wang, H. Guo, L. Liu, W. Xu, G. Duan, *e-Polymers* **2020**, *20*, S. 682–712.

[141] Z. Wang, B. Sun, X. Lu, C. Wang, Z. Su, *Macromolecules* **2019**, *52*, S. 9639–9645.

[142] Y. Han, Y. Xu, S. Zhang, T. Li, S. Ramakrishna, Y. Liu, *Macromol. Mater. Eng.* **2020**, *305*, S. 2000230.

[143] D. Nataraj, R. Reddy, N. Reddy, *Eur. Polym. J.* **2020**, *124*, S. 109484.

[144] C. Braga, A. R. Sampaio, J. Peixoto, C. J. dos Santos Marinho da Silva, A. Zille, *SN Appl. Sci.* **2019**, *1*, S. 558.

[145] N. Chailek, D. Daranarong, W. Punyodom, R. Molloy, P. Worajittiphon, *J. Appl. Polym. Sci.* **2018**, *135*, S. 46318.

[146] K. M. Hatch, J. Hlavatá, K. Paulett, T. Liavitskaya, S. Vyazovkin, A. V. Stanishevsky, *Int. J. Polym. Sci.* **2019**, *2019*, S. 1–12.

[147] K. Nie, S. Han, J. Yang, Q. Sun, X. Wang, X. Li, Q. Li, *Polymers* **2020**, *12*.

[148] H. Tian, L. Yuan, J. Wang, H. Wu, H. Wang, A. Xiang, B. Ashok, A. V. Rajulu, *J. Hazard. Mater.* **2019**, *378*, S. 120751.

[149] M. Hajiabbas, I. Alemzadeh, M. Vossoughi, A. Shamloo, *Chem. Eng. Commun.* **2021**, *208*, S. 976–992.

[150] K. Molnar, B. Jozsa, D. Barczikai, E. Krisch, J. E. Puskas, A. Jedlovszky-Hajdu, *J. Mol. Liq.* **2020**, *303*, S. 112628.

[151] P. Kianfar, A. Vitale, S. Dalle Vacche, R. Bongiovanni, *J. Mater. Sci.* **2021**, *56*, S. 1879–1896.

[152] B. Qu, Y. Xu, L. Ding, B. Rnby, *J. Polym. Sci. A Polym. Chem.* **2000**, *38*, S. 999–1005.

[153] X. Song, P. Dong, J. Gravesande, B. Cheng, J. Xing, *Int. J. Biol. Macromol.* **2018**, *120*, S. 2086–2093.

[154] M. O. Pretscher, G. Sitaru, M. Dietel, H. Schmalz, S. Gekle, S. Agarwal, *ACS Appl. Polym. Mater.* **2021**, *3*, S. 1349–1357.

[155] Kenry, C. T. Lim, *Prog. Polym. Sci.* **2017**, *70*, S. 1–17.

[156] M. K. Purkait, M. K. Sinha, P. Mondal, R. Singh (Hrsg.) *Interface science and technology*, *volume 25*, Academic Press an imprint of Elsevier, London, **2018**.

[157] J. Kamp, S. Emonds, J. Borowec, M. A. Restrepo Toro, M. Wessling, *J. Mem. Sci.* **2021**, *618*, S. 118632.

[158] J.-Y. Zhou, Z.-Y. Luo, M.-J. Yin, N. Wang, Z. Qin, K.-R. Lee, Q.-F. An, *J. Mem. Sci.* **2020**, *610*, S. 118404.

[159] Y. F. Mi, N. Wang, Q. Qi, B. Yu, X. D. Peng, Z. H. Cao, *Sep. Purif. Technol.* **2020**, *248*, S. 117079.

[160] C. Jiang, L. Zhang, P. Li, H. Sun, Y. Hou, Q. J. Niu, *ACS Appl. Mater. Interfaces* **2020**, *12*, S. 25304–25315.

[161] K. Froehlich, S. Nasir, M. Ali, P. Ramirez, J. Cervera, S. Mafe, W. Ensinger, *J. Mem. Sci.* **2021**, *617*, S. 118633.

[162] M. V. Zdorovets, A. B. Yeszhanov, I. V. Korolkov, O. Güven, S. S. Dosmagambetova, D. I. Shlimas, Z.K. Zhatkanbayeva, I. S. Zhidkov, P. V. Kharkin, V. N. Gluchshenko et al., *Progr. Nucl. Energy* **2020**, *118*, S. 103128.

[163] D. Ji, C. Xiao, K. Chen, F. Zhou, Y. Gao, T. Zhang, H. Ling, *J. Mem. Sci.* **2021**, *621*, S. 118953.

[164] D. Ji, C. Xiao, S. An, K. Chen, Y. Gao, F. Zhou, T. Zhang, *J. Hazard. Mater.* **2020**, *398*, S. 122823.

[165] K. C. Khulbe, C. Y. Feng, T. Matsuura, *Synthetic Polymeric Membranes. Characterization by Atomic Force Microscopy*, Springer-Verlag, Berlin, Heidelberg, **2008**.

[166] M. Sadrzahdeh, T. Mohammadi (Hrsg.) *Nanocomposite Membranes for Water and Gas Separation. Micro and Nano Technologies*, Elsevier, **2020**.

[167] K. Yoon, K. Kim, X. Wang, D. Fang, B. S. Hsiao, B. Chu, *Polymer* **2006**, *47*, S. 2434–2441.

[168] B. S. Lalia, V. Kochkodan, R. Hashaikeh, N. Hilal, *Desalination* **2013**, *326*, S. 77–95.

[169] R. W. Baker, *Membrane Technology and Applications,* 3. Aufl., Wiley, Chichester, UK, **2012**.

[170] J. G. Wijmans, R. W. Baker, *J. Mem. Sci.* **1995**, *107*, S. 1–21.

[171] I. M. Hutten, *Handbook of Nonwoven Filter Media*, Elsevier/BH, Amsterdam, **2007**.

[172] Z. Wang, C. Crandall, R. Sahadevan, T. J. Menkhaus, H. Fong, *Polymer* **2017**, *114*, S. 64–72.

[173] M. Li, J. Li, M. Zhou, Y. Xian, Y. Shui, M. Wu, Y. Yao, *J. Appl. Polym. Sci.* **2019**, *137*, S. 48416.

[174] S. Tul Muntha, A. Kausar, M. Siddiq, *Polym. Plast. Technol. Eng.* **2017**, *56*, S. 841–856.

[175] N. García Doménech, F. Purcell-Milton, Y. K. Gun'ko, *Mater. Today Commun.* **2020**, *23*, S. 100888.

[176] R. H. Hailemariam, Y. C. Woo, M. M. Damtie, B. C. Kim, K.-D. Park, J.-S. Choi, *Adv. Colloid Interface Sci.* **2020**, *276*, S. 102100.

[177] Z. Yang, D. Saeki, H. Matsuyama, *J. Mem. Sci.* **2018**, *550*, S. 332–339.

[178] Z. Berk, *Food Process Engineering and Technology*, 1. Aufl., Elsevier/Academic Press, Amsterdam, Boston, **2009**.

[179] C. R. Gough, K. Callaway, E. Spencer, K. Leisy, G. Jiang, S. Yang, X. Hu, *ACS omega* **2021**, *6*, S. 11804–11812.

[180] A. Mamun, T. Blachowicz, L. Sabantina, *Polymers* **2021**, *13*.

[181] B. Robert, G. Nallathambi, *Colloid Interface Sci. Commun.* **2020**, *37*, S. 100275.

[182] S. Han, J. Kim, S. H. Ko, *Mater. Today Adv.* **2021**, *9*, S. 100134.

[183] Y. Li, X. Yin, J. Yu, B. Ding, *Compos. Commun.* **2019**, *15*, S. 6–19.

[184] W. W.-F. Leung, C.-H. Hung, P.-T. Yuen, *Sep. Purif. Technol.* **2010**, *71*, S. 30–37.

[185] Y. Bian, S. Wang, L. Zhang, C. Chen, *Build. Environ.* **2020**, *170*, S. 106628.

[186] P. Bahmani, A. Maleki, H. Daraei, R. Rezaee, M. Khamforoush, S. Dehestani Athar, F. Gharibi, A. H. Ziaee, G. McKay, *Environ. Sci. Pollut. Res. Int.* **2019**, *26*, S. 21993–22009.

[187] J. R. McCutcheon, M. Elimelech, *J. Mem. Sci.* **2008**, *318*, S. 458–466.

[188] X. Liu, H. Ma, B. S. Hsiao, *ACS Appl. Nano Mater.* **2019**, *2*, S. 3606–3614.

[189] S. Zhang, N. Tang, L. Cao, X. Yin, J. Yu, B. Ding, *ACS Appl. Mater. Interfaces* **2016**, *8*, S. 29062–29072.

[190] K. M. Yun, A. B. Suryamas, F. Iskandar, L. Bao, H. Niinuma, K. Okuyama, *Sep. Purif. Technol.* **2010**, *75*, S. 340–345.

[191] A. Mautner, *Polym. Int.* **2020**, *69*, S. 741–751.

[192] S. Jiang, Y. Li, B. P. Ladewig, *Sci. Total Environ.* **2017**, *595*, S. 567–583.

[193] T. Melin, R. Rautenbach, *Membranverfahren. Grundlagen der Modul- und Anlagenauslegung ; mit 76 Tabellen*, 3. Aufl., Springer, Berlin, **2007**.

[194] A. Bogler, E. Bar-Zeev, *Environ. Sci. Technol.* **2018**, *52*, S. 10019–10029.

[195] R. Cruz-Silva, Y. Takizawa, A. Nakaruk, M. Katouda, A. Yamanaka, J. Ortiz-Medina, A. Morelos-Gomez, S. Tejima, M. Obata, K. Takeuchi et al., *Environ. Sci. Technol.* **2019**, *53*, S. 6255–6263.

[196] Y. Ding, B. Ma, H. Liu, J. Qu, *J. Environ. Sci.* **2019**, *77*, S. 273–281.

[197] Q. Liu, G.-R. Xu, R. Das, *Desalination* **2019**, *468*, S. 114065.

[198] W. Guo, H. Ngo, J. Li, *Bioresour. Technol.* **2012**, S. 27–34.

[199] A. F. Ismail, M. A. Rahman, M. H. D. Othman, T. Matsuura (Hrsg.) *Handbooks in separation science*, Elsevier, Amsterdam, Netherlands, **2019**.

[200] C. Regula, E. Carretier, Y. Wyart, G. Gésan-Guiziou, A. Vincent, D. Boudot, P. Moulin, *Water Res.* **2014**, *56*, S. 325–365.

[201] E. Obotey Ezugbe, S. Rathilal, *Membranes* **2020**, *10*.

[202] J. C.-T. Lin, D.-J. Lee, C. Huang, *Sep. Sci. Technol.* **2010**, *45*, S. 858–872.

[203] X. Shi, G. Tal, N. P. Hankins, V. Gitis, *J. Water Proc. Eng.* **2014**, *1*, S. 121–138.

[204] D. Zhao, S. Yu, *Desalination Water Treat.* **2014**, *55*, S. 870–891.

[205] G. Moradi, L. Rajabi, F. Dabirian, S. Zinadini, *J. Appl. Polym. Sci.* **2018**, *135*, S. 45738.

[206] D. J. Miller, D. R. Dreyer, C. W. Bielawski, D. R. Paul, B. D. Freeman, *Angew. Chem.* **2017**, *56*, S. 4662–4711.

[207] R. S. Kurusu, N. R. Demarquette, *Int. Mater. Rev.* **2018**, *64*, S. 249–287.

[208] M. Dufay, M. Jimenez, S. Degoutin, *ACS Appl. Bio Mater.* **2020**, *3*, S. 4696–4716.

[209] Q. Zia, M. Tabassum, J. Meng, Z. Xin, H. Gong, J. Li, *Int. J. Biol. Macromol.* **2021**, *167*, S. 1479–1490.

[210] Y.-H. Chiao, S.-T. Chen, M. Sivakumar, M. B. M. Y. Ang, T. Patra, J. Almodovar, S. R. Wickramasinghe, W.-S. Hung, J.-Y. Lai, *Polymers* **2020**, *12*.

[211] P. Sagitha, C. R. Reshmi, S. P. Sundaran, A. Sujith, *Eur. Polym. J.* **2018**, *105*, S. 227–249.

[212] J. J. Ahire, D. P. Neveling, L. M. T. Dicks, *Appl. Microbiol. Biotechnol.* **2018**, *102*, S. 7171–7181.

[213] B. Al-Ghafri, W.-J. Lau, M. Al-Abri, P.-S. Goh, A. F. Ismail, *J. Water Process Eng.* **2019**, *32*, S. 100970.

[214] D. Lv, R. Wang, G. Tang, Z. Mou, J. Lei, J. Han, S. de Smedt, R. Xiong, C. Huang, *ACS Appl. Mater. Interfaces* **2019**, *11*, S. 12880–12889.

[215] P. Cheng, X. Wang, Y. Liu, C. Kong, N. Liu, Y. Wan, Q. Guo, K. Liu, Z. Lu, M. Li et al., *Appl. Surf. Sci.* **2020**, *506*, S. 144664.

[216] M. Toriello, M. Afsari, H. K. Shon, L. D. Tijing, *Membranes* **2020**, *10*.

[217] F. Navarro-Pardo, A. L. Martinez-Hernandez, C. Velasco-Santos, *J. Nanomater.* **2016**, *2016*, S. 1–16.

[218] X. Gao, S. Han, R. Zhang, G. Liu, J. Wu, *J. Mater. Chem. B* **2019**, *7*, S. 7075–7089.

[219] H. Zhao, S. Chen, X. Quan, H. Yu, H. Zhao, *Appl. Catal. Environ.* **2016**, *194*, S. 134–140.

[220] B. J. Deka, J. Guo, A. K. An, *J. Mem. Sci.* **2021**, *624*, S. 119089.

[221] Y. Yang, Y. Li, L. Cao, Y. Wang, L. Li, W. Li, *Sep. Purif. Technol.* **2021**, *269*, S. 118726.

[222] X. Li, X. Yu, C. Cheng, L. Deng, M. Wang, X. Wang, *ACS Appl. Mater. Interfaces* **2015**, *7*, S. 21919–21930.

[223] A. C. Canalli Bortolassi, V. G. Guerra, M. L. Aguiar, L. Soussan, D. Cornu, P. Miele, M. Bechelany, *J. Nanomater.* **2019**, *9*.

[224] X. Ji, Y. Xu, W. Zhang, L. Cui, J. Liu, *Compos. Appl. Sci. Manuf.* **2016**, *87*, S. 29–45.

[225] N. Madima, S. B. Mishra, I. Inamuddin, A. K. Mishra, *Environ. Chem. Lett.* **2020**, *18*, S. 1169–1191.

[226] K. Wang, T. C. Zhang, B. Wei, S. Chen, Y. Liang, S. Yuan, *Colloids Surf. Physicochem. Eng. Asp.* **2021**, *608*, S. 125342.

[227] L. Wang, Y. Chen, L. Lin, H. Wang, X. Huang, H. Xue, J. Gao, *Chem. Eng. J.* **2019**, *362*, S. 89–98.

[228] C. Li, J. Yang, L. Zhang, S. Li, Y. Yuan, X. Xiao, X. Fan, C. Song, *Environ. Chem. Lett.* **2021**, *19*, S. 1457–1475.

[229] E. Santoso, R. Ediati, Y. Kusumawati, H. Bahruji, D. O. Sulistiono, D. Prasetyoko, *Mater. Today Chem.* **2020**, *16*, S. 100233.

[230] C. Zhang, L. Yao, Z. Yang, E. S.-W. Kong, X. Zhu, Y. Zhang, *ACS Appl. Nano Mater.* **2019**, *2*, S. 3916–3924.

[231] J. Lee, J. Yoon, J.-H. Kim, T. Lee, H. Byun, *J. Appl. Polym. Sci.* **2018**, *135*, S. 45858.

[232] R. Al-Attabi, Y. Morsi, J. A. Schütz, D. Cornu, M. Maghe, L. F. Dumée, *Sci. Total Environ.* **2021**, *754*, S. 142231.

[233] K. P. Gopinath, D.-V. N. Vo, D. Gnana Prakash, A. Adithya Joseph, S. Viswanathan, J. Arun, *Environ. Chem. Lett.* **2021**, *19*, S. 557–582.

[234] L. Du, X. Quan, X. Fan, G. Wei, S. Chen, *J. Mem. Sci.* **2020**, *596*, S. 117613.

[235] Q. Wang, O. Yildiz, A. Li, K. Aly, Y. Qiu, Q. Jiang, D. Y.H. Pui, S.-C. Chen, P. D. Bradford, *Sep. Purif. Technol.* **2020**, *236*, S. 116255.

[236] L. Xie, Y. Shu, Y. Hu, J. Cheng, Y. Chen, *Chemosphere* **2020**, *251*, S. 126286.

[237] P. A. Kobielska, A. J. Howarth, O. K. Farha, S. Nayak, *Coord. Chem. Rev.* **2018**, *358*, S. 92–107.

[238] Y. Dou, W. Zhang, A. Kaiser, *Adv. Sci.* **2020**, *7*, S. 1902590.

[239] J. Wen, Y. Fang, G. Zeng, *Chemosphere* **2018**, *201*, S. 627–643.

[240] R. Zhao, Y. Tian, G. Zhu, *J. Mater. Chem.* **2019**, *7*, S. 22559–22570.

[241] H. Chen, M. Huang, Y. Liu, L. Meng, M. Ma, *Sci. Total Environ.* **2020**, *739*, S. 139944.

[242] J. Cui, F. Li, Y. Wang, Q. Zhang, W. Ma, C. Huang, *Sep. Purif. Technol.* **2020**, *250*, S. 117116.

[243] M. Mazzucato **2018**.

[244] "Grüner Baum", zu finden unter https://www.pexels.com/de-de/foto/gruner-baum-auf-grasfeld-wahrend-des-tages-53435/.

[245] "Seetang", zu finden unter https://pixabay.com/de/photos/seetang-unterwasser-gr%C3%BCn-wasser-1129226/.

[246] "Krabbe", zu finden unter https://pixabay.com/de/photos/krebstier-krabbe-meer-strand-klaue-3377646/.

[247] R. Brandes, F. Brouillette, B. Chabot, *J. Appl. Polym. Sci.* **2021**, *138*, S. 50021.

[248] A. Kakoria, S. Sinha-Ray, *Fibers* **2018**, *6*, S. 45.

[249] D. Gandavadi, S. Sundarrajan, S. Ramakrishna, *Macromol. Mater. Eng.* **2019**, *304*, S. 1900345.

[250] Q. Zia, M. Tabassum, Z. Lu, M. T. Khawar, J. Song, H. Gong, J. Meng, Z. Li, J. Li, *Carbohydr. Polym.* **2020**, *227*, S. 115343.

[251] T. C. Mokhena, M. J. Mochane, A. Mtibe, M. J. John, E. R. Sadiku, J. S. Sefadi, *Materials* **2020**, *13*.

[252] P. Kianfar, A. Vitale, S. Dalle Vacche, R. Bongiovanni, *Carbohyd. Polym.* **2019**, *217*, S. 144–151.

[253] S. Wilk, A. Benko, *J. Funct. Biomater.* **2021**, *12*.

[254] S. S. Vedula, G. D. Yadav, *J. Indian Chem. Soc.* **2021**, *98*, S. 100017.

[255] I. I. Cárdenas Bates, É. Loranger, A. P. Mathew, B. Chabot, *Cellulose* **2021**, *28*, S. 4865–4885.

[256] D. Yang, L. Li, B. Chen, S. Shi, J. Nie, G. Ma, *Polymer* **2019**, *163*, S. 74–85.

[257] D.-N. Phan, M. Q. Khan, N.-T. Nguyen, T.-T. Phan, A. Ullah, M. Khatri, N. N. Kien, I.-S. Kim, *Carbohydr. Polym.* **2021**, *252*, S. 117175.

[258] S. A. Parekh, R. N. David, K. K. R. Bannuru, L. Krishnaswamy, A. Baji, *Membranes* **2018**, *8*.

[259] L. Qi, Z. Liu, N. Wang, Y. Hu, *Appl. Surf. Sci.* **2018**, *456*, S. 95–103.

[260] A. Joubert, S. A. Z. Abd Ali, M. Frossard, Y. Andrès, *Environ. Sci. Pollut. Res. Int.* **2021**, *28*, S. 39907–39919.

[261] H. Shen, Z. Zhou, H. Wang, M. Zhang, M. Han, D. P. Durkin, D. Shuai, Y. Shen, *Environ. Sci. Technol. Lett.* **2021**, *8*, S. 545–550.

[262] C. Xu, J. Jiang, H. Oguzlu, Y. Zheng, F. Jiang, *Carbohydr. Polym.* **2020**, *250*, S. 116960.

[263] W.-C. Chen, C.-Y. Ko, K.-C. Chang, C.-H. Chen, *Mater. Chem. Phys.* **2020**, *254*, S. 123300.

[264] M. K. Selatile, V. Ojijo, R. Sadiku, S. S. Ray, *Polym. Degrad. Stab.* **2020**, *178*, S. 109205.

[265] I. S. Kurtz, J. D. Schiffman, *Materials* **2018**, *11*.

[266] B. Zeytuncu, M. Ürper, İ. Koyuncu, V. V. Tarabara, *Sep. Purif. Technol.* **2018**, *197*, S. 432–438.

[267] C. Wang, J. Fan, R. Xu, L. Zhang, S. Zhong, W. Wang, D. Yu, *J. Mater. Sci.* **2019**, *54*, S. 12522–12532.

[268] J. Hoque, U. Adhikary, V. Yadav, S. Samaddar, M. M. Konai, R. G. Prakash, K. Paramanandham, B. R. Shome, K. Sanyal, J. Haldar, *Mol. Pharm.* **2016**, *13*, S. 3578–3589.

[269] M. Azizi-Lalabadi, H. Hashemi, J. Feng, S. M. Jafari, *Adv. Colloid Interface Sci.* **2020**, *284*, S. 102250.

[270] M. A. Saleemi, P. V. C. Yong, E. H. Wong, *Nano-Struct. Nano-Objects* **2020**, *24*, S. 100612.

[271] Y. Han, Z.-C. Zhou, L. Zhu, Y.-Y. Wei, W.-Q. Feng, L. Xu, Y. Liu, Z.-J. Lin, X.-Y. Shuai, Z.-J. Zhang et al., *Environ. Sci. Pollut. Res. Int.* **2019**, *26*, S. 28352–28360.

[272] E. Wistrand-Yuen, M. Knopp, K. Hjort, S. Koskiniemi, O. G. Berg, D. I. Andersson, *Nat. Commun.* **2018**, *9*, S. 1599.

[273] E. Y. Klein, T. P. van Boeckel, E. M. Martinez, S. Pant, S. Gandra, S. A. Levin, H. Goossens, R. Laxminarayan, *Proc. Natl. Acad. Sci.* **2018**, *115*, E3463-E3470.

[274] P. Kovalakova, L. Cizmas, T. J. McDonald, B. Marsalek, M. Feng, V. K. Sharma, *Chemosphere* **2020**, *251*, S. 126351.

[275] Y. Liang, J. Liu, Q. Zhong, D. Yu, J. Yao, T. Huang, M. Zhu, T. Zhou, *J. Pharm. Biomed. Anal.* **2019**, *174*, S. 330–339.

[276] L. Paradis-Tanguay, A. Camiré, M. Renaud, B. Chabot, A. Lajeunesse, *J. Polym. Eng.* **2019**, *39*, S. 207–215.

[277] A. Camiré, J. Espinasse, B. Chabot, A. Lajeunesse, *Environ. Sci. Pollut. Res. Int.* **2020**, *27*, S. 3560–3573.

[278] L. D. Nghiem, A. I. Schäfer, M. Elimelech, *Environ. Sci. Technol.* **2005**, *39*, S. 7698–7705.

[279] X. Wei, Q. Zhang, S. Cao, X. Xu, Y. Chen, L. Liu, R. Yang, J. Chen, B. Lv, *Environ. Sci. Pollut. Res. Int.* **2021**, *28*, S. 8486–8497.

[280] J. Hao, Q. Zhang, P. Chen, X. Zheng, Y. Wu, D. Ma, D. Wei, H. Liu, G. Liu, W. Lv, *Environ. Sci. Nano* **2019**, *6*, S. 3374–3387.

[281] T. G. Kebede, S. Dube, M. M. Nindi, *J. Environ. Chem. Eng.* **2019**, *7*, S. 103330.

[282] R. Castagna, S. Donini, P. Colnago, A. Serafini, E. Parisini, C. Bertarelli, *ACS omega* **2019**, *4*, S. 13270–13278.

[283] K. C. Hui, H. Suhaimi, N. S. Sambudi, *Rev. Chem. Eng.* **2019**, *0*.

[284] Y. Cui, Z. Jiang, C. Xu, M. Zhu, W. Li, C. Wang, *RSC Adv.* **2021**, *11*, S. 19579–19586.

[285] H. S. Zakria, M. H. D. Othman, R. Kamaludin, S. H. Sheikh Abdul Kadir, T. A. Kurniawan, A. Jilani, *RSC Adv.* **2021**, *11*, S. 6985–7014.

[286] H. Zhang, Y. Wan, J. Luo, S. B. Darling, *ACS Appl. Mater. Interfaces* **2021**, *13*, S. 14844–14865.

[287] M. Sillanpää, M. C. Ncibi, A. Matilainen, *J. Environ. Manage.* **2018**, *208*, S. 56–76.

[288] M. Coto, S. C. Troughton, J. Duan, R. V. Kumar, T. W. Clyne, *Appl. Surf. Sci.* **2018**, *433*, S. 101–107.

[289] J. Guo, D. Y.S. Yan, F. L.-Y. Lam, B. J. Deka, X. Lv, Y. H. Ng, A. K. An, *Chem. Eng. J.* **2019**, *378*, S. 122137.

[290] Y. Gao, N. Yan, C. Jiang, C. Xu, S. Yu, P. Liang, X. Zhang, S. Liang, X. Huang, *Appl. Catal. B* **2020**, *268*, S. 118737.

[291] W. S. Koe, J. W. Lee, W. C. Chong, Y. L. Pang, L. C. Sim, *Environ. Sci. Pollut. Res. Int.* **2020**, *27*, S. 2522–2565.

[292] Y. Shi, J. Huang, G. Zeng, W. Cheng, J. Hu, *J. Mem. Sci.* **2019**, *584*, S. 364–392.

[293] Y. Zhan, J. Lan, J. Shang, L. Yang, X. Guan, W. Li, S. Chen, Y. Qi, S. Lin, *J. Alloys Compd.* **2020**, *822*, S. 153579.

[294] L. Zhang, Y. He, L. Ma, J. Chen, Y. Fan, S. Zhang, H. Shi, Z. Li, P. Luo, *ACS Appl. Mater. Interfaces* **2019**, *11*, S. 34487–34496.

[295] X. Li, G. Huang, X. Chen, J. Huang, M. Li, J. Yin, Y. Liang, Y. Yao, Y. Li, *Sci. Total Environ.* **2021**, *792*, S. 148462.

[296] H. Ali, E. Khan, *Toxicol. Environ. Chem.* **2018**, *100*, S. 6–19.

[297] A. R. Esfahani, Z. Zhang, Y. Y. L. Sip, L. Zhai, A.H.M. A. Sadmani, *J. Water Process Eng.* **2020**, *37*, S. 101438.

[298] E. S. Mansor, H. Ali, A. Abdel-Karim, *Colloid Interface Sci. Commun.* **2020**, *39*, S. 100314.

[299] L. Huang, M. He, B. Chen, B. Hu, *Chemosphere* **2018**, *199*, S. 435–444.

[300] D. Morillo Martín, M. Faccini, M. A. García, D. Amantia, *J. Environ. Chem. Eng.* **2018**, *6*, S. 236–245.

[301] D.-N. Phan, H. Lee, B. Huang, Y. Mukai, I.-S. Kim, *Cellulose* **2019**, *26*, S. 1781–1793.

[302] F. Zhu, Y.-M. Zheng, B.-G. Zhang, Y.-R. Dai, *J. Hazard. Mater.* **2021**, *401*, S. 123608.

[303] Y. Huang, Y.-E. Miao, T. Liu, *J. Appl. Polym. Sci.* **2014**, *131*, n/a-n/a.

[304] M. Faccini, G. Borja, D. Amantia, *J. Nanomater.* **2015**, *2015*, S. 1–9.

[305] N. Mahanta, S. Valiyaveettil, *Nanoscale* **2011**, *3*, S. 4625–4631.

[306] M. Enfrin, J. Lee, P. Le-Clech, L. F. Dumée, *J. Mem. Sci.* **2020**, *601*, S. 117890.

[307] X. Liu, B. Jiang, X. Yin, H. Ma, B. S. Hsiao, *Sep. Purif. Technol.* **2020**, *233*, S. 115976.

[308] R. Wang, L. Zhang, B. Chen, X. Zhu, *J. Mem. Sci.* **2020**, *614*, S. 118470.

[309] Z. Karim, A. P. Mathew, V. Kokol, J. Wei, M. Grahn, *RSC Adv.* **2016**, *6*, S. 20644–20653.

[310] A. Onur, A. Ng, W. Batchelor, G. Garnier, *Front. Chem.* **2018**, *6*, S. 417.

[311] H. Cai, E. G. Xu, F. Du, R. Li, J. Liu, H. Shi, *Chem. Eng. J.* **2021**, *410*, S. 128208.

[312] P. Li, Q. Li, Z. Hao, S. Yu, J. Liu, *J. Environ. Sci.* **2020**, *94*, S. 88–99.

[313] J. T. Buchman, N. V. Hudson-Smith, K. M. Landy, C. L. Haynes, *Acc. Chem. Res.* **2019**, *52*, S. 1632–1642.

[314] E. Giebel, C. Mattheis, S. Agarwal, A. Greiner, *Adv. Funct. Mater.* **2013**, *23*, S. 3156–3163.

6. Conclusion

In this thesis, the filtration of certain metal, metal oxide, and plastic nanoparticles with electrospun membranes was investigated. The electrospun membranes achieved high filtration efficiencies by interaction based filtration mechanisms and, thus, might be more often utilized in filter design in the future. The utilized electrospun membranes were fabricated with pore sizes of roughly 1 µm to ensure similar conditions for all executed filtration experiments. It was already demonstrated that the pore size has a major impact on the pressure drop on the membrane, but it might also influence the filtration efficiency. Thus, the relation between pore size and filtration efficiency might be another key parameter, which should be investigated for understanding affinity membranes in depth.

The electrospun membranes have been demonstrated to be a useful tool for water filtration, especially for emerging contaminants. These pollutants can hardly be addressed by common filtration methods, showing the outstanding properties of the prepared electrospun membranes to specifically adsorb these contaminants. Thus, these electrospun membranes are most valuable for filtration of specific contaminants and should be protected from becoming polluted by common wastewater pollutants. This might be regulated by implementing these electrospun membranes in stacked-layers with other filter materials, where each layer is selected for its own function, e.g. addressing different particle sizes or contaminant properties, mechanical support.[310]

The membranes were regenerated after filtration by rinsing with low concentrated acids. This procedure removes the contaminants from the fiber surfaces and allows the reuse of the membranes. However, not all contaminants might be detached from the fibers under acidic conditions. Furthermore, every cleaning procedure might contribute to the membrane degradation. Thus, other membrane regeneration methods should be considered.

The filtration experiments were conducted in a dead-end filtration setup, which is very common for a variety of commercial used filtration systems. However, this setup is limited by some inherent drawbacks, such as cake formation and high pressure drops. Those limitations might be overcome by other filter designs.

7. Outlook

The purification of nanoparticle-contaminated environmental media will attract more and more attention in the next few years, because potentially released amounts of nanoparticles with unknown adverse effects on biological systems will increase.

Prospective developments in the **field of nanoparticle fate and safety** need to include improved detection methods of nanoparticles in environmental media. To date, one major limiting factor for observing nanoparticle numbers and their fate in the environment is the lack of suitable detection methods.[311],[312] Furthermore, different publications highlighted the influence of nanoparticle properties, such as shape, size, and ligands, on their toxicity. Thus, nanoparticles commercially used should be designed considering these influences with the intention of reducing their toxicity.[313]

Filtration of environmental media provides a fast and efficient approach but faces particular limitations. So far, commercially applied membranes are used mainly for size-exclusion separation, resulting in high pressure drops (**chapter 1.3.1**). Thus, more research needs to be done to reduce the pressure drop, which can be approached by utilizing affinity membranes. Here, the maximum pore size should be determined at which high filtration efficiencies can still be reached. The adsorption of specific contaminates by membrane surface modifications can be a suitable approach for improving the filtration efficiency. In general, filtration systems have to be more specific because a rising number of new contaminants might deteriorate water purification dealt with by common treatment methods. Contaminants, such as persistent organic pollutants, hormones, and pharmaceuticals, can hardly be addressed by charged membranes but need more specific adsorption sites. Additionally, more sophisticated membrane regeneration methods need to be developed to prolong the membrane lifetime and contribute less to membrane degradation.

Additionally, the membrane material and manufacturing process must be reviewed considering **sustainability aspects**. Electrospinning, for example, from aqueous media has already reported and the utilization of carbohydrate polymers implemented.[314],[247] Research here should focus on the investigation of scale-up procedures for the electrospinning of bio-based carbohydrate polymers from water.

8. Acknowledgments

First of all, I would like to thank Prof. Andreas Greiner for giving me the opportunity to work on my doctoral thesis in his group. I am very grateful to have been able to do research in such an exciting field, which has become more and more popular and relevant during my time as a doctoral student. I also appreciate the opportunity to work in interdisciplinary collaborations. Thank you for the constructive discussions and your support in writing publications and all other aspects of life.

I would also like to thank Prof. Agarwal, who has always advanced the research on my doctoral thesis topic with interesting questions and raised new perspectives.

I would also like to thank all my colleagues at MC 2 for welcoming me warmly into the team and making it a pleasure to go to work every day. Thank you for the support, interesting discussions, hilarious hours and a lot of fun. This is especially true for my direct colleagues in the lab: Pin Hu, Chen Liang, Lisa Leitner, Simon Neumann, Thomas Schmidt, Nikola Majstorovic, Felix Bretschneider, Marius Schmidt and Sophie Fritze.

Special thanks to my family who have always supported me and made this path possible. Thank you for backing me up and being there for me in all situations in life.

9. Eidesstattliche Versicherungen und Erklärungen

(§ 9 Satz Nr. 3 PromO BayNat, 2021)

Hiermit versichere ich eidesstattlich, dass ich die Arbeit selbstständig verfasst und keine andere als die von angegebenen Quellen und Hilfsmittel benutzt habe (vgl. Art. 64 Abs. 1 Satz 6 BayHSchG).

(§ 9 Satz Nr.3 PromO BayNat, 2021)

Hiermit erkläre ich, dass ich die Dissertation nicht bereits zur Erlangung eines akademischen Grades eingereicht habe und dass ich nicht bereits diese oder eine gleichartige Doktorprüfung endgültig nicht bestanden habe.

(§ 9 Nr.4 PromO BayNat, 2021)

Hiermit erkläre ich, dass ich Hilfe von gewerblichen Promotionsberatern bzw. –vermittlern oder ähnlichen Dienstleistern weder bisher in Anspruch genommen habe noch künftig in Anspruch nehmen werde.

(§ 9 Nr.7 PromO BayNat, 2021)

Hiermit erkläre ich mein Einverständnis, dass die elektronische Fassung der Dissertation unter Wahrung meiner Urheberrechte und des Datenschutzes einer gesonderten Prüfung unterzogen werden kann.

(§ 9 Nr. 9 PromO BayNat, 2021)

Hiermit erkläre ich mein Einverständnis, dass bei Verdacht auf wissenschaftliches Fehlverhalten Ermittlungen durch universitätsinterne Organe der wissenschaftlichen Selbstkontrolle stattfinden können.

_____ _____

(Ort, Datum) (Unterschrift)